



University
of Glasgow

Ismail, Norilmi Amilia (2012) *The dynamics of a flexible Motorised Momentum Exchange Tether (MMET)*.
PhD thesis.

<http://theses.gla.ac.uk/3115/>

Copyright and moral rights for this thesis are retained by the author

A copy can be downloaded for personal non-commercial research or study, without prior permission or charge

This thesis cannot be reproduced or quoted extensively from without first obtaining permission in writing from the Author

The content must not be changed in any way or sold commercially in any format or medium without the formal permission of the Author

When referring to this work, full bibliographic details including the author, title, awarding institution and date of the thesis must be given



THE DYNAMICS OF A FLEXIBLE MOTORISED MOMENTUM EXCHANGE TETHER (MMET)

by

Norilmi Amilia Ismail

Submitted in fulfilment of the requirement for the

Degree of Doctor Philosophy

School of Engineering

University of Glasgow

October 2011

Verily, With Hardship Comes Ease (Surah al-Sharh,94)

Abstract

This research presents a more complete flexible model for the Motorised Momentum Exchange Tether (MMET) concept. In order to analyse the vibration aspect of the problem the tether is modelled as a string governed by partial differential equations of motion, with specific static and dynamic boundary conditions and the tether sub-span is flexible and elastic, thereby allowing three dimensional displacements of the motorised tether. The boundary conditions lead to a specific frequency equation and the Eigenvalues from this provide the natural frequencies of the orbiting flexible motorised tether when static, accelerating in spin, and at terminal angular velocity. The rotation matrix is utilized to get the position vectors of the system's components in an inertial frame. The spatio-temporal coordinates $u(x,t)$, $v(x,t)$ and $w(x,t)$ are transformed to modal coordinates before applying Lagrange's equations and the pre-selected linear modes are included in generating the equations of motion. The equations of motion contain inertial nonlinearities of cubic order, and these show the potential for intricate intermodal coupling effects.

The study of planar and non-planar motions has been carried out and the differences in the modal responses in both motions between the rigid body and flexible model are highlighted and discussed. The dynamics and stability of the flexible MMET is investigated using the dynamical analysis tools for representing the behaviour of the tether system. The study also includes the engineering side of the MMET by investigating the power requirements of an electric motor located in the central facility of the Motorised Momentum Exchange Tether (MMET). A simulation was run using a specially written computer program to obtain the required minimum power for a typical duty cycle, and also to study the responses for three different operating conditions; before payload release, torque-off and reverse torques conditions for both the propulsion and outrigger system on both circular and elliptical orbits. The differences in the responses when using rigid body and flexible models of MMET are highlighted and discussed in order to look at the sensitivity of the model to the power budget calculations. The study then continues with a comparative study between the MMET and conventional propulsion systems in terms of the energy used specifically for an Earth-Moon return mission for circular and elliptical orbits.

Table of Contents

Abstract	i
Table of Contents	ii
List of Tables.....	v
List of Figures	vi
Acknowledgement.....	xii
Acknowledgement.....	xii
Nomenclature	xiii
Chapter 1	1
Introduction	1
1.1 Motivations	1
1.2 Research Aims and Objectives.....	2
1.3 Thesis Overview.....	3
Chapter 2	4
Literature Review of Space Tethers	4
2.1 Background History	4
2.2 Space Tethers: Concepts and Applications	6
2.3 The Tether Missions.....	14
2.4 Tether dynamics	19
Chapter 3	23
Dynamics of the Two Dimensional Flexible Tether Model.....	23
3.1 Introduction	23
3.2 Tether Modelling.....	23
3.3 Modelling of the Flexible Model of the MMET	26
3.4 Equations of Motion.....	42
3.5 Tether Simulation.....	48
3.6 Conclusions	59
Chapter 4	60
Dynamics of Three Dimensional Rigid Body and Flexible Motorised Tethers.....	60
4.1 Introduction	60
4.2 Three Dimensional Model of Rigid Body.....	60
4.3 Kinetic Energy of the Rigid Body Model	63

4.4	Potential Energy of the Rigid Body Model.....	64
4.5	Equations of Motion for the Rigid Body Model	64
4.6	Simulation of the Rigid Body Model	65
4.7	Dynamics of a Three Dimensional Flexible MMET.....	71
4.8	Coordinate transformation	72
4.9	Energy Expression	74
4.10	Mode Shape Function for the Static Boundary Condition.....	75
4.11	Derivation of the Equations of Motion (EOM).....	76
4.12	Simulation of Flexible Model of MMET	76
4.13	Conclusions	87
Chapter 5		88
Dynamic Boundary Conditions.....		88
5.1	Introduction	88
5.2	Fixed-Attached Mass Boundary Condition.....	88
5.3	Boundary Conditions where Both Ends of the Sub span terminate in Masses..	101
5.4	Mode Shape Equation for Axial vibration	111
5.5	Discussions.....	117
5.6	Conclusions	120
Chapter 6		121
Dynamical System Analysis		121
6.1	Introduction	121
6.2	Equations of Motions for Dynamical System Analysis	121
6.3	Numerical Methods	124
6.4	Transition from Libration to Spin	126
6.5	Transition from Regular to Chaotic Motion.....	132
6.6	Comparison between the Onset of Spin and Chaos	139
6.7	Route to Chaos for a Three Dimensional Flexible Tether	144
6.8	Velocity Increment Generation for the Flexible Tether	155
6.9	Conclusions	158
Chapter 7		159
In-service Power Requirements for the Motorised Momentum Exchange Tether		159
7.1	Introduction	159
7.2	Escape velocity.....	159
7.3	Minimum Torque Analysis	160

7.4	Comparison of Orbital Performance.....	166
7.5	Operational conditions	167
7.6	Power Consumption and Energy.....	170
7.7	Power Profile of Rigid and Flexible Tether Models	171
7.8	Outrigger system	174
7.9	Energy Comparison.....	176
7.10	Conclusions	179
Chapter 8	180
Conclusions	180
8.1	Summary and Conclusions.....	180
8.2	Future works	182
References	183
Publications	192
Appendix A	193
Appendix B	198
Appendix C	202
Appendix D	207
Appendix E	213
Appendix F	223

List of Tables

Table 2.1 : Joint US and Japanese Mission.....	15
Table 5.1 : Roots of equation (5.11)	92
Table 5.2 : Natural frequencies of three different conditions	106
Table 5.3 : Total Centripetal force and tensile force.....	119
Table 7.1 : Orbital and tether parameters.....	178
Table 7.2 : Parameters for the outrigger system	178
Table 7.3 : Energy usage comparison for payload transfer to the moon.....	178

List of Figures

Figure 1.1 : Symmetrical Motorised Momentum Exchange Tethers.....	1
Figure 2.1: The tapered cable for the skyhook concept	5
Figure 2.2 : Configuration of Electrodynamic drag tether	9
Figure 2.3 : Debris removal process by electrodynamic tether.....	10
Figure 2.4 : Orbital path of a payload released above the tether's COM	11
Figure 3.1 : Displaced element of a flexible tether	27
Figure 3.2 : Orbital elements for a geocentric inertial co-ordinate system.....	29
Figure 3.3 : Local co-ordinate system for the two dimensional flexible model	30
Figure 3.4 : Position of point P' on the deformed tether	30
Figure 3.5 : Cylindrical shape of MMET components	36
Figure 3.6 : Unmotorised tether responses for the flexible model (line)	51
Figure 3.7 : Longitudinal and transverse vibration	51
Figure 3.8 : Angular displacement and angular velocity.	52
Figure 3.9 : The difference in the angular displacement.....	52
Figure 3.10 : Longitudinal and transverse vibration	53
Figure 3.11 : Angular displacement and angular velocity.	54
Figure 3.12 : Difference in the angular displacement.....	54
Figure 3.13 : The radius and true anomaly of the tether	55
Figure 3.14 : Longitudinal and Transverse vibration.....	55
Figure 3.15 : Angular displacement and angular velocity	56
Figure 3.16 : Difference in the angular displacement.....	56
Figure 3.17: Longitudinal vibration of the motorised flexible tether.....	57
Figure 3.18 : Transverse vibration of the motorised flexible tether.....	57
Figure 3.19 : Kinetic and Potential energy of the rigid body.....	58
Figure 3.20 : The elastic and gravitational potential energy	58
Figure 3.21 : The elastic and gravitational potential energy	59
Figure 4.1 : Geometry of a Motorised Momentum Exchange Tether.....	60

Figure 4.2 : Components of forces, after (Ziegler, 2003).	62
Figure 4.3 : Planar and non-planar motions of Massless tether 1 (dashed)	66
Figure 4.4 : Angular displacement of Massless tether 1 (dashed)	67
Figure 4.5 : Planar and non-planar motions of Massless tether 1 (dashed).	67
Figure 4.6 : Planar and non-planar motions of Massless tether 1 (dashed)	69
Figure 4.7 : (a) & (b) - Comparison of response between 2D (line).....	70
Figure 4.8 : Comparison of orbital parameters between 2D (line)	71
Figure 4.9 : Three dimensional flexible model of an MMET on orbit	72
Figure 4.10 : Translation of the central facility.....	72
Figure 4.11 : Rotation of the MMET system.	73
Figure 4.12 : Planar and non-planar motions of a rigid body tether (dashed)	77
Figure 4.13 : Angular displacement of a rigid body tether (dashed)	77
Figure 4.14 : Planar and non-planar motions of a rigid body tether (red)	78
Figure 4.15 : Displacements of the 3D Flexible model.	79
Figure 4.16 : Planar motions of a rigid body tether (dashed).....	80
Figure 4.17 : Planar motions of a rigid body tether (dashed).....	81
Figure 4.18 : Non-planar motions of a rigid body tether (dashed).....	81
Figure 4.19 : Planar and non planar motions of a rigid body tether (dashed).....	82
Figure 4.20 : Orbital parameters for 3D motion of a rigid body tether (dashed).....	83
Figure 4.21 : Displacements of the 3D Flexible model of the MMET	84
Figure 4.22 : Comparison of the response between the 2D (line).....	85
Figure 4.23 : The difference in orbital parameters between 2D	86
Figure 4.24 : Longitudinal and transverse displacement of 2D (line).....	86
Figure 5.1 : (a) Configuration of MMET (b) Schematic diagram.....	89
Figure 5.2 : The deflection angle of the string	89
Figure 5.3 : Modes shape for the transverse vibration.....	92
Figure 5.4 : Responses for the tether on a circular orbit	95
Figure 5.5 : Responses for tether on an elliptical orbit	96
Figure 5.6 : Responses of motorised MMET on a circular orbit	98

Figure 5.7 : Responses of the motorised MMET on an elliptical orbit.....	99
Figure 5.8 : Difference between the angular velocity for the tether	100
Figure 5.9 : Natural frequency for the first mode shape for the tether.....	100
Figure 5.10 : Schematic Diagram of masses connected to the tether sub-span	101
Figure 5.11 : Relationship between transverse oscillation frequency.....	106
Figure 5.12 : The first five mode shapes for the L.....	107
Figure 5.13 : Tether's response for $\dot{\psi} = 0.01$ rad/s, $\omega=0.0126$ rad/s over 5000 sec	109
Figure 5.14 : Tether's response for $\dot{\psi} = 0.01$ rad/s, $\omega=0.0126$ rad/s over 50000 sec	109
Figure 5.15 : Tether's responses with initial condition.....	110
Figure 5.16 : Tether's responses with initial condition.....	110
Figure 5.17 : Tether's response for an angular velocity of 0.062 rad/s	111
Figure 5.18 : Free body diagram of forces action in longitudinal direction	112
Figure 5.19 : Free body diagram of acting forces in axial direction	115
Figure 5.20 : Mode shape for : (a) fixed-attach mass boundary condition	117
Figure 5.21 : Geometric configuration of a statically rotating.....	119
Figure 6.1 : A Poincaré section with an intersecting orbit. (Thomsen, 2003)	125
Figure 6.2 : Time history of angular displacement for the flexible model.	127
Figure 6.3 : Time history of angular displacement for the flexible model	127
Figure 6.4 : Comparison of the effect of initial angular displacement.....	128
Figure 6.5 : Effect of initial angular displacement.....	129
Figure 6.6 : Effect of initial angular displacement.....	129
Figure 6.7 : Onset tether spin for the flexible model during first orbit.....	130
Figure 6.8 : Onset tether spin for rigid body model during first orbit	131
Figure 6.9 : Number of orbit passings before the tether begins to spin	132
Figure 6.10 : Bifurcation Diagram of the angular displacement.....	133
Figure 6.11 : Bifurcation Diagram of the angular displacement.....	133
Figure 6.12 : Bifurcation Diagram of the angular displacement.....	134
Figure 6.13 : Phase portrait and Poincaré Map for flexible tether motion.....	134

Figure 6.14 : Poincaré map for the flexible tether	135
Figure 6.15 : Poincaré map for the rigid body tether	135
Figure 6.16 : Poincaré map for the flexible tether	136
Figure 6.17 : Poincaré map for the flexible tether	136
Figure 6.18 : Poincaré Map for the flexible tether	136
Figure 6.19 : Poincaré map for the rigid body tether	137
Figure 6.20 : Bifurcation Diagram of the angular displacement.....	137
Figure 6.21 : Bifurcation Diagram of the angular displacement.....	138
Figure 6.22 : Bifurcation Diagram of the angular displacement.....	139
Figure 6.23 : Poincaré map for the flexible tether with initial condition.....	139
Figure 6.24 : Time history, phase plane, Poincaré map	140
Figure 6.25 : Time history, phase Plane, Poincaré map.....	140
Figure 6.26 : Time history, phase plane, Poincaré map	141
Figure 6.27 : Time history, phase plane, Poincaré map	141
Figure 6.28 : Time history, phase plane, Poincaré map	142
Figure 6.29 : Time history, phase plane, Poincaré map	142
Figure 6.30 : Time history, phase plane, Poincaré map	143
Figure 6.31 : Time history, phase plane, Poincaré map	143
Figure 6.32 : Bifurcation Diagram of the angular displacement.....	144
Figure 6.33 : Poincaré map of the tether with initial conditions.....	145
Figure 6.34 : Time history of the tether's pitch motion	147
Figure 6.35 : Time history of the tether's pitch motion	148
Figure 6.36 : Time history of the tether's pitch motion	149
Figure 6.37 : Time history of the tether's pitch motion	150
Figure 6.38 : Time history of the tether's pitch motion	151
Figure 6.39 : Time history of the tether's pitch motion	152
Figure 6.40 : Time history of the tether's pitch motion	153
Figure 6.41 : Time history of the tether's pitch motion	154

Figure 6.42 : Comparison of ψ_p obtained at perigee	156
Figure 6.43 : Comparison of ΔV obtained at perigee	156
Figure 6.44 : ΔV obtained at perigee after a full orbit	157
Figure 6.45 : ΔV obtained at perigee after a full orbit	157
Figure 6.46 : Comparison of ΔV obtained at perigee	158
Figure 7.1 : Single staging tether for payload transfer.....	161
Figure 7.2 : Oscillation conditions on a circular orbit	161
Figure 7.3 : Pure spin conditions on a circular orbit.....	162
Figure 7.4 : Angular velocity for tether sub-span	162
Figure 7.5 : Tether in an oscillation condition on an elliptical orbit.....	163
Figure 7.6 : Tether in the pure spin condition.....	164
Figure 7.7 : 3Orbital parameters for an elliptical orbit	164
Figure 7.8 : The release payload windows on an elliptical orbit	165
Figure 7.9 : Angular velocity for the spin up condition.....	165
Figure 7.10 : Time to release the payload.....	166
Figure 7.11 : Angular velocity for the tether on circular and elliptical orbits	166
Figure 7.12 : Angular velocity of the tether on circular and elliptical orbits.....	167
Figure 7.13 : Tether responses in the torque off condition for the circular orbit.....	168
Figure 7.14 : Tether responses in the torque off condition for the elliptical orbit.....	168
Figure 7.15 : The angular velocity of the tether on circular and elliptical orbits.....	169
Figure 7.16 : Profile of the angular displacement	169
Figure 7.17 : Profile of the angular velocity	170
Figure 7.18 : Power profile for the tether on a circular orbit.....	171
Figure 7.19 : Power profile for the tether on an elliptical orbit	171
Figure 7.20 : The difference in angular velocities	172
Figure 7.21 : The difference in angular velocities	172
Figure 7.22 : Power profile for the rigid body and flexible models.....	173
Figure 7.23 : Power profile for the rigid body and flexible models.....	173

Figure 7.24 : Responses of the outrigger system on a circular orbit.....	174
Figure 7.25 : Power consumption of the outrigger system on the circular orbit.....	174
Figure 7.26 : Angular velocity profile for the propulsion.....	175
Figure 7.27 : Angular velocity profile for the propulsion.....	175
Figure 7.28 : Earth-Moon Payload exchange by Cartmell & Ziegler (1999)	177

Acknowledgement

All praise is due to Allah. May Allah's peace and blessings be upon the one after whom there is no other prophet.

I would like to thank the many people who have helped this dissertation along over the years. As time went on, the list of the women and men who made it possible to complete this project grew longer and although these precious names are going to escape me, this is in no way lessens the importance of their presence and contribution.

During this academic year, my work has been accompanied by the presence of the amazing Professor Matthew Cartmell, of University of Glasgow who has guided me to complete this work in the best possible conditions through his constant guidance and brilliant suggestions. This dissertation has gained immeasurably through his expertise.

I am truly grateful to the Ministry of Higher Education of Malaysia and University Sains Malaysia for their sponsorship has enabled me to complete my study.

I am forever indebted to my beloved parents, Amri Ali and Ismail Sohod for their constant accompaniment, maternal advise and support. To all of my family members who have surrounded me with their unobstructive support and positive advise, I would here like to express my deepest gratitude.

At the University of Glasgow, everyone whom I have worked with has been extremely helpful. With all my heart, I would like to thank my sweetest friends Zaleha Mustafa, Rainah Ismail, Dr.Nuraishah and Rafidah Cusairi very warmly for their continuous help, permanent enthusiasm, friendship, and for being with me on this long journey of contemplation, tears and sweat. Not forgetting Rayyan Radzi for her devotion in helping me throughout the final submission.

For myself, this dissertation has been a personal accomplishment which I hope will benefit others as much as it has to me.

Nomenclature

α	non-planar angle
$\beta(x)$	mode shape function for lateral vibration
γ	angular displacement of motor torque axis about the tether's longitudinal axis
$\delta x, \delta y, \delta z$	Cartesian component of virtual displacement
δW	virtual work
ε_e	strain due to axial extension
ε_T	total strain due to axial extension and centripetal force
η	discreet quantity measuring last perigee passing prior to the onset of tether tumbling.
θ	true anomaly
μ	Earth's gravitational constant
$\xi(x)$	mode shape function for transverse vibration
ρ	density
σ	stress
τ	motor torque
$\phi(x)$	mode shape function for axial vibration
ψ	angular displacement of tether within the orbital angle
ψ_p	angular displacement at perigee within the orbital angle
$\dot{\psi}$	angular velocity of tether
ω	argument of perigee
ω_v	frequency for fixed-attached mass boundary condition
Ω_v	frequency for the static boundary condition
A	cross sectional area
a	semimajor axis for ecliptic orbit

ds	displaced element
E	modulus elasticity
E_t	total energy
e	orbit eccentricity
F_x, F_y, F_z	Cartesian component of the force = τ / L
f_{m1}	frequency massless tether 1
f_{m2}	frequency of massless tether 2
f_{RB}	frequency of a rigid body tether
g_o	gravity constant of 9.81 m/s^2
I_i	mass moment of inertia
I_{sp}	specific impulse
i	the inclination of the orbit
L	tether sub-span
M_m	mass of central facility
M_p	mass of payload
m	fuel mass
P_t	total power consumed by the tether
P'	an arbitrary point on the deformed tether
Q_i	non-conservatives forces acting on tether
$q_1(t)$	modal coordinate for axial vibration
$q_3(t)$	modal coordinate for lateral vibration
$q_2(t)$	modal coordinate for transverse vibration
R	distance from the central facility to the centre of the Earth
R_p	orbital radius at perigee
$R_{Y,\alpha}$	rotation matrix for non-planar movement

$R_{Z,\psi+\theta}$	rotation matrix for planar movement
r_m	radius of central facility
r_p	radius of payload
r_T	radius of tether's cross section
T	string's tension
T_o	centripetal forces
T_{rot}	kinetic energy for rotational motion
T_{trans}	kinetic energy for translational motion
T_k	total kinetic energy
$U_{E1,E2}$	elastic potential energy
U_G	gravitational potential energy
U_p	total potential energy
$u(x,t)$	longitudinal displacement
V_{orbit}	orbital velocity
V_{Total}	total velocity
$v(x,t)$	transverse displacement
$w(x,t)$	lateral displacement
X,Y,Z	coordinate frame, with the origin at the centre of the Earth
X_o,Y_o,Z_o	coordinate frame, with the origin at the centre of facility
$x_{t2p}, y_{t2p}, z_{t2p}$	Cartesian components for position of point P at sub-span
$x_{t1p}, y_{t1p}, z_{t1p}$	Cartesian components for position of point P at upper sub-span
x_{mm}, y_{mm}, z_{mm}	Cartesian components for the central facility
x_{P2}, y_{P2}, z_{P2}	Cartesian components for the lower end mass
x_{P1}, y_{P1}, z_{P1}	Cartesian components for the upper end mass
ΔV	tether's tip velocity

Chapter 1

Introduction

1.1 Motivations

The evolution of space transportation has created more ideas and advances concepts for space exploration and the rapid development of space exploration activities accentuates the general needs for efficient space transportation. The evolution based on two main objectives; first is to obtain huge saving in the operational cost and the second is to increase mission reliability and crew safety (Hammond, 1999). The achievement of low operating cost is dependent on large scale changes in the way vehicles are designed, developed, managed, contracted, and operated. The space tether is one of the concepts that have real potential to fulfil the objective of efficient space transportation.

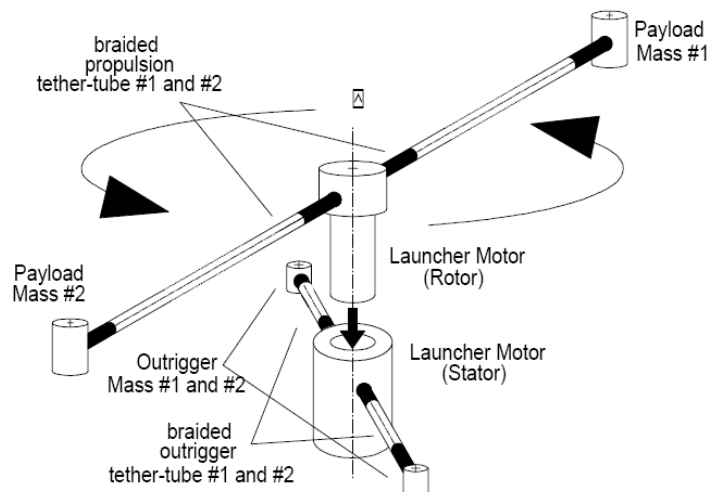


Figure 1.1 : Symmetrical Motorised Momentum Exchange Tethers after Cartmell (1998), Ziegler & Cartmell (2001)

A space tether is defined as a high strength, low density cable that connects satellites, probes or the space station to each other in space. The cables are typically very long structures ranging from a few hundred meters to several kilometres, and they have relatively small diameters, possibly being only a few millimetres thick. Space Tethers are mainly found in two categories; the electrodynamic tether and the momentum exchange tether. There have been extensive studies conducted for different models of momentum exchange space tethers, and so this thesis will study the dynamics for the Motorised

Momentum Exchange Tether (MMET) as proposed by Cartmell in 1996. The MMET is symmetrical system that has tether connected the payload to the central facility and power up by motor to spin up the tether to generate additional ΔV . Figure 1.1 shows the schematic for a double ended motorized tether concept, suggested by Cartmell (1998) and Ziegler and Cartmell (2001).

1.2 Research Aims and Objectives

The previous study by Ziegler (2003) modelled the MMET as a rigid body and Chen (2009) added axial flexibility to study the control and performance of the MMET. The rigid body model provided a good basis for the study of tether dynamics. The objective of this research is to study the MMET with more realistic model in order to have a precise motion for the tether's operation in space. This study aims to develop the tether's model to include flexibility and investigates the flexural effect to the global motion of the tether that significantly affects the tether's performance. Based on the objective of this study, this thesis will focus on:

- I. Develop the mathematical model of the MMET that incorporating the flexibility in two and three dimension by using Lagrange Equation.
- II. Explores the global and local dynamics of the flexible tethers and the relationship between them.
- III. Compares the performance of the flexible tether to the rigid body tether.
- IV. Study the influence of boundary conditions applied to the tether in deriving the equation of motion.
- V. Investigates the flexible tether libration motion, link to the onset spin and the routes to the chaos and relation of tether's flexibility to the unstable motion.
- VI. Calculate the power requirement for MMET's Earth-Moon mission and compares the energy requirement of flexible model to the rigid body model of the tether. The comparative study is also conducted between conventional systems to the tether system.

All the flexible models of MMET in this thesis were originally developed by the author in order to study the dynamics and performance of the MMET. The studies of this flexible model are summarised in Ismail and Cartmell (2009), Ismail and Cartmell (2010a), and Ismail and Cartmell (2010b).

1.3 Thesis Overview

Chapter 2 presents the critical review of literatures of space tether concept, the history, the mission and the dynamics of the space tether.

Chapter 3 derives the equations of motions and analyse of the dynamics of two dimensional flexible tether model. The differences between the rigid body and flexible models are compared, and the impact of tether's flexibility to the global motion of the tether is investigated.

Chapter 4 investigates the three dimensional dynamics of the MMET for both rigid body and flexible models. The main objective is to uncover the relationships between planar and non planar motions, and the effect of the coupling between these two parameters on the circular and elliptical orbits.

Chapter 5 presents a more complete continuum model that includes appropriate dynamic boundary conditions, which provides further fidelity in the representation of the dynamics which may not otherwise be seen. This chapter investigates the MMET responses for two different dynamic boundary conditions: the fixed-attached mass condition, and when both ends are attached to masses. The differences in the modal responses when applying the dynamic and static boundary conditions are highlighted and discussed, providing more insight into the subtleties of the dynamics of motorised orbiting space tethers.

Chapter 6 presents the dynamical analysis of the tether which includes the libration/spin and regular/chaos motion using the dynamical analysis tools.

Chapter 7 explores the minimum torque and power requirement for the MMET in various operation conditions for the rigid body and flexible body model. This study will proceed with the reassessment of the system equations for Earth-Moon transfers and will study of the behaviour of the flexible tether for both applications.

Chapter 8 concludes this PhD research and suggests the potential future works.

Chapter 2

Literature Review of Space Tethers

2.1 Background History

Konstantin Tsiolkovsky, the father of rocketry as described by Beletsky and Levin (1993), was the first to come up with the idea of having a structure reaching all the way into space, this having been inspired by his visit to the Eiffel Tower. In his book, entitled “Dream of Earth and Sky” published in 1885, he described a massive tower built on the surface of the Earth, extending up to geostationary orbit at a height of 36,000 km, on the top of which is a celestial castle that could be reached by elevator. The centrifugal force acting on the system would counteract the pull of gravity; therefore, the tower would be supported in tension.

Building a free-standing tower that is more than ten thousand kilometres high would be impossible. However, in 1960 Yuri Artsutanov proposed a more practical concept, making it possible to build the space elevator. The idea was to use a satellite, placed at geosynchronous orbit. A cable would be lowered down from the satellite towards the surface of the Earth, and a counterweight would be extended away from the Earth, to the satellite, simultaneously, keeping the centre of mass remaining at stationary point. However, Artsutanov pointed out that a material strong enough to realise this idea was unlikely to exist in the 1960s. Earlier than that, in the 1950s, John McCarthy in the United States was also thinking of building a space elevator, but had to abandon the idea, due to the same problem of the material requirement. Later, he invented the rotating skyhook. The arm of the skyhook was long enough to collect the payloads at the Earth’s surface to be transported into space. McCarthy’s contributions made Van Pelt (2009) consider him the father of the momentum exchange tether. According to Clarke (1981), Isaac *et al.* (1966) had discovered the same concept, but were unaware that the idea was the same as Artsutanov’s and McCarthy’s. This concept was further studied for its feasibility, and Isaac *et al.* (1966) duly found that the strength needed by the tether was twice what was then available.

As the forces on the cable are not the same everywhere, Artsutanov considered using a tapered cross section cable. The parts of the cable that require higher strength are thicker,

and the parts where the forces are applied are lower and therefore require a thinner and lighter cable. The idea of this concept can be illustrated, as in Figure 2.1:

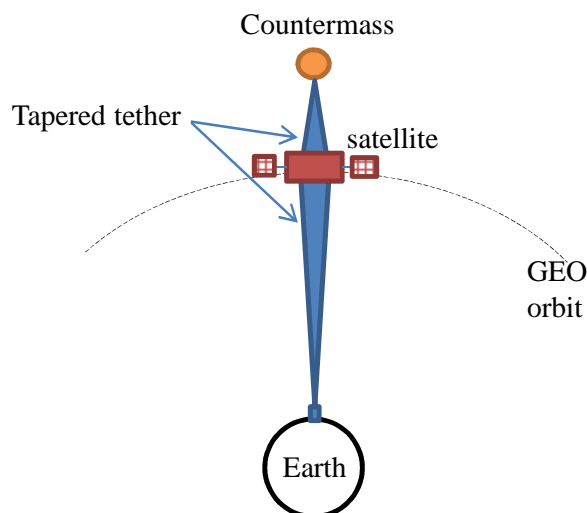


Figure 2.1: The tapered cable for the skyhook concept by Arsutanov (1960) and Pearson (1975)

The use of a tapered cable was studied in detail by Pearson (1975), who discovered that the concept of an orbital tower can be realised by overcoming the problems of buckling, strength, and dynamic stability. The buckling can be overcome by having a tower extended from geostationary orbit, and make it experience an upward force which balances the downward force due to the compressive stress at the base. Theoretically, the calculated altitude needed to obtain a balanced tower was shown to be 144,000 km. Pearson (1975) introduced the ratio between the thickest and the thinnest part of the tapered cable, and showed that this taper ratio should be more than three in order to provide a stable tower for the inclusion of the perturbation force of lunar tides in the calculation. For the required strength to weight ratio, the material that was available at that time was the perfect crystal whiskers of graphite. The tower could also be used in principle for a linear induction propulsion system, as suggested by Thornton (1973), therefore launching the payload from geostationary orbit to a higher orbit by utilising the energy from the Earth's rotation. It could also be used as a radioactive waste disposal system, where the payload containing the waste could be fired to a higher orbit nearer the Sun, and then released into the sun. A number of applications have been proposed by Pearson, and he extended the skyhook concept to the lunar application in work reported in Pearson (1979).

Colombo *et al.* (1974) proposed a "Shuttle Borne Skyhook" for low orbital altitude research, which was claimed by Kumar (2006) and Van Pelt (2009) to have marked the

beginning of the Tethered Satellite System (TSS). The skyhook system was composed of a subsatellite attached to a long wire on a reel, and used the gravity gradient and atmospheric drag to keep the tether almost vertical and in tension, and to unreel the tether. This tether could be lowered down, reaching a lower altitude at which all the experiments with regards to this region could be conducted continuously. A new concept for the orbital skyhook was proposed by Moravec (1977). This was in the form of a rotating tether with the central facility as the centre of the mass, and attached with symmetrical arms. This orbital skyhook would rotate with a tether velocity equal to the orbital velocity so that the tether tip might periodically touch down on the planet's surface.

Colombo *et al.* (1982), Bekey (1983), and Bekey and Penzo (1986) studied the use of momentum exchange tethers for payload orbital transfer. Bekey (1983) summarised the principal of momentum exchange and electrodynamic tethers, and discussed the application of cryogenic propellant storage and transfer, two dimensional tethered constellations, passive stable platform connected by tethers, payload orbit lowering and raising, and a two-piece-tether elevator that transfers a payload from LEO to GEO. Carroll (1986) has also given a general overview of tether history and applications, and discussed shuttle payload boosting and electrodynamic boosting. Furthermore, he remarked of his concern about the low number of practical, as opposed to the theoretical studies that have been conducted and the requirement for advanced studies mainly in tether control in order to make applications possible.

It can be seen here that research on space tethers has a very long history, and is truly international. These previous studies on tethers have laid the theoretical basis for more advanced studies of tethers in the future. Some practical experiments have been carried out, and various applications for tethers have been introduced, and more advanced concepts, such as the tether elevator, space web, and many more, are beginning to receive serious attention.

2.2 Space Tethers: Concepts and Applications

Generally, modern tethers are categorised into conductive and non-conductive applications. The conductive tether permits interaction with the Earth's magnetic field, and is known as an electrodynamic tether; whilst the non-conductive tether category refers to gravity gradient stabilised tethers and liberating and spinning momentum exchange tethers. McKenzie (2010) described rotating tethers as those that have logical progression,

which he referred to as Momentum Exchange Tether; whilst non-rotating tethers tend to denote gravity gradient and electrodynamic tethers.

2.2.1 Gravity Gradient Stabilisation

The basic principle of gravity gradient stabilisation is to use the balance of the Earth's gravity and the centrifugal force to keep spacecraft aligned in the desired orientation. For two masses connected by a tether, the mass that is closer to the Earth experiences a larger gravitational force than centrifugal force; whilst the mass at the other tether tip, which is further from the Earth, has a higher centrifugal force than gravitational force. The lower end mass experiences a net force pointing to the Earth, and the net force of the upper mass, which is directed away from the Earth, puts the tether into tension, establishing an equilibrium to the system, which then gives a stable vertical configuration for the tether. According to Cosmo and Lorenzini (1997), the gravitational and centrifugal forces are equal and balanced at the system's centre of gravity only, and the system is constrained to the Earth orbit with the same angular velocity as the centre of gravity, and the masses experience the tension of the tether as artificial gravity. Without the other forces that perturb the tether, it will remain aligned to the gravity vector, and this configuration is also called a 'hanging tether' (Ziegler, 2003). In (McInnes and Cartmell, 2006), Cartmell has given a formal treatment to the hanging tether where the altitude of gain and loss has been derived for the payload raising and lowering application.

This concept was first successfully demonstrated during the Gemini 12 mission in 1966. The many potential applications for gravity gradient stabilisation and artificial gravity have been discussed by Beletsky and Levin (1993), Cosmo and Lorenzini (1997), and Van Pelt (2009). According to Beletsky and Levin (1993), Tsiolkovsky was the first to introduce artificial gravity based on a tethered pair, and this was first experimented with during the Gemini 11 mission in September 1966. Van Pelt (2009) outlined the applications of artificial gravity, which enables astronauts to live more normally, and protects them from the effects of psychological change, especially on the ISS. He also mentioned that microgravity is useful for combustion experiments and, according to Beletsky and Levin (1993), Bekey (1983) proposed the use of microgravity from gravity gradient stabilisation for refuelling a spacecraft in orbit. The technique of supplying the propellant using a gravity gradient stabilised tether was discussed in depth by Kroll (1985), where he remarked that for the case of tether swinging in orbit, the length of the tether increases gradually with the increasing swing angle.

2.2.2 Electrodynamic Tether

An electrodynamic tether is a long conducting wire which can be used for producing low thrust and generating electrical power, and is even useful for aerobraking. The wire or cable is made from conductive material, and the preferable design is to have a high electrical conductivity and low mass. The electrodynamic tether operates on a similar principle to a generator or motor where it converts kinetic energy to electrical energy, or vice versa. The motion of a deployed conductive tether across the Earth's magnetic field induces voltages along the length of the tether. The voltage along the tether will attract the free, negatively charged electrons at its positively charged end, this being the anode. The electrons then will moves to the other end, namely the plasma contactor or cathode, and generate a closed loop electrical circuit, enabling the flow of electrical current. According to Van Pelt (2009), an uninsulated tether can be used instead of using the large, spherical and metallic anode to collect the electrons. This concept is called the 'bare tether' and can prevent the electrons from piling up in the small area, thus increasing the efficiency of the tether. He also mentioned that a 20-km-long wire in a low Earth orbit can potentially produce up to 40 kW of power. Samantha Roy *et al.* (1992) have shown in their study that the combination of bare tethers with a contractor can significantly improve the performance of the tether.

The interaction of the induced current flow with the Earth's magnetic field causes a Lorentz Force that is always in the opposite direction to the motion of the wire in a magnetic field, thus causing the tether to decelerate. This 'electromagnetic drag' can be utilised to lower the orbit of the satellite, or even de-orbit it into the atmosphere. In addition, reversing the operation will cause the Lorentz Force to work in the other direction, and boost the spacecraft instead of slowing it down. In this case, electrical power supplied by the solar panels will be used to drive the current through the tether. Making the current flow in the opposite direction from the previous electromagnetic drag's configuration causes the Lorentz Force to work in the other direction, thus pushing the spacecraft. The configurations of both the electrodynamic drag and the propulsion tether are shown in Figure 2.2.

The study by Estes *et al.* (2000) shows that a conceptual design of bare tethers for electrodynamic spacecraft propulsion is capable of delivering 0.5-0.8 N of thrust to the ISS using a 10-km-long aluminium tether, by utilizing 10 kW of space station power, and could save propellant requirements for station reboost over a 10-year lifetime. An experiment

testing this bare electrodynamic tether was conducted in 2000 for the ProSeds mission. Furthermore, the study by Vas *et al.* (2000) has shown that using an electrodynamic tether instead of using flights to deliver propellant to the station, with a tether force of 0.43N (5kW) to reboost the ISS, could give a saving of more than one billion dollars over the ISS's lifetime; and for a higher reboost value of up to 0.7N (10kW), would give twice the saving.

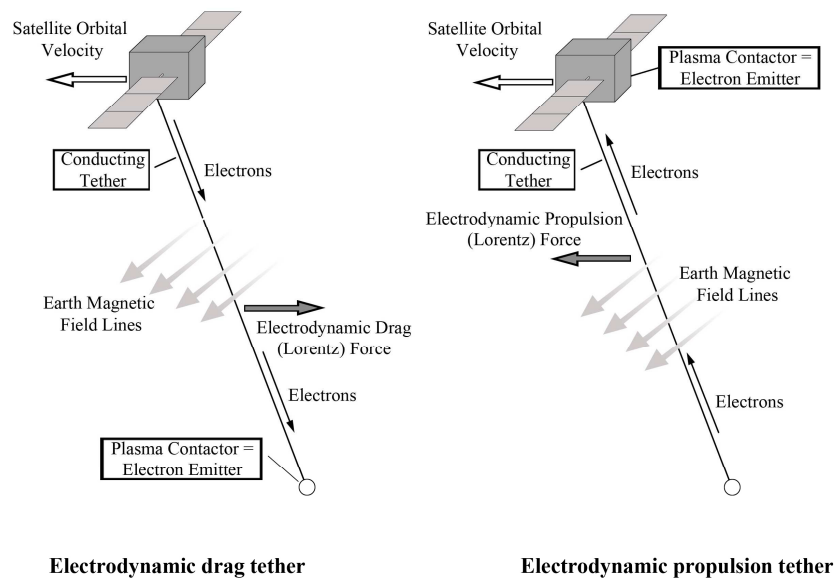


Figure 2.2 : Configuration of Electrodynamic drag tether and Electrodynamic propulsion tether (Van Pelt, 2009)

The other interesting application for an electrodynamic tether is to use it to remove charged particles from the Earth's orbit. The idea is to bring an electrodynamic tether into the Van Allen belts, and charge it to a very high voltage level, in order to generate an electromagnetic field that can scatter the radiation particles, and, over time, send them out from the radiation belt, thus lowering the overall radiation levels.

The use of an electrodynamic tether for space debris removal has also been discussed by Ishige *et al.* (2004). In that study they proposed an operation to remove space debris in six phases, as shown in Figure 2.3. The sequence of operations is: I) The service satellite tether approaches the debris by transferring its orbit; II) The service satellite tether retrieves the tether and uses thrusters for rendezvous; III) As the target is attached to the end of the service satellite, it re-deploys the tether at the descent (using electromagnetic drag tether concept); IV) When it reaches an orbit with a lifetime of less than 25 years, the debris is released, and the tether is fully deployed; V) The debris descends, and will eventually burn

out in the atmosphere, and the service satellite will operate as an electrodynamic propulsive tether and will gain its altitude; VI) The service satellite will precisely control its orbit to head for the next target debris.

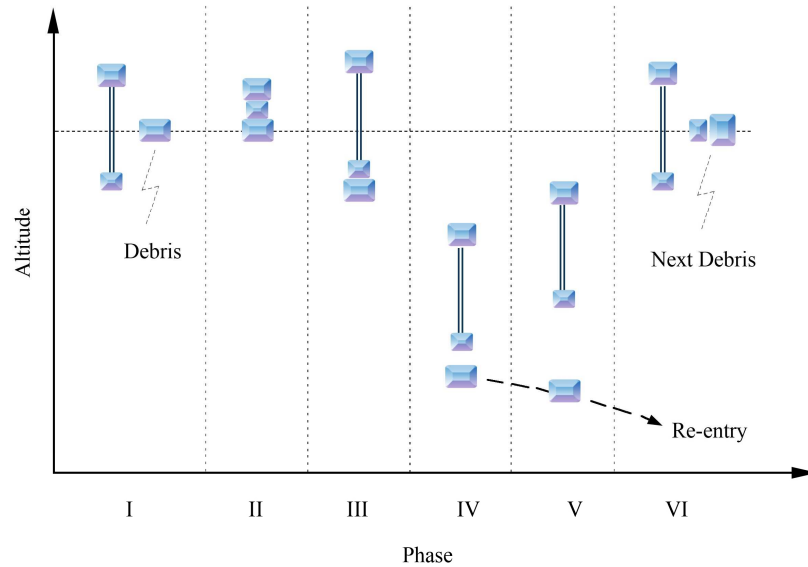


Figure 2.3 : Debris removal process by electrodynamic tether, by Ishige *et al.* (2004)

2.2.3 Momentum Exchange Tether

A momentum exchange tether is a long thin line used to connect two bodies in space. This enables momentum and energy to be transferred between them. The two tethered bodies usually orbit a source of gravity in space at their common centre of mass and orbital angular velocity, and align themselves along a local vertical due to gravity gradient stabilisation, with the upper end mass having the same angular velocity but greater linear velocity, and lower end also having the same angular velocity with lower tangential translational velocity. Due to the difference in gravity at different orbital altitudes on both bodies, the velocity along the tangent to the orbit required for the lower mass to stay at the same orbit is greater than its current linear velocity if it released at this point, whilst the upper payload requires less than its current linear velocity.

Figure 2.4 shows that the upper mass is released from the tether into an elliptical orbit, because the payload carries more velocity than is required to stay in that orbit but not enough to escape the influence of the Earth. The payload release point is at the perigee of that elliptical orbit. On the release of the upper mass, the lower mass does not have enough velocity to stay in the orbit, so it goes into an elliptical orbit, with the release point at the apogee. Half an orbit later, the upper mass reaches its apogee, furthest from the Earth, and

the lower mass reaches its perigee, closer to the Earth. By adding prograde swing or spin, one can increase the velocity to the upper mass and also subtract it from the lower mass. Conversely, a retrograde swing will act on the upper mass and the lower mass in an opposite manner to the prograde swing.

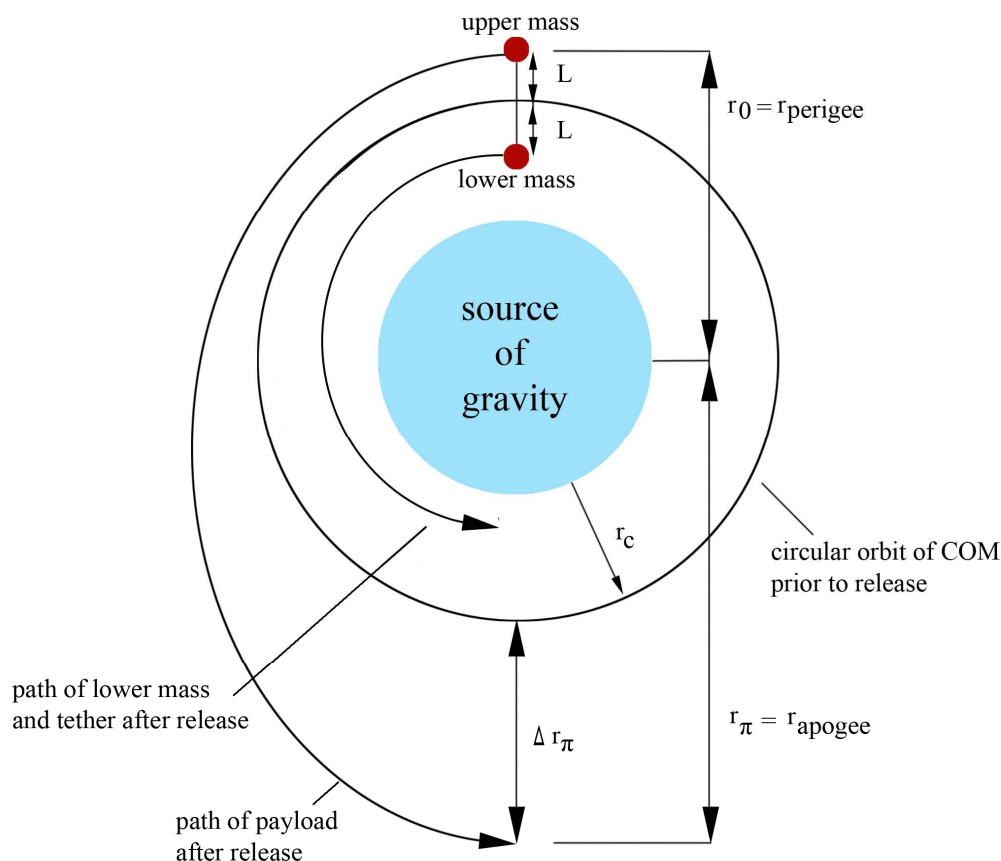


Figure 2.4: Orbital path of a payload released above the tether's COM on circular orbit (Ziegler, 2003)

According to Ziegler (2003), this format payload raising and lowering was first proposed by Colombo *et al.* (1982). Later on, a single stage payload transfer from a Low Earth Orbit (LEO) into a Geostationary Orbit (GEO) was suggested by Bekey and Penzo (1986). This utilized a spinning tether for picking up the payloads and tossing them into the desired orbit. Earlier than that, Bekey (1983) introduced this form of payload raising and lowering for delivering a Shuttle External Tank (ET). He also remarked that the separation half an orbit after release will be 7 times the tether length for a hanging release, up to 14 times for a librating release and more than 14 times in the case of a spinning release. These estimates were also mentioned by Carroll (1986), Cosmo and Lorenzini (1997), and Lorenzini *et al.* (2000) but Bekey (1983) also stated that the separation after half orbit could be more than 25 times the tethers length for a spinning release.

A rotovator is a rotating orbiting momentum exchange tether, with a retrograde motion of the tip, and is designed in such a way that the tether's tip touches the planet's surface to capture a payload and release it to a new trajectory. This concept was first introduced by Artsutanov (1967), and reinvented by Moravec (1977). During the contact between the tether's tip and the planet's surface, the tether's rotation is selected so that the tether tip's velocity cancels the orbital velocity thus permitting the payload to be transferred, or 'grabbed' by a capture mechanism from the tether to the planet, or vice versa. Moravec (1997) proposed a tapered and orbiting rotavator which he called a skyhook. This skyhook could be used on a lunar orbit, so it is also known as a Lunavator. Moravec (1997) found that the mass can be minimised by having an arm length equal to one-sixth of the diameter of the moon so that each of the two arms can touch the surface three times per orbit. This Lunavator concept was studied in detail by Hoyt and Uphoff (2000) for their Cislunar Tether Transport System which they devised to transport payloads between LEO to the surface of the moon. Their study shows that the cislunar tether transport system would require less than 28 times of on-orbit mass to transport many payloads, as compared with a conventional rocket system which would consume a propellant mass equal to 16 times the mass of the payload for each mission. Therefore, the cislunar tether transport system could greatly reduce the round-trip travel time between LEO and the surface of the moon.

Momentum exchange tethers can also be used as slings for throwing payloads into another orbit. This concept was mentioned by Carroll (1986), for catapulting rocks from the moon's surface. Puig-Suari *et al.* (1995) also proposed a tapered tether sling for lunar and interplanetary payload transfer, and they were the first to introduce the application of external torque to spin up a tether. The torque was generated by a solar-powered electric motor, and a detailed calculation of the power requirement was presented in that paper. An additional counter rotating tether has been proposed by Puig-Suari *et al.* (1995) to overcome the problem with the higher spin rate by the motor's stator due to the application of a resistive torque for the motor stator to contra-rotate.

The advanced concept of using a tether sling to transport humans between the Earth and Mars was presented by Jokic and Longuski (2002), and they focused on the study of trajectory design and tether material. The study shows that the mass required for the tether sling is 10 times more than the propellant mass requirement. But, the capability of multiple launches by the tether sling gives an enormous reduction in the operational cost.

Cartmell (1998) also proposed a Motorised Momentum Exchange Tether, which became known as the MMET based on work presented to ESA in 1996. The MMET is a symmetrical momentum exchange system with a motorised spin up and a counter inertia. The inclusion of a motor, powered by electricity from a solar panel or a fuel cell, gives the opportunity for generating additional ΔV . Later on, Cartmell and Ziegler (1999) proposed a symmetrically laden momentum exchange tether model for the application of a continuous two-way interplanetary payload exchange. The tether system consists of a central facility for locating the motor and power supply, two symmetrical propulsion tethers with payloads at the end of the tether's spans, and two outrigger tethers with dummy payloads at those tether tips to provide counter-inertia to the motor torque. McKenzie and Cartmell (2004) demonstrated a mission to transfer a payload from LEO to Lunar Capture using the MMET. The study shows that the payload can be launched at a rate of once per month throughout the life of the mission by using the Weak Stability Boundary method.

2.2.4 Other applications

A space tether could also be used for probe towing, especially for upper atmosphere exploration, where the altitude cannot be reached by an aircraft, and to which a sounding rocket could only travel for a very short period. A large satellite or a space shuttle in higher orbit could deploy a long tether that connects with the probe through the upper atmosphere. The aerodynamic drag on the probe and tether would slow down the satellite, which could then be compensated by means of a rocket engine. Lorenzini *et al.* (1990) studied the configuration and dynamics of a tethered probe in the dense atmosphere of Mars. This study shows that the tethered probe can operate for a long operational time at a 90 km altitude. Control of a tethered probe has been studied by Biswell and Puig-Suari (1998), and they have shown that the use of a hypersonic lifting body could give effective control of the probe's altitude.

A constellation of satellites that are physically interconnected by tethers could in principle be built in order to replace a very large spacecraft. Van Pelt (2009) gives an example of replacing a large antenna with a series of smaller antennas on smaller spacecrafts in a constellation. The spacecrafts are connected to the tether to keep the position of each spacecraft accurate.

More advanced concepts have been developed recently, widening the applications of tethers in space. The concepts of tethered satellite constellations and formation flying have expanded, resulting in a new concept in which a large structure called a space-web is deployed. The idea of the space-web was originated by Nakasuka *et al.* (2001), and was applied to the Furoshiki satellite. An experiment to deploy a space-web was successfully achieved and the results were discussed in Nakasuka *et al.* (2006). Cartmell and McKenzie (2006) have also proposed a space-web structure in which robots move over the surface of the web. McKenzie (2010) studied the dynamics and stability of the space web and the robots crawler in considerable depth.

A new concept of a Tethered Solar Power Satellite (Tethered-SPS) was proposed by Sasaki *et al.* (2007). The Tethered-SPS is potentially composed of a 100m x 95m sub-panel, tethered by four wires connected to a bus system, with the capability of generating power up to a maximum of 490 Watts. This concept, however, needs further studies to confirm its technical feasibility.

Most the tether applications are dependent on the strength of the selected material for the tether. Advanced studies in materials for space applications are required in order to put all the tether application concepts into reality. The next section will discuss principal tether missions/experiments up to this year.

2.3 The Tether Missions

Bekey (1983), Beletsky and Levin (1993), and Van Pelt (2009) all state that Gemini 11 which consisted of two spacecrafts: Agena and Gemini, was the first real tether mission to be flown in space, and this was launched on 12 September 1966. This manned spaceflight mission carried out two experiments: the first was a gravity-gradient test; and the second was to induce rotation, making the two spacecraft rotate around the common centre of mass. In the first experiment, Gemini 11 encountered a problem in deploying the tether, where both spacecrafts experienced a jerk and moved towards each other, making it difficult to align Gemini and Agena vertically with the Earth. Due to complicated motions of the tether which affected the stability of the spacecraft, this experiment was then abandoned. In the second experiment the tether underwent skip-rope motion during the transient phase, but continued to be stable when the centripetal force pulled the tether straight, and finally rotated at 38 degrees per minute in this station-keeping mode. When the spin rate was increased the tether experienced a so-called “big sling-shot effect”, and

the crew switched on the control thrusters to stop the oscillation, and managed to achieve nearly 1 deg per second. This experiment produced a low level of artificial gravity, but this could not be felt by the crew. Due to the failure of the first experiment, Gemini 12, which was launched on November 11, 1966, conducted another gravity-gradient experiment. During that experiment the tether deployed smoothly but only tautened occasionally. The Gemini managed to stabilise with a small difference of gravity between both spacecrafts which stayed at slightly different orbital attitudes. According to Van Pelt (2009), both missions managed to demonstrate tether rotation for artificial gravity, and have shown some level of gravity gradient affects, but more test were needed to understand completely the complex dynamics involved.

Fourteen years after the first tether mission in space, a joint project at the Institute of Space and Astronautical Sciences (ISAS) in Japan and the Centre for Atmospheric and Space Science at Utah State University, named the Tethered Payload Experiment (TPE), was launched in a series of five missions, as shown in Table 2.1. The TPE was launched, not to orbit, but to very high altitude using a sounding rocket. The mission was to deploy a daughter payload from the main mother payload, to measure inside and outside the charged gasses after the ejection of electrons from the rocket into the atmosphere.

Missions	Launch date	Tether length (km)	Length of deployment (km)
TPE-1	16 January 1980	0.4	0.038
TPE-2	29 January 1981	0.4	0.065
TPE-3 /CHARGES-1	8 August 1983	0.418	0.418
CHARGES-2	14 December 1985	0.426	0.426
CHARGES-2B	1992	0.4	0.4

Table 2.1 : Joint US and Japanese Mission for the Tethered Payload Experiment from 1980 to 1992.

TPE-1 and TPE-2 failed to deploy the tether fully, and the electron beam also didn't work. The third flight, TPE-3, or CHARGES, was redesigned to minimize friction during deployment, and managed to deploy to its full length, but it still had problems with the electron beam.

Finally, in the next mission named CHARGES-2, both the deployment of the tether and the ejection of the electrons successfully worked, and the experimental results were presented

by Kawashima *et al.* (1988). The experiment was continued in the next mission, CHARGES-2B with similar equipment, but at this time the electromagnetic wave was generated and measured. According to Van Pelt (2009), this mission also worked according to plan. On February 8, 1988, the other suborbital flight, named ECHO-7, was launched in order to study the artificial electron beam propagated along the magnetic field lines in space. Unfortunately, this experiment failed due to problems with onboard equipment.

A mission using a sounding rocket in the form of OEDIPUS A (Observation of Electric-Field Distribution in the Ionospheric Plasma), was flown on 30 January 1989 on a Black Brant X, a three-stage sounding rocket. OEDIPUS A's mission was to make a passive observation of the aurora ionosphere, by measuring weak electric fields in the plasma of the aurora. The tethered payload consisted of two spinning masses connected with a 958 m tether, and, according to Cosmo and Lorenzini (1997) and Van Pelt (2009) it was the longest electrodynamic tether to have been flown at that time. The second flight of this experiment was OEDIPUS C, which was launched on 6 November 1995 with similar scientific objectives. OEDIPUS C flew up to a higher altitude than the previous mission, up to 843 km, and deployed a longer tether with a length of 1174 m.

The experiment conducted at the higher altitude gave a good basis for tether deployment in microgravity, and after Gemini 12, there were more experiment conducted at the lower Earth orbit. The Tethered Satellite System (TSS) was the next mission and involved deploying and retrieving a payload from the Space Shuttle connected by the tether. The deployment of a satellite with a long gravity gradient stabilised tether provided a facility for space environment research. TSS-1 was launched on 31 July 1992 on the STS-46 space shuttle. The TSS-1 experiments discussed by Cosmo and Lorenzini (1997) have demonstrated the feasibility of deploying a satellite to long distances using a tether, allowing for experiments to fulfil the scientific objectives of the mission, even though they faced difficulties at the beginning. According to Carroll and Oldson (1995) a late design change caused a fault in the deployment mechanism which resulted in only 250 m of the 20 km of available tether being deployed. However, this problem led to the discovery that the deployment of short tethers could be more stable than expected. Another flight was launched in February 1996 on STS-75, named TSS-1R with the mission objective to conduct exploratory experiments in space plasma physics. During the mission the tether suddenly broke after being nearly fully deployed at 19.7 km, and an investigation showed that the prevailing electric current had in fact melted the tether. Although the experiment

failed much scientific data was collected, and an analysis was undertaken by Stone *et al.* (1999), which concluded that the results were extremely encouraging for the study of electrodynamic tether application, and led to an improvement in understanding tether dynamics.

The first orbital tether experiment was the Small Expendable Deployer Systems (SEDS-1), which was launched on 29 March 1993, and then SEDS-2 on 9 March 1994. The idea of these experiments was to send the satellite to a selected orbit using a rocket, and autonomously to deploy and retrieve the tether from the satellite. Carroll (1993) summarised that SEDS-1 had a full deployment without any problems, the received data all made sense, the unexpected transverse vibration caused no problem for the tether motion, and the pause in the deployment did not induce tether fouling. The vibrations were also damped very effectively, but the brake law needed feedback for a controlled stop. SEDS-2 had an improved braking system to ensure that the satellite stopped flying out when the whole tether was deployed, and also to prevent bouncing. According to Van Pelt (2009) this mission proved that a tether might be accurately deployed to a stable position in orbit by feedback control and a simple frictional brake.

On 26 June 1993 the Plasma Motor Generator (PMG) experiment was launched and consisted of a far-end package connected to a Delta II Second Stage by a 0.5-km-long tether. The PMG demonstrated the configuration of an electrodynamic tether that could be used to generate electric current, or for orbit boosting. As mentioned in Cosmo and Lorenzini (1997), the experiment lasted 7 hours until the batteries expired.

A simple experiment named TiPS (Tether Physics and Survivability) was designed to study tether motion over a long time, and to show how it would survive in a region of orbital debris. TiPS consisted of two satellites connected by a 4-km-long tether and placed in a circular orbit at an altitude of 1022 km, and was launched on May 12, 1996. The tether system was observed using satellite laser ranging which stopped functioning in 1995 while the tether was still intact. After 10 years of operation, the tether was broken, and so this mission proved that tethers can potentially be made to be survivable.

The Advanced Tether Experiment, or ATeX, continued the challenge of undertaking tether dynamics experiments. It was launched from a parent spacecraft, called STeX, on October 3, 1998. The two end-mass satellites of ATeX were connected by a 6.2 km tether of polyethylene tape with three strands of Spectra Material. The upper end mass was to be

deployed, while the lower end mass was attached to the parent spacecraft. Unfortunately, the deployment of ATeX was stopped at a tether deployment length of 22 m because sensors had detected that the tether had moved away at an angle and this triggered the automatic safety system, making both spacecrafts continue to orbit on a short piece of tether. The analysis verified that thermal expansion had contributed to the failure of the deployment.

The first Young Engineer's Satellite (YES) mission started in 2002, and was developed by the space research and system engineering division of Embedded instruments and Systems S.L under joint sponsoring by ESA and the Dutch aerospace development agency NIVR. It was launched together with TORI (Tethered Orbit Insertable) which was connected to YES by a 35 km tether. YES's primary objective was to investigate dumbbell dynamics, and tether deployment in Geostationary Transfer Orbit (GTO). Due to the change in launch time, YES potentially had a longer than expected orbital lifetime, and the Space Debris Committee determined that the collision risk was high, therefore, the tether was not allowed to deploy. Without deployment of the tether the main mission objective was not achievable.

A tether application for formation flying was a mission involving two miniature satellites developed by the Aerospace Corporation, Picosat-1 and Picosat-2 launched in January 26, 2000. The two picosats were designed to perform formation flying and were connected with a 30 m tether to ensure they would stay close to each other. This mission performed a basic test of a Micro Electro-Mechanical System (MEMS) radio frequency switch. After the success of this mission, the experiment was repeated by Picosat-7 and -8 in July of the same year. MEPSI-1A was a larger set of tethered satellites developed by the Aerospace Corporation which was launched on December 2, 2002 with a mass of about 1 kg for 2 cubic masses which were connected by a 15 m tether.

Small tethered satellites continued to be developed, and students from the Technical University of Denmark developed DTUsat-1 and launched it in 2003, with a mission to deploy a 450 m copper wire tether. Unfortunately this mission failed due to a failure in the communication system of the satellite. In Japan the small CUTE 1.7 (Cubical Tokyo Tech Engineering Satellite) was launched on February 22, 2006, based on the previous development of CUTE-1, the first CubeSat in the world, as documented by Ashida *et al.* (2010). In addition to the primary mission to demonstrate microsatellite technology CUTE 1.7 was also designed to test deorbit technology using an electrodynamic tether. However,

the deployment of this tether was unsuccessful due to a defect in the communication system.

Tethers Unlimited, Inc (TUI) and Stanford University together developed the MAST (Multi-Application Survivable tether) experiment and launched it in April 2007. This experiment consisted of three picosatellites, named “Ted”, “Ralph”, and “Gadget”. The experiment was to have Ted and Ralph deploy a 1000 m length of tether from the satellite, and then Gadget was to crawl along Ted and Ralph. This experiment used the patented ‘Hoytether’ to increase the tether’s lifetime. Nevertheless communication was only established between the ground base and Gadget, but not with the other picosatellites, resulting in only a few metres of tether being successfully deployed. Later, on September 14, 2007, the 32 kg YES-2 experiment was launched by a Soyuz rocket as part of the Foton-M3 microgravity research capsule and as a continuation of the YES-1 mission. At this time Kruijff and Van der Heide (2009) stated that the tether managed to deploy in the downward direction of a 37.1 km long tether connected to a small capsule named Fotino on September 25, 2007. In the post deployment phase it was reported that the tether system behaved as a pendulum, and swung back towards the vertical equilibrium position, and then the tether was cut to release the MASS and the Fotino. The braking plan at the end of deployment failed, resulting in the tether experiencing a shock which made the Fotino unable to fly on the exact planned re-entry trajectory. The Space Surveillance Network was unable to detect the Fotino, and the team believed that it entered the atmosphere, or that the radio system may have been damaged.

The latest tether mission was JAXA’s Tether Technology Rocket Experiment (T-REX), launched on August 31, 2010, from a sounding rocket type S-250-25. This mission successfully conducted basic experiments on an electrodynamic tether in the ionosphere. It consisted of the deployment of the tether, a quick ignition test of the hollow cathode system, and a demonstration of the operation of the electrodynamic tether system, while making a sub-orbital flight for about 10 minutes to reach a maximum altitude of 300 km.

2.4 Tether dynamics

The vast amount of literature covering the dynamics of the space tether, and an excellent monograph by Beletsky and Levin (1993), offer comprehensive analyses of various aspects of the dynamics of space tether systems. The topics discussed cover the dynamics and stability of the tether of the Newtonian field, atmospheric probes, electrodynamic tethers,

libration and rotation, deployment and retrieval, and lunar anchored and satellite ring systems. Misra and Modi (1986) reviewed the dynamics and control of Shuttle-borne tethered satellite systems, and presented a dynamical analysis on the three body space-station based tethered system. The review concluded that there was a requirement for more ground experiments to verify the efficiency of tether deployment and retrieval, and that further works were needed to understand the dynamics of the tethered space station. Furthermore, past and recent studies of the space tether have been summarised in excellent review articles by Kumar (2006), and Cartmell and McKenzie (2008).

The dynamics of tethers are mainly studied in three operational phases; station keeping, deployment, and the retrieval phase. In the station keeping phase, the stability of the tether is of most concern. Liaw and Abed (1990) studied the stabilisation control of rigid and massless tethers during station keeping, where a stabilising controller was constructed using linear and quadratic feedback. No and Cochran (1995) showed in their study of tethered flight vehicles that aerodynamic control could be an alternative to reaction control for station keeping. The deployment and retrieval phases are the most critical in which the application of a length rate control law is demanded. Previous flown missions have shown that the instability of tether deployments, which have frequently contributed to mission failure, were due to unexpected phenomena, such as tether slackness. Misra & Modi (1982) remarked that the control gains for tether deployment and retrieval should be carefully chosen as the gains that damp out the swing could also result in large vibration displacements. They also mentioned that the deployment will be stable as long as the commanded length rate in the control law is small. The work of Kokubun & Fujii (1996) on tether retrieval under elastic effects showed that the use of large-deflection theory can avoid the incorrect assumption that tethers will be slack during deployment or retrieval.

The discovery of the so-called 'weird phenomenon' by the crews during the experiments of Gemini 11 and 12, proved that the tether dynamics were more complicated and problematic than the theory had predicted. This weird phenomenon was actually the 'skip-rope' motion of the tether which Chapel and Flanders (1993) have studied in detail in the TSS-1 mission. They indicated that this skip-rope motion occurred due to the current flowing in the electrodynamic tether. Chapel and Flanders (1993) also examined libration, plunge, and pendulous motion, and the string dynamics of a tethered satellite system based on the dynamic data from the TSS-1 mission. The first three motions: libration, the plunge mode, and the pendulous mode are mentioned as the principal vibration modes that involve rigid body motions of the spacecraft. The plunge mode is where the tether behaves more a

like spring-mass system involving tether contraction and extension; and the pendulous mode is where the tether rotates rather than translates and the frequency depends on the tether's tension. Chapel and Flanders (1993) have shown that libration motion depends upon the ratio of tether length rate to tether length during the deployment and retrieval phases. Ziegler and Cartmell (2001) investigated prograde libration performances for payload raising and lowering. They showed that a prograde librating tether that has a large maximum libration angle, and is orbiting near to the Earth, performs the best during payload raising; whilst a prograde librating tether with a maximum libration angle, but moving far from the Earth, performed the best for payload lowering. This showed the advantages of a librating tether for payload increment gain, as compared to the hanging tether, but the spinning tether is known to give the best performance. A study by Takeichi *et al.* (2001) clarified that the divergence of libration for tethered systems subjected to atmospheric drag was determined by the drag area, drag coefficient, orbital altitude, and eccentricity. The study also showed that the larger the mass of sub-satellite, the smaller the tether's cross-sectional; and the longer the tether, the more it contributes to the instability of tether libration, and vice versa.

The spinning motion of a tether also has a significant impact on tether dynamics and stability, and the Gemini 11 and 12 missions were the first to involve a tether spinning around the centre of mass, and to use this for station keeping and generating artificial gravity. The earliest study of a spinning tether was conducted by DeCou (1989). That study investigated the three-dimensional motion of a spinning TSS with several configurations including a dumbbell, a carousel and a triangle. This work showed that the rotation rate of a triangular tether is constant, but this is not the case for a dumbbell tether. Luo *et al.* (1996) studied a stretched tether spinning about its longitudinal axis, and presented the exact solution for a nonlinear damped and undamped tether. The dynamical analysis for this model was carried out for a linear and nonlinear model, and the results showed that the resonant motion for undamped vibration is always stable, whilst the damped forced vibration is unstable. Min, Misra, and Modi (1999) studied a nonlinear spinning tether in depth, and found that the model has the potential for skip-rope motion about the longitudinal axis. The research also found that the steady transverse vibration has a mono-frequency characteristic. In the work done by Tyc and Han (2001) it was found that tether root bending could play a major role in the dynamics of a spinning tethered vehicle. The work of Luo *et al.* (1996), Min *et al.* (1999), and Tyc and Han (2001) all considered the tether spinning about a nominal axis where the spin is generated by the end body for spin stabilization. The tether which spins about an axis normal to the nominal axis was studied

by Puig-Suari *et al.* (1995), where the concept of a tether sling was applied for payload transportation. An investigation of a payload transfer system, using two stages of a spinning tether, was conducted by Lorenzini *et al.* (2000). Ziegler and Cartmell (2001) studied the dynamics of the Motorised Momentum Exchange Tether (MMET), which included the tether spinning for the application of payload transfer. The spinning tether was also investigated by Lorenzini (2004), who worked on the configuration of the capture mechanism and the rendezvous dynamics of a spinning tether for payload transfer to GTO.

The other option on which to model a tether, other than as a rigid dumbbell, is to model it as a string-like flexible tether. A string-like flexible tether will experience string dynamics in which the elasticity of the tether contributes to the displacement in the transverse or longitudinal directions, and, in the three dimensional case, the tether will display motion in two transverse directions and a longitudinal direction. Misra *et al.* (1986) investigated three-dimensional transverse and longitudinal vibrations of tethers connecting a sub-satellite to the shuttle. That work showed that the transverse vibration frequency is dependent on the orbital frequency, but that the longitudinal vibration is not. They also mentioned that the transverse vibrations have a small effect on the rotation. Misra (2008) conducted an analytical study on elastic tethers, and presented an exact solution for the longitudinal vibration. In studying the damping tether, He and Powell (1990) damped the longitudinal and transverse vibrations in the skip-rope mode by means of manipulated material properties. The decay time was prolonged by the damping mechanism which was based on longitudinal stretching, which was induced by lateral motion.

This literature survey on the dynamics of a flexible tether is continued in the next chapter where it focuses more on tether modelling. The literature that has been summarised in this chapter laid the fundamentals for tether studies and gives a good understanding in order to explore more interesting dynamical phenomena.

Chapter 3

Dynamics of the Two Dimensional Flexible Tether Model

3.1 Introduction

This chapter presents a more complete flexural model for the Motorised Momentum Exchange Tether (MMET). A continuous string-like sub-span model is taken in which the sub-span is flexible and elastic, thereby allowing three dimensional displacements of the motorised tether. The differences between the rigid body and flexible models are compared, and the impact of the tether's flexibility on the global motion of the tether is investigated. However, this chapter focuses on the dynamics of the two dimensional flexible tether only, in order to give a basis for the study of planar motion of the MMET.

3.2 Tether Modelling

A tether should be modelled based on the objectives to be achieved, and the desired analysis to be conducted. A simple model will reduce the complexity but will maybe introduce a lack of accuracy since some important phenomena will not be taken into account. Generally, tether models can be categorised into three types, these being the rigid rod, the sequence of elements approach, and the continuum model.

The simplest model describing rigid body motion is based on a massless rigid rod in which bending and stretching are negligible. This model was used by Bainum and Kumar (1980) to develop a control law for the operation of the Shuttle-Tethered-Sub satellite system. Liaw and Abed (1990) used the same model to study the stabilization of tethered satellites during station keeping through a nonlinear control system. Netzer and Kane (1993) also assumed the tether as a massless straight object to optimise a control law for deployment and retrieval of the tether. Studies by Modi *et al.* (1981), Puig-Suari and Longuski (1991), and Ziegler and Cartmell (2001) have all employed the assumption of the tether as a massive rigid rod. The benefit of including the tether's mass is to generate accurate data for where quantitative analysis is required. A study by Modi *et al.* (1981) showed that the simple point mass model provided useful information for developing a control strategy for retrieval operation of the Space Shuttle based tethered system. Netzer and Kane (1993) also showed the optimal solution for tether control using a simple model may be applicable to a more realistic model. In order to include the effect of the first longitudinal stretch

mode to the system, Fujii and Ishijima (1989) enhanced the tether model to be an extensible, massless rod.

The next category is represented by a sequence of elements which allows some form of flexibility in the model. Banerjee (1990) studied a lumped mass model connected by massless springs, and proposed a deployment rate control law for the system. The lumped mass and massless spring element model was studied by No and Cochran (1995) to develop aerodynamic control thought to be viable for station keeping and manoeuvrings. Netzer and Kane (1995) represented the tether by eight inextensible rigid massive rods in order to describe the analysis during the station-keeping phase. They also mentioned that the sequence element model is often used to simulate the behaviour of such systems, but not for the controller. Puig-Suari *et al.* (1995) extended the previous work of Puig-Suari *et al.* (1992) to study the possibility of applying tethered spacecraft to perform aerobraking maneuvers at any atmosphere bearing planet in the solar system. Their latter work enhanced the tether model where flexibility effects were included by considered the tether as a chain of linked rigid rods with spring dampers to model the elastic behaviour. The result for a Mars aerocapture maneuver demonstrated that the flexible system behaves like the rigid one then changes when it enters the atmosphere due to the tether's bending which creates a large force, resulting in an unacceptable manoeuvre. This confirmed the previous assumption by Puig-Suari *et al.* (1993) that the requirement to minimize the normal force in a rigid rod model is essential to create an acceptable manoeuvre.

Biswell *et al.* (1998) used a different model to demonstrate flexible behaviour for aerobraking tethers. The tether is modelled as hinged rigid bodies connected with massless springs and dampers. The strength of this model is in its ability to model precisely the aerodynamics and gravitational forces, and the moment, with a limited numbers of elements which may in turn give a reduction in the computational cost.

Danilin *et al.* (1999) studied the dynamics of an elastic deploying tether in the gravitational field using a tether model by No and Cochran (1995) but with different variables and approach. The tether is modelled as a series of discrete masses connected by massless elements and with internal viscous damping. The equation of motion was obtained by using the finite element model. Danilin *et al.* (1999) also studied two examples of the motion, the swinging of a cable and the plane motion of a space vehicle with a deploying tether system on orbit to verify the mathematical model and computer code, and also to estimate the accuracy of calculation. Cartmell and McKenzie (2008) remarked on the

important point made by Danilin *et al.* (1999) that tether element forces cannot be compressive, so conditions within the numerical solution algorithm have to be set up to accommodate the consequential effect of this.

Netzer and Kane (1995) and Kumar (2006) suggested that the more elements that are used the more accurate the tether model will be, and the more closely it represents a continuous system. In fact, Vadali and Kim (1995) showed the bead model has the advantage of capturing most of the phenomena of the problem in comparison with the more computationally expensive continuum model.

The other category for tether modelling is the continuous massive tether. Such a model can be elastic or inextensible. This approach is in general considered to be a way to model the tether, and is found in most of the nonlinear literature. Modi and Misra (1979) studied three dimensional motions for a massive continuous tether during the deployment and retrieval phases for a tether connected to two body systems. This study showed that transverse vibration can increase due to the Coriolis excitation, even when there is no initial deformation. The initial out-of-plane motion also decays during deployment but builds up when the terminal phase is reached due to aerodynamic forces and small initial librations, and vibrations are also increased during retrieval. Misra and Modi (1986) revisited this continuous model of the tether but focused on the dynamics during retrieval by taking into account the nonlinearity in the strain-displacement relationship, where this particular geometric linearity was found to have a noticeable stiffening effect against lateral vibration.

Beletskii and Levin (1985) treat a tether which they consider as an Orbital Cable System (OCS), as a heavy, extensible, and flexible string in order to study stationary and periodical system motions in the atmosphere. The cable shows a wave-like configuration in stationary motion and may produce a destabilizing effect dependent on the cable diameter and altitude.

Discretisation is required to obtain the solution for the partial differential equations which constitute the equations of motion for a flexible and extensible tether. Min *et al.* (1999) stated that discretisation procedures can be categorized into two classes; analytical procedures such as Galerkin methods, and physical discretisation procedures such as the finite element method, and these authors chose to use an assumed-mode method to solve their non-linear continuum tether model. Steiner *et al.* (1995) used both the Galerkin and

finite element methods to calculate large amplitude motions for a two satellite continuous tether system. The result shows that the finite element approach can be applied in both the formulation of the equations of motion in rotating and non-rotating coordinate frames, and more straightforwardly in comparison with the Galerkin method which can be only used in a rotating coordinate frame. The Galerkin or Assumed Mode method was also used by Keshmiri *et al.* (1996) and Luo *et al.* (1996) to reduce the nonlinear model of a spinning tether to a linear and nonlinear coupled system, and this was also used by Tyc and Han (2001) in conjunction with Lagrange's equations for a spinning tether.

3.3 Modelling of the Flexible Model of the MMET

The modelling strategy for the MMET, to date, has mainly been to use rigid body modelling in order to keep the resulting analytical models as tractable as possible. This was based on the fair and reasonable justification that centripetal stiffening eliminates some of the flexural response, and that much of the ensuing behaviour will therefore be similar to that of a rigid body. The three dimensional mathematical models by Ziegler (2003) were used to explain successfully many of the fundamental motions possible for an MMET. However, the previous model strategies by Cartmell (1998) and Ziegler (2003) both discount the flexural characteristics of the tether sub-spans, and so some important phenomena may not be captured because of this. A further development, by Chen and Cartmell (2007) has shown that incorporating limited flexibility, in the form of an axial stretch coordinate, shows that significant axial oscillations can be uncovered, with obvious relevance to payload release and capture scenarios. In this thesis, a continuous flexible model has been chosen for modelling the MMET in order to study the dynamics of the tether more precisely. *Mathematica*TM software has been used for deriving and integrating the equations of motion together with the application of the equation solver NDSolve to find a numerical solution to these ordinary differential equations.

3.3.1 String model

In modelling the flexible MMET, the tether is assumed to be a string which is connected to the masses at both ends. Figure 3.1 shows an element of the tether associated with the three dimensional displacement given by $u(x,t)$, $v(x,t)$, and $w(x,t)$. The position vector of a displaced element, ds as shown in unpublished notes by Cartmell (1999), which were based on a discussion originally given by Nayfeh and Mook (1979), is given by,

$$\bar{r}_{A'B'} = \left((1+u')\bar{i} + v'\bar{j} + w'\bar{k} \right) dx \quad (3.1)$$

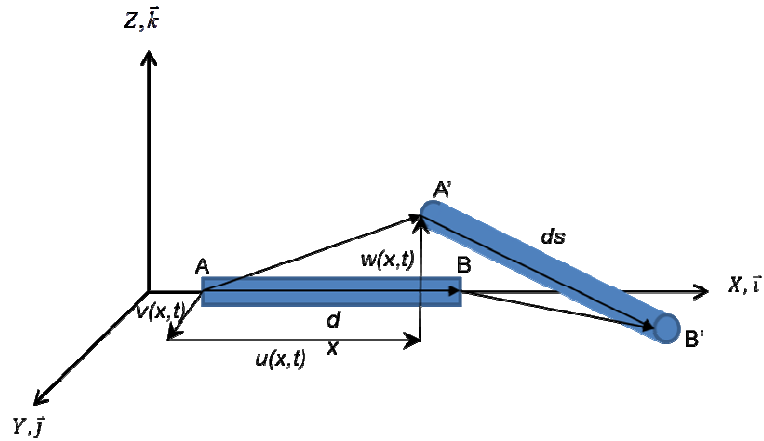


Figure 3.1 : Displaced element of a flexible tether

where the prime denotes differentiation with respect to x . Therefore, the scalar length of the deformed element, ds , is given by,

$$ds = |\bar{r}| = \left[(1+u')^2 + v'^2 + w'^2 \right]^{1/2} dx \quad (3.2)$$

The strain due to axial extension of the element is,

$$\varepsilon_e = \frac{ds - dx}{dx} = \frac{ds}{dx} - 1 \quad (3.3)$$

Therefore, substitution of (3.2) into (3.3) gives,

$$\varepsilon_e = \left[(1+u')^2 + v'^2 + w'^2 \right]^{1/2} - 1 \quad (3.4)$$

The strain expression can be re-stated using the Binomial series,

$$(1+z)^s = \sum_{n=0}^{\infty} \binom{s}{n} z^n = 1 + \binom{s}{1} z + \binom{s}{2} z^2 + \dots \quad (3.5)$$

Therefore,

$$(1+z)^{1/2} = 1 + \frac{1}{2}z - \frac{1}{8}z^2 + \frac{1}{16}z^3 \dots \quad (3.6)$$

The strain expression in terms of u', v', w' is given by equation (3.4) for which the expansion for $(1 + u')^2$ is included,

$$\varepsilon_e = [1 + 2u' + u'^2 + v'^2 + w'^2]^{1/2} - 1 \quad (3.7)$$

The evaluation of the strain expression using the Binomial Series from equation (3.6), where $z = 2u' + u'^2 + v'^2 + w'^2$, and using *Mathematica*TM, leads to,

$$\begin{aligned} z^2 &= 4u'^2 + 4u'^3 + u'^4 + 4u'v'^2 + 2u'^2v'^2 + v'^4 + 4u'w'^2 + 2u'^2w'^2 + 2v'^2w'^2 + w'^4 \\ z^3 &= 8u'^3 + 12u'^4 + 6u'^5 + u'^6 + 12u'^2v'^2 + 12u'^3v'^2 + 3u'^4v'^2 + 6u'v'^4 + 3u'^2v'^4 + v'^6 \\ &+ 12u'^2w'^2 + 12u'^3w'^2 + 3u'^4w'^2 + 12u'v'^2w'^2 + 6u'^2v'^2w'^2 + 3v'^4w'^2 + 6u'w'^4 + 3v'^2w'^4 + w'^6 \end{aligned} \quad (3.8)$$

Evaluation up to and including fourth order terms leads to the following approximation,

$$\begin{aligned} (1 + z)^{1/2} &= 1 + \frac{1}{2}u'^2 + u' + \frac{1}{2}v'^2 + \frac{1}{2}w'^2 - \frac{1}{2}u'^2 - \frac{1}{2}u'^3 - \frac{1}{8}u'^4 - \frac{1}{2}u'v'^2 - \frac{1}{4}u'^2v'^2 - \frac{1}{8}v'^4 \\ &- \frac{1}{2}u'w'^2 - \frac{1}{4}u'^2w'^2 - \frac{1}{4}v'^2w'^2 - \frac{1}{8}w'^4 + \frac{1}{2}u'^3 + \frac{3}{4}u'^4 + \frac{3}{4}u'^2v'^2 + \frac{3}{4}u'^2w'^2 \end{aligned} \quad (3.9)$$

Simplification, and subsequent substitution of equation (3.9) into (3.7) gives,

$$\varepsilon_e = u' + \frac{1}{2}(v'^2 + w'^2) - \frac{1}{2}u'(v'^2 + w'^2) + \frac{1}{2}u'^2(v'^2 + w'^2) - \frac{1}{8}(v'^2 + w'^2)^2 + \frac{5}{8}u'^4 \dots \quad (3.10)$$

Expanding to get ε_e^2 , again using computer algebra, with evaluation up to and including fourth order terms gives,

$$\varepsilon_e^2 = u'^2 + u'(v'^2 + w'^2) - u'^2(v'^2 + w'^2) + \frac{1}{4}(v'^2 + w'^2)^2 \dots \quad (3.11)$$

This strain squared expression will be used later in the derivation of the potential energy of the tether in equation (3.72).

3.3.2 Flexible Tether on Orbit

The inertial coordinate system for the tether is given by an assumed inertial X, Y, Z coordinate frame, with the origin at the centre of the Earth, as shown in Figure 3.2. The Z axis is pointing towards the Earth's North Pole and the X axis towards the vernal equinox point.

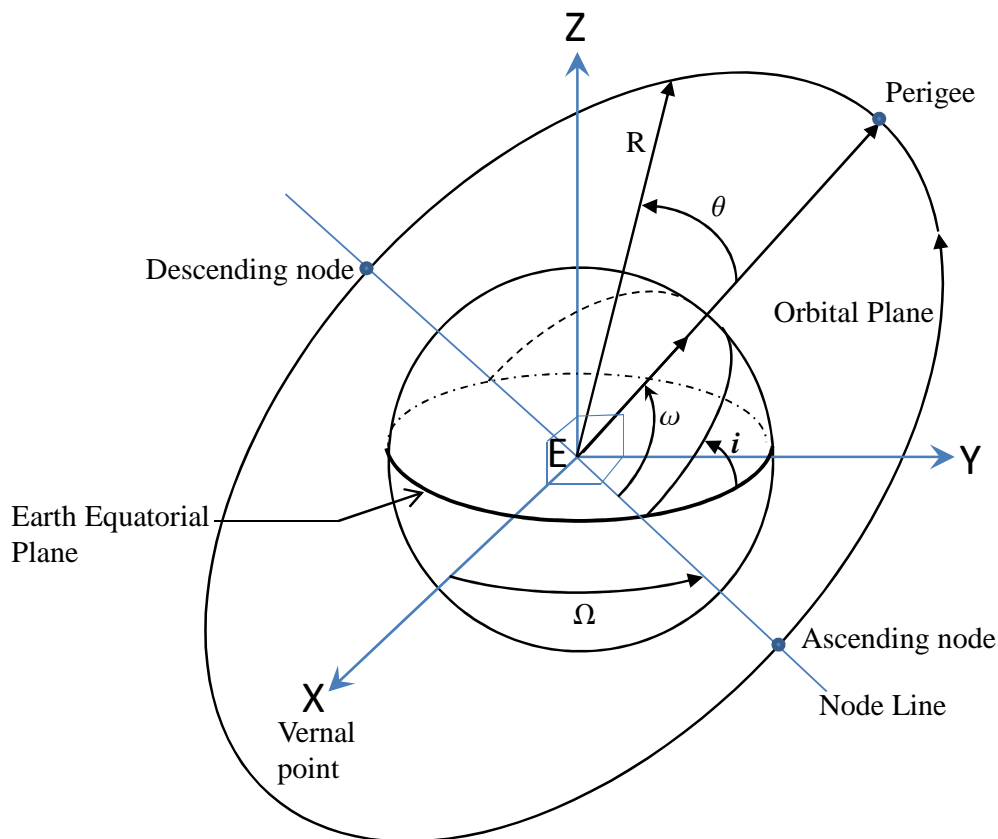


Figure 3.2 : Orbital elements for a geocentric inertial co-ordinate system

The orbital motion of the tether is described by the orbital elements in which R is defined as the distance from the central facility to the centre of the Earth. The angle from the direction of perigee of the orbit to the centre of mass is given by the true anomaly, θ and the inclination of the orbit is denoted by i . The three dimensional system in Figure 3.2 has been reduced to the two dimensional system which is given by the local coordinates shown in Figure 3.3, in order to reduce the complexity of the system and to be a basis for the flexible tether motion on orbit. Furthermore, orbit inclination is not considered in this study. The tether's centre of mass is at the origin of the relative rotating co-ordinate system, X_o-Y_o . The $X-Y$ plane and the X_o-Y_o plane lie within the orbital plane. The X axis is aligned to the direction of the perigee of the orbit and the X_o axis aligned to the position

vector of length R . The angle from the direction of perigee of the orbit to the centre of mass is given by the true anomaly, θ . The in-plane angle ψ is the angle from the X_o axis to the position of the tether on the plane. The payload masses, M_{P1} and M_{P2} are connected to the central facility, M_m , by the tether sub-span of length L .

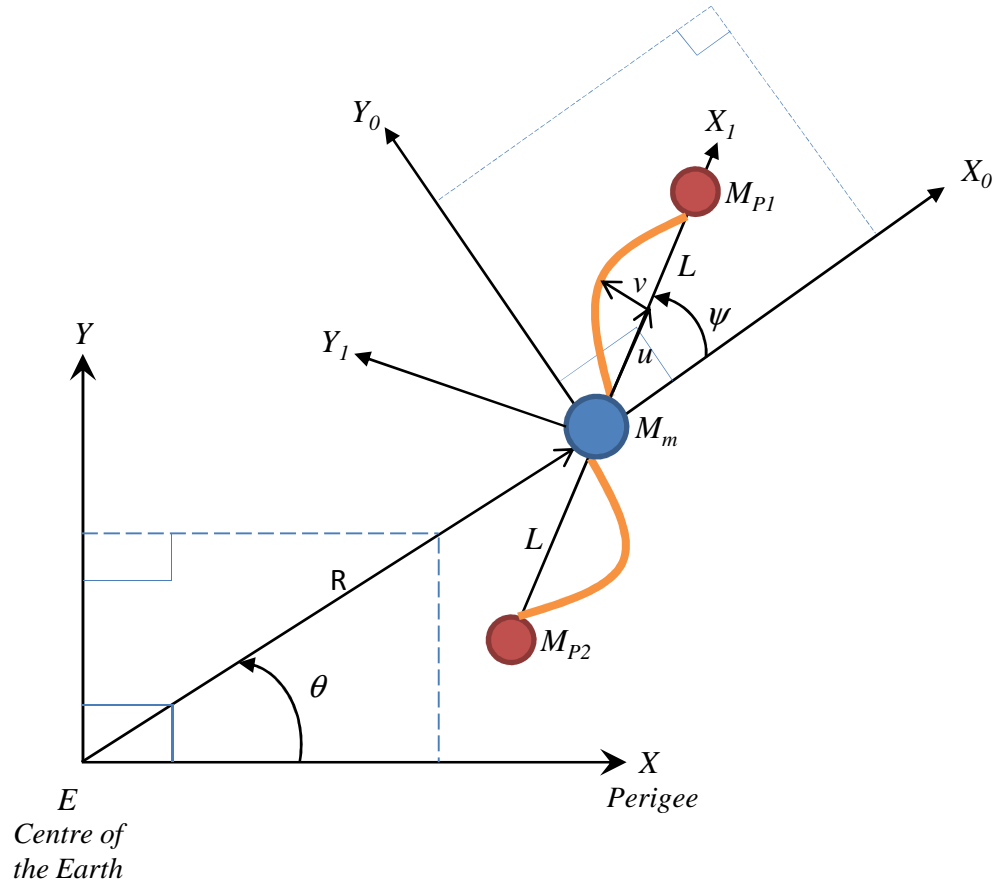


Figure 3.3 : Local co-ordinate system for the two dimensional flexible model of the MMET

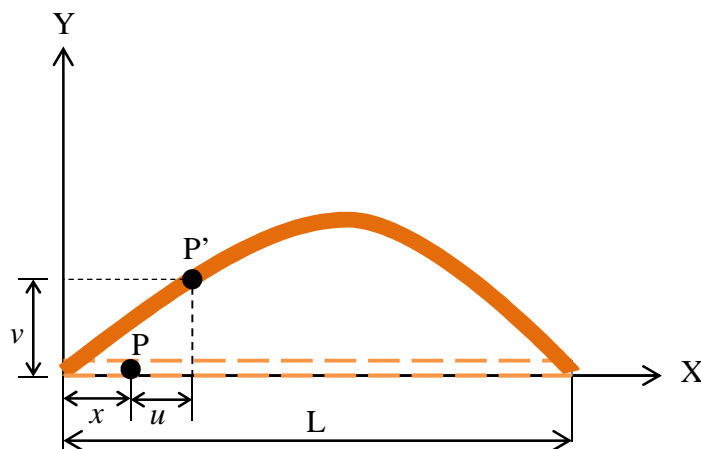


Figure 3.4 : Position of point P' on the deformed tether

The X - Y co-ordinate system for a deformed tether is shown in Figure 3.4, and the position of an arbitrary point on the deformed tether is given by point P' . The longitudinal deformation of the arbitrary point on the tether is denoted by $u(x,t)$ and the transverse deformation is given by $v(x,t)$. The distance of the point P from the central facility in the undeformed configuration is given by x .

3.3.3 Cartesian components

As shown in Ziegler and Cartmell (2001), the Cartesian components for the payload and the central facility when considered for planar motion, are given by,

$$x_{p1} = R \cos \theta + L \cos(\psi + \theta) \quad (3.12)$$

$$y_{p1} = R \sin \theta + L \sin(\psi + \theta) \quad (3.13)$$

$$x_{p2} = R \cos \theta - L \cos(\psi + \theta) \quad (3.14)$$

$$y_{p2} = R \sin \theta - L \sin(\psi + \theta) \quad (3.15)$$

and the coordinates of the central facility are,

$$x_{mm} = R \cos \theta \quad (3.16)$$

$$y_{mm} = R \sin \theta \quad (3.17)$$

and in this flexible model the position of point P' along the tether with respect to the centre of the Earth, as in Figure 3.4, is given by the following Cartesian components,

$$x_{t1p} = R \cos \theta + (u + x) \cos(\psi + \theta) - v \sin(\psi + \theta) \quad (3.18)$$

$$y_{t1p} = R \sin \theta + (u + x) \sin(\psi + \theta) + v \cos(\psi + \theta) \quad (3.19)$$

$$x_{t2p} = R \cos \theta - (u + x) \cos(\psi + \theta) + v \sin(\psi + \theta) \quad (3.20)$$

$$y_{t2p} = R \sin \theta - (u + x) \sin(\psi + \theta) - v \cos(\psi + \theta) \quad (3.21)$$

3.3.4 Separation of variables

The elastic displacements $u(x,t)$ and $v(x,t)$ are functions dependent both on space and time and can be separated in the usual manner by recourse to the Bubnov-Galerkin method,

$$u(x,t) = \sum_{i=1}^n \phi_i(x) q_{1i}(t); \quad v(x,t) = \sum_{i=1}^n \xi_i(x) q_{2i}(t); \quad (3.22)$$

where the $\phi_i(x)$ and $\xi_i(x)$ are spatial linear mode shape functions and $q_{1i}(t)$ and $q_{2i}(t)$ are time dependent modal coordinates.

Therefore, first mode approximations are given by,

$$u(x,t) = \phi(x) q_1(t); \quad v(x,t) = \xi(x) q_2(t); \quad (3.23)$$

where $\phi(x)$ and $\xi(x)$ can be taken to represent the relevant fundamental mode shapes, and $q_1(t)$ and $q_2(t)$ represent the generalised coordinates associated with those modes.

The equation for forced lateral vibration for a uniform string is as in equation (3.24) taken from Rao (2007) and Meirovitch (2001), where the tension is constant,

$$T \frac{d^2 v(x,t)}{dx^2} + f(x,t) = \rho \frac{d^2 v(x,t)}{dt^2} \quad (3.24)$$

Considering the free vibration case, for which $f(x,t) = 0$, the equation reduces to,

$$T \frac{d^2 v(x,t)}{dx^2} = \rho \frac{d^2 v(x,t)}{dt^2} \quad (3.25)$$

or,

$$c^2 \frac{d^2 v}{dx^2} = \frac{d^2 v}{dt^2} \quad (3.26)$$

where

$$c = \left(\frac{T}{\rho} \right)^{1/2} \quad (3.27)$$

Substitution of the second member of equations (3.23) for the displacement v , gives,

$$\frac{c^2}{f_2} \frac{d^2 \xi_i}{dx^2} = \frac{1}{q_{2i}} \frac{d^2 q_{2i}}{dt^2} \quad (3.28)$$

As expected, the left hand side of the equation is dependent on x , and the right hand side is dependent on t , therefore each side must be a constant which can be denoted by a ,

$$\frac{c^2}{f_2} \frac{d^2 \xi_i}{dx^2} = \frac{1}{q_{2i}} \frac{d^2 q_{2i}}{dt^2} = a \quad (3.29)$$

from which two ordinary differential equations can be obtained,

$$\frac{d^2 \xi_i}{dx^2} - \frac{a}{c^2} \xi_i = 0 \quad (3.30)$$

$$\frac{d^2 q_{2i}}{dt^2} - a q_{2i} = 0 \quad (3.31)$$

by setting set $a = -\omega^2$, equations (3.30) and (3.31) become,

$$\frac{d^2 \xi_i}{dx^2} + \frac{\omega^2}{c^2} \xi_i = 0 \quad (3.32)$$

$$\frac{d^2 q_{2i}}{dt^2} + \omega^2 q_{2i} = 0 \quad (3.33)$$

with the general solutions,

$$\xi(x) = A_1 \sin \frac{\omega}{c} x + B_1 \cos \frac{\omega}{c} x \quad (3.34)$$

$$q_1(t) = C_1 \cos \omega t + D_1 \sin \omega t \quad (3.35)$$

Assuming initially that the payload and central facility are so massive that the tether sub-spans experience them as being equivalent to built-in ends, then the tether motion has displacement boundary conditions as follows,

$$v(0) = v(L) = 0 \quad (3.36)$$

Substituting (3.36) in (3.34) and (3.35) and solving the linear homogeneous equation, gives the mode shapes in the form of,

$$\xi(x) = A_1 \sin \frac{i\pi x}{l} \quad i=1,2,\dots \quad (3.37)$$

This approach for the boundary conditions is echoed in the work of Luo *et al.* (1996), where the same assumption of fixed end boundary conditions is used to get the mode shape functions thereby simplifying the derivation of the equations of motion for a stretched spinning tether.

The axial vibration of the string can be assumed to be treatable similarly to the axial vibration of a thin rod which is governed by the same boundary conditions as for the transverse vibration of the string. Therefore, for this case the boundary condition is,

$$u(0) = u(L) = 0 \quad (3.38)$$

This gives a mode shape for axial vibration which is essentially the same as for transverse vibration,

$$\phi(x) = A_2 \sin \frac{i\pi x}{l} ; \quad i=1,2,\dots \quad (3.39)$$

where A_1 , and A_2 are arbitrary constants dependent on the boundary and initial conditions.

In this study, only the fundamental mode is considered. Restricting the analysis to the fundamental mode in each case simplifies the study and may still give a good basis for the dynamics of the flexible tether for future study. More simplification is applied to equation (3.39) in normalizing the modes by setting A_1 and A_2 to 1, to give the mode shapes as,

$$\phi(x) = \sin \frac{\pi x}{l}; \quad \xi(x) = \sin \frac{\pi x}{l}; \quad (3.40)$$

Therefore, the longitudinal and transverse displacements can be written as,

$$u(x,t) = \sin \frac{\pi x}{l} q_1(t); \quad v(x,t) = \sin \frac{\pi x}{l} q_2(t) \quad (3.41)$$

3.3.5 Kinetic Energy

The kinetic energy for the system takes into account translational and rotational motions, and for overall two dimensional translational motion is,

$$\begin{aligned} T_{trans} = & \frac{1}{2} M_{p1} (\dot{x}_{M_{p1}}^2 + \dot{y}_{M_{p1}}^2) + \frac{1}{2} M_{p2} (\dot{x}_{M_{p2}}^2 + \dot{y}_{M_{p2}}^2) + \frac{1}{2} M_m (\dot{x}_{M_m}^2 + \dot{y}_{M_m}^2) \\ & + \frac{1}{2} \rho AL (\dot{x}_{t1}^2 + \dot{y}_{t1}^2) + \frac{1}{2} \rho AL (\dot{x}_{t2}^2 + \dot{y}_{t2}^2) \end{aligned} \quad (3.42)$$

and the rotation kinetic energy is given by,

$$T_{rot} = \frac{1}{2} I_i \omega_i^2 \quad (3.43)$$

where I_i is the mass moment inertia, ω is the angular velocity, and i refers to the chosen rotation axis. In the case of the MMET system the angular velocities due to rotation about the X, Y and Z axes are given by,

$$\omega_x^2 = (\dot{\gamma})^2 \quad (3.44)$$

$$\omega_y^2 = (\dot{\alpha})^2 \quad (3.45)$$

$$\omega_z^2 = (\dot{\psi} + \dot{\theta})^2 \quad (3.46)$$

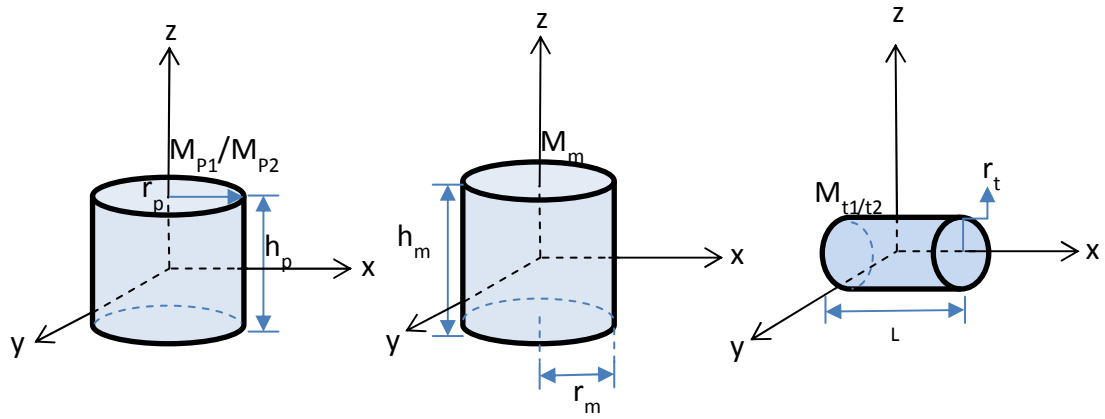


Figure 3.5 : Cylindrical shape of MMET components

The mass moments of inertia in equation (3.43) can be derived on the assumption that all components are cylindrical in shape as shown in Figure 3.5, and so the mass moment of inertia for rotation about the X axis is,

$$\begin{pmatrix} I_{X_{MP1}} \\ I_{X_{MP2}} \\ I_{X_{Mm}} \\ I_{X_{t1}} \\ I_{X_{t2}} \end{pmatrix} = \begin{pmatrix} \frac{1}{12} M_{P1} (3r_p^2 + h_p^2) \\ \frac{1}{12} M_{P2} (3r_p^2 + h_p^2) \\ \frac{1}{12} M_M (3r_m^2 + h_m^2) \\ \frac{1}{2} M_{P1} r_t^2 \\ \frac{1}{2} M_{P2} r_t^2 \end{pmatrix} \quad (3.47)$$

The mass moment of inertia for rotation about the Y axis is,

$$\begin{pmatrix} I_{Y_{MP1}} \\ I_{Y_{MP2}} \\ I_{Y_{Mm}} \\ I_{Y_{t1}} \\ I_{Y_{t2}} \end{pmatrix} = \begin{pmatrix} \frac{1}{12} M_{P1} (3r_p^2 + h_p^2) \\ \frac{1}{12} M_{P2} (3r_p^2 + h_p^2) \\ \frac{1}{12} M_m (3r_m^2 + h_m^2) \\ \frac{1}{12} \rho AL (3r_t^2 + L^2) \\ \frac{1}{12} \rho AL (3r_t^2 + L^2) \end{pmatrix} \quad (3.48)$$

and finally the mass moment of inertia for rotation about the Z axis is,

$$\begin{pmatrix} I_{Z_{MP1}} \\ I_{Z_{MP2}} \\ I_{Z_{Mm}} \\ I_{Z_{t1}} \\ I_{Z_{t2}} \end{pmatrix} = \begin{pmatrix} \frac{1}{2} M_{P1} r_p^2 \\ \frac{1}{2} M_{P2} r_p^2 \\ \frac{1}{2} M_m r_m^2 \\ \frac{1}{12} \rho A L (3r_t^2 + L^2) \\ \frac{1}{12} \rho A L (3r_t^2 + L^2) \end{pmatrix} \quad (3.49)$$

Adding equations (3.42) and (3.43) and considering that $M_{P1}=M_{P2} = M_P$, the kinetic energy for the payloads and the central facility as given by Cartmell (1998) and Ziegler (2003) is,

$$\begin{aligned} T_P &= \frac{1}{2} (M_m + 2M_P) (\dot{R}^2 + R^2 \dot{\theta}^2) + \left(2L^2 M_P + \frac{1}{2} M_m r_m^2 + M_P r_p^2 \right) \dot{\theta} \dot{\psi} \\ &+ \left(M_P L^2 + \frac{1}{4} M_m r_m^2 + \frac{1}{2} M_P r_p^2 \right) (\dot{\theta}^2 + \dot{\psi}^2) \end{aligned} \quad (3.50)$$

Furthermore, the kinetic energy associated with translation and rotation of the tether is given by,

$$T_T = \int_0^L \frac{1}{2} \rho A (\dot{x}_{t1p}^2 + \dot{y}_{t1p}^2) dx + \int_0^L \frac{1}{2} \rho A (\dot{x}_{t2p}^2 + \dot{y}_{t2p}^2) dx + I_T (\dot{\psi} + \dot{\theta})^2 \quad (3.51)$$

The tether is assumed for this model to be in the form of a solid circular cross-sectional line of radius r_T , area A , and density ρ , for which the mass moment of inertia is given by,

$$I_T = \frac{1}{12} \rho A L (3r_T^2 + L^2) \quad (3.52)$$

Using the separated variables for displacements u and v in (3.41), the first time derivative of the quantities in equations (3.18) to (3.21) are given by,

$$\begin{aligned}\dot{x}_{t1p} &= \dot{R} \cos \theta - R \dot{\theta} \sin \theta + \sin \frac{\pi x}{L} \dot{q}_1 \cos(\theta + \psi) - \sin \frac{\pi x}{L} \dot{q}_2 \sin(\theta + \psi) \\ &- \sin \frac{\pi x}{L} (\dot{\theta} + \dot{\psi}) q_2 \cos(\theta + \psi) - \left(x + q_1 \sin \frac{\pi x}{L} \right) (\dot{\theta} + \dot{\psi}) \sin(\theta + \psi)\end{aligned}\quad (3.53)$$

$$\begin{aligned}\dot{y}_{t1p} &= \dot{R} \sin \theta + R \dot{\theta} \cos \theta + \sin \frac{\pi x}{L} \dot{q}_1 \sin(\theta + \psi) + \sin \frac{\pi x}{L} \dot{q}_2 \cos(\theta + \psi) \\ &- \sin \frac{\pi x}{L} (\dot{\theta} + \dot{\psi}) q_2 \sin(\theta + \psi) + \left(x + q_1 \sin \frac{\pi x}{L} \right) (\dot{\theta} + \dot{\psi}) \cos(\theta + \psi)\end{aligned}\quad (3.54)$$

$$\begin{aligned}\dot{x}_{t2p} &= \dot{R} \cos \theta - R \dot{\theta} \sin \theta - \sin \frac{\pi x}{L} \dot{q}_1 \cos(\theta + \psi) + \sin \frac{\pi x}{L} \dot{q}_2 \sin(\theta + \psi) \\ &+ \sin \frac{\pi x}{L} (\dot{\theta} + \dot{\psi}) q_2 \cos(\theta + \psi) + \left(x + q_1 \sin \frac{\pi x}{L} \right) (\dot{\theta} + \dot{\psi}) \sin(\theta + \psi)\end{aligned}\quad (3.55)$$

$$\begin{aligned}\dot{y}_{t2p} &= \dot{R} \sin \theta + R \dot{\theta} \cos \theta - \sin \frac{\pi x}{L} \dot{q}_1 \sin(\theta + \psi) - \sin \frac{\pi x}{L} \dot{q}_2 \cos(\theta + \psi) \\ &+ \sin \frac{\pi x}{L} (\dot{\theta} + \dot{\psi}) q_2 \sin(\theta + \psi) - \left(x + q_1 \sin \frac{\pi x}{L} \right) (\dot{\theta} + \dot{\psi}) \cos(\theta + \psi)\end{aligned}\quad (3.56)$$

Substituting equations (3.53) to (3.56) into (3.51) gives the final form of T_T ,

$$\begin{aligned}T_T &= \frac{1}{2} \rho AL (\dot{q}_1^2 + \dot{q}_2^2) + \rho AL \dot{R}^2 + \rho AL R^2 \dot{\theta}^2 + \left(\rho AL (q_1 \dot{q}_2 - q_2 \dot{q}_1) + \frac{2}{\pi} \rho AL^2 \dot{q}_2 \right) (\dot{\theta} + \dot{\psi}) \\ &+ \left(\frac{5}{6} \rho AL^3 + \frac{4}{\pi} \rho AL^2 q_1 + \rho AL (q_1^2 + q_2^2) + \frac{1}{2} \rho AL r_T^2 \right) (\dot{\theta} \dot{\psi}) \\ &+ \left(\frac{5}{12} \rho AL^3 + \frac{2}{\pi} \rho AL^2 q_1 + \frac{1}{2} \rho AL (q_1^2 + q_2^2) + \frac{1}{4} \rho AL r_T^2 \right) (\dot{\theta}^2 + \dot{\psi}^2)\end{aligned}\quad (3.57)$$

3.3.6 Potential Energy

The previous work of Ziegler and Cartmell (2001) considered the potential energy for the system, consisting of gravitational potential energy given by,

$$U_G = U_{m1} + U_{m2} + U_{mm} + U_{t1} + U_{t2}\quad (3.58)$$

where U_{m1} , U_{m2} , U_{mm} , U_{t1} and U_{t2} are,

$$U_{m1} = -\frac{\mu M_{p1}}{\sqrt{R^2 + L^2 + 2LR \cos \varphi}} \quad (3.59)$$

$$U_{m2} = -\frac{\mu M_{p2}}{\sqrt{R^2 + L^2 - 2LR \cos \varphi}} \quad (3.60)$$

$$U_{mm} = -\frac{\mu M_m}{R} \quad (3.61)$$

$$\begin{aligned} U_{i1} &= -\mu \rho A \int_0^L (R^2 + l^2 + 2Rl \cos \psi)^{-\frac{1}{2}} dl \\ &= \mu \rho A \ln \frac{R(1 + \cos \psi)}{L + R \cos \psi + \sqrt{R^2 + L^2 + 2RL \cos \psi}} \end{aligned} \quad (3.62)$$

$$\begin{aligned} U_{i1} &= -\mu \rho A \int_0^L (R^2 + l^2 - 2Rl \cos \psi)^{-\frac{1}{2}} dl \\ &= \mu \rho A \ln \frac{R(1 + \cos \psi)}{L + R \cos \psi + \sqrt{R^2 + L^2 - 2RL \cos \psi}} \end{aligned} \quad (3.63)$$

It was mentioned by Ziegler (2003) and proved by Chen (2009) that equations (3.62) and (3.63) can generate a numerical singularity for $\psi = \pi$ for any non-zero constants value. Therefore, when numerically integrating the equations, the following discrete approximations as proposed by Ziegler (2003) can be used for the two sub-span contributions,

$$U_{i1} = -\sum_{i=1}^N \frac{\mu \rho A L}{N \sqrt{R^2 + \left[\frac{(2i-1)L}{2N} \right]^2 + \frac{2(2i-1)RL}{2N} \cos \psi}} \quad (3.64)$$

$$U_{i2} = -\sum_{i=1}^N \frac{\mu \rho A L}{N \sqrt{R^2 + \left[\frac{(2i-1)L}{2N} \right]^2 - \frac{2(2i-1)RL}{2N} \cos \psi}} \quad (3.65)$$

Ziegler (2003) showed that in general $N = 10$ to 15 is a sufficiently fine discretisation for accurate representation of the potential energy of the sub-span.

In this flexible model, the tether has additional potential energy due to its own elastic effects. The elastic potential energy is,

$$U = \frac{1}{2} \int_0^l EA \varepsilon_T^2 dx \quad (3.66)$$

where ε_T is the total strain. The tension, T for the string is given by

$$T = T_o + EA \varepsilon_e \quad (3.67)$$

where T_o is the tension when the string is in the nominal configuration and this would normally come from the centripetal load in the MMET, and $EA \varepsilon_e$ is the tension due to elemental stretch. T_o is defined by,

$$T_o = \left(M_p L + \int_0^L \rho A x dx \right) \dot{\psi}^2 \quad (3.68)$$

where $\dot{\psi}$ is the angular velocity of the system.

A simple stress-strain relationship is assumed for the axially loaded MMET,

$$\sigma = \frac{F}{A} = E \varepsilon_T \quad (3.69)$$

where the cross-sectional area, A , is considered to remain constant during and after axial extension of the element, and force F for this case is the tension, T .

Substitution of equation (3.67) into (3.68) gives the strain function as,

$$\varepsilon_T = \frac{T_o + EA \varepsilon_e}{EA} = \frac{T_o}{EA} + \varepsilon_e \quad (3.70)$$

Therefore, substitution of equation (3.70) into (3.66) gives the potential energy in this form,

$$U_{E1,E2} = \frac{1}{2} \int_0^l EA \left(\frac{T_o}{EA} + \varepsilon_e \right)^2 dx$$

$$\begin{aligned}
&= \frac{1}{2} \int_0^l \left(\frac{T_o^2}{EA} + 2T_o \varepsilon_e + EA \varepsilon_e^2 \right) dx \\
&= \int_0^l \left(\frac{1}{2} \frac{T_o^2}{EA} + T_o \varepsilon_e + \frac{1}{2} EA \varepsilon_e^2 \right) dx \tag{3.71}
\end{aligned}$$

and substitution of the strain expressions (3.10) and (3.11) into (3.71) gives the elastic potential energy for the tether in the following form,

$$\begin{aligned}
U_{E1,E2} &= \int_0^L \left[\frac{1}{2} \frac{T_o^2}{EA} + T_o \left(u' + \frac{1}{2} (v'^2) - \frac{1}{2} u'(v'^2) + \frac{1}{2} u'^2 (v'^2) - \frac{1}{8} (v')^4 + \frac{5}{8} u'^4 \right) \right. \\
&\quad \left. + \frac{1}{2} EA \left(u'^2 + u'(v'^2) - u'^2 (v'^2) + \frac{1}{4} (v')^4 \right) \right] dx \tag{3.72}
\end{aligned}$$

Substituting equation (3.41) into equation (3.72) and applying the integration from 0 to L gives the potential energy as,

$$\begin{aligned}
U_{E1,E2} &= \frac{LT_o}{AE} + \frac{AE\pi^2 q_1^2}{2L} + \frac{T_o\pi^2 q_2^2}{2L} - \frac{3AE\pi^4 q_1^2 q_2^2}{8L^3} + \frac{3T_o\pi^4 q_1^2 q_2^2}{8L^3} + \frac{3AE\pi^4 q_2^4}{32L^3} \\
&\quad + \frac{15T_o\pi^4 q_1^4}{32L^3} + \frac{3T_o\pi^4 q_2^4}{32L^3} \tag{3.73}
\end{aligned}$$

3.3.7 Total Kinetic Energy and Potential Energy

Adding equations (3.50) and (3.57) gives the total kinetic energy for the system,

$$\begin{aligned}
T_k &= \frac{1}{2} \rho AL (\dot{q}_1^2 + \dot{q}_2^2) + \left(\rho AL + \frac{1}{2} M_M + M_P \right) \dot{R}^2 + \frac{1}{2} (M_M + 2M_P + 2\rho AL) R^2 \dot{\theta}^2 \\
&\quad + \left(\frac{5}{6} \rho AL^3 + \frac{4}{\pi} \rho AL^2 q_1 + \rho AL (q_1^2 + q_2^2) + \frac{1}{2} \rho AL r_T^2 + (2L^2 + r_P^2) M_P + \frac{1}{2} M_M r_m^2 \right) (\dot{\theta} \dot{\psi}) \\
&\quad + \left(\frac{2\rho AL^2}{\pi} \dot{q}_2 + \rho AL (q_1 \dot{q}_2 - q_2 \dot{q}_1) \right) (\dot{\theta} + \dot{\psi}) + \left(M_P L^2 + \frac{5}{12} \rho AL^3 + \frac{2\rho AL^2}{\pi} q_1 \right. \\
&\quad \left. + \frac{1}{2} \rho AL (q_1^2 + q_2^2) + \frac{1}{4} M_m r_m^2 + \frac{1}{2} M_P r_P^2 + \frac{1}{4} \rho AL r_T^2 \right) (\dot{\theta}^2 + \dot{\psi}^2) \tag{3.74}
\end{aligned}$$

Substituting the various constituent part into equation (3.58), and adding equation (3.73) to this gives the total potential energy for the system,

$$\begin{aligned}
U_P = & -\frac{\mu M_{P1}}{\sqrt{R^2 + L^2 + 2LR\cos\phi}} - \frac{\mu M_{P2}}{\sqrt{R^2 + L^2 - 2LR\cos\phi}} - \frac{\mu M_m}{R} \\
& - \sum_{i=1}^N \frac{\mu\rho AL}{N\sqrt{R^2 + \left[\frac{(2i-1)L}{2N}\right]^2 + \frac{2(2i-1)RL}{2N}\cos\psi}} - \sum_{i=1}^N \frac{\mu\rho AL}{N\sqrt{R^2 + \left[\frac{(2i-1)L}{2N}\right]^2 - \frac{2(2i-1)RL}{2N}\cos\psi}} \\
& + \frac{LT_o}{AE} + \frac{AE\pi^2 q_1^2}{2L} + \frac{T_o\pi^2 q_2^2}{2L} - \frac{3AE\pi^4 q_1^2 q_2^2}{8L^3} + \frac{3T_o\pi^4 q_1^2 q_2^2}{8L^3} + \frac{3AE\pi^4 q_2^4}{32L^3} + \\
& + \frac{15T_o\pi^4 q_1^4}{32L^3} + \frac{3T_o\pi^4 q_2^4}{32L^3}
\end{aligned} \tag{3.75}$$

3.4 Equations of Motion

The equations of motions are derived using Lagrangian dynamics. Lagrange's equation is given in the common undamped form as follows,

$$\frac{d}{dt} \left(\frac{\partial T}{\partial \dot{q}_k} \right) - \frac{\partial T}{\partial q_k} + \frac{\partial U}{\partial q_k} = \tilde{Q}_k \tag{3.76}$$

Previously, the damped system of MMET has been studied by Gandara (2009), where damping in the system due to the bearings in the motor and transmission and general frictional heat dissipation was included in the derivation of the equations of motion. In this study the flexibility of the tether has already introduced great complexity into the system, therefore damping was abandoned not to make this system even more complex. The previous model by Ziegler (2003) also did not include the damping of the system in order for a comparison to be made between the flexible and rigid models.

In this current system, the generalised coordinates are given by $\{q_k\} = \{\psi, \theta, R, q_1, q_2\}$ and in the unmotorised case there is obviously no external force acting on the MMET system so the generalised force in equation (3.76) is equal to zero. This means that the MMET motor drive is not actuated in this instance, hence the tether dynamics are entirely dependent on the initial conditions. However, the generalised force terms are clearly non-zero for the motorised case.

Starting with generalised coordinate ψ . Operating on equation (3.74) gives,

$$\frac{\partial T}{\partial \psi} = 0 \quad (3.77)$$

Then, we obtain,

$$\begin{aligned} \frac{\partial T}{\partial \dot{\psi}} &= \rho AL(q_1 \dot{q}_2 - q_2 \dot{q}_1) + \frac{2\rho AL^2 \dot{q}_2}{\pi} + \left(\frac{5}{6} \rho AL^3 + \frac{4\rho AL^2 q_1}{\pi} + \rho ALq_1^2 + \rho ALq_2^2 \right) (\dot{\theta} + \dot{\psi}) \\ &+ \left(2L^2 M_p + \frac{1}{2} M_m r_m^2 + M_p r_p^2 + \frac{1}{2} \rho ALr_T^2 \right) (\dot{\theta} + \dot{\psi}) \end{aligned} \quad (3.78)$$

From which, we get,

$$\begin{aligned} \frac{d}{dt} \left(\frac{\partial T}{\partial \dot{\psi}} \right) &= \left(\frac{4}{\pi} \rho AL^2 \dot{q}_1 + 2\rho ALq_1 \dot{q}_1 + 2\rho ALq_2 \dot{q}_2 \right) (\dot{\theta} + \dot{\psi}) + \frac{2}{\pi} \rho AL^2 \ddot{q}_2 \\ &+ \rho AL(q_1 \ddot{q}_2 - q_2 \ddot{q}_1) + \left(\frac{5}{6} \rho AL^3 + \frac{4}{\pi} \rho AL^2 q_1 + \rho ALq_1^2 + \rho ALq_2^2 \right) (\ddot{\theta} + \ddot{\psi}) \\ &\left(2L^2 M_p + \frac{1}{2} M_m r_m^2 + M_p r_p^2 + \frac{1}{2} \rho ALr_T^2 \right) (\ddot{\theta} + \ddot{\psi}) \end{aligned} \quad (3.79)$$

Finally from equation (3.75) we obtain,

$$\begin{aligned} \frac{\partial U}{\partial \psi} &= \frac{M_p LR\mu \sin \psi}{(L^2 + R^2 - 2LR \cos \psi)^{3/2}} - \frac{M_p LR\mu \sin \psi}{(L^2 + R^2 + 2LR \cos \psi)^{3/2}} \\ &- \sum_{i=1}^N \frac{\mu \rho AL^2 R(2i-1) \sin \psi}{2N^2 \left(R^2 + \frac{(2i-1)^2 L^2}{4N^2} - \frac{(2i-1)RL}{N} \cos \psi \right)^{3/2}} \\ &\sum_{i=1}^N \frac{\mu \rho AL^2 R(2i-1) \sin \psi}{2N^2 \left(R^2 + \frac{(2i-1)^2 L^2}{4N^2} + \frac{(2i-1)RL}{N} \cos \psi \right)^{3/2}} \end{aligned} \quad (3.80)$$

Inserting equations (3.77) to (3.80) into Lagrange's equation, as stated in equation (3.76), gives,

$$\begin{aligned}
& \left(\frac{5}{6} \rho AL^3 + \frac{4}{\pi} \rho AL^2 q_1 + \rho AL q_1^2 + \rho AL q_2^2 + 2L^2 M_P + \frac{1}{2} M_m r_m^2 + M_P r_P^2 \right. \\
& \quad \left. + \frac{1}{2} \rho AL r_T^2 \right) (\ddot{\theta} + \ddot{\psi}) + \left(\frac{4}{\pi} \rho AL^2 \dot{q}_1 + 2\rho AL q_1 \dot{q}_1 + 2\rho AL q_2 \dot{q}_2 \right) (\dot{\theta} + \dot{\psi}) \\
& \quad - \frac{M_P LR \mu \sin \psi}{(L^2 + R^2 - 2LR \cos \psi)^{3/2}} - \frac{M_P LR \mu \sin \psi}{(L^2 + R^2 + 2LR \cos \psi)^{3/2}} + \rho AL q_1 \ddot{q}_2 \\
& \quad - \rho AL q_2 \ddot{q}_1 + \frac{2}{\pi} \rho AL^2 \ddot{q}_2 - \sum_{i=1}^N - \frac{\mu \rho AL^2 R (2i-1) \sin \psi}{2N^2 \left(R^2 + \frac{(2i-1)^2 L^2}{4N^2} - \frac{(2i-1) RL}{N} \cos \psi \right)^{3/2}} \\
& \quad - \sum_{i=1}^N \frac{\mu \rho AL^2 R (2i-1) \sin \psi}{2N^2 \left(R^2 + \frac{(2i-1)^2 L^2}{4N^2} + \frac{(2i-1) RL}{N} \cos \psi \right)^{3/2}} = 0
\end{aligned} \tag{3.81}$$

Next, for generalised coordinate θ ,

$$\frac{\partial T}{\partial \theta} = 0 \tag{3.82}$$

$$\begin{aligned}
\frac{\partial T}{\partial \dot{\theta}} &= (M_M + 2M_P + 2\rho AL) R^2 \dot{\theta} + \left(\frac{5}{6} \rho AL^3 + \frac{4\rho AL^2 q_1}{\pi} + \rho AL (q_1^2 + q_2^2) + \right. \\
& \quad \left. 2L^2 M_P + \frac{1}{2} M_m r_m^2 + M_P r_P^2 + \frac{1}{2} \rho AL r_T^2 \right) (\dot{\theta} + \dot{\psi}) + \frac{2\rho AL^2}{\pi} \dot{q}_2 + \rho AL (q_1 \dot{q}_2 - q_2 \dot{q}_1)
\end{aligned} \tag{3.83}$$

$$\begin{aligned}
\frac{d}{dt} \left(\frac{\partial T}{\partial \dot{\theta}} \right) &= (M_M + 2M_P + 2\rho AL) R^2 \ddot{\theta} + (2M_M + 4M_P + 4\rho AL) R \dot{R} \dot{\theta} + \\
& \quad \left(\frac{5}{6} \rho AL^3 + \frac{4\rho AL^2 q_1}{\pi} + \rho AL (q_1^2 + q_2^2) + 2L^2 M_P + \frac{1}{2} M_m r_m^2 + M_P r_P^2 + \frac{1}{2} \rho AL r_T^2 \right) (\ddot{\theta} + \ddot{\psi}) \\
& \quad \left(\frac{4\rho AL^2 \dot{q}_1}{\pi} + 2\rho AL q_1 \dot{q}_1 + 2\rho AL q_2 \dot{q}_2 \right) (\dot{\theta} + \dot{\psi}) - \rho AL (q_1 \ddot{q}_2 - q_2 \ddot{q}_1) + \frac{2\rho AL^2}{\pi} \ddot{q}_2
\end{aligned} \tag{3.84}$$

Finally, we note that,

$$\frac{\partial U}{\partial \theta} = 0 \quad (3.85)$$

Inserting equations (3.82) to (3.85) appropriately into Lagrange's equation, leads to,

$$\begin{aligned} & (M_M + 2M_P + 2\rho AL)R^2\ddot{\theta} + (2M_M + 4M_P + 4\rho AL)RR\dot{\theta} + \\ & \left(\frac{5}{6}\rho AL^3 + \frac{4\rho AL^2 q_1}{\pi} + \rho AL(q_1^2 + q_2^2) + 2L^2 M_P + \frac{1}{2}M_m r_m^2 + M_P r_P^2 + \frac{1}{2}\rho ALr_T^2 \right) (\ddot{\theta} + \ddot{\psi}) \\ & \left(\frac{4\rho AL^2 \dot{q}_1}{\pi} + 2\rho ALq_1\dot{q}_1 + 2\rho ALq_2\dot{q}_2 \right) (\dot{\theta} + \dot{\psi}) - \rho AL(q_1\ddot{q}_2 - q_2\ddot{q}_1) + \frac{2\rho AL^2}{\pi}\ddot{q}_2 = 0 \end{aligned} \quad (3.86)$$

In the case of generalised coordinate R the following differentiations apply,

$$\frac{\partial T}{\partial R} = (M_M + 2M_P + 2\rho AL)R\dot{\theta}^2 \quad (3.87)$$

$$\frac{\partial T}{\partial \dot{R}} = (M_M + 2M_P + 2\rho AL)\dot{R} \quad (3.88)$$

$$\frac{d}{dt} \left(\frac{\partial T}{\partial \dot{R}} \right) = (M_M + 2M_P + 2\rho AL)\ddot{R} \quad (3.89)$$

$$\begin{aligned} \frac{\partial U}{\partial R} = & \frac{\mu M_M}{R^2} - \frac{M_P \mu (L \cos \psi + R)}{(R^2 + L^2 - 2RL \cos \psi)^{3/2}} + \frac{M_P \mu (L \cos \psi + R)}{(R^2 + L^2 + 2RL \cos \psi)^{3/2}} \\ & - \sum_{i=1}^N \frac{\mu \rho AL \left(2R - \frac{(2i-1)L \cos \psi}{N} \right)}{2N^2 \left(R^2 + \frac{(2i-1)^2 L^2}{4N^2} - \frac{(2i-1)RL}{N} \cos \psi \right)^{3/2}} \\ & - \sum_{i=1}^N \frac{\mu \rho AL \left(2R + \frac{(2i-1)L \cos \psi}{N} \right)}{2N^2 \left(R^2 + \frac{(2i-1)^2 L^2}{4N^2} + \frac{(2i-1)RL}{N} \cos \psi \right)^{3/2}} \end{aligned} \quad (3.90)$$

Substituting equations (3.87) to (3.90) as required into Lagrange's equation, leads to,

$$\begin{aligned}
& (M_M + 2M_P + 2\rho AL)\ddot{R} - (M_M + 2M_P + 2\rho AL)R\dot{\theta}^2 + \frac{\mu M_M}{R^2} \\
& - \frac{M_P \mu (L \cos \psi + R)}{(R^2 + L^2 - 2RL \cos \psi)^{3/2}} + \frac{M_P \mu (L \cos \psi + R)}{(R^2 + L^2 + 2RL \cos \psi)^{3/2}} \\
& - \sum_{i=1}^N - \frac{\mu \rho AL \left(2R - \frac{(2i-1)L \cos \psi}{N} \right)}{2N^2 \left(R^2 + \frac{(2i-1)^2 L^2}{4N^2} - \frac{(2i-1)RL}{N} \cos \psi \right)^{3/2}} \\
& - \sum_{i=1}^N - \frac{\mu \rho AL \left(2R + \frac{(2i-1)L \cos \psi}{N} \right)}{2N^2 \left(R^2 + \frac{(2i-1)^2 L^2}{4N^2} + \frac{(2i-1)RL}{N} \cos \psi \right)^{3/2}} = 0
\end{aligned} \tag{3.91}$$

Then for generalised modal coordinate q_1 ,

$$\frac{\partial T}{\partial q_1} = (\rho AL \dot{q}_2) (\dot{\theta} + \dot{\psi}) + \left(\frac{2}{\pi} \rho AL^2 + \rho AL q_1 \right) (\dot{\theta}^2 + \dot{\psi}^2) + \left(\frac{4}{\pi} \rho AL^2 + 2\rho AL q_1 \right) \dot{\theta} \dot{\psi} \tag{3.92}$$

$$\frac{\partial T}{\partial \dot{q}_1} = \rho AL \dot{q}_1 - \rho AL q_2 \dot{\theta} - \rho AL q_2 \dot{\psi} \tag{3.93}$$

$$\frac{d}{dt} \left(\frac{\partial T}{\partial \dot{q}_1} \right) = \rho AL \ddot{q}_1 - \rho AL \dot{q}_2 (\dot{\theta} + \dot{\psi}) - \rho AL q_2 (\ddot{\theta} + \ddot{\psi}) \tag{3.94}$$

$$\frac{\partial U}{\partial q_1} = \frac{EA\pi^2}{L} q_1 + \left(\frac{3\pi^4}{4L^3} \right) (T_o - EA) q_1 q_2^2 + \frac{15T_o \pi^4}{8L^3} q_1^3 \tag{3.95}$$

Taking equations (3.92) to (3.95) and substituting them into Lagrange's equation, gives the following,

$$\begin{aligned}
& \rho AL \ddot{q}_1 - 2\rho AL \dot{q}_2 (\dot{\theta} + \dot{\psi}) - \left(\frac{2\rho AL^2}{\pi} + \rho AL q_1 \right) (\dot{\theta}^2 + \dot{\psi}^2) - \left(\frac{4}{\pi} \rho AL^2 + 2\rho AL q_1 \right) \dot{\theta} \dot{\psi} \\
& + \frac{EA\pi^2}{L} q_1 + \left(\frac{3\pi^4}{4L^3} \right) (T_o - EA) q_1 q_2^2 + \frac{15T_o \pi^4}{8L^3} q_1^3 - \rho AL q_2 (\ddot{\theta} + \ddot{\psi}) = 0
\end{aligned} \tag{3.96}$$

Finally, for generalised modal coordinate q_2 ,

$$\frac{\partial T}{\partial q_2} = -\rho AL\dot{q}_1\dot{\theta} - \rho AL\dot{q}_1\dot{\psi} + \rho ALq_2\dot{\theta}^2 + \rho ALq_2\dot{\psi}^2 + 2\rho ALq_2\dot{\theta}\dot{\psi} \quad (3.97)$$

$$\frac{\partial T}{\partial \dot{q}_2} = \rho AL\dot{q}_2 + \left(\frac{2}{\pi}\rho AL^2 + \rho ALq_1\right)(\dot{\theta} + \dot{\psi}) \quad (3.98)$$

$$\frac{d}{dt}\left(\frac{\partial T}{\partial \dot{q}_2}\right) = \rho AL\ddot{q}_2 + \left(\frac{2}{\pi}\rho AL^2 + \rho ALq_1\right)(\ddot{\theta} + \ddot{\psi}) + \rho AL\dot{q}_1(\dot{\theta} + \dot{\psi}) \quad (3.99)$$

$$\frac{\partial U}{\partial q_1} = \frac{T_o\pi^2}{L}q_2 + \frac{3\pi^4}{4L^3}(T_o - EA)q_1^2q_2 + \frac{3\pi^4}{8L^3}(EA - T_o)q_2^3 \quad (3.100)$$

Following the same process takes us to,

$$\begin{aligned} &\rho AL\ddot{q}_2 - \rho ALq_2(\dot{\theta}^2 + \dot{\psi}^2) - 2\rho ALq_2\dot{\theta}\dot{\psi} + \frac{T_o\pi^2}{L}q_2 + \frac{3\pi^4}{4L^3}(T_o - EA)q_1^2q_2 \\ &+ \frac{3\pi^4}{8L^3}(EA - T_o)q_2^3 + \left(\frac{2}{\pi}\rho AL^2 + \rho ALq_1\right)(\ddot{\theta} + \ddot{\psi}) + 2\rho AL\dot{q}_1(\dot{\theta} + \dot{\psi}) = 0 \end{aligned} \quad (3.101)$$

Dividing equations (3.81), (3.86), (3.91), (3.96) and (3.101) by ρAL gives second order ordinary differential equations of motion for the system in reasonably standard form, thus $M\ddot{x}(t) + c\dot{x}(t) + kx(t) = F$, where the force on the right hand side is given by the applied torque from the motor in the central facility,

$$\begin{aligned} &\left(\frac{5}{6}L^2 + \frac{4}{\pi}Lq_1 + q_1^2 + q_2^2 + \frac{1}{\rho AL}\left(2L^2M_p + \frac{1}{2}M_m r_m^2 + M_p r_p^2\right) + \frac{1}{2}r_T^2\right)(\ddot{\theta} + \ddot{\psi}) \\ &+ \left(\frac{4}{\pi}L\dot{q}_1 + 2q_1\dot{q}_1 + 2q_2\dot{q}_2\right)(\dot{\theta} + \dot{\psi}) + \frac{M_p LR\mu \sin \psi}{\rho AL(L^2 + R^2 - 2LR \cos \psi)^{3/2}} \\ &- \frac{M_p LR\mu \sin \psi}{\rho AL(L^2 + R^2 + 2LR \cos \psi)^{3/2}} + q_1\ddot{q}_2 - q_2\ddot{q}_1 + \frac{2}{\pi}L\ddot{q}_2 \\ &- \sum_{i=1}^N \frac{\mu LR(2i-1)\sin \psi}{2N^2\left(R^2 + \frac{(2i-1)^2 L^2}{4N^2} - \frac{(2i-1)RL}{N}\cos \psi\right)^{3/2}} \\ &- \sum_{i=1}^N \frac{\mu LR(2i-1)\sin \psi}{2N^2\left(R^2 + \frac{(2i-1)^2 L^2}{4N^2} + \frac{(2i-1)RL}{N}\cos \psi\right)^{3/2}} = \tau \end{aligned} \quad (3.102)$$

$$\begin{aligned}
& \frac{1}{\rho AL} (M_M + 2M_P + 2\rho AL) R^2 \ddot{\theta} + \frac{1}{\rho AL} (2M_M + 4M_P + 4\rho AL) R \dot{R} \dot{\theta} + \\
& \left(\frac{5}{6} L^2 + \frac{4Lq_1}{\pi} + (q_1^2 + q_2^2) + \frac{1}{\rho AL} \left(2L^2 M_P + \frac{1}{2} M_m r_m^2 + M_P r_P^2 \right) + \frac{1}{2} r_T^2 \right) (\ddot{\theta} + \ddot{\psi}) \\
& \left(\frac{4L\dot{q}_1}{\pi} + 2q_1 \dot{q}_1 + 2q_2 \dot{q}_2 \right) (\dot{\theta} + \dot{\psi}) - (q_1 \ddot{q}_2 - q_2 \ddot{q}_1) + \frac{2L}{\pi} \ddot{q}_2 = 0
\end{aligned} \tag{3.103}$$

$$\begin{aligned}
& \frac{1}{\rho AL} (M_M + 2M_P + 2\rho AL) \ddot{R} - \frac{1}{\rho AL} (M_M + 2M_P + 2\rho AL) R \dot{\theta}^2 + \frac{\mu M_M}{\rho AL R^2} \\
& - \frac{M_P \mu (L \cos \psi + R)}{\rho AL (R^2 + L^2 - 2RL \cos \psi)^{3/2}} + \frac{M_P \mu (L \cos \psi + R)}{\rho AL (R^2 + L^2 + 2RL \cos \psi)^{3/2}} \\
& - \sum_{i=1}^N - \frac{\mu \left(2R - \frac{(2i-1)L \cos \psi}{N} \right)}{2N^2 \left(R^2 + \frac{(2i-1)^2 L^2}{4N^2} - \frac{(2i-1)RL \cos \psi}{N} \right)^{3/2}} \\
& - \sum_{i=1}^N - \frac{\mu \left(2R + \frac{(2i-1)L \cos \psi}{N} \right)}{2N^2 \left(R^2 + \frac{(2i-1)^2 L^2}{4N^2} + \frac{(2i-1)RL \cos \psi}{N} \right)^{3/2}} = 0
\end{aligned} \tag{3.104}$$

$$\begin{aligned}
& \ddot{q}_1 - q_2 (\ddot{\theta} + \ddot{\psi}) - \left(\frac{2L}{\pi} + q_1 \right) (\dot{\theta}^2 + \dot{\psi}^2) - 2\dot{q}_2 (\dot{\theta} + \dot{\psi}) - \left(\frac{4L}{\pi} + 2q_1 \right) \dot{\theta} \dot{\psi} \\
& + \frac{EA \pi^2}{\rho AL^2} q_1 + \left(\frac{3\pi^4}{4\rho AL^4} \right) (T_o - EA) q_1 q_2^2 + \frac{15T_o \pi^4}{8\rho AL^4} q_1^3 = 0
\end{aligned} \tag{3.105}$$

$$\begin{aligned}
& \ddot{q}_2 + \left(\frac{2L}{\pi} + q_1 \right) (\ddot{\theta} + \ddot{\psi}) - q_2 (\dot{\theta}^2 + \dot{\psi}^2) + 2\dot{q}_1 (\dot{\theta} + \dot{\psi}) - 2q_2 \dot{\theta} \dot{\psi} \\
& + \frac{T_o \pi^2}{\rho AL^2} q_2 + \frac{3\pi^4}{8\rho AL^4} (EA - T_o) q_2^3 + \frac{3\pi^4}{4\rho AL^4} (T_o - EA) q_1^2 q_2 = 0
\end{aligned} \tag{3.106}$$

3.5 Tether Simulation

Four operating conditions have been considered in this study of the tether's motion on orbit. The conditions are as follows,

- i. Circular orbit, unmotorised (no torque is applied to the system). Initial conditions only are driving this version of the model.

- ii. Circular orbit, motorised. The torque is applied and predominates the motion of the system.
- iii. Elliptical orbit, unmotorised (no torque is applied to the system). Initial conditions only are driving this version of the model.
- iv. Elliptical orbit, motorised. The torque is applied and predominates the motion of the system.

The angular velocity is the main parameter to determine the required ΔV in payload transfer. The best practice is to release the payload when the tether is aligned exactly along the gravity vector at perigee. However, Ziegler (2003) discussed the case when the tether is not released perigee, showing that the displacement of the tether from the perigee will reduce the tangential velocity of the released payload, and will cause a change in the orbital elements of the released payload due to the ΔV vector not being aligned with the tangential orbital velocity vector. Therefore, the payload transfer process should be designed so that the transfer happens only at perigee.

Unless stated otherwise all the results were generated using the following parameters, largely in common with other planar studies in Ziegler and Cartmell (2001), Ziegler (2003), and Chen and Cartmell (2007) where the tether material data is based on the manufacturer's specification for Spectra 2000.

Parameters	Value	Unit
L	10 000	m
M_p	1000	kg
M_m	5000	kg
A	62.83×10^{-6}	m^2
ρ	970	$kg\ m^{-3}$
r_m	0.5	m
r_p	0.5	m
E	113	GPa
μ	3.9877848×10^{14}	$m^3 s^{-2}$
R/R_p	6 728 000	m

Table 3.1 : Parameters for tether simulations

3.5.1 Circular orbit, unmotorised.

The results in Figure 3.6 and 3.7 were obtained by numerically integrating equation (3.102) to (3.106) with no application of torque, and so the motion of the tether is based on the following initial conditions,

$$\psi(0) = -0.9 \text{ rad}, \quad \dot{\psi}(0) = 0 \text{ rad/s}, \quad u(0) = v(0) = 0 \text{ m}, \quad \dot{u}(0) = \dot{v}(0) = 0 \text{ m/s} \quad (3.107)$$

and T_o is set to zero.

The angular velocity of the tether centre of mass on orbit is given by,

$$\dot{\theta} = \sqrt{\frac{\mu}{R^3}} \quad (3.108)$$

The responses of the unmotorised tether in Figure 3.6 (a) and (b) show the steady state oscillations for both models which equate to libration of the tether in the circular orbit.

A phase shift is noticeable in which the rigid body tether lags the flexible tether. The differences in the responses can clearly be seen after the first five orbits. These differences increase within the integration time and are shown in Figure 3.6 (c) and (d). Figure 3.7 shows the longitudinal and transverse vibration of the flexible tether. The longitudinal displacements are periodic but non-harmonic, with a maximum displacement of approximately 0.005 m. The transverse displacement also shows periodicity, but with an amplitude of approximately +/- 45 m.

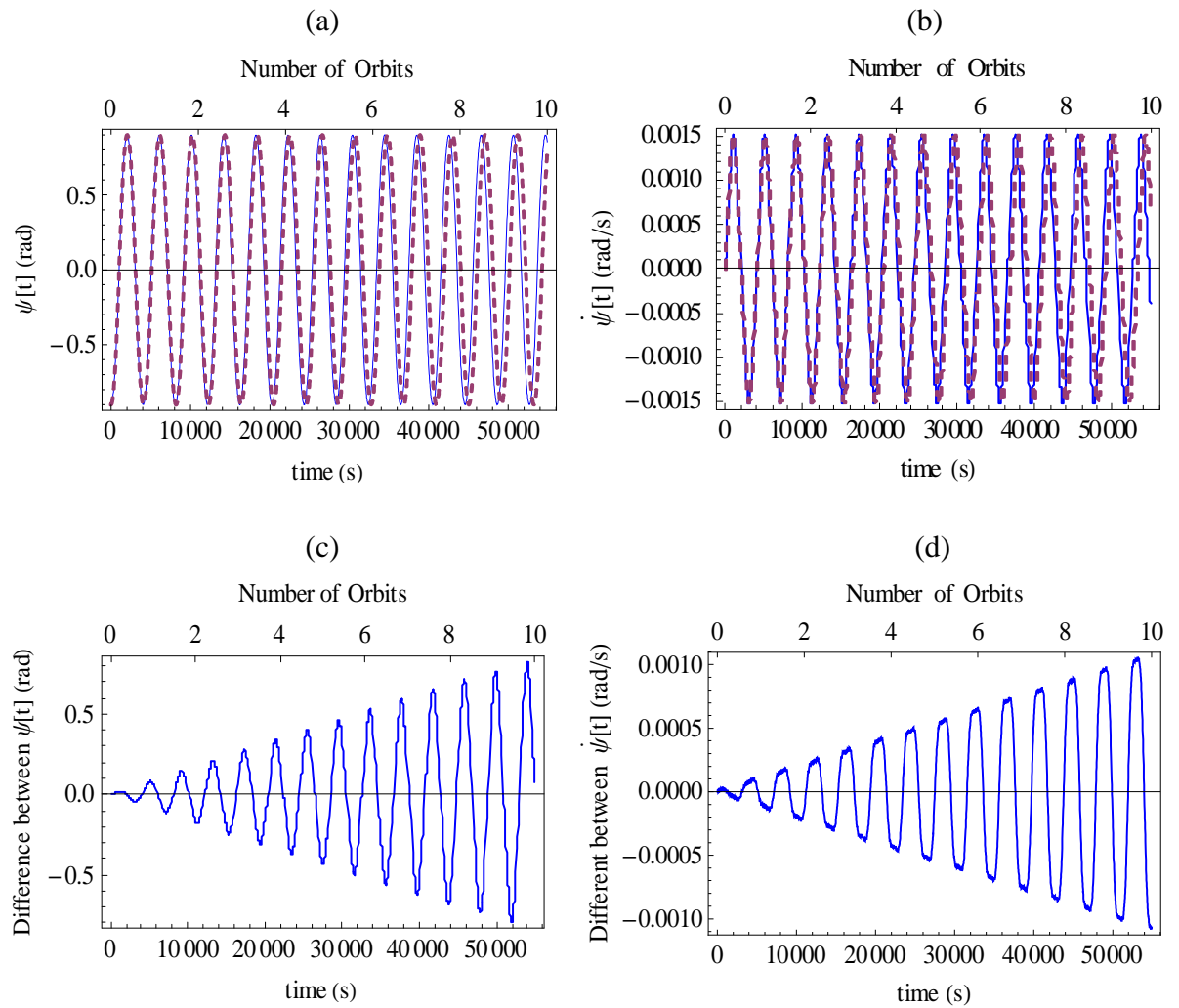


Figure 3.6 : Unmotorised tether responses for the flexible model (line) and the rigid body (dashed) on a circular orbit, and the difference between the responses of the two models over ten orbits.

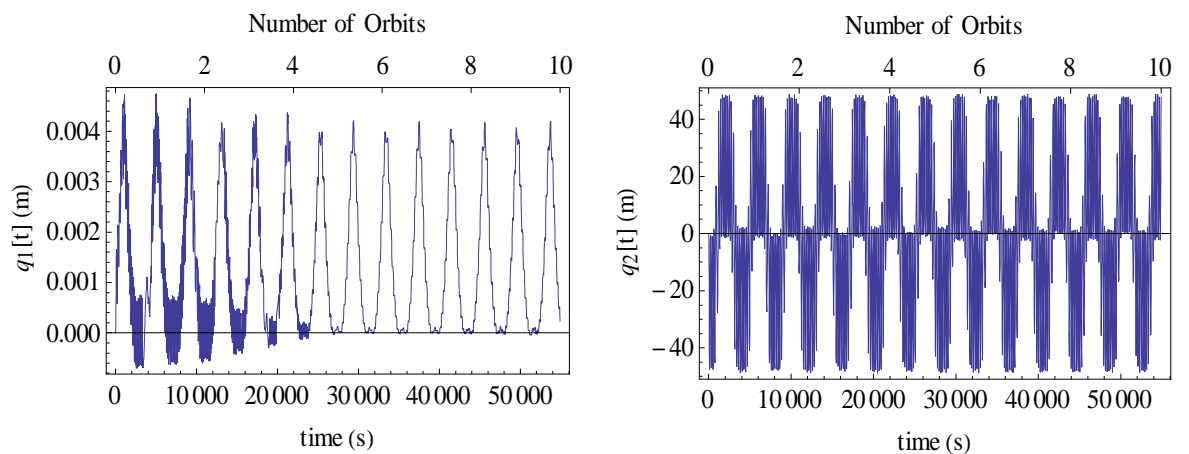


Figure 3.7 : Longitudinal and transverse vibration of the unmotorised flexible tether on a circular orbit, with time.

3.5.2 Circular Orbit, motorised.

For the condition in which the motorised tether is operating in the circular orbit, equations (3.102) (3.106) were again numerically integrated but an applied torque of 250 kNm used in equation (3.102), and the initial conditions were adopted again from equations (3.107).

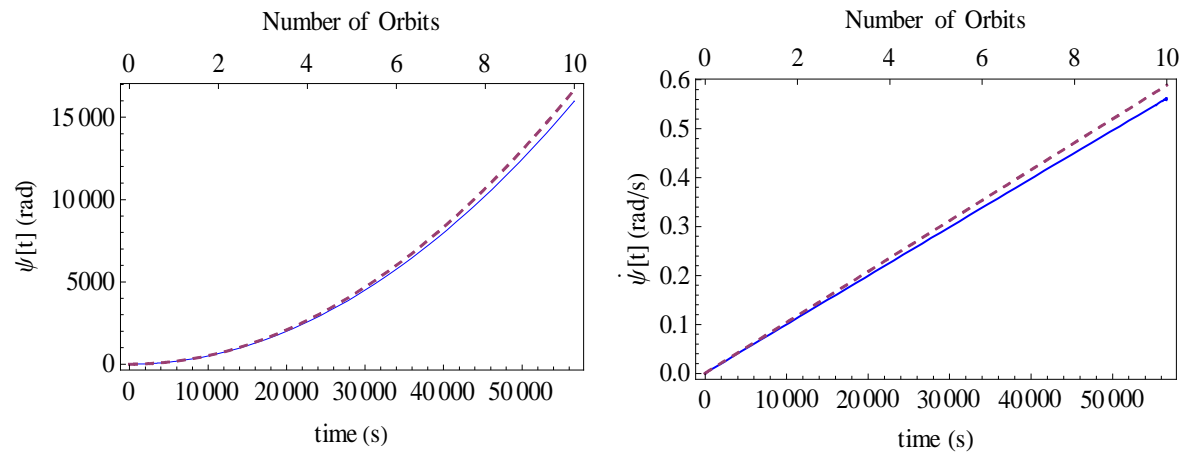


Figure 3.8 : Angular displacement and angular velocity of the motorised tether on a circular orbit, with time. (line = flexible tether, dashed = rigid body tether).

The motor torque causes both tether models to spin up, as shown in Figure 3.8. The flexible model increases its angular displacement and angular velocity at a slightly slower rate as compared to that of the rigid body model, within the integration time. However the differences are small, and only appear after two orbits. The differences between the responses of the flexible and rigid body tether models are shown in Figure 3.9 below.

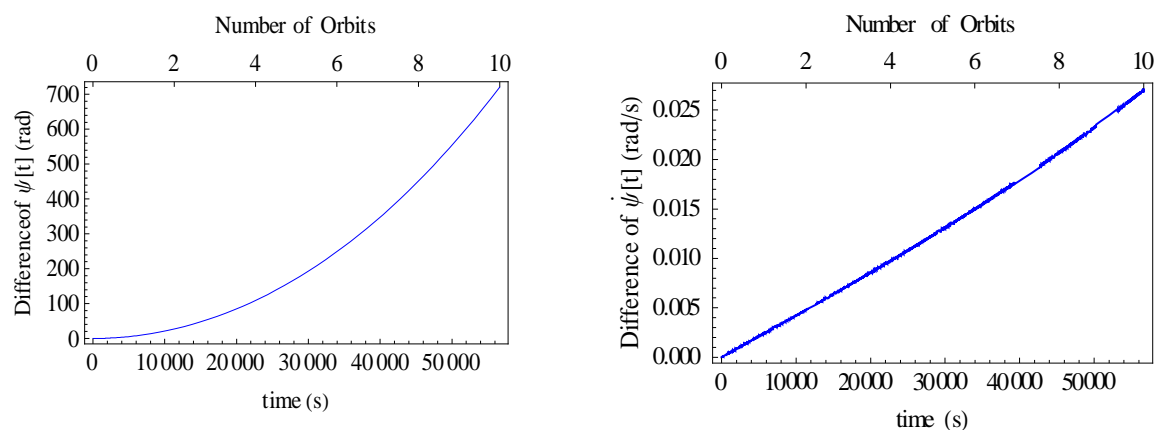


Figure 3.9 : The difference in the angular displacement and the angular velocity between the Flexible model and the Rigid body model, with time.

Unlike the unmotorised flexible tether, the application of torque and the effect of centripetal load both cause the longitudinal displacement of the tether to increase

significantly within the integration time, as shown in Figure 3.10. Conversely, the transverse vibration has shown a qualitatively different response, in which the vibration decays with time. However this is not an obviously dissipative effect and this phenomenon is connected to the stiffening effect due to the centripetal load experienced by the spinning tether. The centripetal load in the longitudinal direction increases the displacement, whilst the lateral stiffening effect reduces the amplitude of vibration in the transverse and lateral directions.

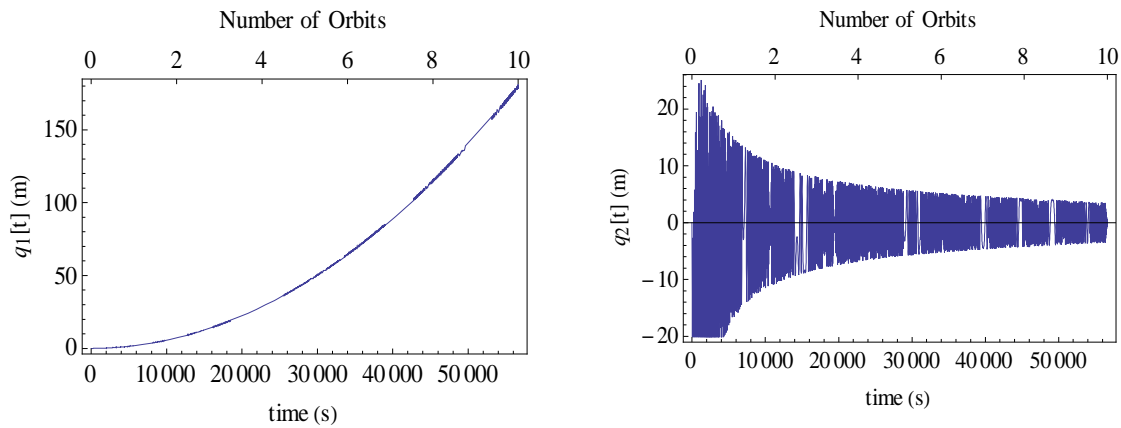


Figure 3.10 : Longitudinal and transverse vibration of the motorised flexible tether, with time

3.5.3 Elliptical orbit, unmotorised.

Equations (3.102) to (3.106) have also been numerically integrated for the tether moving on an elliptical orbit with the following parameters and initial conditions:

$$e = 0.25, \quad u(0) = v(0) = 0 \text{ m}, \quad \dot{u}(0) = \dot{v}(0) = 0 \text{ m/s}, \quad \psi(0) = 0 \text{ rad}, \quad \dot{\psi}(0) = 0.00873 \text{ rad/s}, \\ \theta = 0 \text{ rad}, \quad \dot{\theta} = 0.00146 \text{ rad/s}$$

where R_p is the perigee of the ellipse and e is the orbital eccentricity. The applied torque and T_o is set to zero.

Figure 3.11 shows the angular displacement and angular velocity of the flexible and rigid body tethers on the chosen elliptical orbit. The initial conditions initiate the response of the tethers. The angular displacements have monotonically increased, but the angular velocities of both models are periodic. The differences between the responses of the flexible and rigid body tethers are too small to be significant practically, but Figure 3.12 shows these differences. Figure 3.13 shows the position of the tether on the elliptical orbit,

and the true anomaly of the orbit within the integration time. The simulation starts at perigee and the highest peak in (a) is referring to the apogee of the elliptical orbit.

The longitudinal and transverse displacements of the flexible tether are shown in Figure 3.14. The maximum displacement in the longitudinal direction is approximately 0.11 m whilst the transverse displacement has an amplitude of approximately ± 60 m.

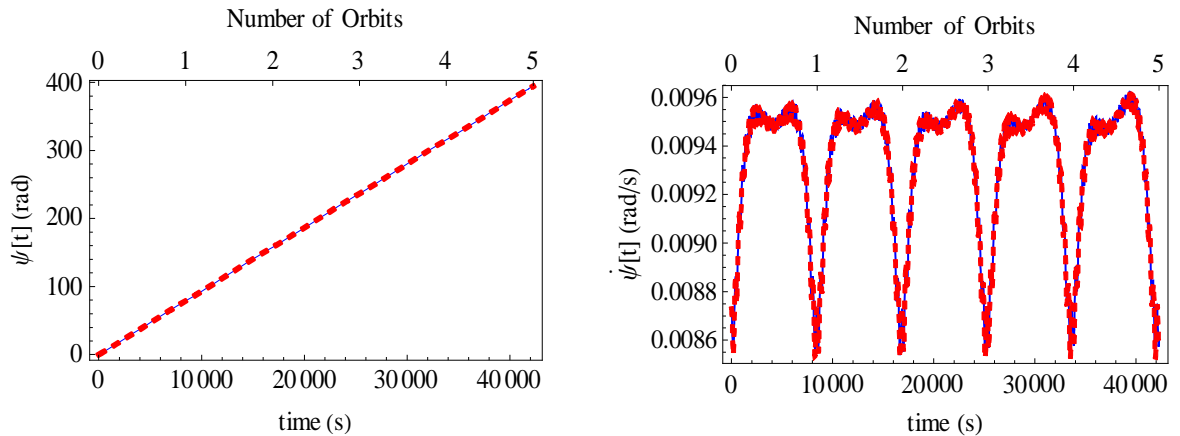


Figure 3.11 : Angular displacement and angular velocity of the unmotorised tether on the elliptical orbit, with time, at $e = 0.25$ (line = flexible tether, dashed = rigid body tether).

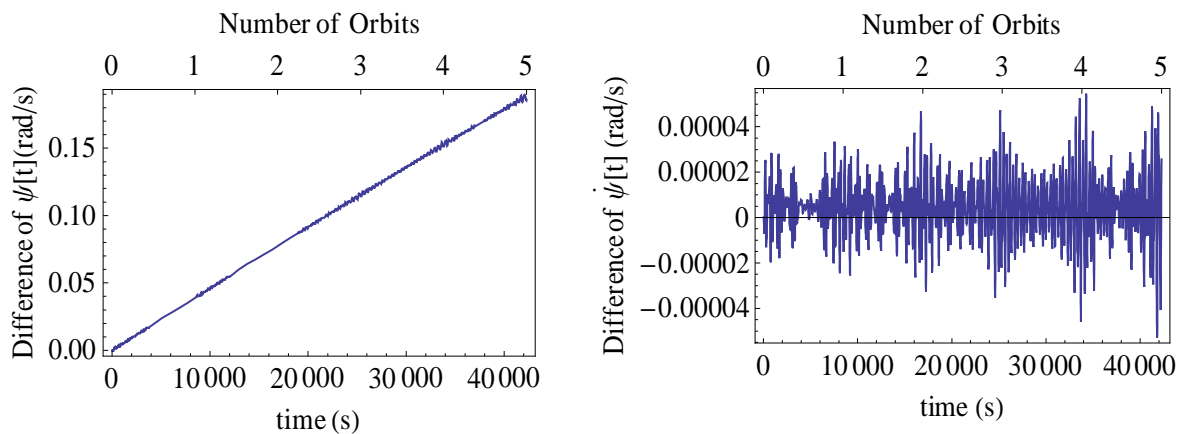


Figure 3.12 : Difference in the angular displacement and the angular velocity between the flexible model and the rigid body model, with time, at $e = 0.25$.

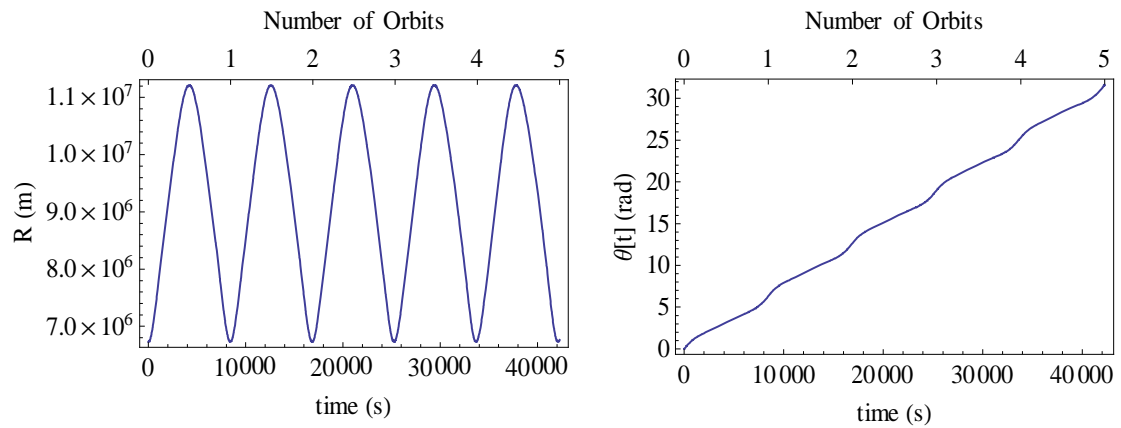


Figure 3.13 : The radius and true anomaly of the tether on the elliptical orbit, with time, at $e = 0.25$

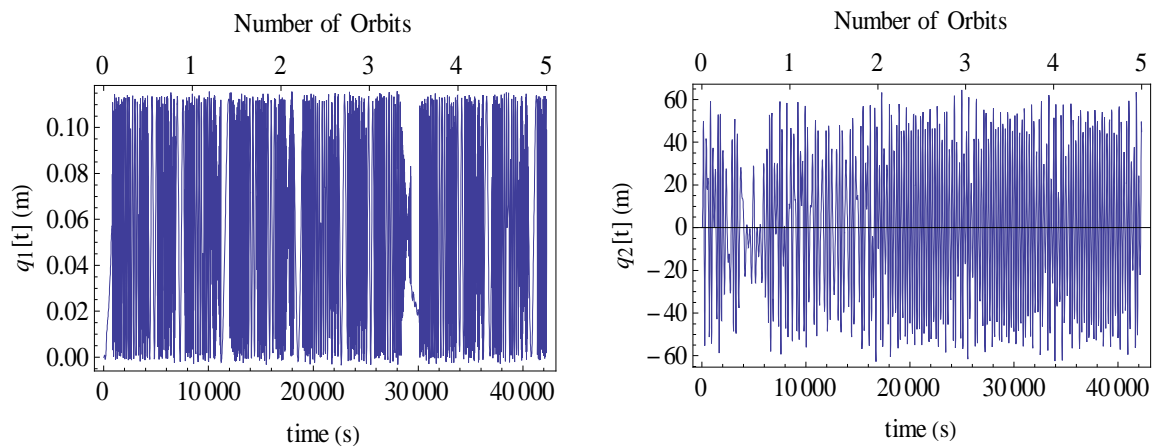


Figure 3.14 : Longitudinal and Transverse vibration of the flexible tether, with time, at $e = 0.25$

3.5.4 Elliptical orbit, motorised.

For the condition of the motorised tether on an elliptical orbit, 250 kNm of torque is applied for both the flexible and the rigid body models. The results are as shown in Figure 3.15.

Both of the tether models are in the spin-up condition, and the flexible tether shows an increase in the angular displacement and angular velocity at a slower rate as compared to that of the rigid body model within the integration time. The differences are shown in Figure 3.16.

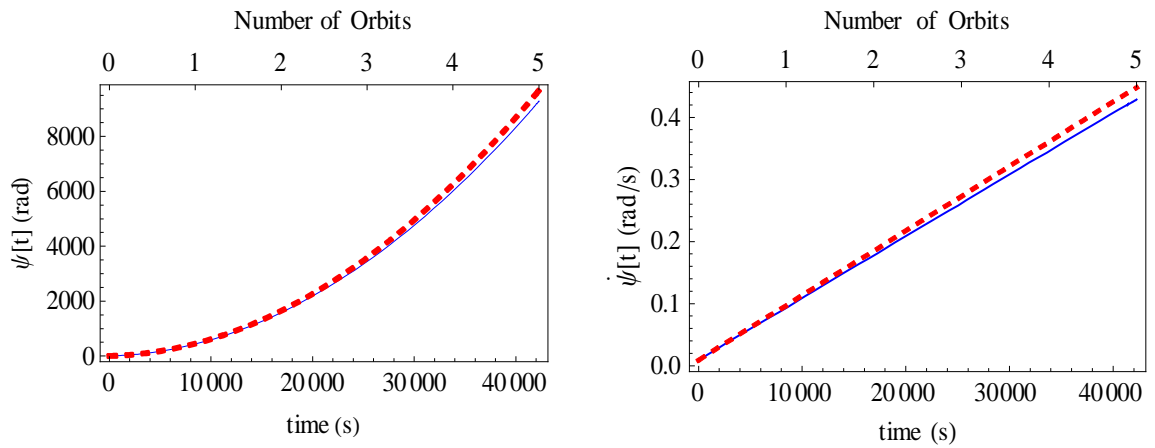


Figure 3.15 : Angular displacement and angular velocity of the motorised tether on the elliptical orbit, with time. (line = flexible tether, dashed = rigid body tether).

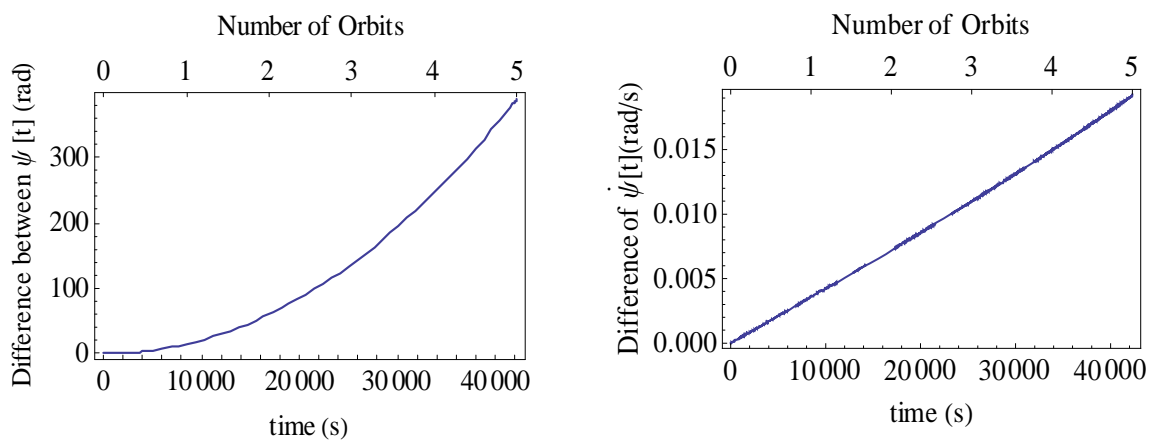


Figure 3.16 : Difference in the angular displacement and the angular velocity between the motorised flexible model and the rigid body model on elliptical orbit, with time.

The longitudinal displacement of the flexible tether in an elliptical orbit periodically increases, as shown in Figure 3.17. The displacement is at a maximum of 104.6 m when the tether has reached the 5th orbit. Figure 3.18 shows that the flexible tether is oscillating in the transverse direction with a maximum transient amplitude at -50 m. In addition, the tether demonstrates decaying oscillation in the transverse direction within the integration time.

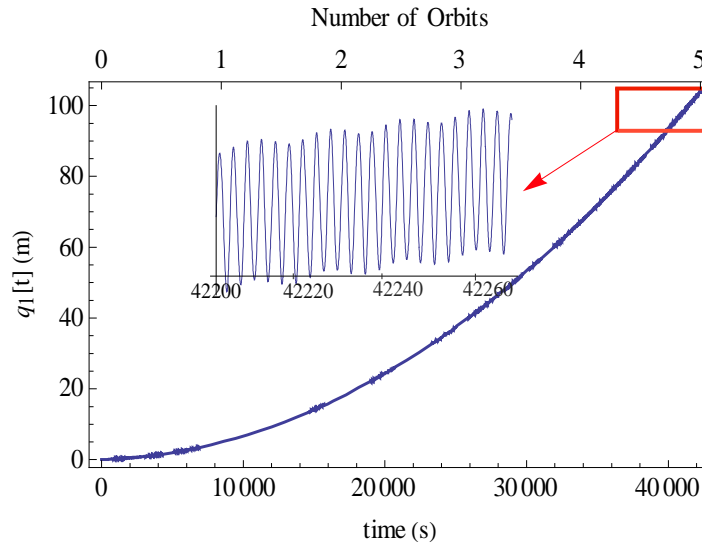


Figure 3.17: Longitudinal vibration of the motorised flexible tether on an elliptical orbit, with time.

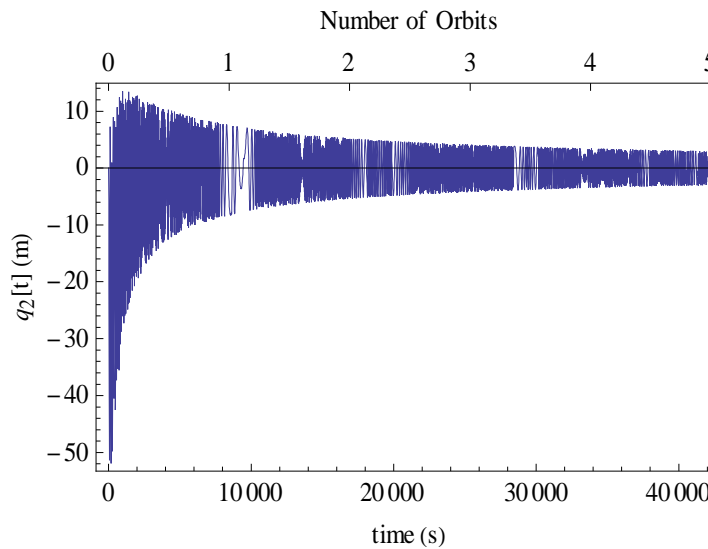


Figure 3.18 : Transverse vibration of the motorised flexible tether in an elliptical orbit, with time.

3.5.5 Energy Consideration

The effect of treating the tether as flexible and extensible is also shown in the energy expressions for the tether. The kinetic energy expression in equation (3.74) can be depicted as in Figure 3.19. The Figure shows that both rigid body and flexible models have almost the same amounts of energy when simulated in the unmotorised condition. The additional energy contributed by the elasticity in the potential energy is extremely small, and virtually insignificant against the total amount of energy of the tether. This is shown in Figure 3.20 for the untorqued condition and Figure 3.21 for the torqued condition. In one orbital period the maximum elastic energy is about 120 J in the untorqued condition and has reached 80

KJ in the torqued condition as compared to the total potential energy which is nearly 500 GJ.

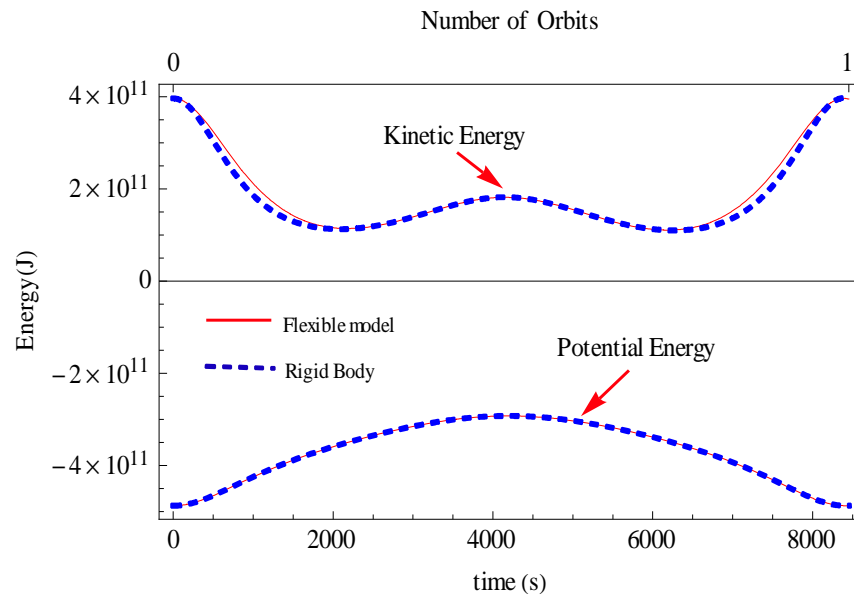


Figure 3.19 : Kinetic and Potential energy of the rigid body and flexible models

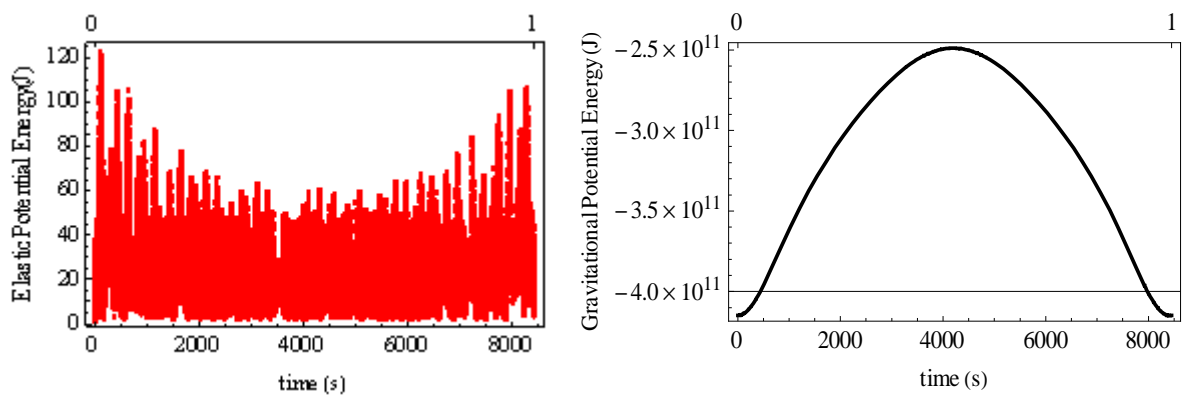


Figure 3.20 : The elastic and gravitational potential energy for an unmotorised flexible tether on an elliptical orbit with $e = 0.25$

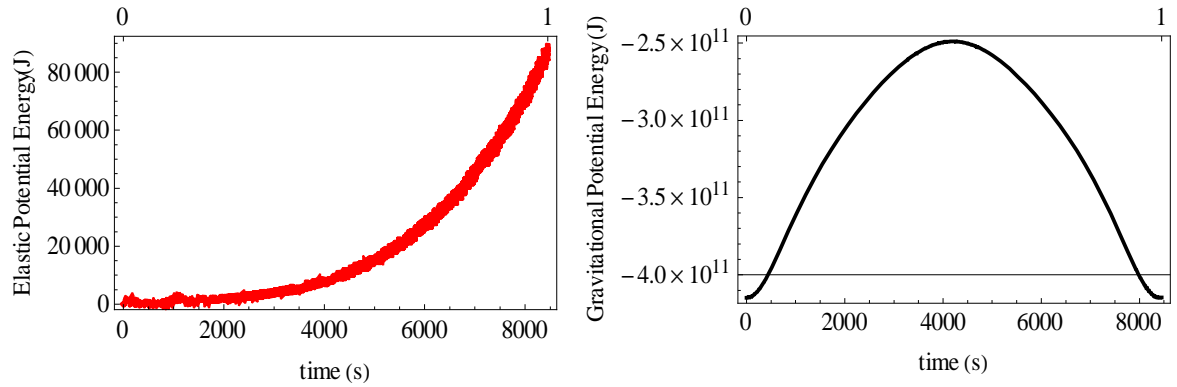


Figure 3.21 : The elastic and gravitational potential energy for an motorised flexible tether on an elliptical orbit with $e = 0.25$

3.6 Conclusions

The equations of motions have been derived for a two dimensional tether modelled as a string. The tether equations of motion are nonlinear differential equations with nonlinearities included up to cubic order, and it is clear that they show coupling terms between the longitudinal, transverse and lateral vibrations. A comparative study between the flexible model and the former rigid body models of the tether shows that the flexible tether has slower response in comparison with rigid body tether for all conditions reported in this chapter. The difference is due to the energy level in the flexible tether which is generally higher than that of the rigid body tether due to the inclusion of elastic potential energy. The existence of centripetal force in the spinning condition reduces the transverse displacement due to the stiffening effect. Therefore, the flexural effect of the tether has been seen to make a significant impact on the global motion of the tether in the long term. The study of the deformations of the flexible tether also provides a good estimation of the tether response. These deformations should necessarily be taken into account, particularly when precise motions predictions are needed.

Chapter 4

Dynamics of Three Dimensional Rigid Body and Flexible Motorised Tethers

4.1 Introduction

This chapter considers the three dimensional dynamics of the MMET for both rigid body and flexible models. The main objective is to uncover the relationships between planar and non-planar motions, and the effect of the coupling between these two parameters on the circular and elliptical orbits.

4.2 Three Dimensional Model of Rigid Body

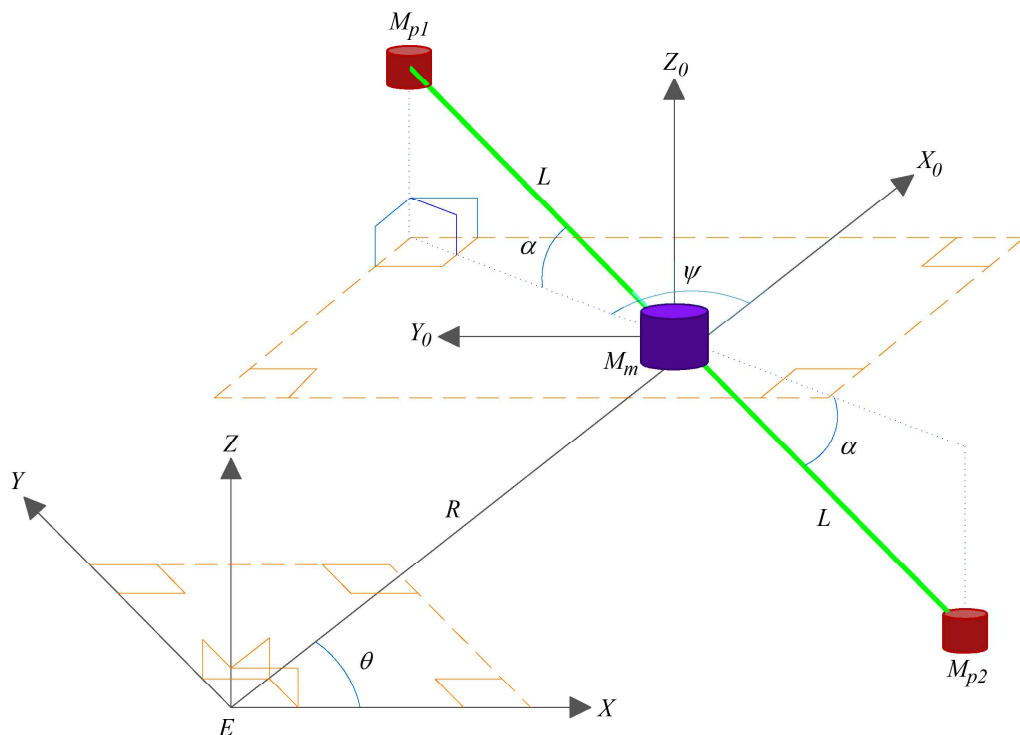


Figure 4.1 : Geometry of a Motorised Momentum Exchange Tether (Ziegler,2003).

In the previous study by Ziegler (2003) the dynamics of three dimensional rigid body motion of a massive tether were not examined due to the complexity of the equations of motions and the need for very long computation times. The simple dumbbell model has been used by Ziegler (2003) to allow the dynamics of the tether system to be efficiently explored without added complexity of the flexible tether dynamics. In this study, with

some advancement in computational technology since 2003, the derivation and simulation of this three body model is accomplishable at a somewhat lower cost and greatly accelerated time.

Figure 4.1 shows the geometry of the motorised tether discussed by Ziegler (2003). The details of the coordinate system have been discussed in the previous chapter. The planar motion of the tether as mentioned in the previous chapter is described by angles θ and ψ , whilst the non-planar motion is defined by angle α .

4.2.1 Position Vectors

The Cartesian components of the central facility and the payloads in the inertial reference frame X, Y , are shown in the previous chapter in the form of equations (3.12) to (3.17). For the three dimensional case based on the inertial frame X, Y, Z the components in the Z direction are given below,

$$z_{p1} = L \sin \alpha \quad (4.1)$$

$$z_{p2} = -L \sin \alpha \quad (4.2)$$

$$z_{mm} = 0 \quad (4.3)$$

From Figure 4.1 taking the centre of mass for the tether at $L/2$ leads to the following tether coordinates,

$$x_{t1} = R \cos \theta + \frac{L}{2} \cos \alpha \cos(\psi + \theta) \quad (4.4)$$

$$x_{t2} = R \cos \theta - \frac{L}{2} \cos \alpha \cos(\psi + \theta) \quad (4.5)$$

$$y_{t1} = R \cos \theta + \frac{L}{2} \cos \alpha \cos(\psi + \theta) \quad (4.6)$$

$$y_{t2} = R \cos \theta - \frac{L}{2} \cos \alpha \cos(\psi + \theta) \quad (4.7)$$

$$z_{t1} = \frac{L}{2} \sin \alpha \quad (4.8)$$

$$z_{t2} = -\frac{L}{2} \sin \alpha \quad (4.9)$$

The components of force in the x, y and z directions are,

$$F_x = -F \cos \gamma \sin \psi - F \sin \gamma \sin \alpha \cos \psi \quad (4.16)$$

$$F_y = F \cos \gamma \cos \psi - F \sin \gamma \sin \alpha \cos \psi \quad (4.17)$$

$$F_z = F \sin \gamma \cos \alpha \quad (4.18)$$

and so partially differentiating the Cartesian component of the end mass with respect to α and ψ , and substituting from equation (4.16), (4.17) and (4.18) into (4.13) and (4.14) gives the generalised forces as (Ziegler, 2003),

$$Q_\psi = \tau \cos \gamma \cos \alpha \quad (4.19)$$

$$Q_\alpha = \tau \sin \gamma \quad (4.20)$$

4.3 Kinetic Energy of the Rigid Body Model

The Kinetic energy for translational motion of the three dimensional system is given as,

$$\begin{aligned} T_{trans} = & \frac{1}{2} M_{P1} (\dot{x}_{M_{P1}}^2 + \dot{y}_{M_{P1}}^2 + \dot{z}_{M_{P1}}^2) + \frac{1}{2} M_{P2} (\dot{x}_{M_{P2}}^2 + \dot{y}_{M_{P2}}^2 + \dot{z}_{M_{P2}}^2) \\ & + \frac{1}{2} M_m (\dot{x}_{M_m}^2 + \dot{y}_{M_m}^2 + \dot{z}_{M_m}^2) + \frac{1}{2} \rho AL (\dot{x}_{t1}^2 + \dot{y}_{t1}^2 + \dot{z}_{t1}^2) + \frac{1}{2} \rho AL (\dot{x}_{t2}^2 + \dot{y}_{t2}^2 + \dot{z}_{t2}^2) \end{aligned} \quad (4.21)$$

and the rotational kinetic energy is given in the previous chapter by equation (3.43).

Substitution of equations (3.44) to (3.49) into equation (3.43) gives the rotational kinetic energy for the system as,

$$\begin{aligned} T_{rot} = & \frac{1}{2} (I_{X_{Mp1}} + I_{X_{Mp2}} + I_{X_{Mm}} + I_{X_{t1}} + I_{X_{t2}}) (\dot{\gamma}^2) + \frac{1}{2} (I_{Y_{Mp1}} + I_{Y_{Mp2}} + \\ & I_{Y_{Mm}} + I_{Y_{t1}} + I_{Y_{t2}}) (\dot{\alpha}^2) + \frac{1}{2} (I_{Z_{Mp1}} + I_{Z_{Mp2}} + I_{Z_{Mm}} + I_{Z_{t1}} + I_{Z_{t2}}) (\dot{\psi} + \dot{\theta})^2 \end{aligned} \quad (4.22)$$

Adding together equations (4.22) and (4.21) gives the total kinetic energy of the system for which the kinetic energy expression details can be found in Appendix A (i).

4.4 Potential Energy of the Rigid Body Model

In deriving the potential energy for the rigid body model of the tether only the gravitational potential energy is considered, as mentioned in the previous chapter. The equation is obtained by adding equation (3.59), (3.60), (3.61), (3.64) and (3.65) and generates the total potential energy as,

$$\begin{aligned}
 U_P = & -\frac{\mu M_{P1}}{\sqrt{R^2 + L^2 + 2LR \cos \alpha \cos \varphi}} - \frac{\mu M_{P2}}{\sqrt{R^2 + L^2 - 2LR \cos \alpha \cos \varphi}} - \frac{\mu M_m}{R} \\
 & - \sum_{i=1}^N \frac{\mu \rho ARL}{N \sqrt{R^2 + \left[\frac{(2i-1)L}{2N} \right]^2 + \frac{(2i-1)RL}{2N} \cos \alpha \cos \psi}} \\
 & - \sum_{i=1}^N \frac{\mu \rho ARL}{N \sqrt{R^2 + \left[\frac{(2i-1)L}{2N} \right]^2 - \frac{(2i-1)RL}{2N} \cos \alpha \cos \psi}} \tag{4.23}
 \end{aligned}$$

In the case of the symmetrical MMET, $M_{P1} = M_{P2}$. Therefore, the mass payload will be denoted as M_p from here on. The potential energy equation is shown in full in Appendix A (ii).

4.5 Equations of Motion for the Rigid Body Model

The equations of motions are derived using Lagrange's equation. The generalized coordinates are given by $\{q_k\} = \{\psi, \theta, \alpha, R, \gamma\}$ and the generalized forces from equations (4.19) and (4.20) for the system are,

$$\begin{pmatrix} Q_\psi \\ Q_\alpha \\ Q_\theta \\ Q_R \\ Q_\gamma \end{pmatrix} = \begin{pmatrix} \tau \cos \gamma \cos \alpha \\ \tau \sin \gamma \\ 0 \\ 0 \\ 0 \end{pmatrix} \tag{4.24}$$

The equations of motions for the rigid body model are stated in full in Appendix A (iii).

4.6 Simulation of the Rigid Body Model

Unless stated otherwise all the results were generated with the default parameters for the MMET which can be found in Ziegler and Cartmell (2001), Ziegler (2003), and Chen and Cartmell (2007).

4.6.1 Circular orbit

Simulations are carried out with initial conditions, $\psi(0) = -0.9$ rad, $\dot{\psi}(0) = 0$ rad/s, $\alpha(0) = -0.01$ rad, and $\alpha'(0) = 0$ rad/s for a tether on a circular orbit. The planar and non-planar motions have been compared between the massless tether and the rigid body tether in Figure 4.3. The motions result from placing the tether on a circular orbit and without applying any torque to the tether.

The massless tether model has been simulated for two different conditions, first with the equations of motion based on the study by Ziegler (2003) where only the translation motion of the tether's components is considered when deriving the kinetic energy and this approach named here as the massless tether 1. The second condition refers to equations of motion of the rigid model tether which included rotational motion of the payload and the central facility in deriving the kinetic energy as in equation (4.21) and is named the massless tether 2. Table 4.1 shows the difference between the models used for this tether's simulation.

Conditions	Massless 1	Massless 2	Rigid Body
Tether mass	No	No	Yes
Translational kinetic energy	Yes	Yes	Yes
Rotational kinetic energy	No	Yes	Yes

Table 4.1 : The difference of the conditions between massless tether 1, massless tether 2 and rigid body model.

Figure 4.3 shows that the in-plane responses of all models are very similar but a significant difference is shown in the non-planar motion, defined by including angle α . The planar steady state motion is indistinguishable between the three models by simulating over a smaller range of time, as in Figure 4.4, in which the difference between the massless tether 1 and the rigid body model, and the massless tether 2 is less than 0.000001 rad.

From Figure 4.3(d), it is clearly shown that the inclusion of rotational kinetic energy has increased the frequency of non-planar motion. The massless tether without rotational motion has the lowest natural frequency, but achieves a higher amplitude as compared with the other two models. For these two models, for which rotational motion has been considered, the rigid body model has a lower frequency of non-planar motion as compared with the massless tether.

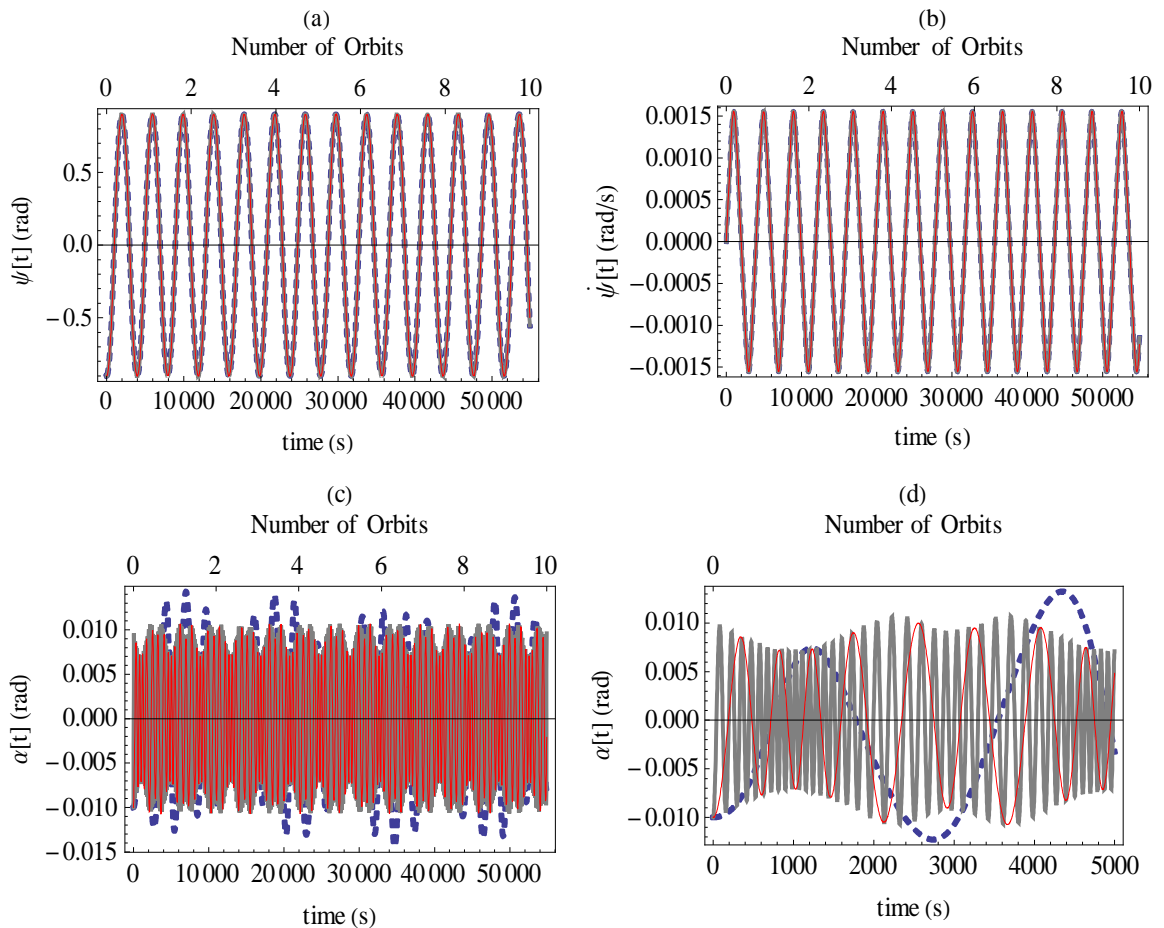


Figure 4.3 : Planar and non-planar motions of Massless tether 1 (dashed), Massless tether 2 (gray) and Rigid Body tether (red) on a circular orbit with zero torque.

For the motorised tether an application of 2.5 MNm of torque to both models results in the responses of Figure 4.5. The rigid body tether in Figure 4.5 (a) and Figure 4.5 (b) shows an increase in the angular displacement and angular velocity at a slower rate as compared to that of the massless tether within the same integration time. Both types of massless tethers have shown an identical response for planar motion. Nevertheless, all models demonstrate decaying oscillations for non-planar motion. The massless tether 1 model decays the fastest, followed by the rigid body tether, and subsequently the massless tether 2 model.

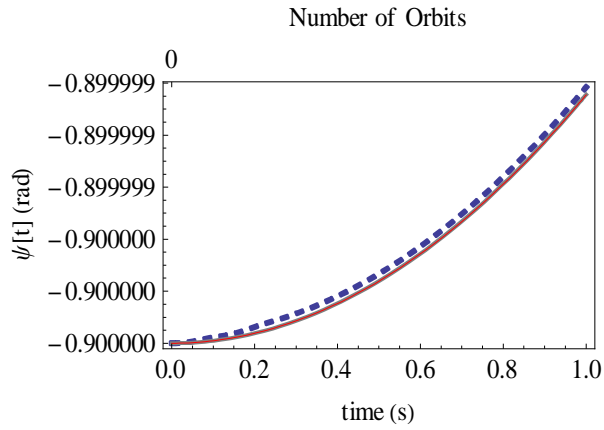


Figure 4.4 : Angular displacement of Massless tether 1 (dashed), Massless tether 2 (gray) and Rigid body tether (red) on a circular orbit with zero torque over a smaller range of simulation time.

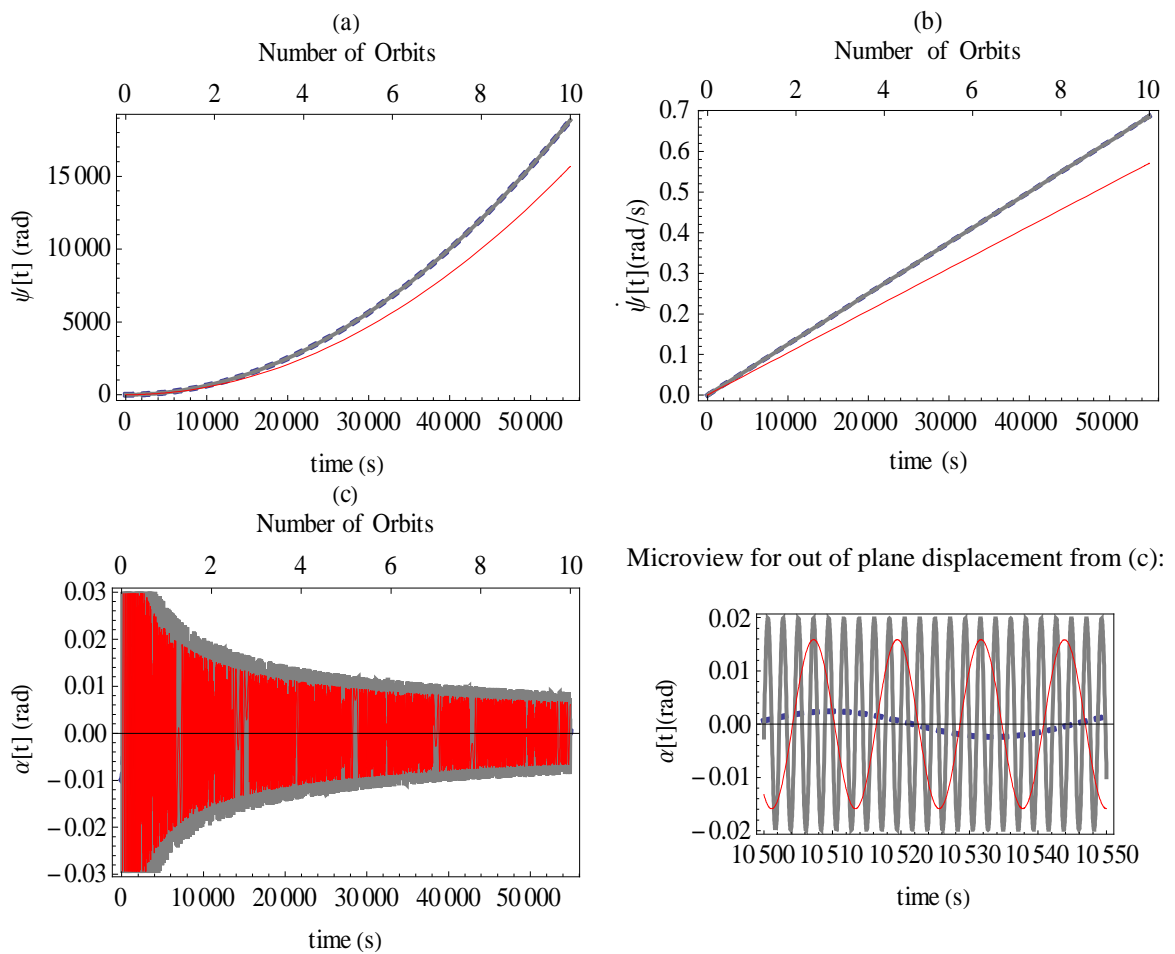


Figure 4.5 : Planar and non-planar motions of Massless tether 1 (dashed), Massless tether 2 (gray) and Rigid Body tether (red) on a circular orbit with 2.5 MNm torque.

4.6.2 Elliptical orbit

Simulation was carried out for the tether on an elliptical orbit with its perigee at 6278 km and an orbital eccentricity of 0.25. The chosen initial conditions were:

$$\psi(0) = 0 \text{ rad}, \quad \dot{\psi}(0) = 0.0873 \text{ rad/s}, \quad \alpha(0) = -0.01 \text{ rad}, \quad \dot{\alpha}(0) = 0 \text{ rad/s}, \quad \theta(0) = 0 \text{ rad} \quad \text{and} \\ \dot{\theta}(0) = 0.00146 \text{ rad/s}$$

The simulation was carried out for torqued conditions with an applied torque of 2.5 MNm. Simulation results are shown in Figure 4.6.

On the elliptical orbit, Figures 4.6(a) and (b) show planar motion for the torqued conditions where the rigid body tether has a slower response as compared with the massless tether. There is no change in the orbital elements with simulations of different models for which the results depicted in Figures 4.6(e) and (f) refer to the radius and true anomaly of the selected orbit. In Figure 4.6 (e1) and (f1) both orbital parameters have shown small differences between these three condition in smaller range of simulation time. The rigid body tether obviously show that the radius of the orbit is different with other two models. This suggested that with increasing of the mass, it could alter the orbital parameters of tether. Similar to tether motion on a circular orbit, the non-planar motion for a tether on an elliptical orbit also shows a decaying response with frequency with the massless tether 2 model being the highest, followed by the rigid body tether, and finally the massless tether 1 model.

For both the circular and elliptical orbits in the applied torque case the rigid body model shows a slower response as compared with other model for planar motion. In comparison to the non-planar responses, it is shown that $f_{m1} < f_{RB} < f_{m2}$ where f_{m1} is the frequency of the massless tether 1, and f_{RB} is the frequency of the rigid body tether, and f_{m2} refers to the massless tether 2.

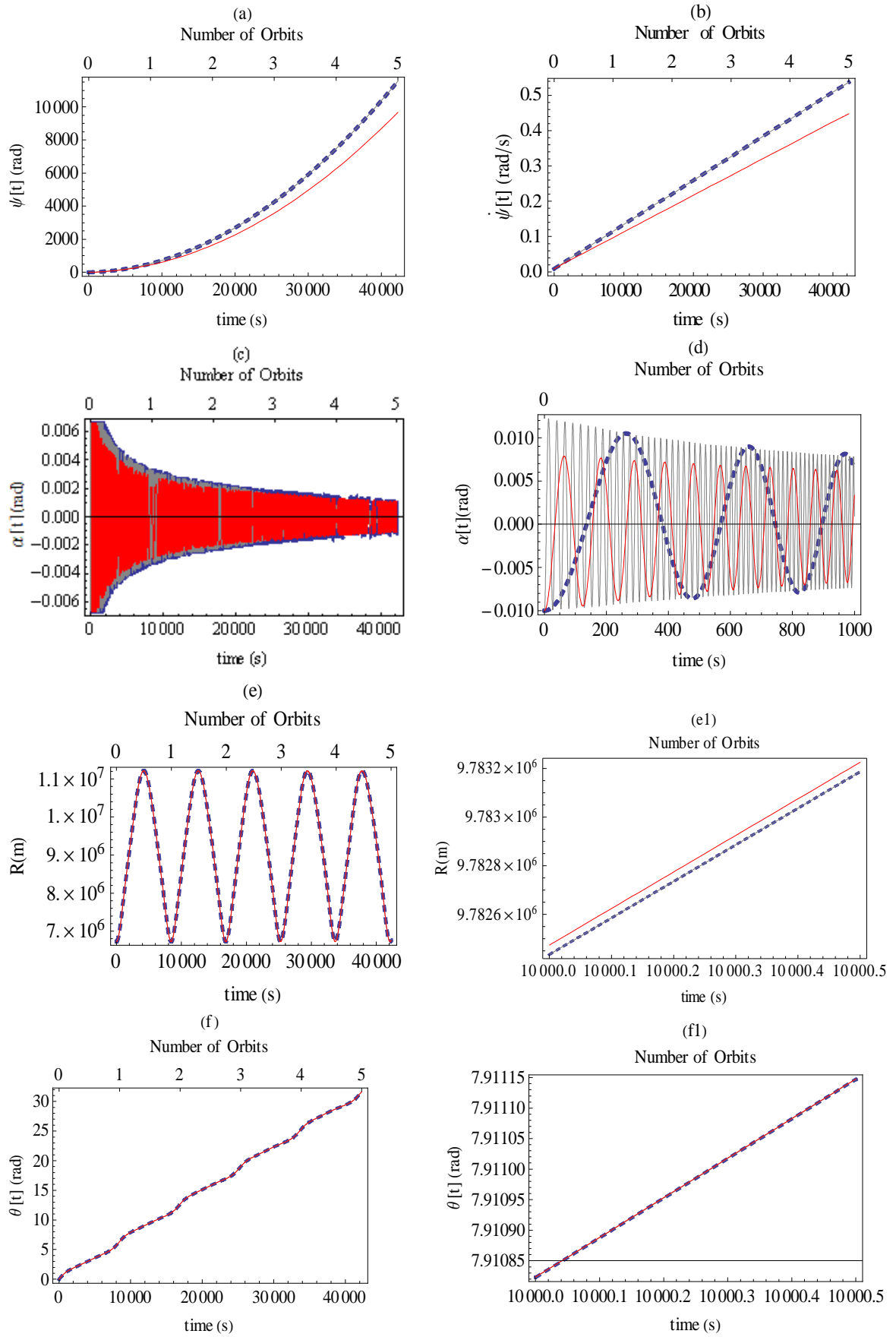


Figure 4.6 : Planar and non-planar motions of Massless tether 1 (dashed), Massless tether 2 (gray) and Rigid Body tether (red) on an elliptical orbit with 2.5 MNm torque.

4.6.3 Comparison between the 2D and 3D Rigid Body Models.

In order to validate the flexible 3D model it has been compared with the 2D model, simulation results are shown in Figure 4.7 and 4.8. Figure 4.7 (a) and (b) show that the in-plane motions are visually indistinguishable for five orbits. Therefore, the difference of the responses between these two models are shown in Figure 4.6 (a1) and (b1) with very small differences shown between both models, whilst the difference increases with simulation time.

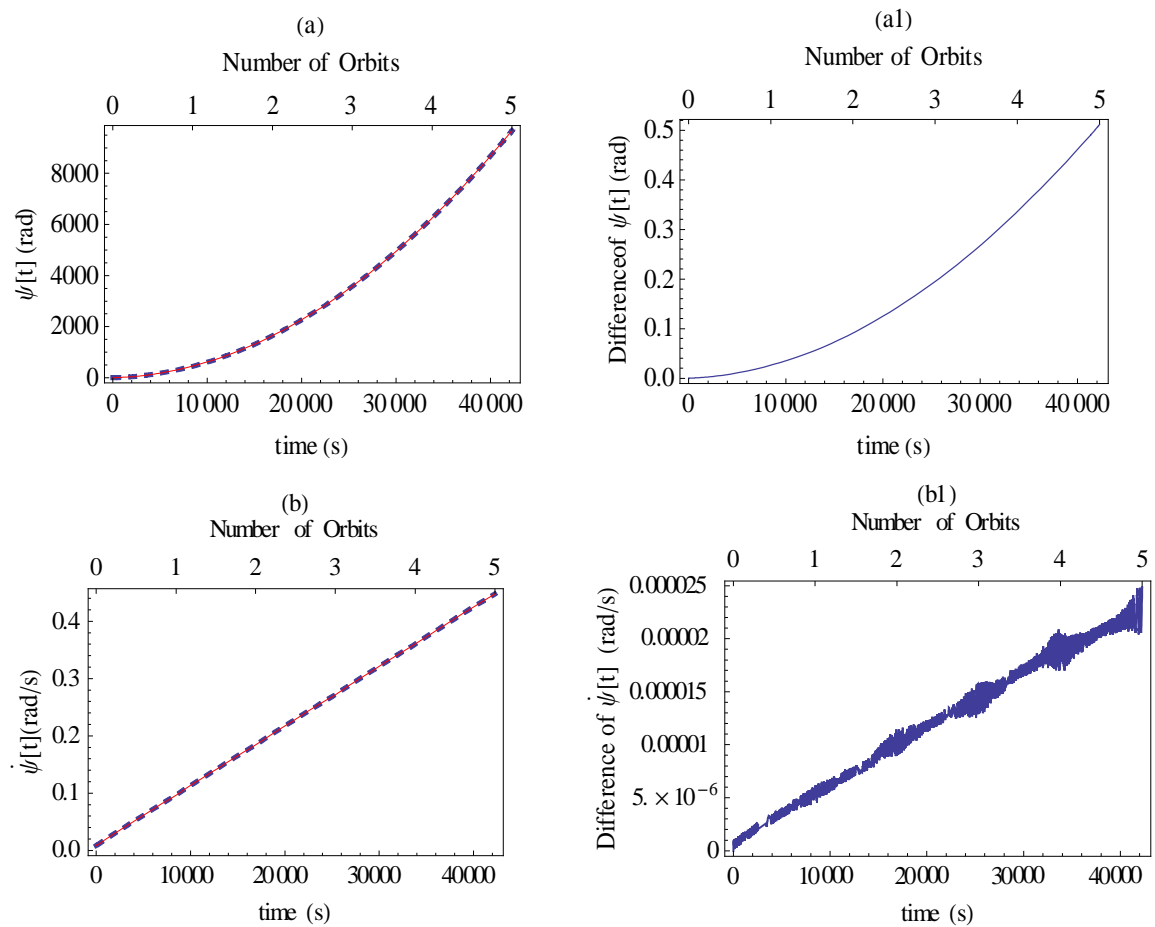


Figure 4.7 : (a) & (b) - Comparison of response between 2D (line) and 3D (dashed) model in rigid body model. (a1) & (b1) - Difference between 2D and 3D models of rigid body MMET.

Figure 4.8 (c1) and (d1) shows the difference in the orbital parameters between the two models and suggests that the presence of the non-planar variable (α) in the equations of motion of the 3D model, for planar motion, has significant influence on the planar motion of the tether. The change in the orbital radius and the true anomaly may affect the payload transfer process whereby the wrong prediction of payload position may occur. This could fail the payload transfer process, or would fail to release the payload to its desired orbit.

Therefore, an additional system to correct the position would be required, which would increase the mass and the cost of the payload.

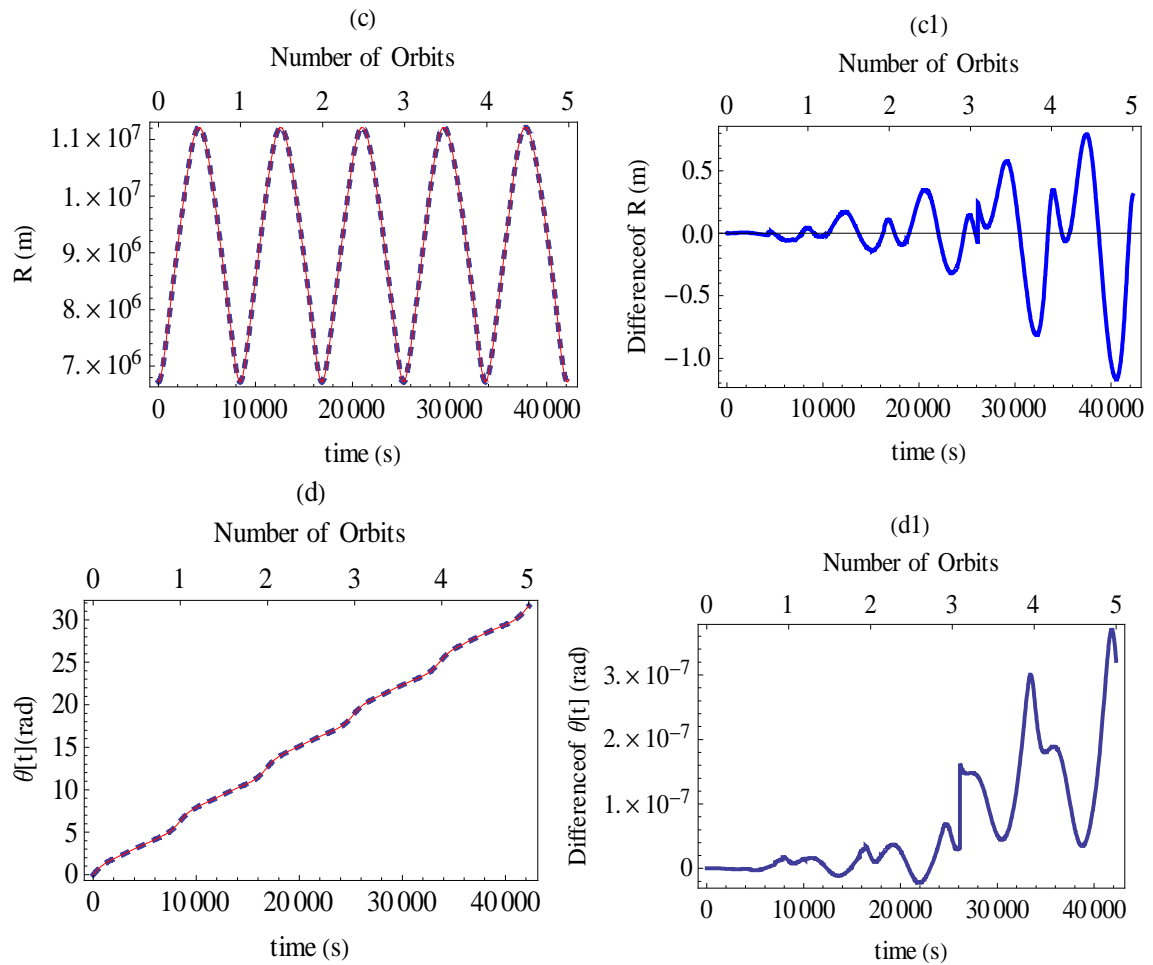


Figure 4.8 : Comparison of orbital parameters between 2D (line) and 3D (dashed) models of a rigid body MMET

4.7 Dynamics of a Three Dimensional Flexible MMET

4.7.1 Initial positions

Figure 4.9 shows the motions of a three dimensional flexible model of an MMET on orbit. The components of flexibility of the MMET have been described by the displacements of tether length in the axial and transverse directions, as explained in the previous chapter and given by u and v . In this three dimensional case, the additional of the displacement in the lateral direction is presented, and this is denoted by w . The local position of a point mass P , is transformed to inertial coordinates by rotating and translating the position vector.

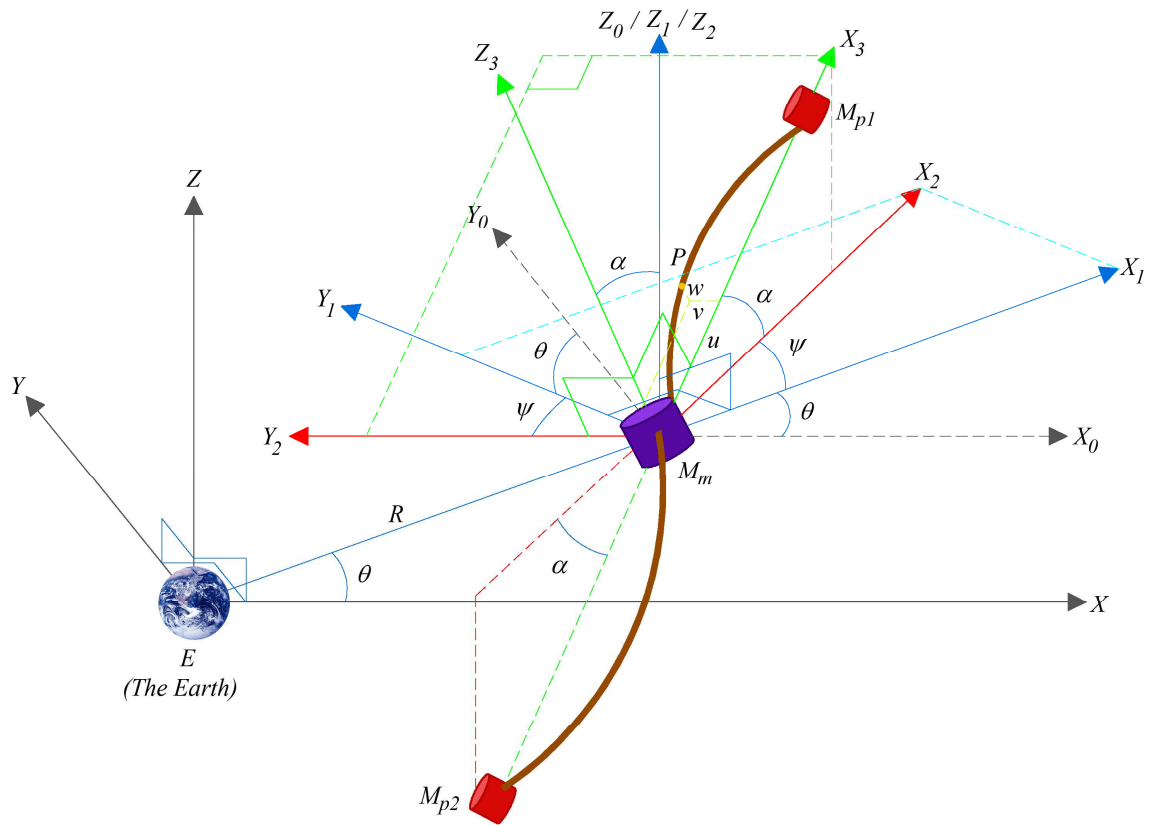


Figure 4.9 : Three dimensional flexible model of an MMET on orbit

4.8 Coordinate transformation

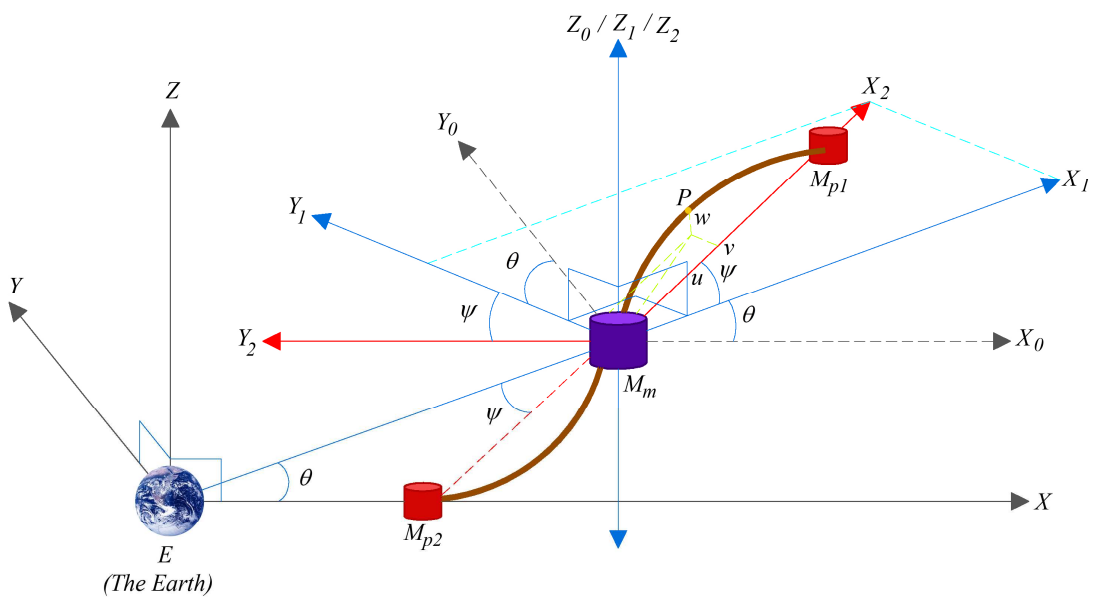


Figure 4.10 : Translation of the central facility within an inertial coordinate system.

The rotation matrix is given by,

$$R_{Y,\alpha} = \begin{pmatrix} \cos(\alpha) & 0 & -\sin(\alpha) \\ 0 & 1 & 0 \\ \sin(\alpha) & 0 & \cos(\alpha) \end{pmatrix} \quad (4.26)$$

Therefore the complete rotation matrix from local coordinates to the inertial coordinates is defined as,

$$R_{ZY} = R_{Z,\psi+\theta} \cdot R_{Y,\alpha} = \begin{pmatrix} \cos \alpha \cos(\theta + \psi) & -\sin(\theta + \psi) & -\sin \alpha \cos(\theta + \psi) \\ \cos \alpha \sin(\theta + \psi) & \cos(\theta + \psi) & -\sin \alpha \sin(\theta + \psi) \\ \sin \alpha & 0 & \cos \alpha \end{pmatrix} \quad (4.27)$$

4.8.1 New Coordinate Positions

The initial coordinates of the payloads with respect to the local origin are given by equations (3.12) to (3.17) in Chapter 3 and equations (4.1) to (4.3) in section 4.2.1. Applying equation (4.27) for the position of the arbitrary point P along the tether gives the new position coordinates in terms of the x,y,z components, for non-planar motion,

$$x_{mt1} = R \cos \theta + (u + x) \cos \alpha \cos(\theta + \psi) - v \sin(\theta + \psi) - w \sin \alpha \cos(\theta + \psi) \quad (4.28)$$

$$x_{mt2} = R \cos \theta + (u + x) \cos \alpha \cos(\theta + \psi) + v \sin(\theta + \psi) + w \sin \alpha \cos(\theta + \psi) \quad (4.29)$$

$$y_{mt1} = R \sin \theta + (u + x) \cos \alpha \sin(\theta + \psi) + v \cos(\theta + \psi) - w \sin \alpha \sin(\theta + \psi) \quad (4.30)$$

$$y_{mt2} = R \sin \theta + (u + x) \cos \alpha \sin(\theta + \psi) - v \cos(\theta + \psi) + w \sin \alpha \sin(\theta + \psi) \quad (4.31)$$

$$z_{mt1} = w \cos \alpha (u + x) \sin \alpha \quad (4.32)$$

$$z_{mt2} = -w \cos \alpha (u + x) \sin \alpha \quad (4.33)$$

4.9 Energy Expression

The kinetic energy of the payloads and central facility are the same as in equations (4.21) and (4.22), and the translational kinetic energy for the tether sub-span are obtained by substituting equations (4.28) to (4.33) into equation (4.36) as follows and integrating along the sub-span length,

$$\begin{aligned}
T_{trans} = & \frac{1}{2}M_{P1}(\dot{x}_{P1}^2 + \dot{y}_{P1}^2 + \dot{z}_{P1}^2) + \frac{1}{2}M_{P2}(\dot{x}_{P2}^2 + \dot{y}_{P2}^2 + \dot{z}_{P2}^2) + \frac{1}{2}M_m(\dot{x}_{mm}^2 + \dot{y}_{mm}^2 + \dot{z}_{mm}^2) \\
& + \int_0^L \frac{1}{2}\rho A(\dot{x}_{mt1}^2 + \dot{y}_{mt1}^2 + \dot{z}_{mt1}^2)dx + \int_0^L \frac{1}{2}\rho A(\dot{x}_{mt2}^2 + \dot{y}_{mt2}^2 + \dot{z}_{mt2}^2)dx
\end{aligned} \quad (4.36)$$

The total kinetic energy for this flexible model of tether is given by the summation of equation (4.36) and equation (4.22) and is presented in full in Appendix B (i).

In the previous study of the 2D model, the contribution of the elastic potential energy due to the flexibility of the tether leads to the total potential energy for the system,

$$\begin{aligned}
U_G = & -\frac{\mu M_1}{\sqrt{R^2 + L^2 + 2LR \cos \alpha \cos \varphi}} - \frac{\mu M_2}{\sqrt{R^2 + L^2 - 2LR \cos \alpha \cos \varphi}} - \frac{\mu M_m}{R} \\
& - \sum_{i=1}^N \frac{\mu \rho A R L}{N \sqrt{R^2 + \left[\frac{(2i-1)L}{2N} \right]^2} + \frac{(2i-1)RL}{2N} \cos \alpha \cos \psi} \\
& - \sum_{i=1}^N \frac{\mu \rho A R L}{N \sqrt{R^2 + \left[\frac{(2i-1)L}{2N} \right]^2} - \frac{(2i-1)RL}{2N} \cos \alpha \cos \psi} \\
& + \int_0^l \left[\frac{1}{2} \frac{T_o^2}{EA} + T_o \left(u' + \frac{1}{2}(v'^2 + w'^2) - \frac{1}{2}u'(v'^2 + w'^2) + \frac{1}{2}u'^2(v'^2 + w'^2) - \frac{1}{8}(v'^2 + w'^2)^2 \right. \right. \\
& \left. \left. + \frac{5}{8}u'^4 \right) + \frac{1}{2}EA \left(u'^2 + u'(v'^2 + w'^2) - u'^2(v'^2 + w'^2) + \frac{1}{4}(v'^2 + w'^2)^2 \right) \right] dx
\end{aligned} \quad (4.37)$$

where T_o is the centripetal force as defined in the 2D model, previously. The complete equation for the potential energy is shown in full in Appendix B (ii).

4.10 Mode Shape Function for the Static Boundary Condition

The displacements in the axial and transverse direction have been written as separated variable functions in the previous chapter in equations (3.40). Therefore, in the three dimensional case the additional lateral displacement is written as,

$$w(x, t) = \sum_{i=1}^n \beta(x) q_3(t) \quad (4.38)$$

where $\beta(x)$ are the chosen mode shape functions. The derivation conditions for these mode shapes have been discussed in previous studies of the flexible 2D tether model. The mode shape functions have been derived from the assumption that the tether has fixed-end boundary conditions, and is given by,

$$\phi(x) = \xi(x) = \beta(x) = \sin \frac{\pi x}{L} \quad (4.39)$$

It has been noted that these mode shape functions were also used by Luo *et al.* (1996) in the transverse and lateral directions for their nonlinear mechanical model of a spinning tether in three dimensional space.

4.11 Derivation of the Equations of Motion (EOM)

The equations of motion have been derived by substituting and differentiating the energy equations for use in Lagrange's Equation. There are eight generalized coordinates given by,

$$(q_k) = (\psi, \alpha, \theta, \gamma, R, q_1, q_2, q_3)^T \quad (4.40)$$

where the first four refer to the rotational motion and the rest define the translational motion of the system. The generalized forces are the same as those stated in equation (4.24). The derived equations of motion are presented in Appendix C.

4.12 Simulation of Flexible Model of MMET

Simulations were carried using the same tether parameters and initial condition as in section 4.6. The simulation results for the flexible model have been compared with those for the rigid body model for circular and elliptical orbits.

4.12.1 Circular Orbit

Figure 4.12 shows the responses of the flexible tether model in comparison with the rigid body model, both on a circular orbit. Both models show a very similar response for planar motion, and minor differences are only obvious within a smaller range of simulation time,

as in Figure 4.13. However, a significant difference between both models is shown for non-planar motion, in Figure 4.12, where the flexible model oscillates at a lower frequency and reaches higher amplitude as compared to that of the rigid body model.

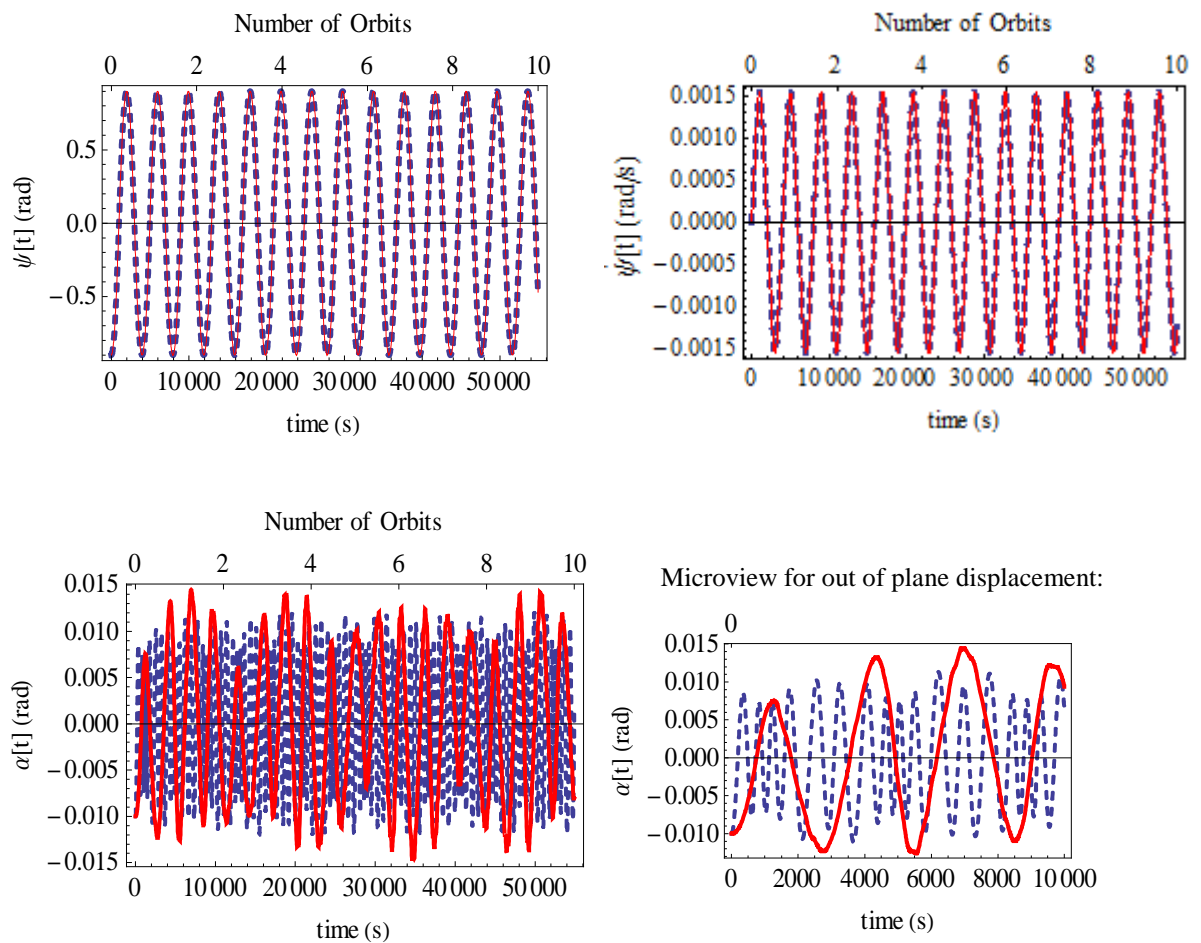


Figure 4.12 : Planar and non-planar motions of a rigid body tether (dashed) and a flexible tether (line) on a circular orbit with zero torque.

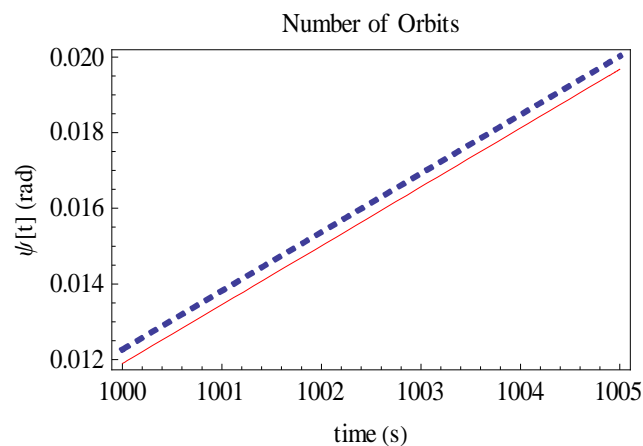


Figure 4.13 : Angular displacement of a rigid body tether (dashed) and a flexible tether (line)

With the application of 2.5MNm torque, both models reach the spin-up condition, and the rigid body model shows a higher rate of planar motion as compared to that of the flexible body, as shown in Figure 4.14. As in the untorqued condition, a significant difference is shown in the non-planar motion between both models, but not in the torque condition. Both models show decaying responses, but the rigid body model has a higher frequency and amplitude for the first eight orbits as compared to those of the flexible model.

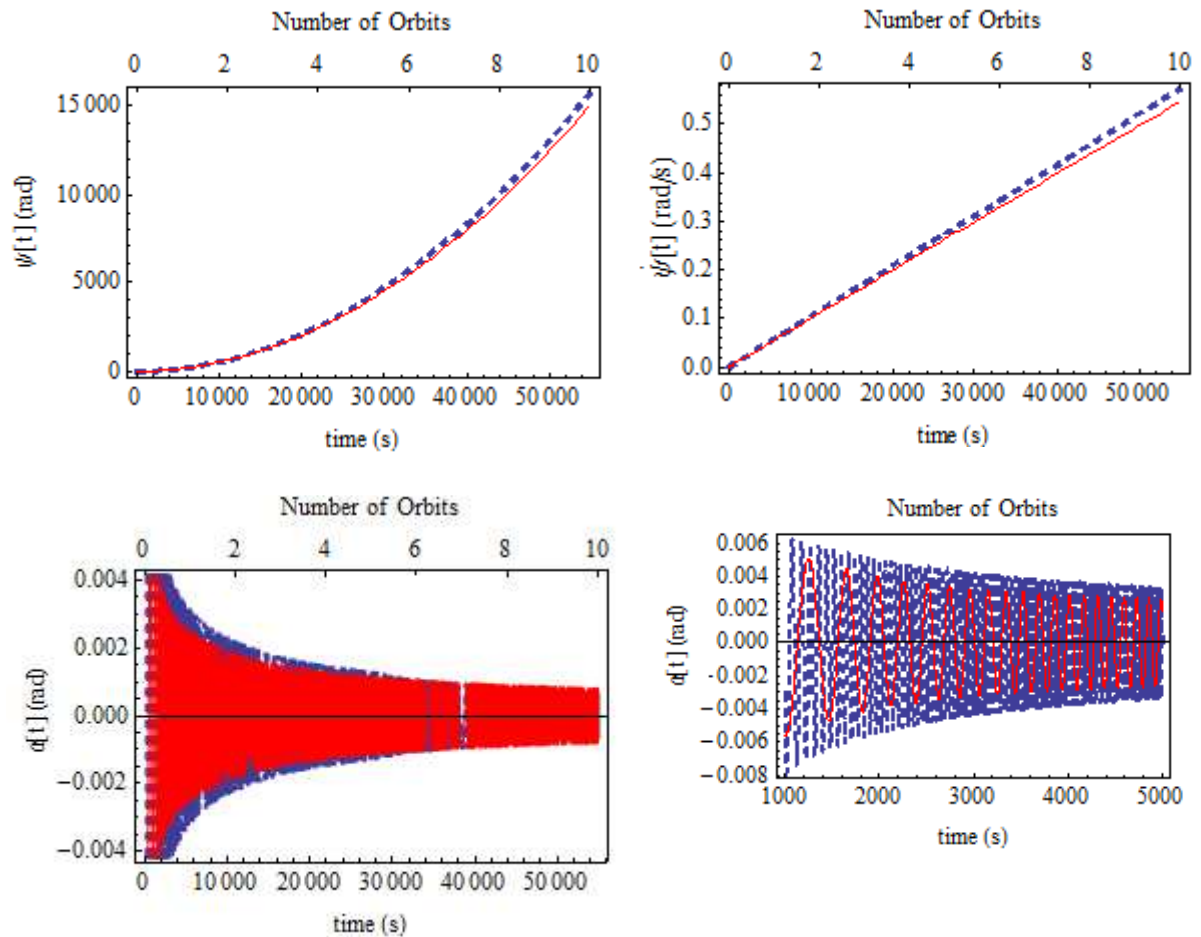
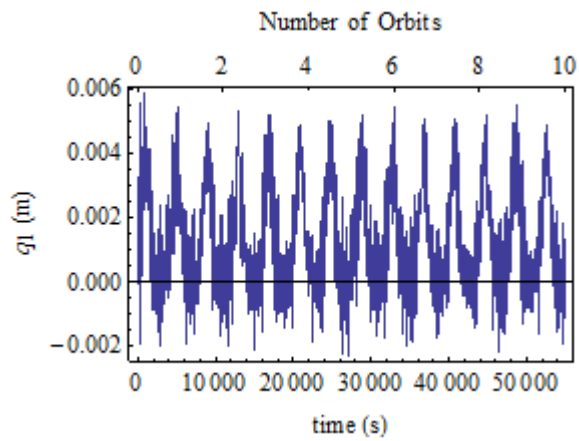


Figure 4.14 : Planar and non-planar motions of a rigid body tether (red) and a flexible tether on a circular orbit with 2.5MNm torque.

The three dimensional displacements in the longitudinal, lateral and transverse directions are shown in Figure 4.15. Figure 4.15 compares the displacement in the free vibration condition and in the torqued condition. The longitudinal, transverse and lateral displacements are oscillating with peak amplitudes of 0.008, 45 and 40 metres for the first condition. With the application of 2.5 MNm of torque, the longitudinal displacement increases monotonically, whilst the transverse and lateral displacements experience amplitudes decaying over time.

without torque



with 2.5 MNm torque

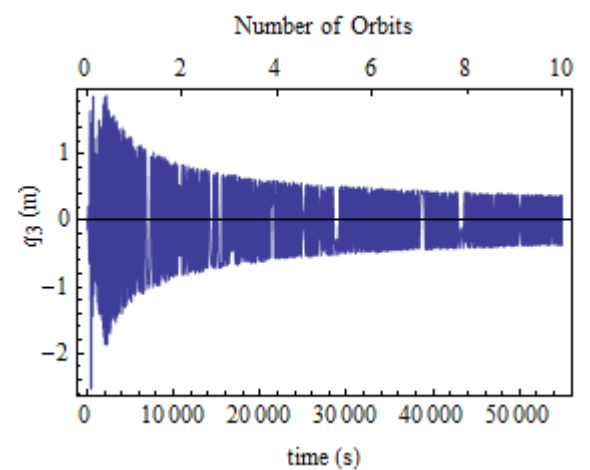
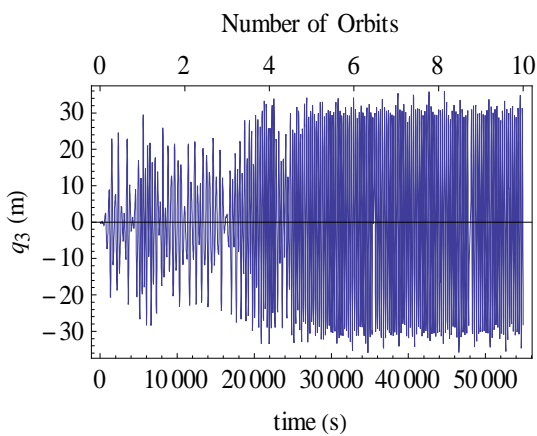
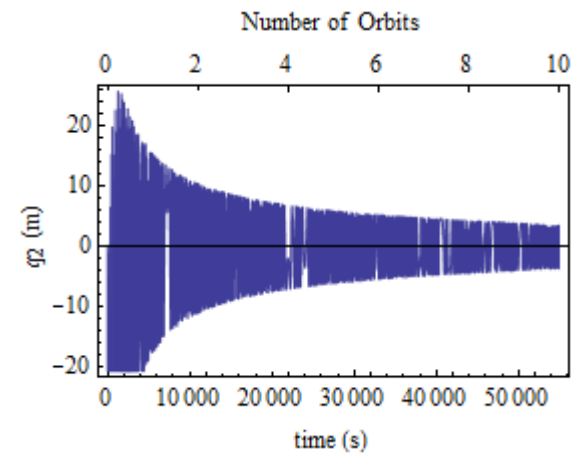
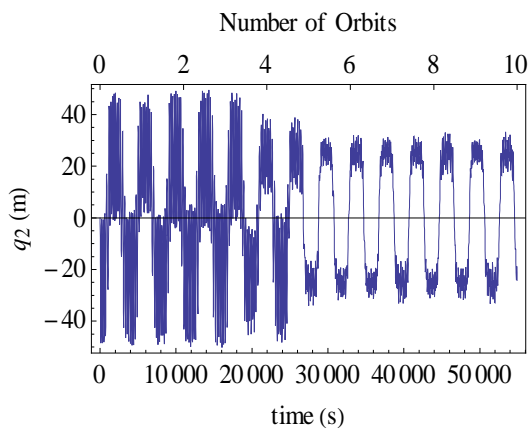
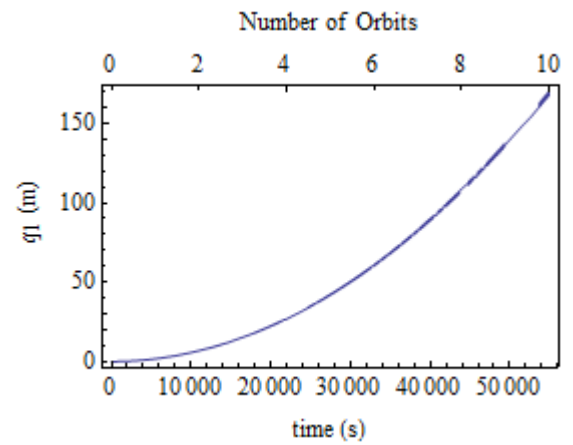


Figure 4.15 : Displacements of the 3D Flexible model of an MMET on a circular orbit.

4.12.2 Elliptical orbit

Simulations were carried out for an elliptical orbit with the following orbital elements,

$$r_p = 7\,000\,000\text{m}, e = 0.1 \quad (4.41)$$

where r_p is the perigee of the elliptical orbit, and e is the orbit eccentricity. The tether simulation starts at perigee with initial conditions ,

$$\psi(0) = -0.575 \text{ rad}, \dot{\psi}(0) = 0 \text{ rad/s}, \alpha(0) = -0.01 \text{ rad}, \dot{\alpha}(0) = 0 \text{ rad/s}, \theta(0) = 0 \text{ rad}$$

$$\dot{\theta}(0) = 0.001131 \text{ rad/s}, \gamma(0) = -0.01 \text{ rad}, \dot{\gamma}(0) = 0 \text{ rad/s}$$

The result is shown in Figure 4.16, with the angular displacements of both tethers being almost identical for the first five orbits but then the rigid body model lags behind the flexible model until the 10th orbit. The difference in the angular displacement and angular velocity of both models are clearly shown in the smaller range of simulation time between 0 to 1000 s, where the differences are increasing within the integration time.

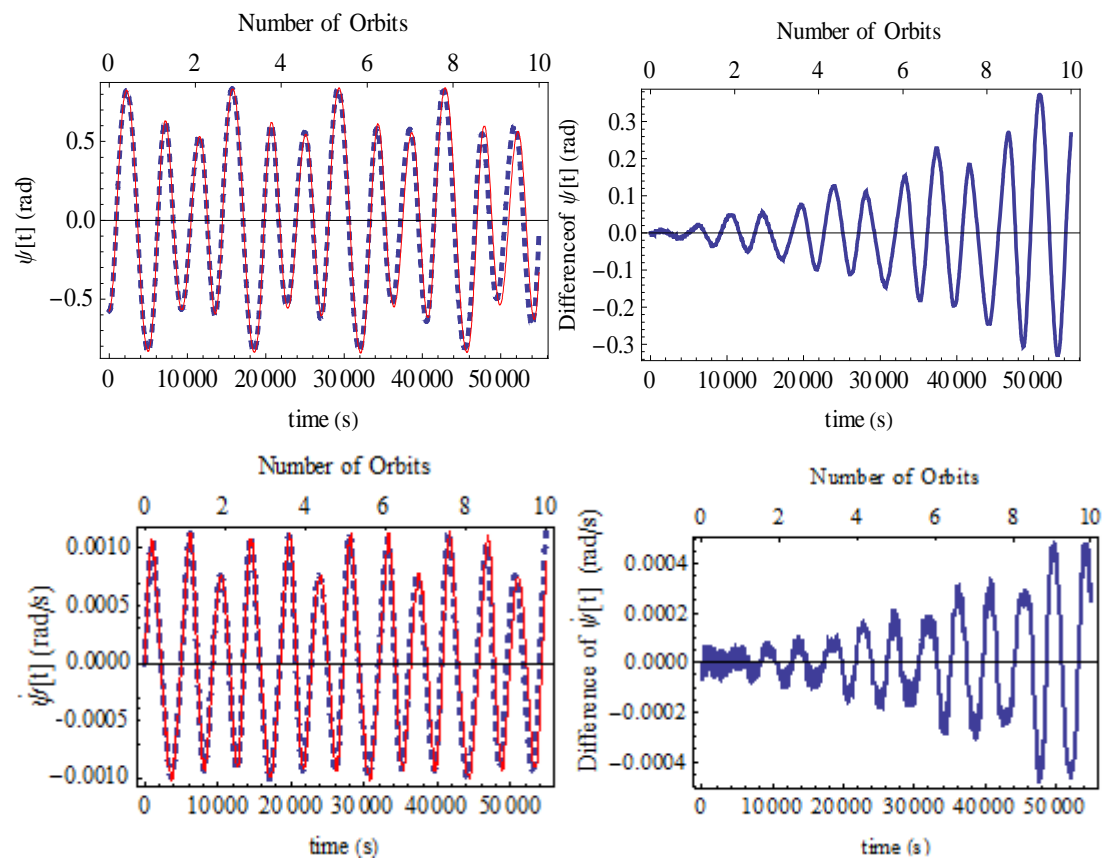


Figure 4.16 : Planar motions of a rigid body tether (dashed) and a flexible tether (red) on an elliptical orbit with zero torque.

The simulation has also shown that the flexibility of the tether has influenced the orbital parameters, where the radius and true anomaly of flexible tether shows the difference along the integration time, as in Figure 4.17. In the case of non-planar motion in Figure 4.18, the flexible tether oscillates with what appears to be a strongly random motion at lower frequency, but with generally higher amplitudes as compared to those of the rigid body model. Both models did not achieve steady state conditions in the first 10 orbits.

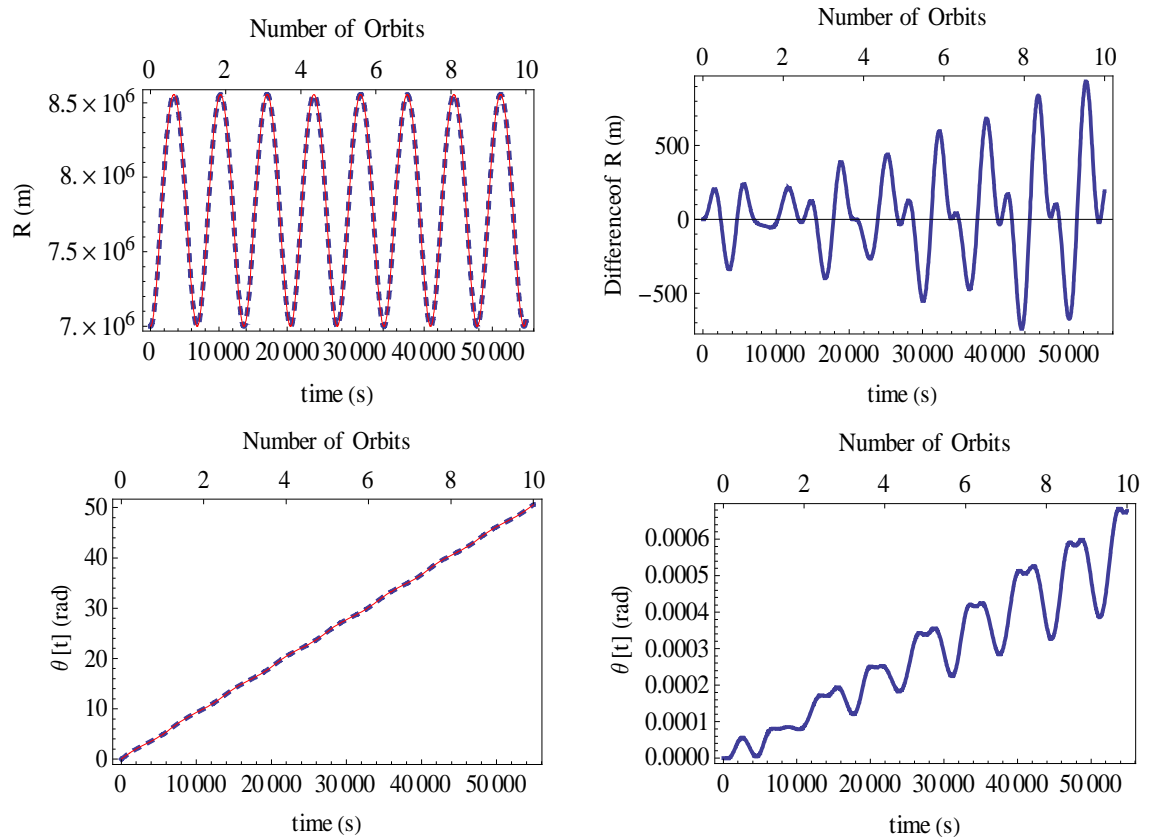


Figure 4.17 : Planar motions of a rigid body tether (dashed) and a flexible tether (line) on an elliptical orbit with zero torque.

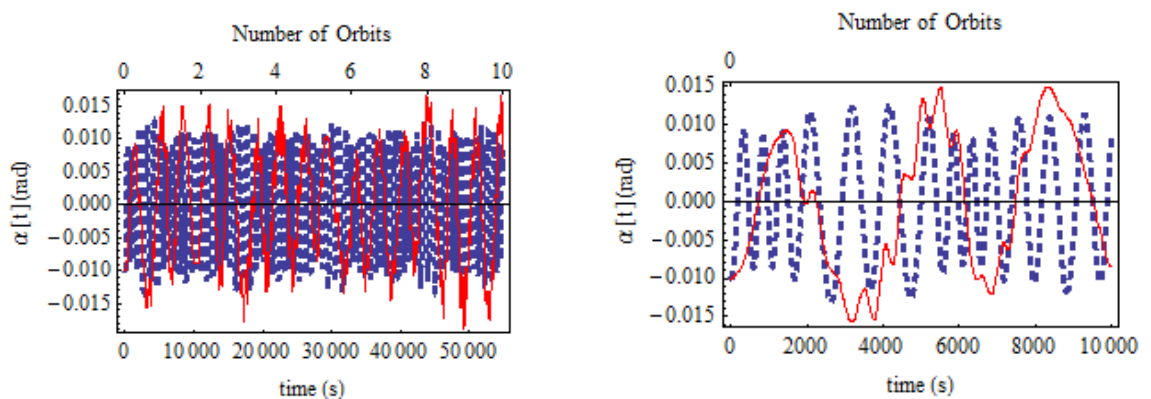


Figure 4.18 : Non-planar motions of a rigid body tether (dashed) and a flexible tether (line) on an elliptical orbit with zero torque.

In comparison to the responses for the tether with an applied torque, as shown in Figure 4.19, the difference in planar motion has shown that the rigid body model moves at a higher rate when compared with the flexible model. But then again, the difference is smaller in comparison to the non-planar motions where the motions in the first orbit show that both models experience decaying motion, with the flexible tether motion decaying at a lower frequency, but with generally higher amplitude. With a longer simulation time the amplitude of the flexible model decreases and is lower than that of the rigid body model, as shown in Figure 4.19(c1).

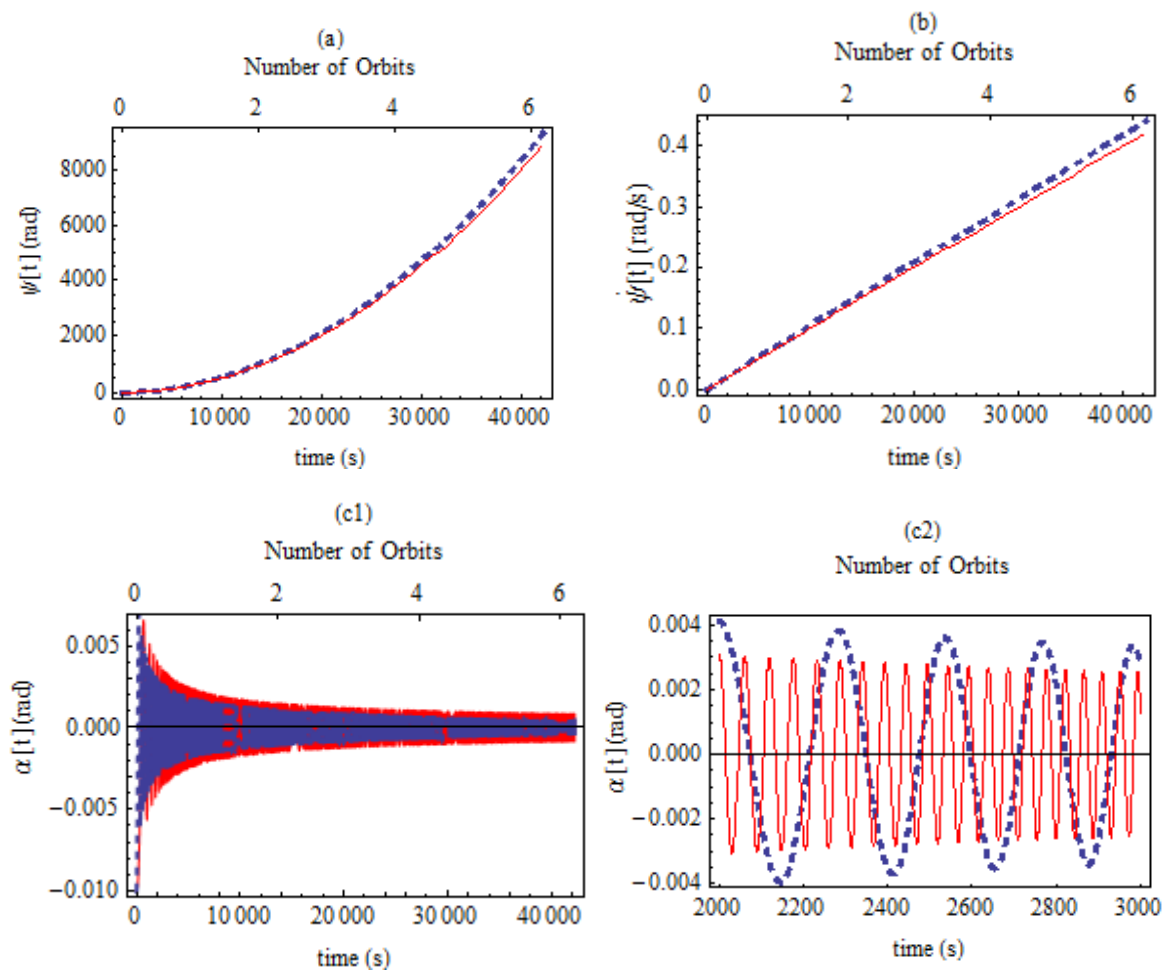


Figure 4.19 : Planar and non planar motions of a rigid body tether (dashed) and a flexible tether (line) on an elliptical orbit with 2.5MNm torque.

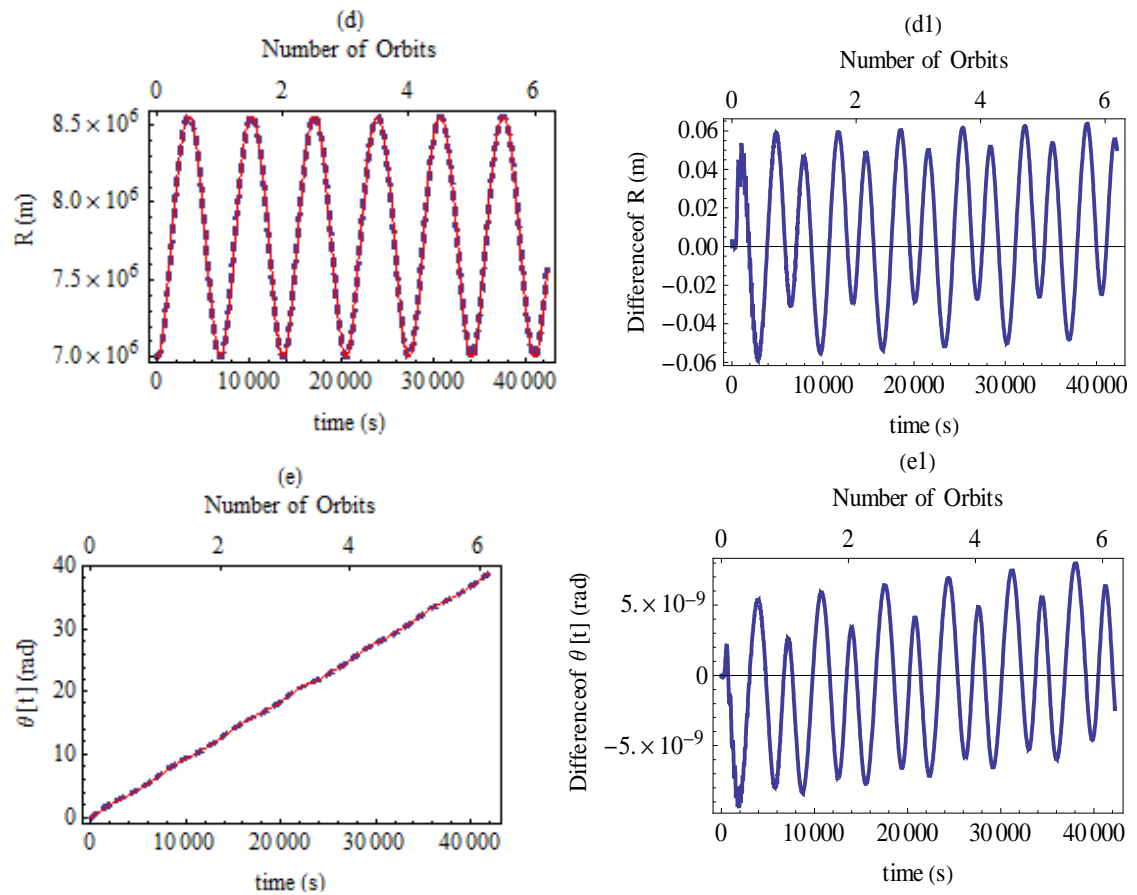


Figure 4.20 : Orbital parameters for 3D motion of a rigid body tether (dashed) and a flexible tether (line) on an elliptical orbit with 2.5MNm torque.

The difference of the orbital elements between flexible and rigid body motion of tether in Figure 4.20 (d) and (e) are indistinguishable over longer period of simulation. Figure 4.20 (d1) and (e1) shown that a very small difference occurs between these two models. This suggests that the flexibility of the tether will make a small alteration of tether's orbit.

The three dimensional displacement for a tether on an elliptical orbit is shown in Figure 4.21. The untorqued condition results in the flexible tether oscillating in all directions, with longitudinal, transverse and lateral vibration showing the highest amplitudes of 0.45 m, 600m and 400 m for tether a length of 10 km.

With application of torque the displacement in the longitudinal direction increases but both the transverse and lateral displacements reduce as shown in Figure 4.21. As mentioned in the previous chapter, this phenomenon is connected to the stiffening effect due to the centripetal load experienced by the spinning tether. The centripetal load in the longitudinal direction increases the axial displacement, whilst the lateral stiffening effect reduces the vibration in the transverse and lateral directions.

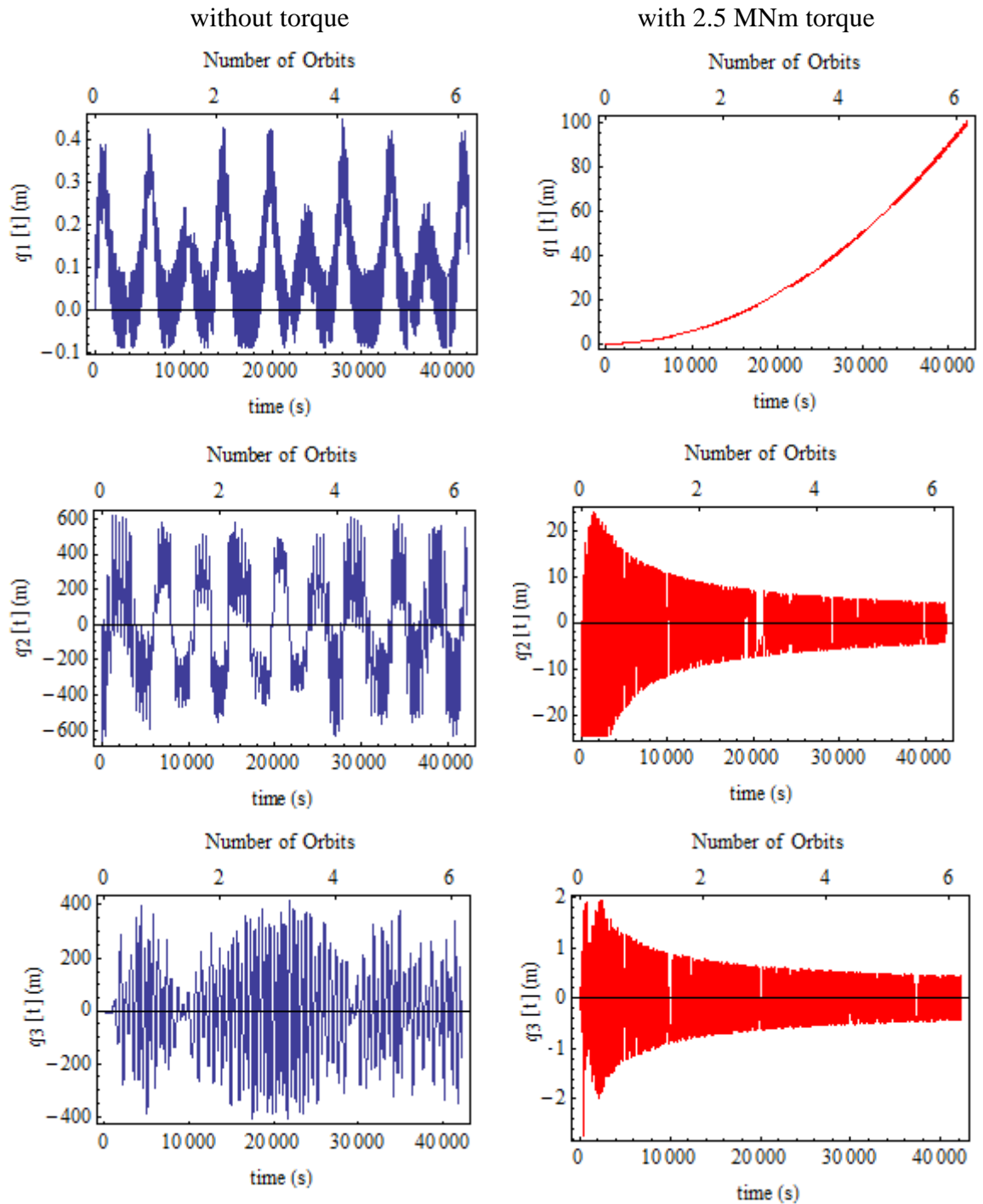


Figure 4.21 : Displacements of the 3D Flexible model of the MMET on an elliptical orbit.

4.12.3 Comparison between the 2D and 3D Flexible Models.

The responses for two dimensional (2D) and three dimensional (3D) motion of the flexible model are shown in Figures 4.22 to 4.24. The 2D and 3D models show an almost similar response in Figure 4.22 (a) and (b). However, simulating the differences in angular displacement and angular velocities between these two models shows that a difference

occurs and even though it is relatively small, it is still significant to the global motion of the tether.

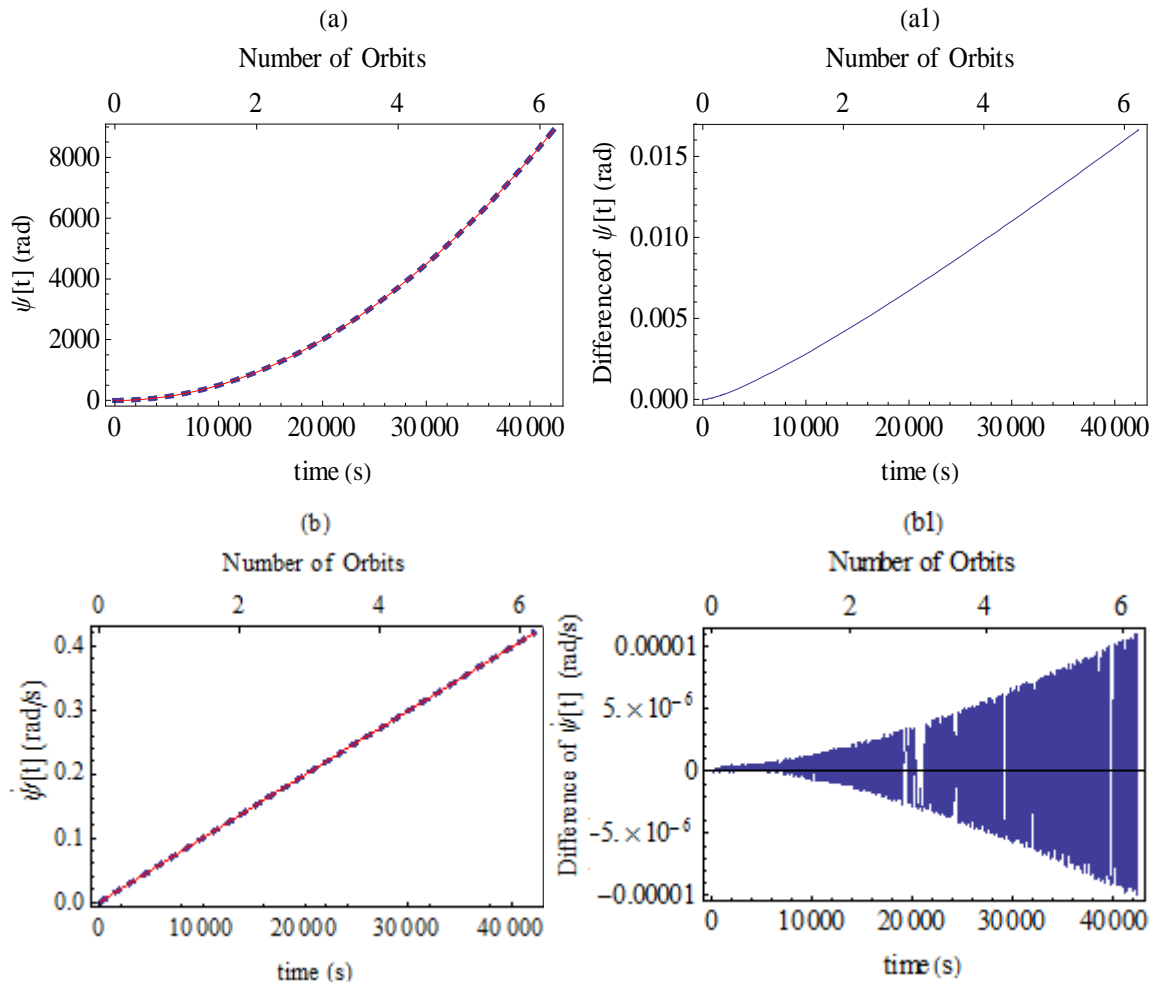


Figure 4.22 : Comparison of the response between the 2D (line) and 3D (dashed) flexible models of the MMET on an elliptical orbit.

The existence of the non-planar variable (α) in the equations of motion of the 3D model alters the orbit of the tether, but at a smaller scale. It is shown, in Figure 4.23 (c1) that the maximum difference within the simulation time is 0.0014 meter and the difference of the true anomaly is insignificant and within the range of 8×10^{-11} rad, as shown in 4.23 (d1).

The local displacement of the tether, Figure 4.24, shows that both models displaying the same trend, where the longitudinal displacement is increasing and the transverse displacement is decaying, with the increase of simulation time due to the stiffening effect cause by centripetal force.

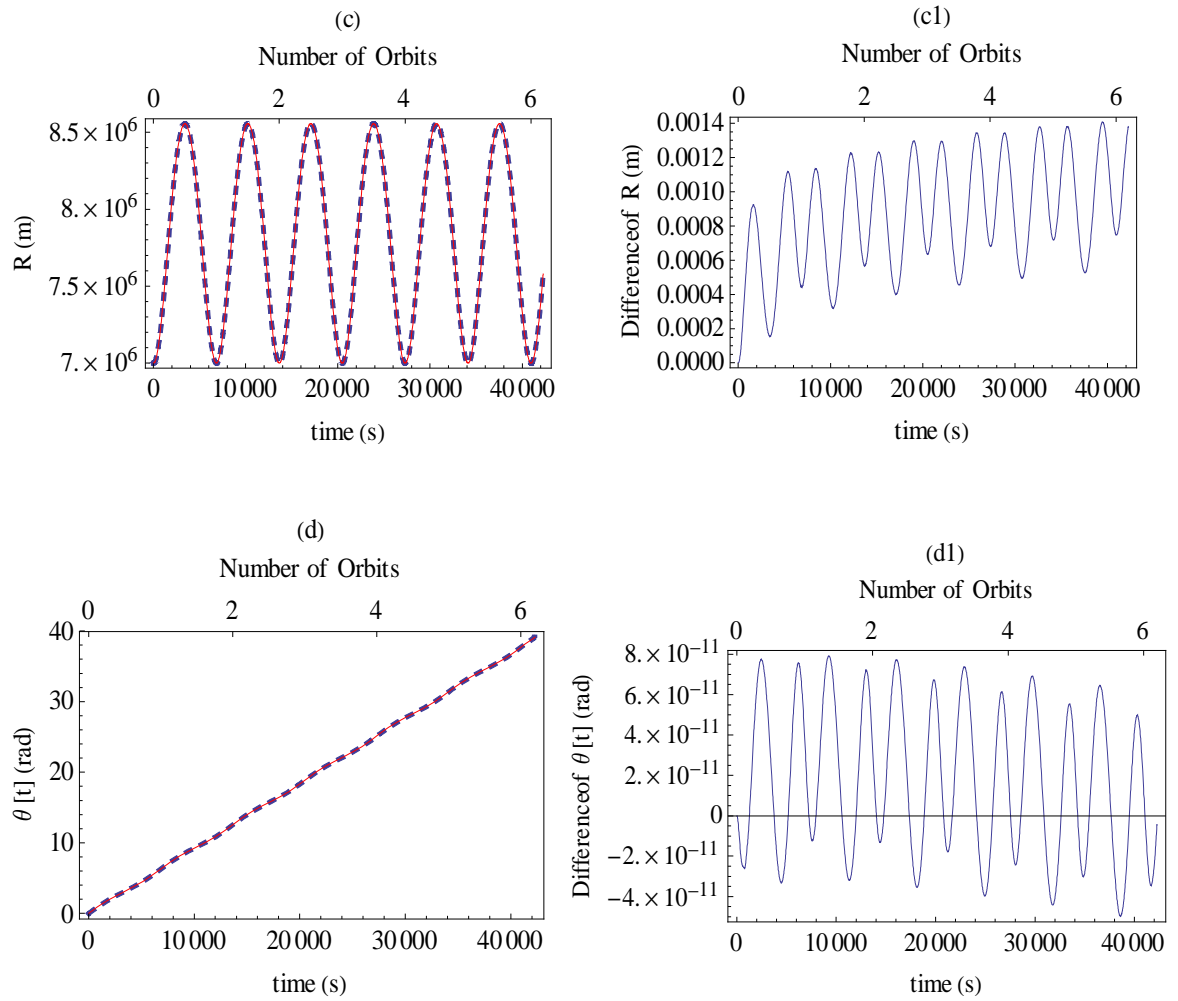


Figure 4.23 : The difference in orbital parameters between 2D and 3D flexible model of MMET on an elliptical orbit.

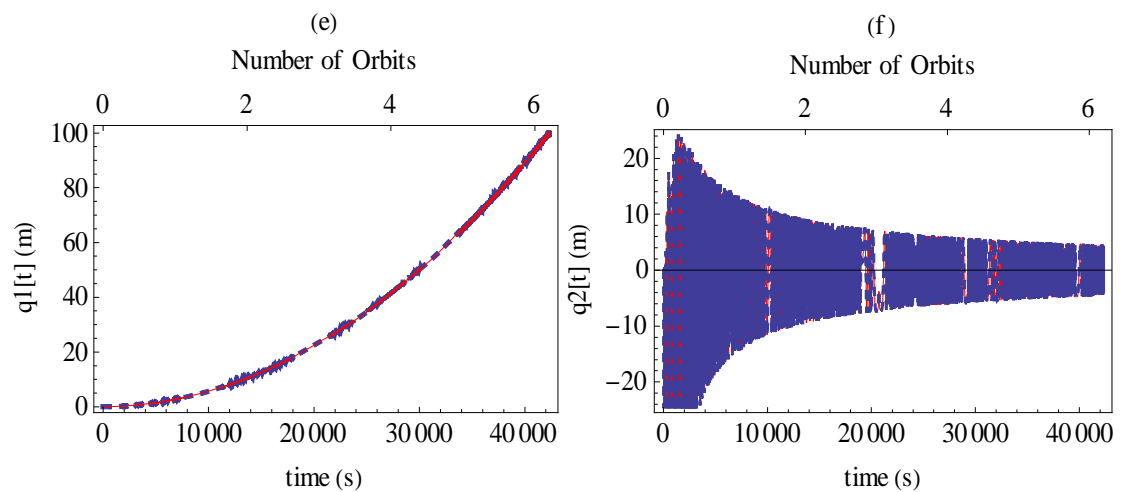


Figure 4.24 : Longitudinal and transverse displacement of 2D (line) and 3D (dashed) flexible model of the MMET on an elliptical orbit.

The longitudinal displacement in Figure 4.24 (e) is appear to have unbounded exponential growth as compared to the transverse vibration in both 2D and 3D model. This phenomena is only occurs when torque applied to the tether. This phenomenon can be explained by taking the relationship between the force and strain for a uniform cross section of a string as given in equation below,

$$F = EA\varepsilon_x \quad (4.42)$$

Where ε_x is the axial strain and define by the axial displacement $\frac{du}{dx}$. In the case of spinning tether, the source of force comes from the centripetal force. Therefore, substitute the displacement in axial direction to equation (4.42) gives the relationship between the force to the displacement as equation below,

$$F = EA \frac{du}{dx} \quad (4.45)$$

Therefore, when the torque is applied, the centripetal force is increased and for a constant Modulus Elasticity, E and tether's cross section A , the displacement will be increased too.

4.13 Conclusions

The study of the 3D rigid body model of an MMET has compared the response of the rigid body model with a massless tether model. The derivation of the EOM for the rigid body model has included rotational kinetic energy, but not in the massless tether model, and this leads to differences in the simulation results. This comparative study between the three dimensional flexible model and the former rigid body models shows that flexible model has lower response as compared with that of the rigid body model. This study shows the influence of mass in tether's motion. The application of torque has increased the longitudinal displacement but the transverse displacement shows the decaying phenomena due to the stiffening effect of rotating tether. This study also shows that relationship between planar and non-planar motion is found to be significant for the global motion of the tether.

Chapter 5

Dynamic Boundary Conditions

5.1 Introduction

This chapter presents a more complete continuum model in which transverse flexibility is accommodated within the tether model; and the model includes appropriate dynamic boundary conditions, which provides further fidelity in the representation of the dynamics which may not otherwise be seen. The boundary conditions lead to a specific frequency equation, and the Eigenvalues from this provide the natural frequencies of the orbiting flexible motorised tether when static, accelerating in spin, and at terminal angular velocity. A parametric study of the nonlinear dynamical model, focusing on transverse vibration, shows the relationships between the angular velocity, the natural frequencies, and the predicted linear mode shapes of the system. This study investigates the MMET responses for two different dynamic boundary conditions: the fixed-attached mass condition, and when both ends are attached to masses. The definitions of these two conditions are explained in the section 5.2 and 5.3. The differences in the modal responses when applying the dynamic and static boundary conditions are highlighted and discussed, providing more insight into the subtleties of the dynamics of motorised orbiting space tethers.

5.2 Fixed-Attached Mass Boundary Condition

The study starts with the derivation of the equations of motions for a flexible tether, governed by a fixed-attached boundary condition (Meirovitch, 2001) and (Rao,2007). This boundary condition is based on the assumption that the central facility is so massive as compared with the payload that the tether sub-spans experiences the equivalent of built-in ends at the connection with the central facility. Figure 5.1 shows the configuration of MMET in (a) and the assumed configuration of the boundary conditions for this case taken from configuration of MMET is shows in Figure 5.1 (b).

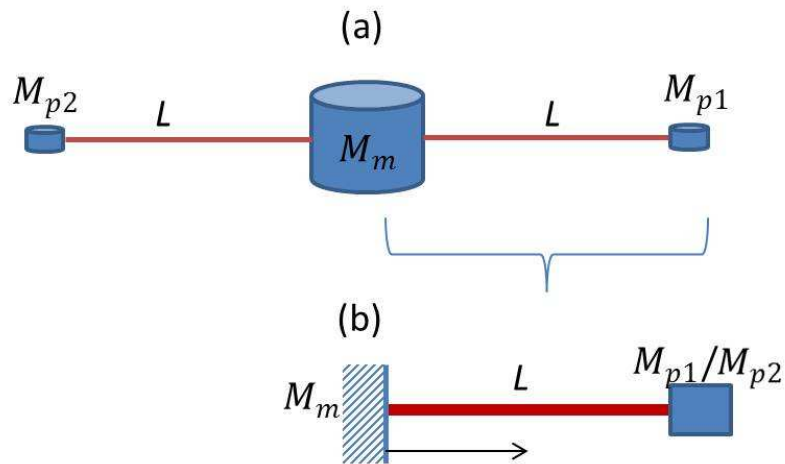


Figure 5.1 : (a) Configuration of MMET (b) Schematic diagram of masses connected to the tether sub-span with fixed-attached mass boundary condition.

Therefore, the displacement boundary condition at the fixed end where $x=0$ in the transverse direction is given by,

$$v(0) = 0 \quad (5.1)$$

In the case of transverse displacement, the angle of deflection in transverse direction as shown in Figure 5.2 is given by,

$$\frac{\partial v}{\partial x} \approx \sin \theta \quad (5.2)$$

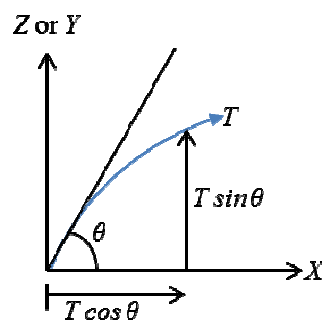


Figure 5.2 : The deflection angle of the string

where T refers to the force acting on the string. Referring to Figure 5.1, the boundary condition at $x=L$ is given by,

$$T(x) \frac{\partial v}{\partial x} \Big|_{x=L} = -M_p \ddot{v} \Big|_{x=L} \quad (5.3)$$

The n th mode of vibration is represented by means of a separation of variables in the transverse direction, and is given by equation (3.23) in Chapter 3. The general solutions for the spatial and temporal parts are given by equations (3.34) and (3.35) leading to

$$v(x,t) = \left(A_v \sin \frac{\omega_v}{c} x + B_v \cos \frac{\omega_v}{c} x \right) (C_v \cos \omega_v t + D_v \sin \omega_v t) \quad (5.4)$$

where the subscript 'v' refers to the value in the transverse direction.

Equations (5.1) and the spatial part of (5.4) as in equation (3.34) give,

$$B_v = 0, \quad (5.5)$$

and hence equation (5.4) reduces to

$$v(x,t) = \left(A_v \sin \frac{\omega_v}{c} x \right) (C_v \cos \omega_v t + D_v \sin \omega_v t) \quad (5.6)$$

Equation (5.6) gives, after differentiation with respect to time,

$$\frac{\partial v}{\partial t} = A_v \frac{\omega_v}{c} \cos \frac{\omega_v x}{c} (C_v \cos \omega_v t + D_v \sin \omega_v t) \quad (5.7)$$

$$\frac{\partial^2 v}{\partial t^2} = -A_v \omega_v^2 \sin \frac{\omega_v x}{c} (C_v \cos \omega_v t + D_v \sin \omega_v t) \quad (5.8)$$

Substituting equation (5.7) and (5.8) into (5.3) for $x=L$ gives,

$$T(l) A_v \frac{\omega_v}{c} \cos \frac{\omega_v L}{c} (C_v \cos \omega_v t + D_v \sin \omega_v t) = M_p A_v \omega_v^2 \sin \frac{\omega_v L}{c} (C_v \cos \omega_v t + D_v \sin \omega_v t) \quad (5.9)$$

and equation (5.9) can be reduced to,

$$\frac{T}{M_p \omega_v c} = \tan \frac{\omega_v L}{c} \quad (5.10)$$

Equation (5.10) can be rewritten as a transcendental equation, given by,

$$\alpha_v \tan \alpha_v = \beta \quad (5.11)$$

where,

$$\alpha_v = \frac{\omega_v L}{c} \quad \text{and} \quad \beta = \frac{TL}{M_p c^2} \quad (5.12), (5.13)$$

Knowing that from equation (3.27) $c = \sqrt{\frac{T}{\rho}}$, and substituting this into equation (5.13), leads to

$$\beta = \frac{\rho L}{M_p} \quad (5.14)$$

Equation (5.11) is a frequency equation which has an infinite number of roots. For the n th root, the equation can be written as,

$$\omega_v = \frac{c \alpha_v}{L} \quad n=1,2,3\dots \quad (5.15)$$

Taking the first mode of vibration, the mode shape corresponding to the natural frequency ω_v , is given by,

$$\xi(x) = A_v \sin \frac{\omega_v}{c} x \quad (5.16)$$

Applying a simple normalisation in the form of $A_v = 1$, the mode shape for the transverse vibration becomes,

$$\xi(x) = \sin \frac{\omega_v}{c} x \quad (5.17)$$

Using the default tether's parameters value defined in section 3.5, and a constant angular velocity of 0.2 rad/s, the first five roots for equation (5.11) are given as in Table 5.1 below,

Roots	Value of α_v
1st	1.571
2nd	1.742
3rd	4.719
4th	7.857
5th	11.000

Table 5.1 : Roots of equation (5.11)

The roots in Table 5.1 were substituted into equation (5.15) and generate the modes shape as shown in Figure 5.3. The plotted mode shape is highly dependent on the end mass in which in the tether case, the end masses refer to the payload masses.

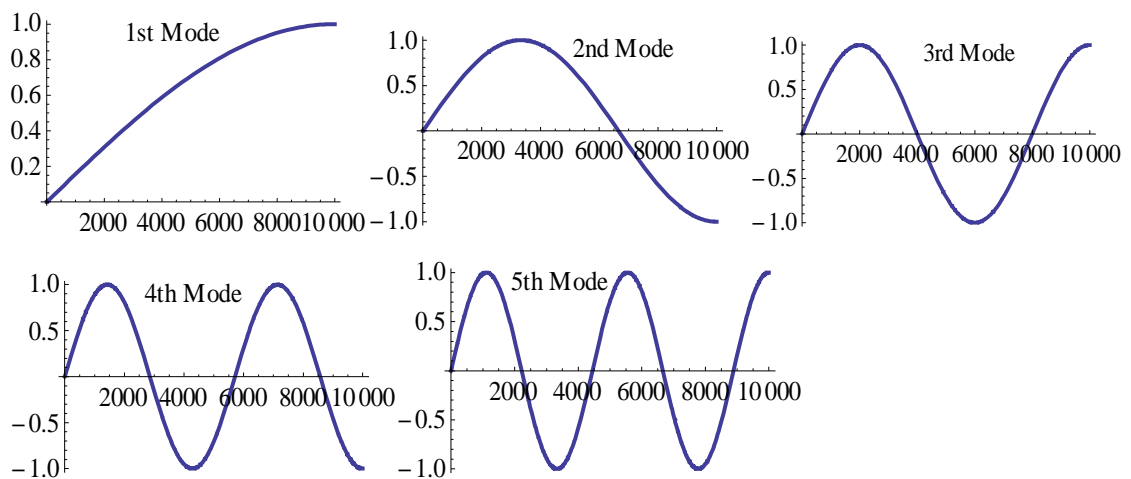


Figure 5.3 : Modes shape for the transverse vibration governed by the fixed-attached boundary condition

5.2.1 Equations of motion

Substituting equation (5.17) into the kinetic and potential equations given by equations (3.74) and (3.75) in Chapter 3, and applying the Lagrange's equation gives the equations of motion derived for transverse vibration in one dimensions for two translational generalised coordinate R and q_2 and two rotational generalised coordinates ψ and θ .

$$\begin{aligned}
& \left(2\rho ALq_2\dot{q}_2 + M_p 4q_2\dot{q}_2 \sin\left(\frac{\omega_v L}{c}\right)^2 - \frac{\rho Acq_2\dot{q}_2}{\omega_v} \sin\left(\frac{2\omega_v L}{c}\right) \right) (\dot{\theta} + \dot{\psi}) + \left(\frac{5}{6}\rho AL^3 + \frac{1}{2}M_m r_m^2 \right. \\
& \left. 2M_p q_2^2 \sin\left(\frac{\omega_v L}{c}\right)^2 - \frac{\rho Acq_2^2}{2\omega_v} \sin\left(\frac{2\omega_v L}{c}\right) + \frac{1}{2}\rho ALr_T^2 + \rho ALq_2^2 + 2M_p L^2 + M_p r_p^2 \right) (\ddot{\theta} + \ddot{\psi}) \\
& \frac{M_p LR\mu \sin \psi}{(L^2 - 2L \cos \psi R + R^2)^{3/2}} - \frac{M_p LR\mu \sin \psi}{(L^2 + 2L \cos \psi R + R^2)^{3/2}} - \frac{2\rho ALc\ddot{q}}{\omega_v} \cos \frac{\omega_v L}{c} \\
& \sum_{i=1}^n \frac{(2i+1)\mu\rho AL^2 \sin \psi}{2n^2 \left(\frac{(2i-1)^2 L^2}{4n^2} - \frac{(2i+1)}{n} LR \cos \psi + R^2 \right)^{3/2}} \\
& - \sum_{i=1}^n \frac{(2i+1)\mu\rho AL^2 \sin \psi}{2n^2 \left(\frac{(2i-1)^2 L^2}{4n^2} + \frac{(2i+1)}{n} LR \cos \psi + R^2 \right)^{3/2}} \\
& + \frac{2\rho ALc^2 \ddot{q}}{\omega_v^2} \sin \frac{\omega_v L}{c} + 2M_p L\ddot{q} \sin \frac{\omega_v L}{c} - \tau = 0 \tag{5.18}
\end{aligned}$$

$$\begin{aligned}
& M_m + 2(\rho LA + M_p)\ddot{R} + \frac{\mu M_m}{R^2} - (M_m + (2(\rho LA + M_p))R)\dot{\theta}^2 - \frac{M_p LR\mu \cos \psi}{(L^2 - 2L \cos \psi R + R^2)^{3/2}} \\
& + \frac{M_p LR\mu \cos \psi}{(L^2 + 2L \cos \psi R + R^2)^{3/2}} + \frac{\mu M_p R}{(L^2 - 2L \cos \psi R + R^2)^{3/2}} + \frac{\mu M_p R}{(L^2 + 2L \cos \psi R + R^2)^{3/2}} \\
& - \sum_{i=1}^n \frac{\mu\rho AL \left(\frac{(2i+1)}{n} L \cos \psi + 2R \right)}{2n \left(\frac{(2i-1)^2 L^2}{4n^2} - \frac{(2i-1)}{n} LR \cos \psi + R^2 \right)^{3/2}} \\
& - \sum_{i=1}^n \frac{\mu\rho AL \left(\frac{(2i+1)}{n} L \cos \psi + 2R \right)}{2n \left(\frac{(2i-1)^2 L^2}{4n^2} + \frac{(2i-1)}{n} LR \cos \psi + R^2 \right)^{3/2}} = 0 \tag{5.19}
\end{aligned}$$

$$\left(\frac{5}{6}\rho AL^3 + 2\rho ALR^2 + M_m R^2 + 2M_p L^2 + 2M_p R^2 + \frac{1}{2}M_m r_m^2 + \frac{1}{2}\rho ALr_T^2 \right) \ddot{\theta}$$

$$\begin{aligned}
& + (2R(2\rho AL + M_m + 2M_p))\dot{R}\dot{\theta} + \left(\rho ALq_2^2 - \frac{\rho Acq_2^2}{2\omega_v} \sin \frac{2L\omega_v}{c} + 2M_p q_2^2 \sin^2 \frac{\omega_v L}{c} \right) (\ddot{\theta} + \ddot{\psi}) \\
& + \left(2\rho ALq_2\dot{q}_2 - \frac{\rho Acq_2\dot{q}_2}{\omega} \sin \frac{2\omega_v L}{c} + 4M_p q_2\dot{q}_2 \sin^2 \frac{2\omega_v L}{c} \right) (\dot{\theta} + \dot{\psi}) \\
& + \left(\frac{5}{6}\rho AL^3 + 2M_p L^2 + 2M_p r_p^2 + \frac{1}{2}M_m r_m^2 + \frac{1}{2}\rho ALr_T^2 \right) \ddot{\psi} + \left(\left(2M_p L + \frac{2\rho Ac^2}{\omega_v^2} \right) \sin \frac{\omega_v L}{c} + \right. \\
& \left. \frac{2\rho ALc}{\omega_v} \cos \frac{\omega_v L}{c} \right) \ddot{q}_2 = 0 \tag{5.20}
\end{aligned}$$

$$\begin{aligned}
& \left(\rho AL - \frac{\rho Ac}{2\omega} \sin \frac{2\omega_v L}{c} + M_p \sin^2 \frac{2\omega_v L}{c} \right) \ddot{q}_2 + \left(12\omega_v L + 8c \sin \frac{2\omega_v L}{c} + c \sin \frac{2\omega_v L}{c} \right) \\
& \left(\frac{\omega_v^3 (AE - T_o)}{32c^4} \right) q_2^3 + \frac{T_o}{2\omega_v c^2} \left(\omega_v^2 \left(2L\omega_v + c \sin \frac{2\omega_v L}{c} \right) \right) q_2 + \\
& \left(\frac{\rho A}{2\omega} \left(c \sin \frac{2\omega_v L}{c} - 2\omega_v L \right) - 2M_p \sin^2 \frac{2\omega_v L}{c} \right) (\dot{\theta} + \dot{\psi}) + \\
& \left(2L \sin \frac{\omega_v L}{c} - \frac{2\rho ALc}{\omega_v} \cos \frac{\omega_v L}{c} + \frac{2\rho Ac^2}{\omega_v^2} \sin \frac{\omega_v L}{c} \right) (\ddot{\theta} + \ddot{\psi}) = 0 \tag{5.21}
\end{aligned}$$

5.2.2 Tether Simulations

The default data for the MMET have been used to simulate the motion for the tether on a circular and an elliptical orbit. The initial conditions used by for simulation on the circular orbit are as follows:

$$\psi(0) = -0.9 \text{ rad}, \quad \dot{\psi}(0) = 0.2 \text{ rad/s}, \quad v(0) = 0 \text{ rad}, \quad \dot{v}(0) = 0 \text{ rad/s} \tag{5.22}$$

The zero or near to zero initial condition for angular velocity has shown generation of infinite expression when integrating equations (5.18) to (5.21) using equation solver *NDSolve* in *Mathematica*TM. Therefore, larger values have been used for the initial angular velocity and the initial condition for angular displacement taken from Ziegler (2003).

5.2.2.1 Circular Orbit, unmotorised

The motions for the untorqued condition are shown in Figure 5.4. The non-zero initial condition of $\psi[0]$ contributes to the monotonic increase of the tether's angular displacement, but not the angular velocity in which the response is still in the oscillation condition in both boundary conditions. These results for the fixed-attached boundary condition are compared with the results from the model using the static boundary condition.

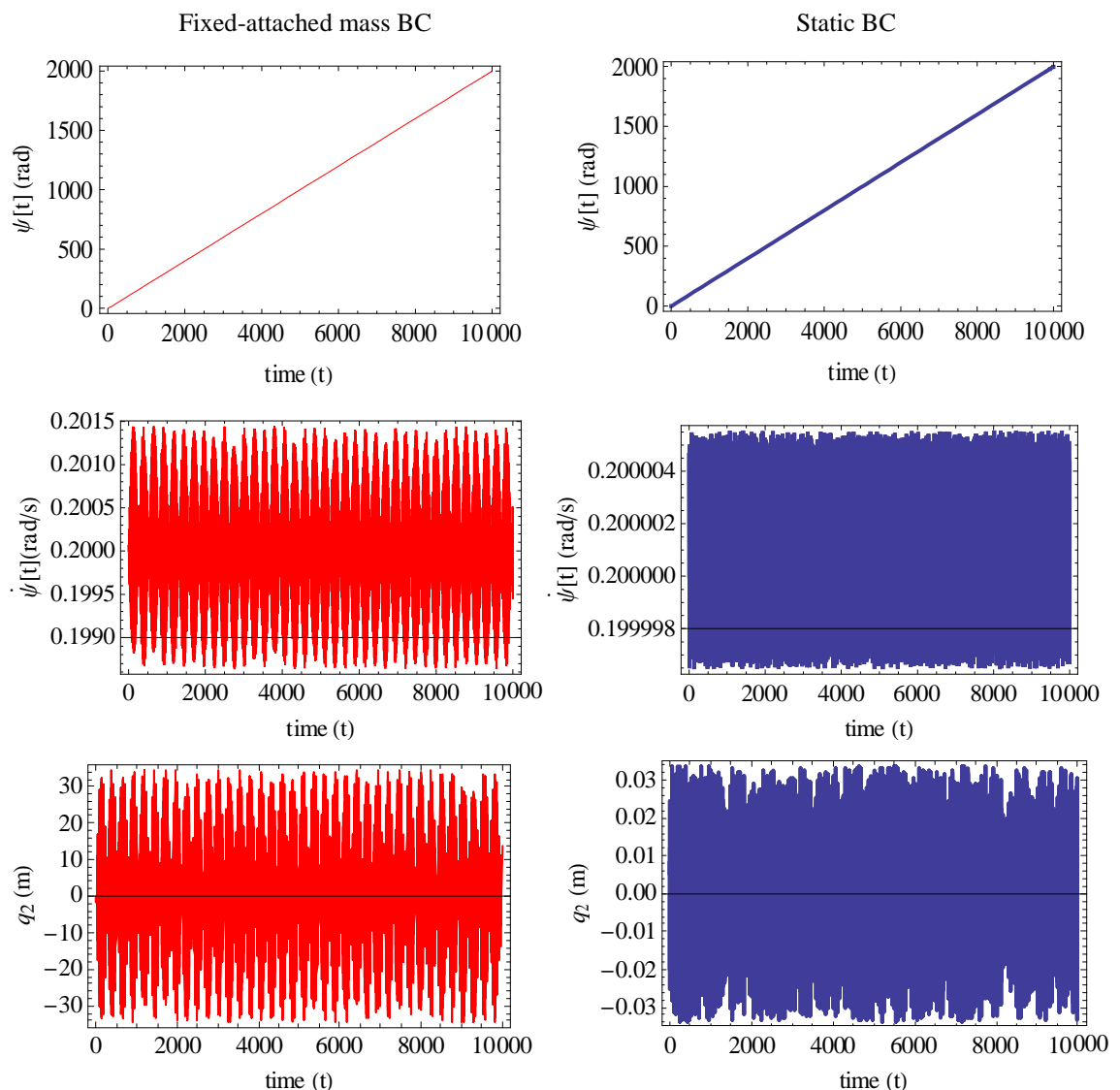


Figure 5.4 : Responses for the tether on a circular orbit with the fixed-attached boundary (red) condition and the static boundary condition (blue)

Figure 5.4 shows the comparison in the responses between these two models. The angular velocities for fixed-attached boundary condition model and static boundary condition are both oscillating, but the fixed-attached boundary condition model suggests a lower natural frequency but achieved a higher value for the maximum angular velocity as compared with

the static boundary condition. The significant difference in the transverse displacement shows that the amplitude achieved by the fixed-attached boundary condition is higher, with a maximum value of ± 30 m whilst the static boundary condition is ± 0.03 m.

5.2.2.2 Elliptical orbit, unmotorised

The differences between the responses of the tether for different boundary conditions on an elliptical orbit have been simulated, and are shown in Figure 5.5.

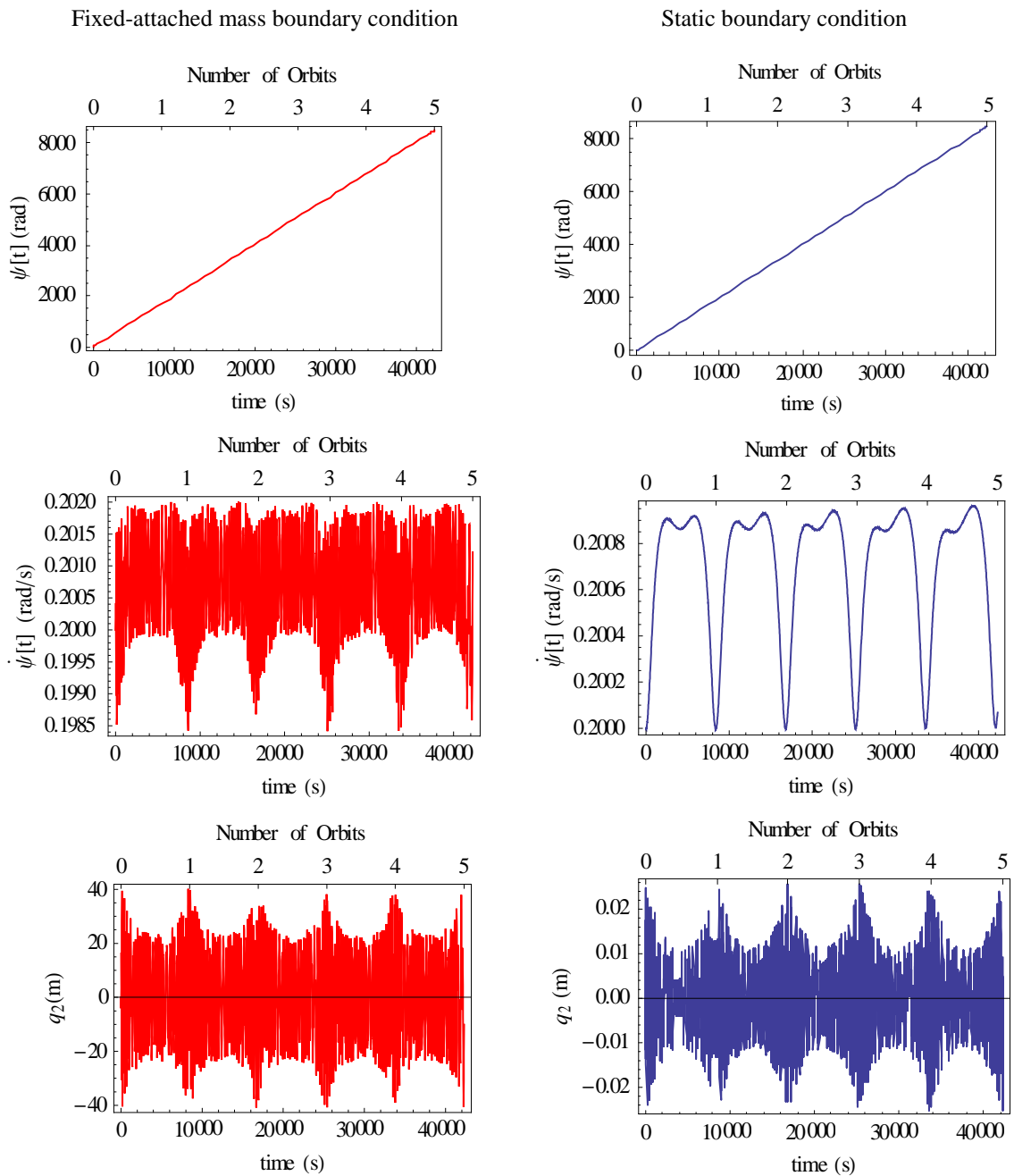


Figure 5.5 : Responses for tether on an elliptical orbit with $e=0.25$ for fixed-attached boundary condition (red) and static boundary condition (blue)

The angular displacement shows similar responses to the tether on a circular orbit, but the angular velocity of the tether with fixed-attached boundary condition shows a significant difference. The maximum angular velocity achieved by this model is marginally higher, as compared to the static boundary condition model. The transverse vibration also gives a similar response to the tether model on a circular orbit, in which the maximum amplitude for fixed-attached boundary condition is ± 40 m and the static boundary condition is around ± 0.02 m.

5.2.2.3 Circular Orbit, motorised

For the condition in which the motorised tether is operating on the circular orbit, equations (5.18) to (5.21) were numerically integrated with an applied torque of 2.5 MNm, and the initial conditions were adopted as shown in equation (5.22). The result for the integration is given in Figure 5.6. The angular displacement and angular velocity for both models show growth within the integration time, achieving the spin-up condition, and the difference between both models can be captured from the Figure 5.6 in which the static boundary condition case reached a higher angular velocity at the end of the simulation time, compared with the tether with a fixed-attached mass boundary condition. This shows that the choice of boundary condition could influence the global motion of the tether system. The transverse vibrations in both models undergo decaying phenomena similar to the simulation results presented in Chapter 3 and Chapter 4 for the motorised condition. Despite having higher amplitude of the displacement, the fixed-attached boundary condition model decays faster than static boundary condition case.

5.2.2.4 Elliptical orbit, motorised

The responses of the tether with the fixed-attached boundary condition on an elliptical orbit are shown in Figure 5.7. The expected responses are portrayed in which the decaying phenomenon occurs in the transverse direction. Interesting phenomena in transverse displacement is discovered where the displacement is increasing (in global motion the trend is decreasing) every time the tether moves towards perigee. However, the differences between the angular displacement and angular velocity of the fixed-attached boundary condition case with the static boundary condition model are inconsequential, with both models achieving spin-up conditions with the application of the torque. The difference in the angular velocity is shown in Figure 5.8.

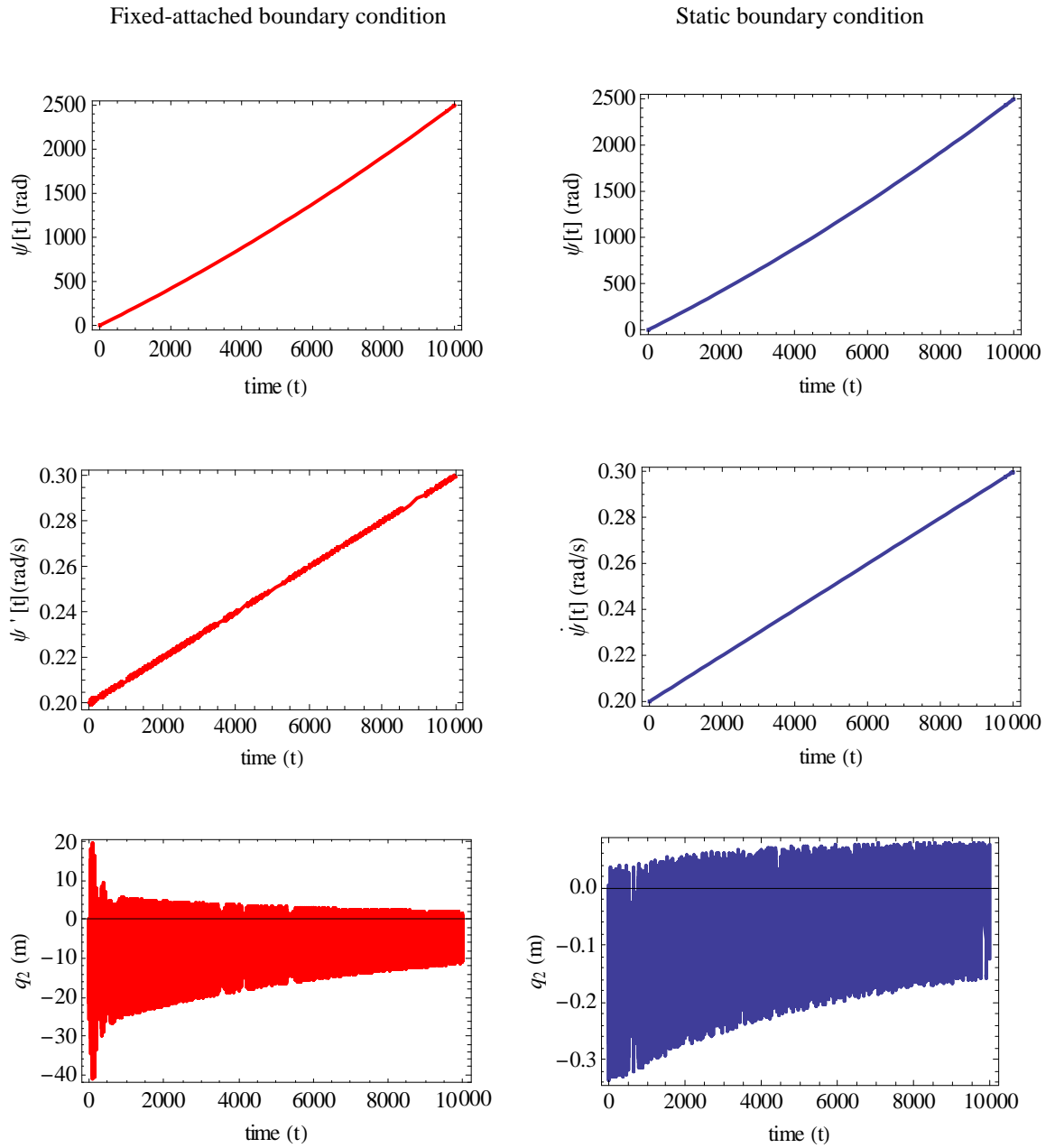


Figure 5.6 : Responses of motorised MMET on a circular orbit for the fixed-attached boundary condition model and the static boundary condition model

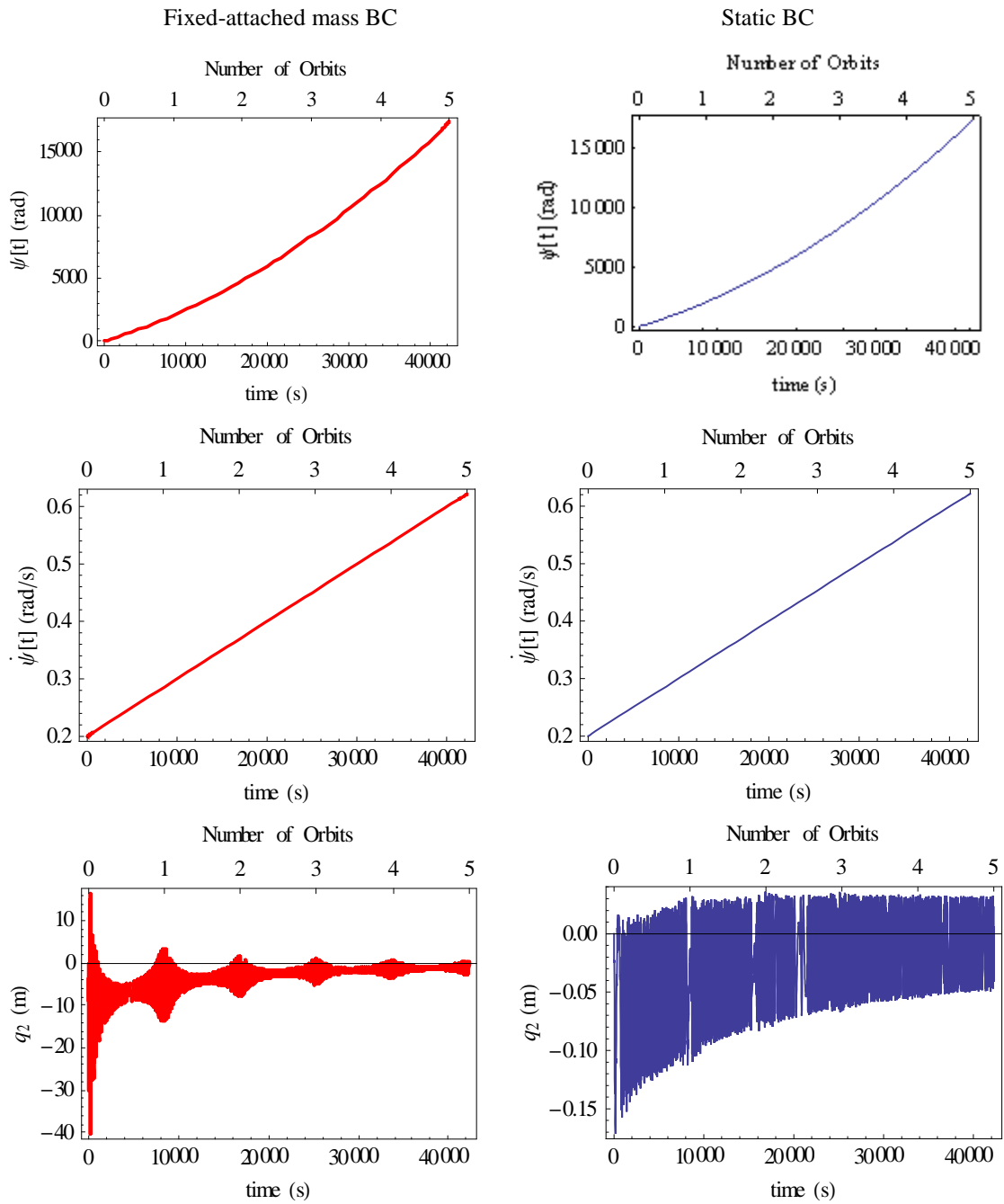


Figure 5.7 : Responses of the motorised MMET on an elliptical orbit for the fixed-attached boundary condition model and static boundary condition model

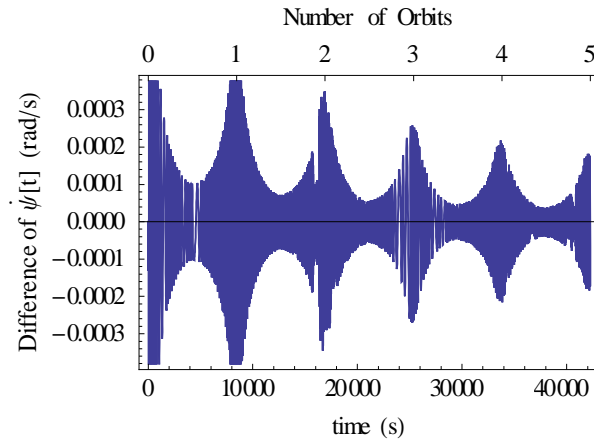


Figure 5.8 : Difference between the angular velocity for the tether with a fixed-attached mass boundary condition and static boundary condition

5.2.3 Comparative study of the natural frequency

The different boundary condition cases give different frequency responses of the model. The frequency equation for the static boundary condition is given by,

$$\Omega_v = n\pi \sqrt{\frac{T}{\rho L^2}}, \quad n=1,2,3\dots \quad (5.23)$$

and for the fixed-attached mass boundary condition, the frequency ω_v is given by equation (5.15).

Based on these two equations, it shows that for the first mode ($n=1$), the value of Ω_v is higher than ω_v in the calculation for the same parameter values of the MMET. Figure 5.9 shows the frequency values for both models in the unmotorised condition and it shows that $\Omega_v > \omega_v$.

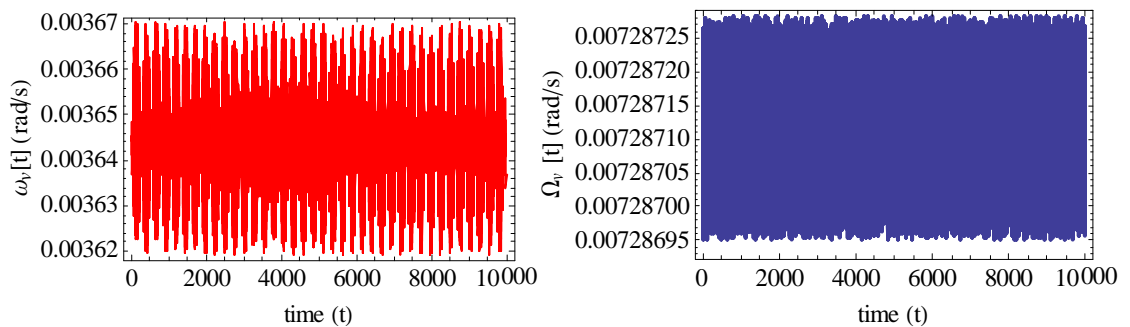


Figure 5.9 : Natural frequency for the first mode shape for the tether with a fixed-attached boundary condition model (red) and a static boundary condition model (blue)

5.3 Boundary Conditions where Both Ends of the Subspan terminate in Masses.

The derivation of this boundary condition is based on derivation of string model by Cartmell (1999).

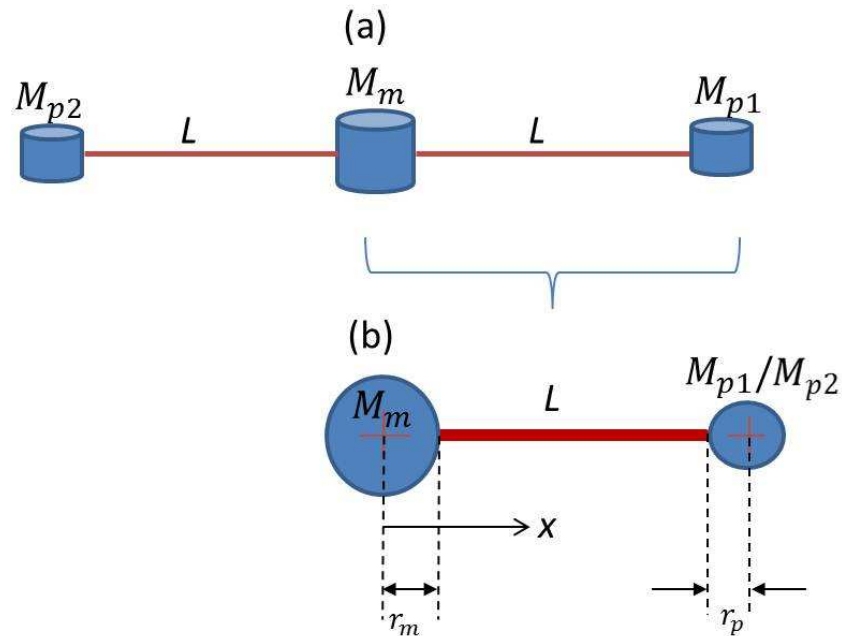


Figure 5.10 : Schematic Diagram of masses connected to the tether sub-span

Based on Figure 5.10, the boundary conditions for the tether in space in the transverse direction are given by,

$$T(r_m) \frac{\partial v}{\partial x} \Big|_{x=r_m} = -M_m \dot{v} \Big|_{x=r_m} \quad (5.24)$$

$$T(L - r_p) \frac{\partial v}{\partial x} \Big|_{x=L-r_p} = -M_p \dot{v} \Big|_{x=L-r_p} \quad (5.25)$$

T refers to the tension from the centripetal force acting on the tether. The central facility, M_m feels an outward pull due to the reaction of the centripetal load, whereas the tension of the tether at the connection to M_p is almost zero. From Figure 5.10, the position of an arbitrary point along the length of the tether is given by x , and at the connection to M_p the position is actually given by $L - r_p$ where r_p is the radius of the payload. Therefore, the tether tension at $x = r_m$ and $x = L - r_p$ given by,

$$T(r_m) = (L - r_m)\dot{\psi}^2 \left(\frac{\rho A(L - r_m)}{2} + M_p \right) \quad (5.26)$$

and

$$\begin{aligned} T(L - r_p) &= (L - L + r_p)\dot{\psi}^2 \left(\frac{\rho A(L - L + r_p)}{2} + M_p \right) \\ &= r_p\dot{\psi}^2 \left(\frac{\rho A r_p}{2} + M_p \right) \end{aligned} \quad (5.27)$$

Equations (5.26) and (5.27) give the boundary conditions in the transverse direction for the tether as,

$$(L - r_m)\dot{\psi}^2 \left(\frac{\rho A(L - r_m)}{2} + M_p \right) \frac{\partial v}{\partial x} \Big|_{x=r_m} = -M_m \dot{v} \Big|_{x=r_m} \quad (5.28)$$

$$r_p\dot{\psi}^2 \left(\frac{\rho A r_p}{2} + M_p \right) \frac{\partial v}{\partial x} \Big|_{x=L-r_p} = -M_p \dot{v} \Big|_{x=L-r_p} \quad (5.29)$$

The general solution for the free vibration of a string are given by equations (3.34) and (3.35) in Chapter 3, and the first and second derivatives of the general solution are given by equations (5.7) and (5.8). Substitutions of (5.7) into (5.24) and equation (5.8) into (5.25) give the boundary conditions at $x = r_m$ in the transverse direction as,

$$T(r_m) \frac{A_v \omega_v}{c} = M_m \omega_v^2 B_v \quad (5.30)$$

and at $x = L - r_p$

$$\begin{aligned} T(L - r_p) \left(\frac{A_v \omega_v}{c} \cos \frac{\omega_v}{c} (L - r_p) - \frac{B_v \omega_v}{c} \sin \frac{\omega_v}{c} (L - r_p) \right) = \\ M_p \omega_v^2 \left(A_v \sin \frac{\omega_v}{c} (L - r_p) + B_v \cos \frac{\omega_v}{c} (L - r_p) \right) \end{aligned} \quad (5.31)$$

Substituting equations (5.26) into (5.30), and (5.27) into (5.31), and rearranging the equations, lead to the following equations for the transverse direction,

$$A_v(L-r_m)\dot{\psi}^2\left(\frac{\rho A(L-r_m)}{2}+M_p\right)\frac{\omega_v}{c}-B_vM_m\omega_v^2=0 \quad (5.32)$$

$$\begin{aligned} A_v\left(r_p\dot{\psi}^2\left(\frac{\rho Ar_p}{2}+M_p\right)\frac{\omega_v}{c}\cos\frac{\omega_v(L-r_p)}{c}-M_p\omega_v^2\sin\frac{\omega_v(L-r_p)}{c}\right)- \\ B_v\left(r_p\dot{\psi}^2\left(\frac{\rho Ar_p}{2}+M_p\right)\frac{\omega_v}{c}\sin\frac{\omega_v(L-r_p)}{c}+M_p\omega_v^2\cos\frac{\omega_v(L-r_p)}{c}\right)=0 \end{aligned} \quad (5.33)$$

Equations (5.32) and (5.33) represent a system of two pairs of homogenous algebraic equations in the two unknown constants A_v and B_v . These equations can be rewritten in matrix form as;

$$\begin{aligned} \left[\begin{array}{c} (L-r_m)\dot{\psi}^2\left(\frac{\rho A(L-r_m)}{2}+M_p\right)\frac{\omega_v}{c} \\ \left(r_p\dot{\psi}^2\left(\frac{\rho Ar_p}{2}+M_p\right)\frac{\omega_v}{c}\cos\frac{\omega_v(L-r_p)}{c}-M_p\omega_v^2\sin\frac{\omega_v(L-r_p)}{c}\right) \\ -\left(r_p\dot{\psi}^2\left(\frac{\rho Ar_p}{2}+M_p\right)\frac{\omega_v}{c}\sin\frac{\omega_v(L-r_p)}{c}+M_p\omega_v^2\cos\frac{\omega_v(L-r_p)}{c}\right) \end{array} \right] \begin{Bmatrix} A_v \\ B_v \end{Bmatrix} = \begin{Bmatrix} 0 \\ 0 \end{Bmatrix} \end{aligned} \quad (5.34)$$

Equations (5.34) have the same determinant of the coefficient matrix, and this is set equal to zero for a nontrivial solution of A_v and B_v to obtain the frequency equation as,

$$\begin{aligned} -(L-r_m)\dot{\psi}^2\left(\frac{\rho A(L-r_m)}{2}+M_p\right)\frac{\omega_v}{c}\left(r_p\dot{\psi}^2\left(\frac{\rho Ar_p}{2}+M_p\right)\frac{\omega_v}{c}\sin\frac{\omega_v(L-r_p)}{c}\right. \\ \left.+M_p\omega_v^2\cos\frac{\omega_v(L-r_p)}{c}\right)+M_m\omega_v^2\left(r_p\dot{\psi}^2\left(\frac{\rho Ar_p}{2}+M_p\right)\frac{\omega_v}{c}\cos\frac{\omega_v(L-r_p)}{c}\right. \\ \left.-M_p\omega_v^2\sin\frac{\omega_v(L-r_p)}{c}\right)=0 \end{aligned} \quad (5.35)$$

Solving equation (5.35) by using typical data for the MMET will give the Eigenvalues, and hence the natural frequencies corresponding to the normal modes as represented by $\xi(x)$. Equations (5.32) and (5.33) are two homogeneous linear equations that can be used to

determine the constants A_v and B_v in equation (3.34). These equations can be rearranged as below:

$$A_v = c_1 B_v \text{ and } A_v = c_2 B_v \quad (5.36),(5.37)$$

where

$$c_1 = \frac{M_m \omega_v^2}{(L - r_m) \dot{\psi}^2 \left(\frac{\rho A (L - r_m)}{2} + M_p \right) \frac{\omega_v}{c}} \quad (5.38)$$

and

$$c_2 = \frac{\left(r_p \dot{\psi}^2 \left(\frac{\rho A r_p}{2} + M_p \right) \frac{\omega_v}{c} \sin \frac{\omega_v (L - r_p)}{c} + M_p \omega_v^2 \cos \frac{\omega_v (L - r_p)}{c} \right)}{\left(r_p \dot{\psi}^2 \left(\frac{\rho A r_p}{2} + M_p \right) \frac{\omega_v}{c} \cos \frac{\omega_v (L - r_p)}{c} - M_p \omega_v^2 \sin \frac{\omega_v (L - r_p)}{c} \right)} \quad (5.39)$$

Computer algebra is used to verify that $c_1 \approx c_2$ as implied in equations (5.36) and (5.37) under the conditions explored here. Therefore, it is sufficient to only solve one of the equations, either (5.38) or (5.39), in order to obtain the mode shape functions. Rearranging leads to an equation for the modes, this can be written as,

$$\xi(x) = B_v \left[\cos \frac{\omega_v}{c} x + \gamma_v \sin \frac{\omega_v}{c} x \right] \quad (5.40)$$

where γ_v is defined as,

$$\gamma_v = \frac{M_m \omega_v^2}{(L - r_m) \dot{\psi}^2 \left(\frac{\rho A (L - r_m)}{2} + M_p \right) \frac{\omega_v}{c}} \quad (5.41)$$

5.3.1 Relationship between the angular tether spin velocity and the natural frequency

A parametric study of the nonlinear dynamical model uncovers a relationship between the angular spin velocity of the tether; the natural frequencies in free, undamped vibration; and

the specific chosen mode shape of the system. This relationship is defined by the following equation,

$$B_v = \frac{\dot{\psi}^2}{k} A_v \quad (5.42)$$

where k is a constant given by

$$k = \frac{M_m \omega_v^2}{L \left(\frac{\rho A L}{2} + M_p \right) \frac{\omega_v}{c}} \quad (5.43)$$

From equation (5.42) it can be shown that for $\dot{\psi} = 0$, B_v is equal to zero and consequently A_v become infinity as zero value of $\dot{\psi}$ divided with zero value of B_v . This also leads to a natural frequency equation from (5.35) which becomes,

$$\omega_v^4 \sin\left(\frac{\omega_v L}{c}\right) M_m M_p = 0 \quad (5.44)$$

for which $c = \sqrt{\frac{T}{\rho}}$ and the tension T is given by,

$$T = (L - r_p) \dot{\psi}^2 \left(\frac{\rho A (L - r_p)}{2} + M_p \right) \quad (5.45)$$

For $\dot{\psi} = 0$, the value of c and therefore equation (5.45) are equal to zero. In order to satisfy equation (5.35), the frequency ω_v has to be zero, as the value of c in that equation is zero. Therefore, equation (3.34) is satisfied when $\dot{\psi} = 0$ and gives $B_v = 0$, A_v is in infinity, and $\omega_v = 0$, for which the mode shape functions $\xi(x)$ are equal to zero.

Unless stated otherwise, all the results were generated using the default data. The linear relationship between the angular velocity and the natural lateral and transverse oscillation frequency is plotted in Figure 5.11 using equation (5.35).

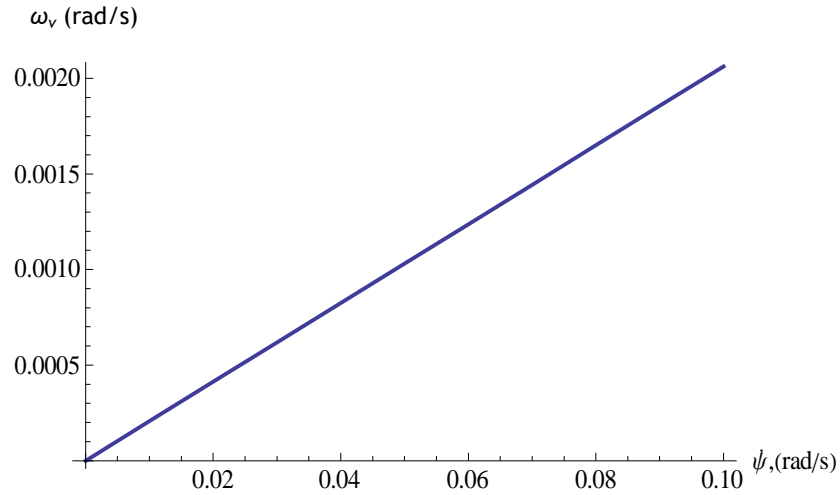


Figure 5.11 : Relationship between transverse oscillation frequency and angular velocity

5.3.2 Mode shapes

The vibration frequencies of two geometrical cases (where the tether length is expressed as $(L - r_p)$ as defined in section 5.3 and then as L) are then compared with the vibration frequencies of the tether with both ends fixed. Table 5.2 shows the first to the fifth natural frequency for each condition, and the five mode shapes for these three conditions are plotted in Figure 5.12. The term “static BCs” in Table 5.2 and Figure 5.12 refers to the static boundary conditions.

Parameters	L (s^{-1})	$(L-r_p)$ (s^{-1})	Diff 1 (%)	Static BCs (s^{-1})	Diff 2 (%)
ω_1	0.0001823	0.0002062	13.12	0.0003644	99.90
ω_2	0.0005468	0.0005558	1.64	0.0007287	33.26
ω_3	0.0009114	0.0009168	0.60	0.0010931	19.94
ω_4	0.0012759	0.0012798	0.30	0.0014574	14.23
ω_5	0.0016404	0.0016435	0.18	0.0018217	11.05

Table 5.2 : Natural frequencies of three different conditions (Diff 1 is the percentage difference between the case of L and $(L-r_p)$ and Diff 2 between the cases of L and static boundary condition)

The natural frequencies calculated for the tether with fixed ends are given by equation (5.23). In comparison, the natural frequencies for the static boundary condition are higher than those for the dynamic boundary condition case. In the dynamic boundary condition

case, the use of $(L - r_p)$ increased the natural frequency of the system, as compared to the calculation using the full length of the sub-span given by L . This conforms intuitively to the physics of the tether, where the shorter tether has a higher natural frequency than the longer tether with the same load applied for both.

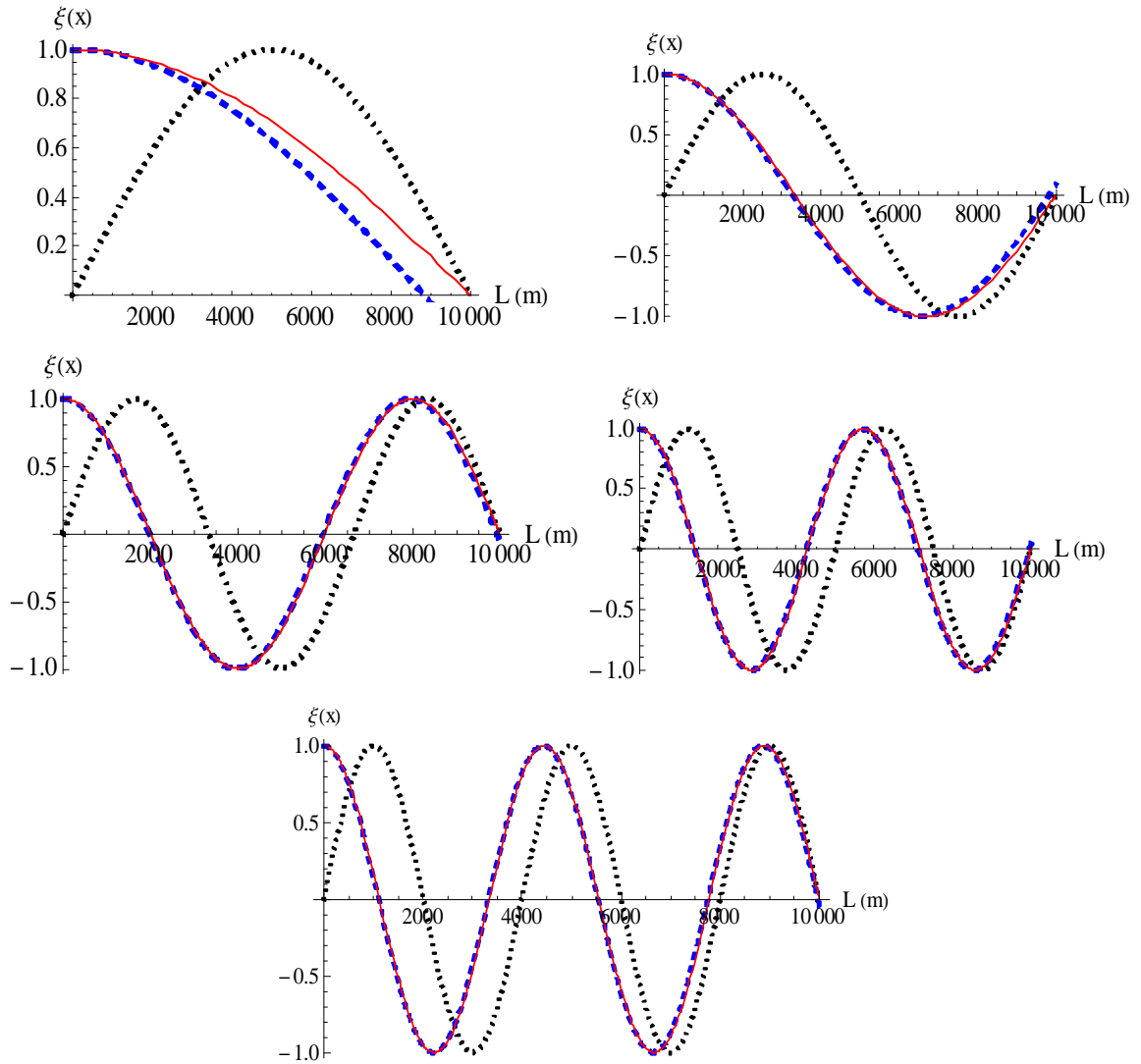


Figure 5.12 : The first five mode shapes for the L (red,line), $(L-r_p)$ (blue,dashed) and fixed end conditions (black, dotted).

5.3.3 Third order derivative of psi ($\ddot{\psi}$)

Equations (5.40) and (5.41) have been substituted into the energy equations to derive the equations of motion for the system.

The equations of motion for a circular orbit have been derived for two generalised coordinates: defining the angular displacement ψ , and the transverse displacement denoted by q_2 . The routine differentiation of the angular velocity, denoted by $\dot{\psi}$, in the kinetic and potential energy equations, and then further differentiation with respect to time in Lagrange's equation, gives a third order derivative of ψ , in the equations of motions for the system with dynamic boundary condition, as in Figure 5.10.

The study established that the third order derivative is just in ψ , and not in one of the actual generalised coordinates defining the vibration of the tether. This third order derivative of ψ physically refers to a jerk in the system, which should clearly be spurious for this tether problem. Therefore, ψ , should in the case be considered as a constant or very slowly varying quantity and not as a generalised coordinate.

5.3.3.1 Constant Value for Angular Velocity

When ψ is removed as a generalised coordinate, by substituting a constant value for angular velocity $\dot{\psi}$, into the Lagrangian model for transverse vibration, this appropriately reduces the complexity of the equation of motion. The source of excitation is now from the angular velocity, and the response is given by the vibration modes.

Figure 5.13 shows the responses of the tether for default values of the MMET parameters with $\dot{\psi} = 0.01$ rad/s and $\omega = 0.0126$ rad/s for a simulation time up to $t = 3000$ sec. The results show that the tether undergoes steady state oscillation in the transverse direction with a maximum amplitude of 40 m. In a longer period of simulation time, the amplitude remains unchanged, as shown in Figure 5.14.

The simulation results also show that the system is not sensitive to small changes ($q_2(0) < 1$) in initial conditions. Figure 5.15 shows the tether's responses at the initial condition $q_2(0) = 0.01, 0.1, \text{ and } 1.0$ metres and the difference are insignificant. But, for the different value of $\dot{q}_2(0)$ as shown in Figure 5.16, the responses show a significant difference in each of the initial condition with Figure 5.16(c) and 5.16(d) perhaps showing fewer higher harmonics when compared to the first two figures, 5.16(a) and 5.16(b). This shows that the tether needs a larger value of the initial condition of $q_2(0)$ to have a significant impact on the tether response.

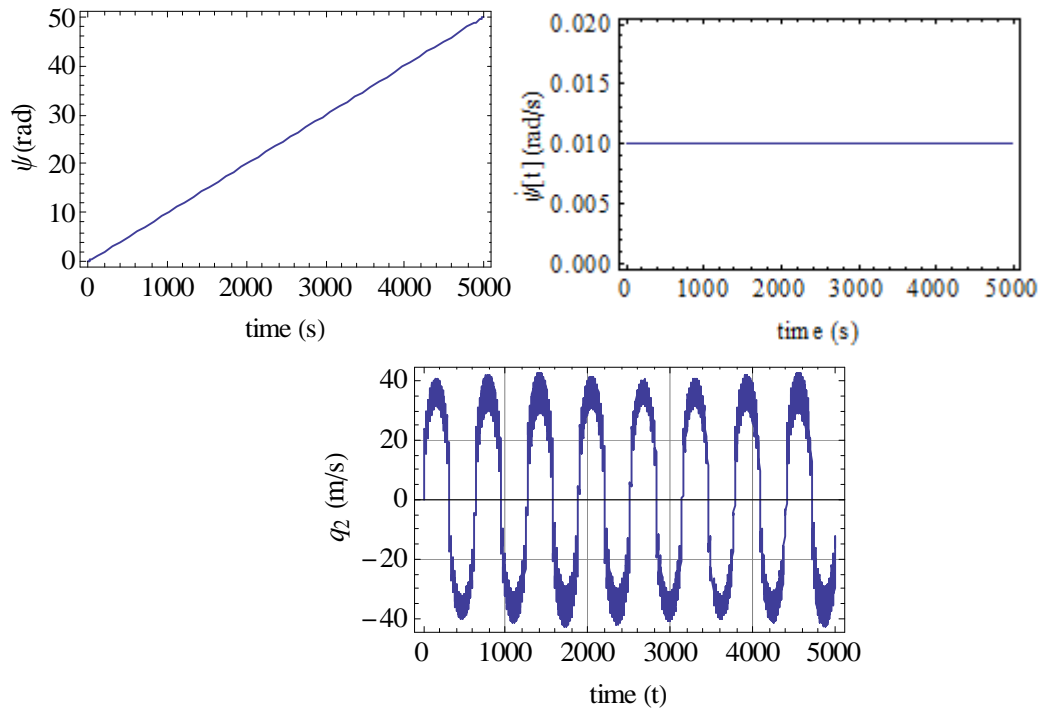


Figure 5.13 : Tether's response for $\dot{\psi} = 0.01$ rad/s, $\omega = 0.0126$ rad/s over 5000 sec

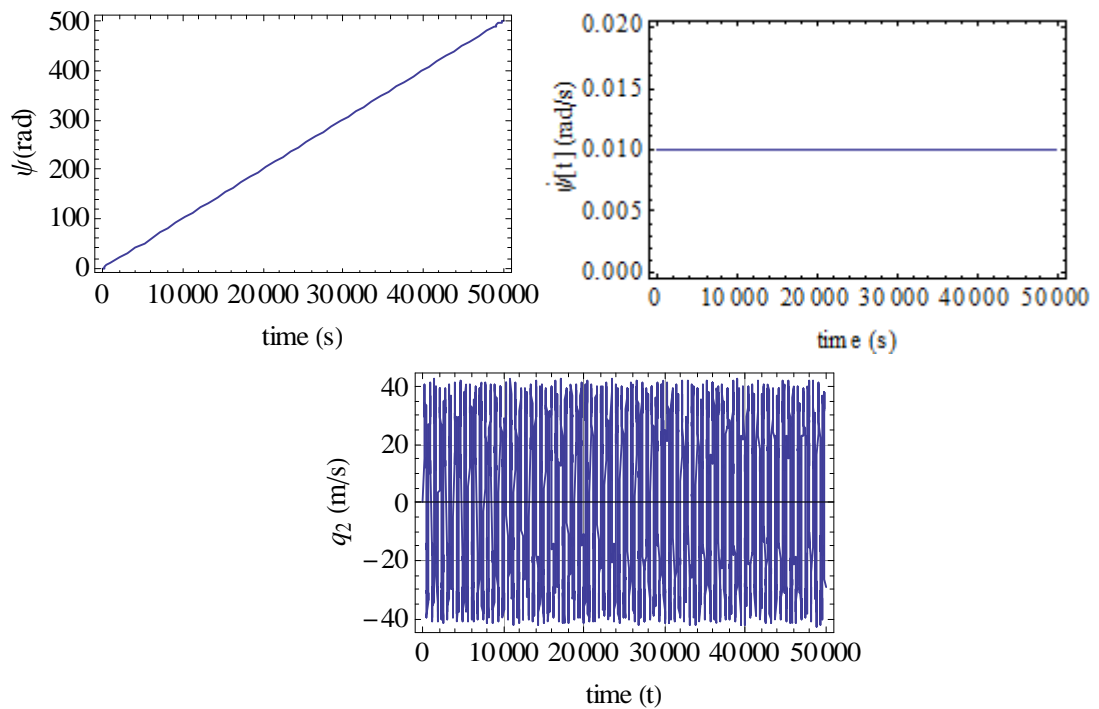


Figure 5.14 : Tether's response for $\dot{\psi} = 0.01$ rad/s, $\omega = 0.0126$ rad/s over 50000 sec

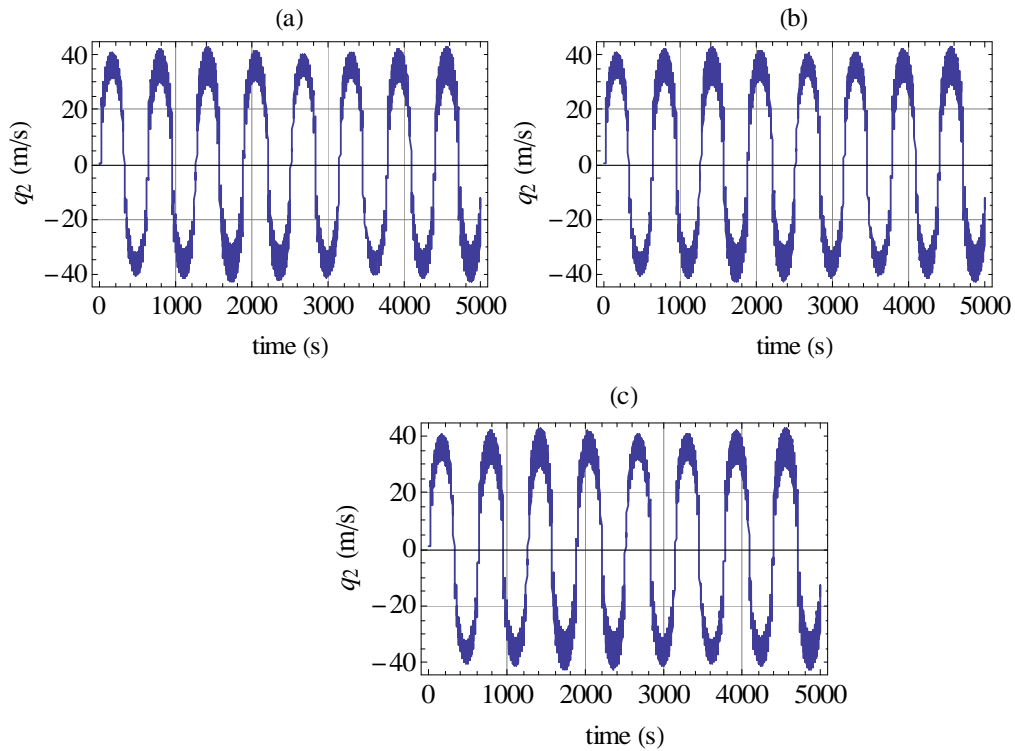


Figure 5.15 : Tether's responses with initial condition of q_2 at (a) 0.01 (b) 0.1 (c) 1.0 metre

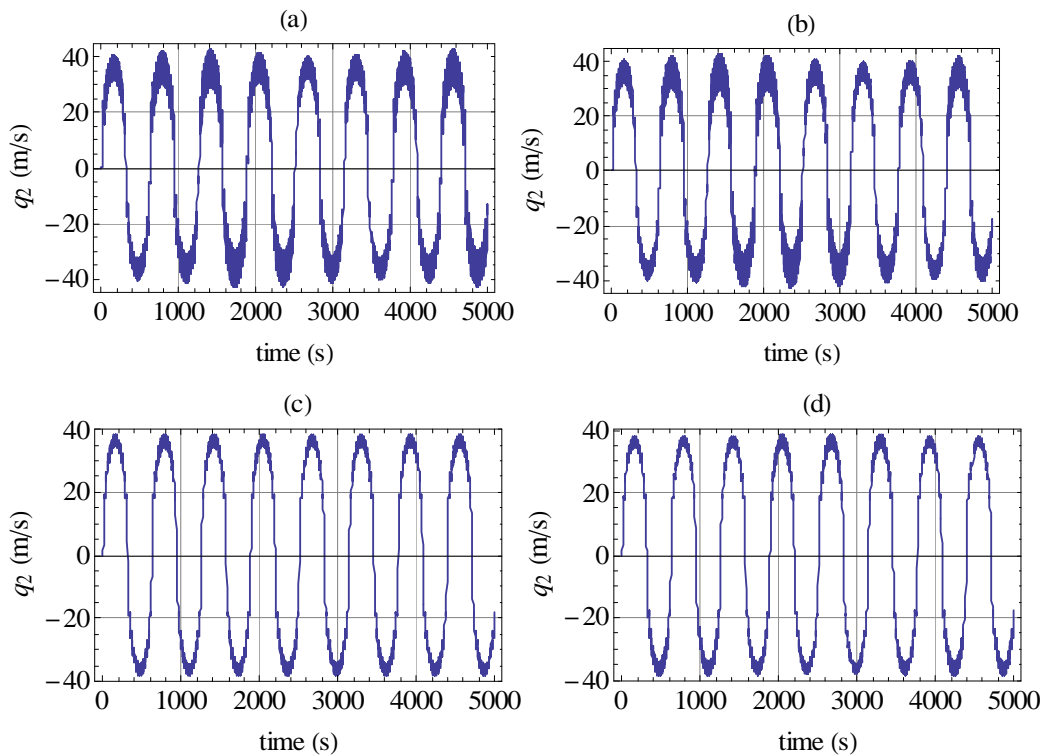


Figure 5.16 : Tether's responses with initial condition of $\dot{q}_2 = 0.01$ and at (a) 0.01 (b) 0.1 (c) 1.0 (d) 1.1 metres

By using a constant value for the angular velocity, the complexity of the equation of motion has been reduced, and a simulation to get the tether's response ran smoothly. This

means that the tether needs to be set to a desired velocity for the payload transfer from the start of the operation time and maintained at that for the duration of the simulation time (as compared to the normal operation of the tether, where the angular velocity will be increased gradually from zero to the desired velocity, and then the payload is released).

For the default value of the MMET, with the angular velocity at 0.062 rad/s, then on releasing the payload to the desired orbit the tether response is as shown in Figure 5.17.

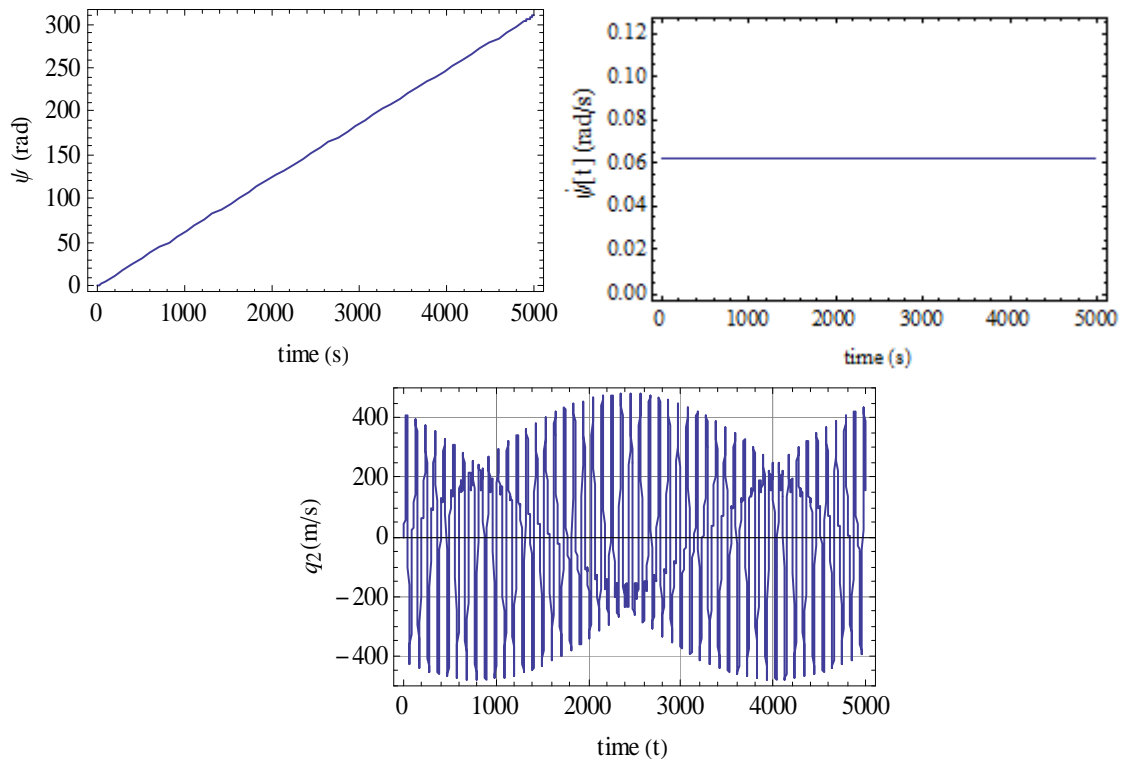


Figure 5.17 : Tether's response for an angular velocity of 0.062 rad/s

In order to get a better result, one needs to increase the working precision of the calculation of *Mathematica*TM simulation. The lower working precision is likely to have a round-off error in the calculations. For this study, the working precision is set to 20.

5.4 Mode Shape Equation for Axial vibration

The study continues with investigation of longitudinal vibration with both selected boundary conditions.

5.4.1 Case 1 : Fixed-Attached Mass Boundary condition

From Figure 5.18, the forces in longitudinal direction acting on the tether is given by following free body diagram,

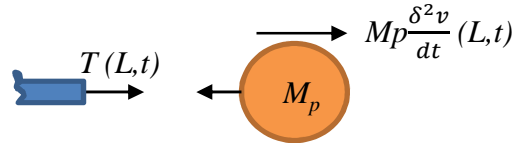


Figure 5.18 : Free body diagram of forces action in longitudinal direction.

Based on Figure 5.18, the boundary conditions for fixed- attached mass boundary condition in longitudinal direction at $x=0$ is given by,

$$u(0,t) = 0 \quad (5.46)$$

and at $x=L$, the boundary condition is

$$T(l - r_p) \frac{\partial u}{\partial x} + EA \frac{\partial u}{\partial x} \Big|_{x=l-r_p} = -M_p \ddot{u} \Big|_{x=l-r_p} \quad (5.47)$$

Noting that, $\frac{\partial u}{\partial x}$ in the first equation on the right hand side refers to angle made by the deflected string with the x axis. From Figure 5.2 the angle of deflection in axial direction is given by,

$$\frac{\partial u}{\partial x} \approx \cos \theta \quad (5.48)$$

and for small θ , $\cos \theta$ is equal to 1. Therefore, equation (5.47) becomes,

$$T(l - r_p) + EA \frac{\partial u}{\partial x} \Big|_{x=l-r_p} = -M_p \ddot{u} \Big|_{x=l-r_p} \quad (5.49)$$

Furthermore, the second equation on the right hand side in equation (5.49) represents the tensile force and that expression which relates to the stress, longitudinal rigidity and strain tensor in axial direction is given by,

$$P = \sigma A = EA\varepsilon(x) \quad (5.50)$$

Where $\varepsilon(x)$ is the strain tensor and defined by $\frac{\partial u}{\partial x}$ (Fung ,1994).

The nth mode of vibration presented as separation of variables in the u direction given by equation (3.22) and for the first mode approximation is given by equation (3.23) in Chapter 3. Rewriting the general solution given by equations (3.34) and (3.35) and the general solution for axial direction is given by equations below,

$$\phi(x) = A_u \sin \frac{\omega_u}{c} x + B_u \cos \frac{\omega_u}{c} x \quad (5.51)$$

$$q_1(t) = C_u \cos \omega_u t + D_u \sin \omega_u t \quad (5.52)$$

and leading to the similar equation (5.3) but expressing in axial direction gives,

$$u(x,t) = \left(A_u \sin \frac{\omega_u}{c} x + B_u \cos \frac{\omega_u}{c} x \right) (C_u \cos \omega_u t + D_u \sin \omega_u t) \quad (5.53)$$

Equation (5.46) reduces equation (5.53) to the following equation,

$$u(x,t) = \left(A_u \sin \frac{\omega_u}{c} x \right) (C_u \cos \omega_u t + D_u \sin \omega_u t) \quad (5.54)$$

and derivative of equation (5.54) gives,

$$\frac{\partial u}{\partial x} = A_u \frac{\omega_u}{c} \cos \frac{\omega_u x}{c} (C_u \cos \omega_u t + D_u \sin \omega_u t) \quad (5.55)$$

$$\frac{\partial^2 u}{\partial t^2} = -A_u \omega_u^2 \sin \frac{\omega_u x}{c} (C_u \cos \omega_u t + D_u \sin \omega_u t) \quad (5.56)$$

Substituting equation (5.55) and (5.56) into (5.47) at $x=L-r_p$ gives,

$$\begin{aligned} T(L-r_p) + EA \left(A_u \frac{\omega_u}{c} \cos \frac{\omega_u(L-r_p)}{c} (C_u \cos \omega_u t + D_u \sin \omega_u t) \right) = \\ -M_p - A_u \omega_u^2 \sin \frac{\omega_u(L-r_p)}{c} (C_u \cos \omega_u t + D_u \sin \omega_u t) \end{aligned} \quad (5.57)$$

Equation (5.57) has four unknowns which could not be solved with one equation only. Therefore, equation (5.52) has been simplified by reducing it into a harmonic solution (Rao, 2007) as the following equation,

$$q_1(t) = \sin \omega_u t \quad (5.58)$$

Rewritten equation (5.54) accordingly, gives

$$u(x,t) = \left(A_u \sin \frac{\omega_u}{c} x \right) \sin \omega_u t \quad (5.59)$$

and the derivatives of equation (5.59) are,

$$\frac{\partial u}{\partial x} = \left(A_u \frac{\omega_u}{c} \cos \frac{\omega_u}{c} x \right) \sin \omega_u t \quad (5.60)$$

$$\frac{\partial^2 u}{\partial t^2} = -A_u \omega_u^2 \sin \frac{\omega_u}{c} x (\sin \omega_u t) \quad (5.61)$$

Substituting equations (5.60), (5.61) and (5.26) into equation (5.49) at $x = L-r_p$ gives,

$$\begin{aligned} r_p \dot{\psi}^2 \left(\frac{\rho A r_p}{2} + M_p \right) + EA \left(A_u \frac{\omega_u}{c} \cos \frac{\omega_u(L-r_p)}{c} \right) \sin \omega_u t \\ = M_p A_u \omega_u^2 \sin \frac{\omega_u(L-r_p)}{c} (\sin \omega_u t) \end{aligned} \quad (5.62)$$

Rearranging equation (5.62) gives,

$$A_u = -\frac{r_p \psi^2 \left(\frac{\rho A r_p}{2} + M_p \right)}{\sin \omega_u t \left(EA \left(A_u \frac{\omega_u}{c} \cos \frac{\omega_u (L - r_p)}{c} \right) \right) + M_p \omega_u^2 \sin \frac{\omega_u (L - r_p)}{c}} \quad (5.63)$$

Substituting equation (5.63) into equation (5.59) presents the mode shape function as,

$$\phi(x) = -\frac{r_p \psi^2 \left(\frac{\rho A r_p}{2} + M_p \right)}{\sin \omega_u t \left(EA \left(A_u \frac{\omega_u}{c} \cos \frac{\omega_u (L - r_p)}{c} \right) \right) + M_p \omega_u^2 \sin \frac{\omega_u (L - r_p)}{c}} \sin \frac{\omega_u}{c} x \quad (5.64)$$

5.4.2 Case 2 : Boundary condition when both ends of sub-span terminate in masses

In this case, the free body diagram is given by the following figure:

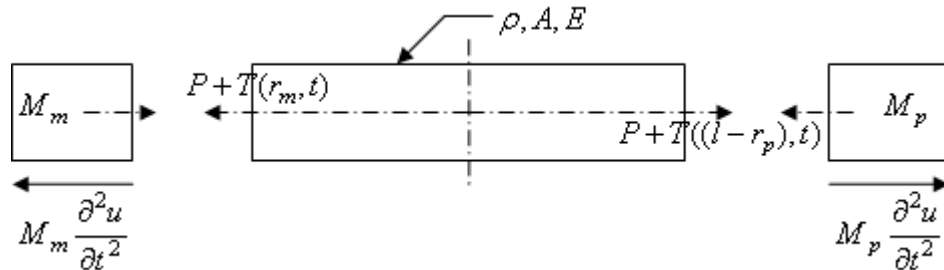


Figure 5.19 : Free body diagram of acting forces in axial direction for mass-mass boundary condition

$$T(r_m) + EA \frac{\partial u}{\partial x} \Big|_{x=r_m} = -M_m \ddot{u} \Big|_{x=r_m} \quad (5.65)$$

$$T(l - r_p) + EA \frac{\partial u}{\partial x} \Big|_{x=l-r_p} = -M_p \ddot{u} \Big|_{x=l-r_p} \quad (5.66)$$

Substitution of equations (5.55) and (5.57) and centripetal force equation in equation (5.27) into equations (5.65) and (5.66) gives,

$$\begin{aligned}
& (l - r_m)\dot{\psi}^2 \left(\frac{\rho A(l - r_m)}{2} + M_p \right) + EA \frac{\omega_u}{c} \left(A_u \cos \frac{\omega_u}{c} r_m - B_u \sin \frac{\omega_u}{c} r_m \right) \sin \omega_u t = \\
& M_m \omega^2 \sin \omega t \left(A_u \sin \frac{\omega_u}{c} r_m + B_u \cos \frac{\omega_u}{c} r_m \right)
\end{aligned} \tag{5.67}$$

$$\begin{aligned}
& r_p \dot{\psi}^2 \left(\frac{\rho A r_p}{2} + M_p \right) + EA \frac{\omega_u}{c} \left(A_u \cos \frac{\omega_u(l - r_p)}{c} - B_u \sin \frac{\omega_u(l - r_p)}{c} \right) \sin \omega_u t = \\
& M_p \omega^2 \sin \omega t \left(A_u \sin \frac{\omega_u(l - r_p)}{c} + B_u \cos \frac{\omega_u(l - r_p)}{c} \right)
\end{aligned} \tag{5.68}$$

Rearranged equation (5.67) and (5.68) gives,

$$\begin{aligned}
& A_u \sin \omega t \left(EA \frac{\omega_u}{c} \cos \frac{\omega_u}{c} r_m - M_m \omega_u^2 \sin \frac{\omega_u}{c} r_m \right) \\
& - B_u \sin \omega_u t \left(EA \frac{\omega_u}{c} \sin \frac{\omega_u}{c} r_m + M_m \omega^2 \cos \frac{\omega_u}{c} r_m \right) + (l - r_m)\dot{\psi}^2 \left(\frac{\rho A(l - r_m)}{2} + M_p \right) = 0
\end{aligned} \tag{5.69}$$

$$\begin{aligned}
& A_1 \sin \omega t \left(EA \frac{\omega}{c} \cos \frac{\omega(l - r_p)}{c} - M_m \omega^2 \sin \frac{\omega(l - r_p)}{c} \right) - B_1 \sin \omega t \left(EA \frac{\omega}{c} \sin \frac{\omega(l - r_p)}{c} \right. \\
& \left. + M_m \omega^2 \cos \frac{\omega(l - r_p)}{c} \right) + r_p \dot{\psi}^2 \left(\frac{\rho A r_p}{2} + M_p \right) = 0
\end{aligned} \tag{5.70}$$

The arbitrary constant of A_u and B_u are solved by using special function named *Solve* in *Mathematica*TM as given in Appendix D. Substitution of the results into mode shape function in equation 5.51 and applying the simplification gives,

$$\begin{aligned}
\Phi(x) = & \left(c C \sec \alpha (2M_p^2 (l - r_m) c \omega \sin \alpha + M_p (Al(2E \cos \alpha + \rho l c \omega \sin \alpha - \right. \\
& 2Ar_m (E \cos \alpha + \rho l c \omega \sin \alpha) + \rho A c \omega r_m^2 \sin \alpha - 2r_p (EA \cos \beta + c \omega \sin \beta) + \\
& \left. \rho A (EA l^2 \cos \alpha - EA r_m \cos \alpha (2l + r_m) - (EA \cos \beta + M_m c \omega \sin \beta) r_m^2)) \dot{\psi}^2 \right) / \\
& \left(2\omega (EA (EA \sin \alpha - M_p c \omega \cos \alpha) + M_m c \omega (EA \cos \alpha - M_p c \omega \sin \alpha)) \right)
\end{aligned} \tag{5.71}$$

where

$$c = \sqrt{\frac{T}{\rho}}, \alpha = \frac{\omega(x + r_p - L)}{c} \text{ and } \beta = \frac{\omega(x - r_m)}{c} \quad (5.72, 5.73, \text{ and } 5.74)$$

Both cases of boundary conditions presented here have produced a very complex mode shape equation inclusive with functions with regards of time term. The example of the mode shapes using equations (5.64) and (5.70) are shown in Figure 5.20 below using the default data with constant angular velocity given by $\dot{\psi} = 0.2 \text{ rad/s}$ and $\omega = 0.0000725 \text{ rad/s}$ for equation (5.64) and $\dot{\psi} = 0.1 \text{ rad/s}$ and $\omega = 0.004 \text{ rad/s}$ for equation (5.70) at $t = 1 \text{ s}$.

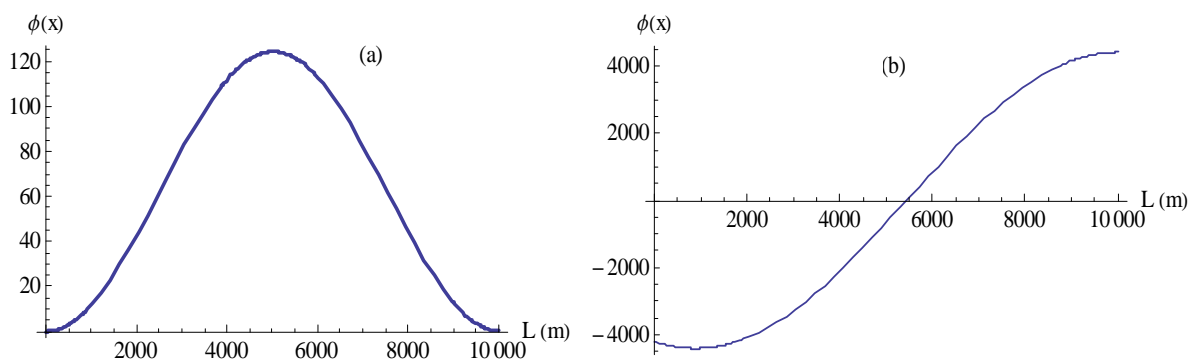


Figure 5.20 : Mode shape for : (a) fixed-attach mass boundary condition, (b) both end of sub-span terminate in masses boundary condition for $L = 10000 \text{ metre}$

5.5 Discussions

The equations of motions for the flexible tether govern by the boundary conditions in both conditions in equations (5.46), (5.47), (5.65) and (5.66) are long and complex. Due to the complexity of the mode shape function, the derivation of equations of motion need a very long computation time and also a powerful computer in term of its memory to execute integrations of the nonlinear ordinary differential equations. The equations of motions were integrated in *Mathematica*TM using a special computer server that has 20GB of RAM, but failed to execute after 10 hours of simulation due to reported low memory errors.

The equation of motion for fixed-mass boundary condition is given in Appendix E. The mode shape function for boundary condition where both ends of the sub-span terminate in masses as in equation (5.70) is more complex than equation (5.63) makes the computation inexecutable with the current single unit computers's specification. A test run was conducted and the integrations were terminated due to insufficient memory of a unit computer.

In order to overcome the problem, it is suggested to study the longitudinal vibration of the flexible tether by using the simplest model in example as presented by the author in Chapter 2. The other option is to develop a parallel computing method where a number of computers will work together to form a bigger memory to run these complex equations. But, this option is subjected to the availability of the software and hardware to set up the parallel system.

A numbers of literatures up to author's knowledge are using simple boundary conditions and some of them abandon the spinning phenomena in deriving the equations of motions. The study by Misra *et al.* (1986) in three dimensional vibration of tethered satellite system were using static boundary condition for transverse vibration, and fixed-attached mass boundary condition for analysis of the longitudinal vibration. However, the model was only including the aerodynamics force and the equations of motion derived for non-spinning tether. The derivation of equations of motion by Misra *et al.* (1986) were using variational formula and the results of tether's simulation have shown that the longitudinal strain was dependent on the transverse displacement through the nonlinear term in the equations of motion. Luongo and Vestroni (1994), Kokubun and Fujii (1996) and Misra and Cohen (2009) all applied fixed-attached mass boundary condition in deriving the equations of motion for their non-spinning tether model. The study of spinning tether by Min *et al.* (1999) has different spinning axis as compared to the model used in this thesis. In that study, Min *et al.* (1999) model's was assumed to spin about the tether axis and they found that the longitudinal modes have higher frequency than the transverse mode and not significantly affected by variation of the nominal tension.

The study of longitudinal vibration for the rod, bar or beam that spin around the centre of mass are a good basis in studying the longitudinal vibration of the tether. A study by Shum and Entwistle (2006) on the whirling rod that has axis of rotation as in Figure 5.21, has proposed that the tensile force is equal to the centripetal force derived from the physical law similar to equation (5.50) , given by,

$$EA\varepsilon(x) = \int_x^L \rho A(x+u)\Omega^2 dz \quad (5.75)$$

where $\varepsilon(x)$ is the strain tensor and Ω is the angular velocity.

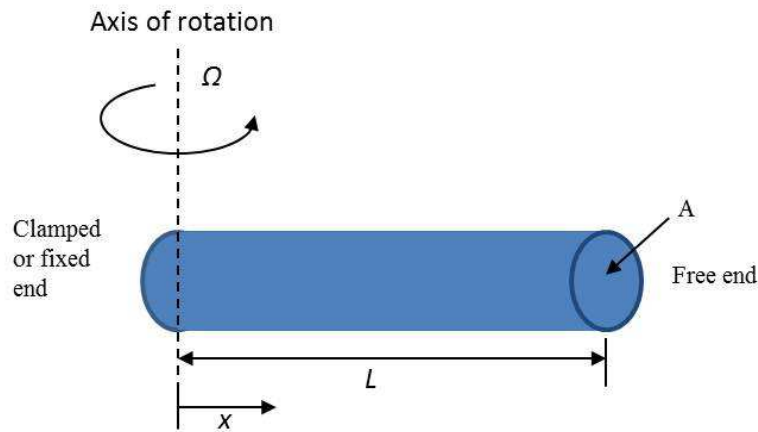


Figure 5.21 : Geometric configuration of a statically rotating about the axis of rotation, (Shum and Entwistle, 2006)

In this current study, a quantitative analysis has been carried out to look for relations between the centripetal force and the tensile force. The calculations are made by using the default tether data with $\dot{\psi} = 0.1 \text{ rad/s}$. Table 5.3 shows the comparison of the calculation's results for the force acting on the tether using equations (5.26), (5.27) and (5.50).

Positions (m)	Centripetal Force (N)	Tensile Force (N)
$x = r_m$,	130465 N	-130454 N
$x = l - r_p$	5.00008 N	-7.96144 N

Table 5.3 : Total Centripetal force and tensile force at $x = r_m$, and $x = l - r_p$

The results show that both forces are having almost the same values but in different direction (indicated by negative sign). This suggests that the tensile force is the reaction force to the centripetal force which agrees with equation (5.75) given by Shum and Entwistle (2006). Therefore, applying the relationship between centripetal force and tensile force in equation (5.75) on the fixed-mass boundary condition for longitudinal vibration at $x = l - r_p$, gives,

$$T(l - r_p) \left. \frac{\partial u}{\partial x} \right|_{x=l-r_p} = -M_p \ddot{u} \Big|_{x=l-r_p} \quad (5.76)$$

and using the same procedure in deriving the mode shape as in section 5.5 gives,

$$\phi(x) = \frac{r_p \dot{\psi}^2 \left(\frac{\rho A r_p}{2} + M_p \right)}{M_p \omega_1^2 \sin \frac{\omega l}{c} (\sin \omega_1 t)} \sin \frac{\omega_1}{c} x \quad (5.77)$$

The derived equations of motion that substituted the mode shape function of equation 5.77 are also long and complex. The integration of this equation of motion using available computer is almost impossible as the program were terminated due to insufficient memory to execute the job. Therefore, this approach has been abandoned.

5.6 Conclusions

The selection of mode shapes and boundary conditions have significant influences on the global motion of the tether. This study shows measureable differences between the natural frequencies of the system with static boundary conditions, and dynamic boundary conditions. The physical parameters also contribute to the changes in the response of the tether. In this study, it has been found that the shorter length of the tether denoted by $(l - r_p)$ has a higher natural frequency as compared to the default length of the tether given by l . In addition, the natural frequency for the static boundary condition is higher than that for the dynamic boundary conditions.

The third order time derivative of ψ appeared due to the differentiation of the mode shape function in the kinetic energy equation and then operation within Lagrange's equations, which contributed adversely to the complexity of the Equations of motion. The $\dot{\psi}$ has since been taken as a constant, in order to remove the third order derivative of ψ . The tether's response has been studied, and the results of the simulation show potential for steady state oscillation in the transverse direction, and that the tether has less sensitivity to small changes in the initial condition of q_2 . The mode shape function of longitudinal vibration is more complex as compared to the transverse vibration. The study shows that the derived equations of motions were inexecutable and need higher memory to run the task. Therefore, it is suggested to study the longitudinal vibration with the simplest model.

Chapter 6

Dynamical System Analysis

6.1 Introduction

In this chapter, an analysis of the non-linear behaviour of a flexible tether has been conducted using dynamical system tools for the calculation of bifurcations, Poincaré mapping, and phase space phenomena, as started previously by Ziegler (2003) for representing the behaviour of the dumbbell tether system, and in this thesis for the flexible tether model. The influence of orbital parameters and the flexibility of the tether in the orbital motion have been investigated by exploring the boundaries between libration and tumbling, and therefore also the boundaries between regular and chaotic motion. This chapter also includes an analysis of the capability of the tether in generating useful velocity increments through orbit-spin coupling. Finally, the dynamics of coupled motion between the out-of-plane and orbital parameters are also uncovered. All the analyses are compared with those for the dumbbell tether to show the significance of the flexural effect on the tether motion.

6.2 Equations of Motions for Dynamical System Analysis

Ziegler (2003) showed an alternative method for expressing the equations of motion of MMET by expressing the dependent variables as a function of the orbit's true anomaly, θ with the assumption that the tether remain in a Keplerian orbit. The transformations from the time domain to the true anomaly for R , α , ψ , q_1 , q_2 , and q_3 , as based on the work of Ziegler (2003) are given by,

$$\dot{\psi} = \frac{d\psi}{d\theta} \frac{d\theta}{dt} = \dot{\theta}\psi' \quad (6.1)$$

$$\dot{\alpha} = \frac{d\alpha}{d\theta} \frac{d\theta}{dt} = \dot{\theta}\alpha' \quad (6.2)$$

$$\dot{q}_1 = \frac{dq_1}{d\theta} \frac{d\theta}{dt} = \dot{\theta}q_1' \quad (6.3)$$

$$\dot{q}_2 = \frac{dq_2}{d\theta} \frac{d\theta}{dt} = \dot{\theta}q_2' \quad (6.4)$$

$$\dot{q}_3 = \frac{dq_3}{d\theta} \frac{d\theta}{dt} = \dot{\theta} q_3' \quad (6.5)$$

where the prime here denotes differentiation with respect to the true anomaly and the first derivative of the true anomaly is,

$$\dot{\theta} = \sqrt{\frac{\mu(1 + e \cos \theta)}{R(\theta)^3}} \quad (6.6)$$

Therefore, the second derivatives of equations (6.1) is derived using the product rule of derivatives that gives,

$$\begin{aligned} \ddot{\psi} &= \frac{d}{dt}(\dot{\theta}\psi') \\ &= \dot{\theta} \cdot \frac{d\psi'}{dt} + \psi' \cdot \frac{d\dot{\theta}}{dt} \end{aligned} \quad (6.7)$$

where,

$$\frac{d\psi'}{dt} = \frac{d\psi'}{d\theta} \cdot \frac{d\theta}{dt} = \dot{\theta}^2 \psi'' \quad \text{and} \quad \frac{d\dot{\theta}}{dt} = \frac{d\dot{\theta}}{d\theta} \cdot \frac{d\theta}{dt} = \dot{\theta} \dot{\theta}' \psi' \quad (6.8), (6.9)$$

Substituting equation (6.8) and (6.9) into equation (6.7) gives the second derivatives of equation (6.1) as,

$$\ddot{\psi} = \frac{d}{dt}(\dot{\theta}\psi') = \dot{\theta}^2 \psi'' + \dot{\theta} \dot{\theta}' \psi' \quad (6.10)$$

Applying the same procedures in deriving equation (6.10) to equations (6.2) to (6.5) give the second derivatives with respect to the true anomaly as,

$$\ddot{\alpha} = \frac{d}{dt}(\dot{\theta}\alpha') = \dot{\theta}^2 \alpha'' + \dot{\theta} \dot{\theta}' \alpha' \quad (6.11)$$

$$\ddot{q}_1 = \frac{d}{dt}(\dot{\theta}q_1') = \dot{\theta}^2 q_1'' + \dot{\theta} \dot{\theta}' q_1' \quad (6.12)$$

$$\ddot{q}_1 = \frac{d}{dt}(\dot{\theta}q_1') = \dot{\theta}^2 q_1'' + \dot{\theta} \dot{\theta}' q_1' \quad (6.13)$$

$$\ddot{q}_3 = \frac{d}{dt}(\dot{\theta}\alpha') = \dot{\theta}^2 q_3'' + \dot{\theta}\dot{\theta}' q_3' \quad (6.14)$$

$$\ddot{\theta} = \frac{d}{dt}(\dot{\theta}) = \dot{\theta}\dot{\theta}' \quad (6.15)$$

The prime denotes differentiation with respect to the true anomaly and $R(\theta)$ and $\dot{\theta}'$ are given by,

$$R(\theta) = \frac{R_p(1+e)}{1+e\cos\theta} \quad (6.16)$$

$$\dot{\theta}' = -2e\sqrt{\frac{\mu}{R_p^3(1+e)^3}}(1+e\cos\theta)\sin\theta \quad (6.17)$$

Where e refers to orbit eccentricity and R_p refers to radius at perigee. Equation (6.16) is the trajectory equations derived from Kepler's First Law and relates the position and true anomaly and equation (6.17) refers to radial rate equation from Vallado (2004).

Substitution of equations (6.1) to (6.17), with the exception of equations (6.5) and (6.14), into equations (3.102), (3.105) and (3.106) gives the system of planar equations of motion for the in-plane angle, and the axial and transverse displacement with respect to true anomaly as,

$$\begin{aligned} & \frac{M_p LR\mu \sin\psi}{(L^2 + R^2 + 2LR\cos\psi)^{3/2}} + \frac{M_p LR\mu \sin\psi}{(L^2 - R^2 + 2LR\cos\psi)^{3/2}} + \left(\frac{5}{6}\rho AL^3 + \frac{4}{\pi}\rho AL^2 q_1 \right. \\ & \left. \rho ALq_1^2 + \rho ALq_2^2 + 2M_p L^2 + \frac{1}{2}M_m r_m^2 + M_p r_p^2 + \frac{1}{2}\rho ALr_T^2 \right) \left((\dot{\theta}\dot{\theta}') + (\dot{\theta}\dot{\theta}'\psi'' + \dot{\theta}^2\psi''') \right) \\ & + \left(\frac{4}{\pi}\rho AL^2 q_1 + 2\rho AL(q_1 q_1' + q_2 q_2') + \frac{4}{\pi}\rho AL^2 \dot{\theta}^2 q_1 \psi' + 2\rho AL(q_1 q_1' + q_2 q_2') \psi' \right) \dot{\theta}^2 \\ & - \rho ALq_2 (\dot{\theta}\dot{\theta}' q_1' + \dot{\theta}^2 q_1'') + \left(\frac{2}{\pi}\rho AL^2 + \rho ALq_1 \right) (\dot{\theta}\dot{\theta}' q_2'' + \dot{\theta}^2 q_2''') + \\ & - \sum_{i=1}^N \frac{(2i-1)\mu\rho AL^2 R \sin\psi}{2N^2 \left(R^2 + \frac{(2i-1)^2 L^2}{4N^2} - \frac{(2i-1)RL}{N} \cos\psi \right)^{3/2}} \\ & - \sum_{i=1}^N \frac{(2i-1)\mu\rho AL^2 R \sin\psi}{2N^2 \left(R^2 + \frac{(2i-1)^2 L^2}{4N^2} - \frac{(2i-1)RL}{N} \cos\psi \right)^{3/2}} = \tau \end{aligned} \quad (6.18)$$

$$\begin{aligned}
& \rho AL(\dot{\theta}\dot{\theta}'q_1' + \dot{\theta}^2q_1'') + \frac{AE_o\pi^2}{L}q_1 + \frac{15}{8L^3}T_o\pi^4q_1^3 + \left(\frac{3}{4L^3}\pi^4(T_o - AE_o)\right)q_1q_2^2 - \\
& \rho ALq_1(\dot{\theta}^2 - 2\dot{\theta}^2\psi') - \left(\rho ALq_1 + \frac{2\rho AL^2}{\pi}\right)(\dot{\theta}^2\psi''^2) - \rho AL(2q_2'\dot{\theta}^2 + q_2\dot{\theta}\dot{\theta}') - \\
& \left(\frac{4\rho AL^2}{\pi} - 2\rho ALq_2'\right)\psi'\dot{\theta}^2 - \rho ALq_2(\dot{\theta}\dot{\theta}'\psi' + \dot{\theta}^2\psi'') = 0
\end{aligned} \tag{6.19}$$

$$\begin{aligned}
& \rho AL(\dot{\theta}\dot{\theta}'q_2' + \dot{\theta}^2q_2'') + \frac{T_o\pi^2}{L}q_2 + \left(\frac{3}{8L^3}\pi^4(AE_o - T_o)\right)q_2^3 - \rho ALq_2(\dot{\theta}^2 + 2\dot{\theta}^2\psi'') \\
& - \rho ALq_2\dot{\theta}^2\psi''^2 + \left(\frac{3}{4L^3}\pi^4(T_o - AE_o)\right)q_1^2q_2 + \left(\frac{2\rho AL^2}{\pi} + \rho ALq_1\right)\dot{\theta}\dot{\theta}' \\
& + 2\rho ALq_1'(\dot{\theta} + \dot{\theta}\psi') + \left(\frac{2\rho AL^2}{\pi} + \rho ALq_1\right)(\dot{\theta}\dot{\theta}'\psi' + \dot{\theta}^2\psi'') = 0
\end{aligned} \tag{6.20}$$

The equations of motion with respect to the true anomaly for tethers in a three dimensional for five generalized coordinates given by $(q_k) = (\psi, \alpha, \gamma, q_1, q_2, q_3)^T$ are lengthy and are shown in Appendix F.

6.3 Numerical Methods

The equations of motions for the flexible model are far more complicated than the equations of motion for the rigid body tether, and are largely responsible for the high computational run-time. The dynamical analysis was carried out using special code written in Mathematica™. As the errors may arise during long computation times, the results were obtained by applying the Explicit Runge Kutta method within *NDSolve*, Mathematica™'s differential equation package.

6.3.1 Poincaré Map

The Poincaré map is named after Henri Poincaré (1854-1912) who developed it as a tool to visualize the flows in a phase space of more than two dimensions. The Poincaré map can be described as a discrete dynamical system which turns a continuous dynamical system into a discrete one by numerically integrating the governing equations of motions and periodically sampling the state variable. The map is constructed by sectioning the spiral orbits at a regular time interval and then projecting the point of intersections of the orbits at the section $x - \dot{x}$ on the plane. As such the intersected point, instead of the curves, are shown on the phase plane in a stroboscopic view, as illustrated in Figure 6.1, and the

system always has the same time span between intersections which is very useful for qualitative analysis. (Thomsen, 2003).

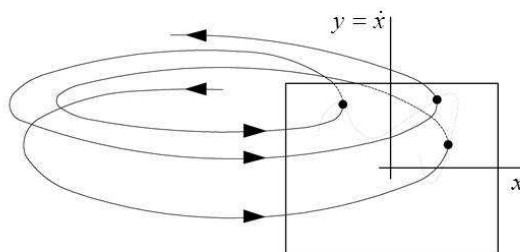


Figure 6.1 : A Poincaré section with an intersecting orbit. (Thomsen, 2003)

However, the Poincaré maps in this chapter sample the angular displacements and the velocity of the tether model every 2π of the true anomaly. Ziegler (2003) gave a justification for the selected method in which the perigee represents the point on the orbit in an orbital transfer application where the tether releases the payload. Therefore, the map gives information on the practicality of transferring a payload at the perigee of an elliptical orbit. The Poincaré map can easily distinguish between periodic and non-periodic motions, and can assist in the definition of chaotic motion. For a system that is oscillating at a single frequency it will periodically return to the same point in the phase space, and in the Poincaré map this will be as a single point. If there are two points, it is indicating period-2 motion and therefore period- n motion generally shows up as n points in the Poincaré map. Quasiperiodic motion manifests itself as infinitely many points filling up a closed curve, and only occurs when the ratio between the frequency of the system oscillation and the sampling frequency is irrational. Chaotic motion reveals itself as infinite number of orderly distributed points as the chaotic orbits visit all parts of the phase space.

6.3.2 Bifurcation

Qualitative changes in system behaviour may occur when the parameters of a system are varied. These changes can be shown by a bifurcation diagram. In this study, the bifurcation diagram is produced by sampling a point of the trajectory in the same way as for producing the Poincaré map, and the angular velocity is plotted with respect to the orbital eccentricity, with the same initial conditions. All bifurcation diagrams presented in this section are sampling the angular displacement with regards to the orbit eccentricity and integrated over 60 orbits. A shorter simulation time is due to the restriction of the available

computer capabilities to run integrations of the complex equations of motion. In order to avoid sudden truncations during simulation, the integration of the equations of motion have been discretised into a few segments, and each segment run on a single computer. At the end of simulation time all the results were collected from each computer and the data processed and analysed.

6.4 Transition from Libration to Spin

The dynamics of the tether are affected by the selection of the tether's physical properties, and also the orbital parameters. Ziegler (2003) has shown that the initial true anomaly has no significant influence on the long term stability boundary between libration and the spin of the dumbbell tether on an elliptical orbit. In studying the influence of eccentricity over the stability of the tether, Ziegler (2003) has simulated the dumbbell tether model over 30 orbits and observed the transition from libration and spin, and found that the tether may continuously liberate after the 30th orbit at certain eccentricities or commence tumbling even after completing numerous orbits.

In this study, the same methods are implemented to investigate the influence of eccentricity on the motion of a flexible tether. The result of integrating equations (6.18) over 35 orbits is shown in Figure 6.2, where the tether is continuously in libration with an eccentricity of 0.1. The tether may or may not continue to librate for an indefinite period of time, and thus maybe dependent on the initial conditions, and also the eccentricity, as shown in Figure 7.2 where Ziegler (2003) has also shown that the dumbbell tether starts to spin after the 10th orbit with an eccentricity of 0.32. However, the tether does not spin continuously and starts to liberate again when it reaches 25 orbits. This result is compared with the massive and flexible tether models in Figure 6.3 to show the influence of mass variation and tether flexibility in the long term stability.

In Figure 6.3, the dumbbell tether shows it has completed approximately 10 orbits before it starts to spin-up and this dumbbell tether has the longest libration period as compared with massive rigid tether model and the flexible tether. The flexible tether is shows that it has completed less than five orbits before the spinning motion is taken over and the massive tether model is in the libration phase for approximately 5 orbits. Therefore, it is shows here, the flexibility and the variation of mass influenced the tether's motion.

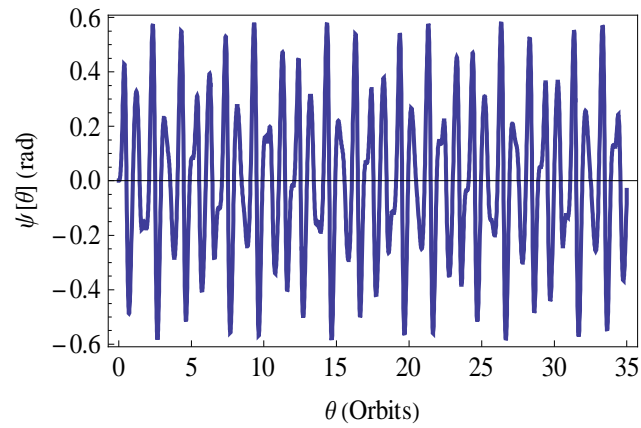


Figure 6.2 : Time history of angular displacement for the flexible model over 35 orbits with $e = 0.1$ and $\psi(0) = 0$ rad, and $\dot{\psi}(0) = 0$ rad/s.

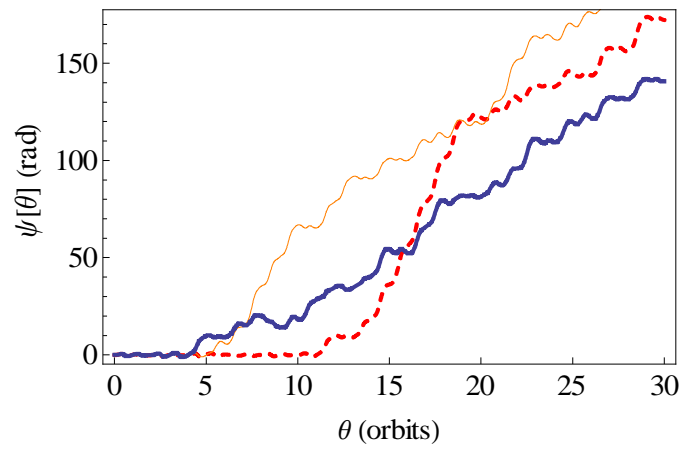


Figure 6.3 : Time history of angular displacement for the flexible model (blue,thick), the dumbbell tether (red, dashed) and the massive tether model (orange,thin) over 30 orbits with $e = 0.32$ and $\psi(0) = 0$ rad, and $\dot{\psi}(0) = 0$ rad/s.

Ziegler (2003) was plotted the long term boundary between libration and spin, and this type of plot was first been shown by Modi and Brereton (1966). The same approach is applied in this study to find the long term boundary between libration and spin for the flexible model. This plot is constructed by integrating equation (6.18) for a duration of 20 orbits for the given initial conditions and eccentricity. The tether simulation was set to start at perigee and Ziegler (2003) proved that the influence of the initial position on the tether dynamics was subsequently insignificant. When the tether reached the 20th perigee crossing the tether's angular displacement could be evaluated. According to Ziegler (2003), if the magnitude of the displacement is between $\pm\pi/2$ then the tether could be considered to be librating, and if not then the tether is in spinning motion. This algorithm is implemented by starting from zero eccentricity until the boundary between libration and spin is found for a given initial angular displacement. The process is repeated for the value of $\psi(0)$ between $\pm\pi/2$. For the study of the flexible tether model the numbers of orbits

taken for simulation are lower than those of Ziegler (2003) due to the complexity of the equations and the fact that it takes a longer computation time. Therefore, the numerical integrations are run for 20 orbits for both the rigid and the flexible bodies. The boundary between libration and spin is shown in Figure 6.4 where the plot for the flexible model is compared with the rigid body model.

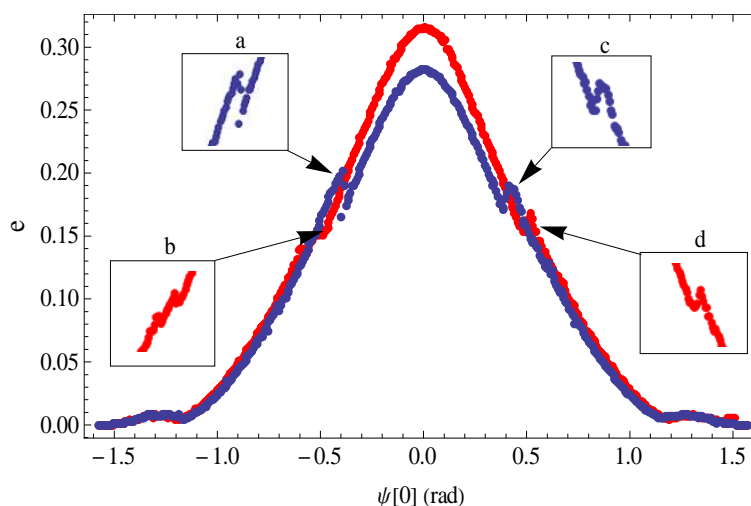


Figure 6.4 : Comparison of the effect of initial angular displacement on the long term stability boundary between the flexible tether (blue) and the rigid body tether (red) on an elliptical orbit. 300 points in the interval between $\pm \pi/2 \leq \psi(0) \leq \pi/2$ and integrating for 20 perigee passings.

The areas below the boundary plots refer to a region where tether has long-term stable motion. The largest stable region for the flexible model is for eccentricities between 0.28 to 0.29 and for the rigid body tether it is between 0.31 to 0.32, where the regions are where the onset of spin occurs. Once the angular displacement moves from the local vertical, the tether eccentricity reduced with the increase of initial angular displacement, and this makes the curves appear to be symmetrical about the local vertical.

The curves also have visible physical features that Ziegler (2003) named as “horns” for which in both models these occur near ± 0.5 rad and “humps” near $\pm \pi/2$ rad. However, the exact location of the horns in the flexible model are different as compared with those of the rigid body model as shown in Figure 6.4 (a),(b),(c), and (d). Even though the curves are generally symmetrical, the horns in Figure 6.4(c) and (d) are not a mirror image of (a) and (b). The difference can clearly be seen also in the magnified image of the humps shown in Figure 6.5 on the left hand side, and in Figure 6.6 on the right hand side, in the libration-spin curve for the flexible tether. The area around the left hump in Figure 6.5 uncovers the

discontinuous boundary points and the peaks and valleys in a complex manner, and the points do not form a smooth and continuous line as for $\psi(0) > -1.4$ rad.

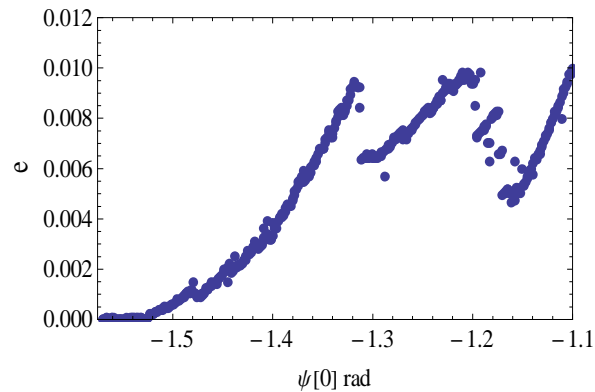


Figure 6.5 : Effect of initial angular displacement on the long-term stability boundary on an elliptical orbit for the flexible model. 500 points in the interval between $-1.57 \leq \psi(0) \leq -1.1$ rad and integrating for 20 perigee passings.

The right hand side hump as magnified in Figure 6.6 evidently shows no a mirror image of Figure 6.5 but the same features of discrete jumps, peaks and valleys which form the discontinuous boundary between $1.16 \leq \psi(0) \leq 1.45$, as compared with smooth lines for $\psi(0) > 1.6$. Hence, these two Figures show that the detail of the libration-spin boundary is not perfectly symmetrical. Therefore, the initial angular displacement is observed to have significant influence on the long term stability boundary. In addition, the difference between the results obtained between the flexible and rigid body tethers in Figure 6.3 shows that the flexibility of the tether has also quantitatively influenced the long term stability boundary.

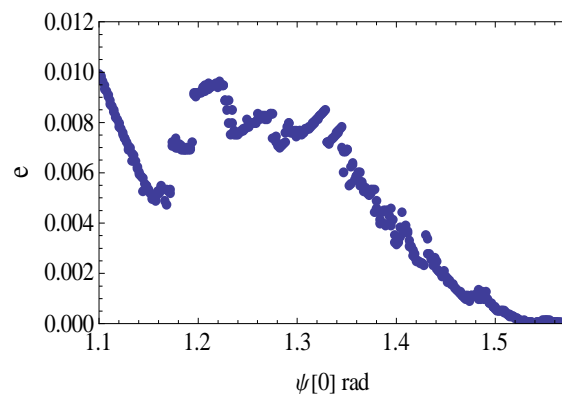


Figure 6.6 : Effect of initial angular displacement on the long-term stability boundary on an elliptical orbit for the flexible model. 500 points in the interval between $1.57 \leq \psi(0) \leq 1.1$ rad and integrating for 20 perigee passings.

The analysis continues with an investigation of the stability boundary of the flexible tether during first completed orbit in order to find the existence of the stability boundary for greater eccentricities than for those shown in Figure 6.4. The same algorithms were used in producing Figure 6.4 to 6.6, and were rerun with limitation to a single orbit between $1.57 \leq \psi(0) \leq 1.57$. The obtained results are plotted in Figure 6.7 and it is shown that the stability boundary is not as symmetrical as in Figure 6.4, and that the spin-libration boundary does exist for a higher eccentricity. The Figure shows a gradual increase of the boundary curve between $1.57 \leq \psi(0) \leq 0.58$ rad indicates that the system is still in stable condition with the increase of initial conditions and the eccentricities. However, between $0.32 \leq \psi(0) \leq 0.75$ the boundary curve is showing a declined trend as compared with previous region and then goes to a steep peak between $0.75 \leq \psi(0) \leq 1.1$ rad. A slump between $1.1 \leq \psi(0) \leq 1.57$ indicates that the single orbit motions of the flexible are more sensitive to the change of initial angular displacements higher than 1.0 rad.

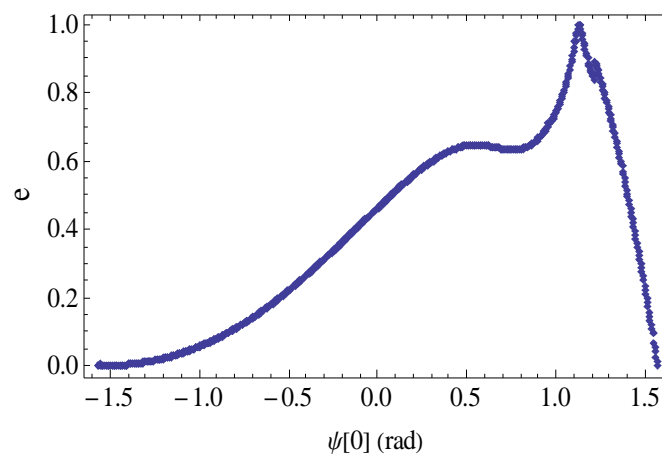


Figure 6.7 : Onset tether spin for the flexible model during first orbit between $-\pi/2 \leq \psi(0) \leq \pi/2$ with a step size e of 0.001

In general, the boundary curve represents the last steady-state tether libration, and the regions covered under the curve as mentioned by Ziegler (2003), can be either where the steady-state libration, or transient libration occurred. Figure 6.7 is qualitatively agrees with the results obtained by Ziegler (2003) shows in Figure 6.8 where both of the models shared the same trend of the boundary curve. In comparison, the difference is only depicted between $1.1 \leq \psi(0) \leq 1.3$ in Figure 6.7 and between $1.4 \leq \psi(0) \leq 1.57$ in Figure 6.8 where the sudden increase and decrease in the eccentricity occurs in difference region of both models.

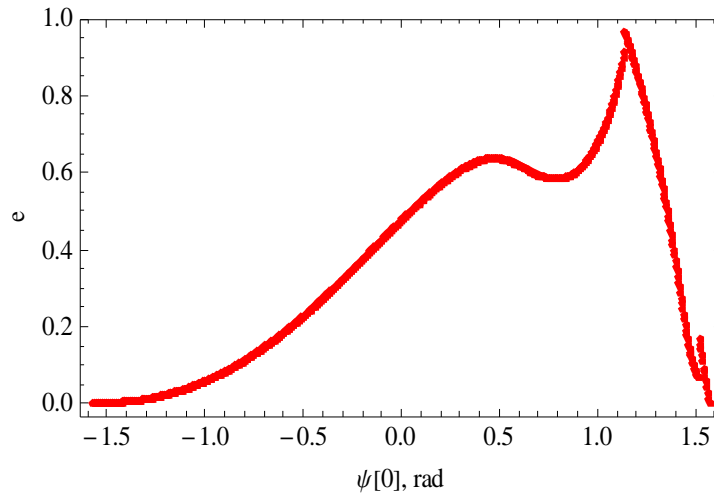


Figure 6.8 : Onset tether spin for rigid body model during first orbit between $-\pi/2 \leq \psi(0) \leq \pi/2$ with a step size e of 0.001

The other observation that can be made to study the dynamics between stability the boundary and the onset spin of the tether is by considering how many orbits are completed by the tether before it starts to spin. This observation was first made by Crellin and Jassens (1996) and then carried out by Ziegler (2003) on the dumbbell model. The number of completed orbits by the flexible tether before the onset of spin occurred for long term behaviour is presented in Figure 6.9. The Figure was constructed by integrating equation (6.18) with $\psi(0) = 0$ rad between $0.28 \leq e \leq 0.4$ for 30 orbits. Each of the plots was examined to look for the perigee where the spin has begun. The number of orbits from the initial simulation time until the last perigee before the spin started was recorded as the quantity η for each eccentricity. Therefore, η in Figure 6.9 is represents the number of completed orbits in which the tether in libration before the spin taken place given by the whole number as $\eta = 1, 2, 3, \dots$

From the same simulation procedures that produced Figure 6.2, the results show that the flexible tether started to spin at $e = 0.282$. Due to computing limitations, Figure 6.9 produced in order to show the tether in a nearly spinning condition in order to look for the required numbers of orbit for the tether to start to spin. The drawback of this approach is the region of steady-state libration which cannot be differentiated from the transient librational motion. However, Figure 6.9 consists of five distinct plateaux at $\eta = 7, 5, 4, 3,$ and 2 showing that the tether is in libration motion. The plateau for $\eta = 2$ suggests that within the region of $e = 0.37$ to 0.40 , less orbit is required for the tether to spin, as compared with the rigid body tether where between $e = 0.375$ to 0.384 it is found that the tether tumbles as show by the scattered dots that clearly distinguish the region. These scattered dots suggest

that the tether is sensitive to the variation of eccentricities between those regions. In the example, tether with $e = 0.317$ is librating until the 6th orbit before the onset spin but when increasing the eccentricity to 0.318 the number of orbit for tether in libration has increased to 15 and increasing more to $e = 0.319$ the number of orbit for tether to start to spin is reduced to 5. Therefore, it shows that the variation of eccentricities strongly influences the tether motion through from libration to tumbling. The differences of the η values produced between the flexible model and the rigid body model for the same range of eccentricities suggest that the flexibility of tether also influences the motion.

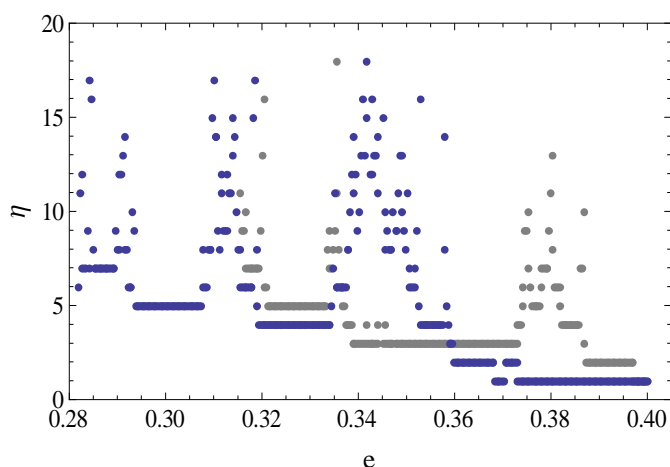


Figure 6.9 : Number of orbit passings before the tether begins to spin for $\psi(0) = 0$ rad, and $\dot{\psi}(0) = 0$ rad/s. 400 points between 0.28 and 0.40. Blue = flexible model; grey = Rigid body model.

6.5 Transition from Regular to Chaotic Motion

Dynamic systems sometimes enter regions of highly unpredictable and chaotic behaviour resulting in impossible future behaviour predictions. When the developed standard general method to solve nonlinear equations of motion fails and does not generate analytical solutions, then one explanation is that the motion could have become chaotic. Chaotic motion refers to motion in a system which has a sensitive dependence to its initial conditions. In this study, the initial conditions may influence the motion of the tether in ψ and also in α for the three dimensional case, where a change in the initial conditions could lead to irregularities in the trajectories in those variables seen when it depicted in a bifurcation diagram or a Poincaré map. This chaotic behaviour is actually exhibited not only in the solution of the mathematical model but also in the actual physical system and modification of the outrigger tether and other tether's parameter can be used to control the chaos. Figure 6.10 shows the motion of the flexible tether entering the chaotic region for

orbit eccentricities approximately more than 0.28, indicated by the dispersed points for $e > 0.28$.

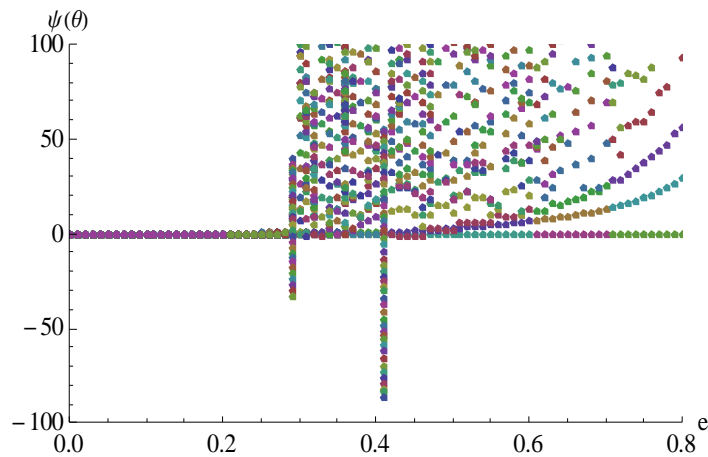


Figure 6.10 : Bifurcation Diagram of the angular displacement with respect to the orbit eccentricity with initial conditions $\psi(0) = 0$ rad, and $\dot{\psi}(0) = 0$ rad/s and a step size of $e = 0.01$.

The region between $0 < e < 0.3$ has been magnified in Figure 6.11 and shows the conical shape of a bifurcation diagram. The structure of the diagram shows periodic windows and bands of points that represent the behaviour of the system both in regular and chaotic motion. From Figure 6.11, the system is clearly seen to start chaotic motion at $e = 0.28$. Period three motion is also visually distinguished within the regular motion region. The bifurcation diagram for the flexible model is compared with the bifurcation diagram of rigid body model in Figure 6.12.

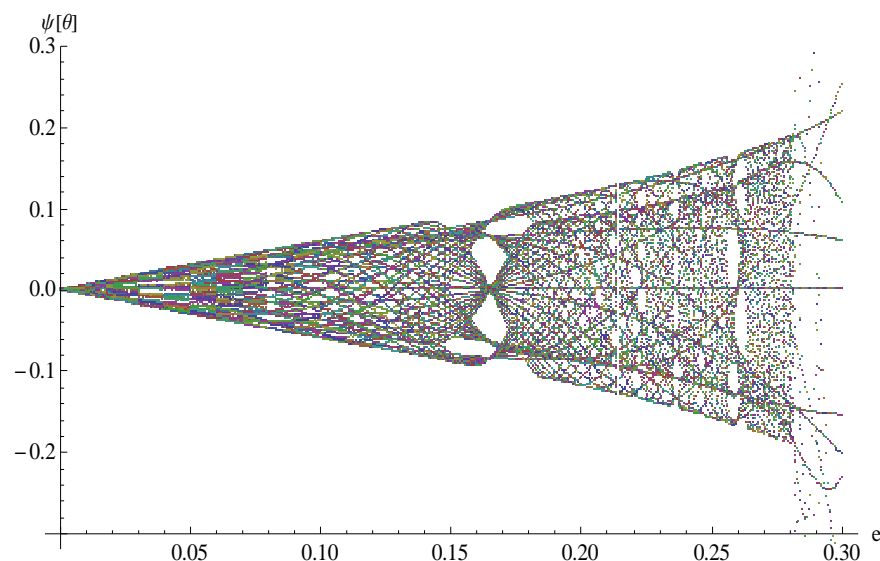


Figure 6.11 : Bifurcation Diagram of the angular displacement of the flexible model with respect to the orbit eccentricity with initial conditions $\psi(0) = 0$ rad, and $\dot{\psi}(0) = 0$ rad/s and a step size of $e = 0.0005$.

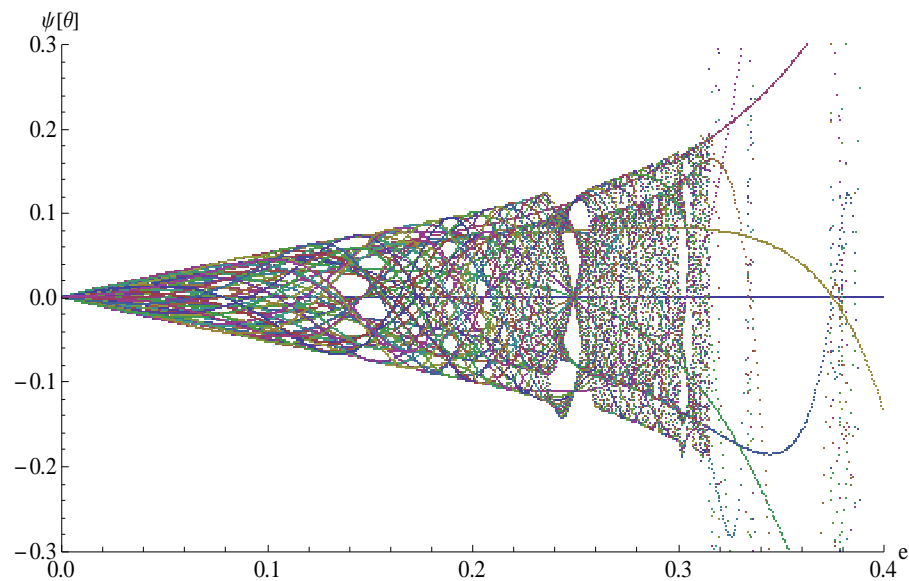


Figure 6.12 : Bifurcation Diagram of the angular displacement of the rigid body model with respect to the orbit eccentricity with initial conditions $\psi(0) = 0$ rad, and $\dot{\psi}(0) = 0$ rad/s and a step size of $e = 0.0005$.

Both Figures agree with the finding by Karasopoloulos and Richardson (1992), Fujii and Ichiki (1996) and Ziegler (2003) where Fujii and Ichiki (1996) found that chaotic motion occurred approximately at $e > 0.28$ for elastic tether with longitudinal rigidity is 10^4 N/m and Karasopoloulos and Richardson (1992) and Ziegler (2003) showed that the rigid body tether should start to spin up at $e > 0.314$.

The initial state of the bifurcation diagram for rigid body tether is a period one per orbit, but on sampling the point at $e = 0$ for flexible model the Poincaré map in Figure 6.13 shows that the flexible model is not displaying the period one motion but the Figure suggests that the motion has crossed the zero point for quite a number of orbits.

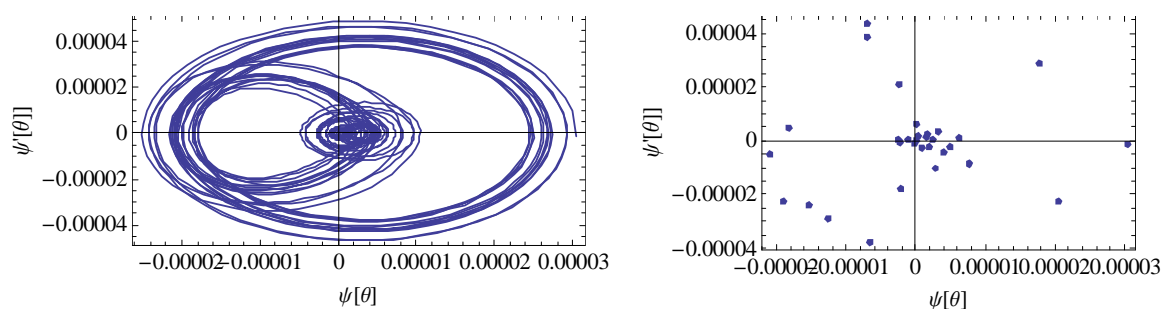


Figure 6.13 : Phase portrait and Poincaré Map for flexible tether motion at $e = 0$ with initial conditions $\psi(0) = 0$ rad, and $\dot{\psi}(0) = 0$ rad/s

In comparison between Figures 6.11 and 6.12, period three occurs in different regions whereby period three motion of the flexible tether is approximately at $e = 0.1654$ and for the rigid body model it is at 0.28. Integrating equation (6.18) for 200 orbits leads to Figure 6.14 which represents the Poincaré map for period three motion of the flexible tether.

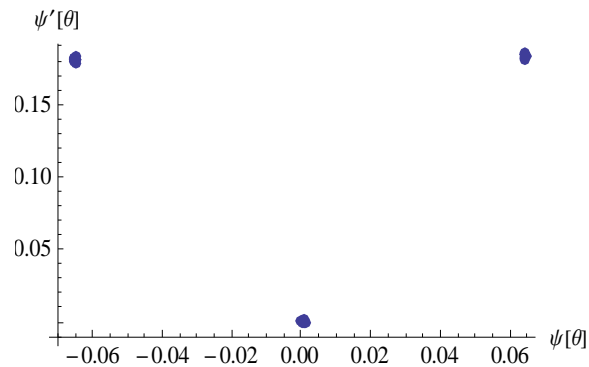


Figure 6.14 : Poincaré map for the flexible tether, sampling at each perigee crossing for 200 orbits with $e = 0.1654$

Sampling the points for 200 orbits of the rigid body model, the Poincaré map shows that the tether is displaying the period three motion but the precise position is drifting quasi-periodically, as shown in Figure 6.15.

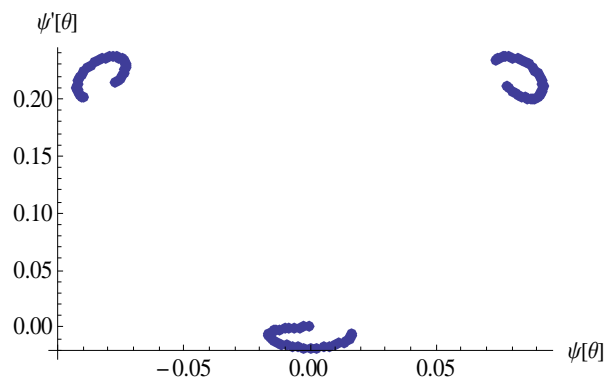


Figure 6.15 : Poincaré map for the rigid body tether, sampling at each perigee crossing for 200 orbits with $e = 0.2479$

On sampling the point at $e = 0.05$ for 200 orbits as in Figure 6.16, it is showed that the motion is stable and periodic.

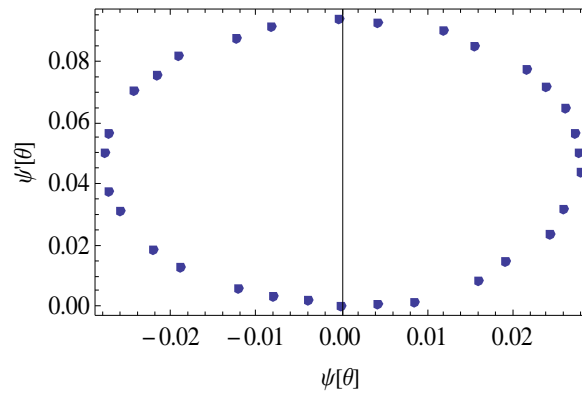


Figure 6.16: Poincaré map for the flexible tether sampling at each perigee crossing for 200 orbits with $e = 0.05$

Motion of period 5 appears at $e = 0.26$ for the flexible tether as shown in Figure 6.17 for the sample of points over 30 orbits. By integrating equation (6.18) for a longer period Figure 6.18 shows the same phenomenon as in Figure 6.15, in which the tether's position is drifting quasi-periodically. Therefore, it is suggested here that the lower sampling period may mislead the prediction of the tether motion in the long term.

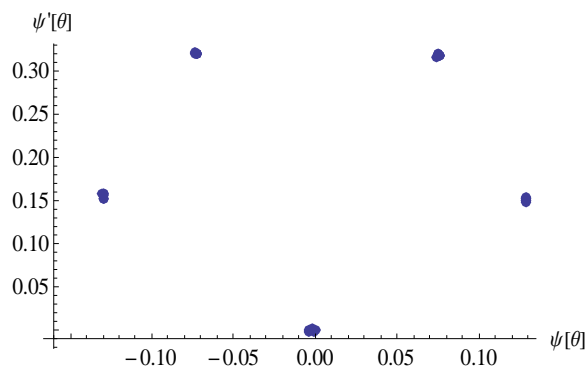


Figure 6.17: Poincaré map for the flexible tether, sampling at each perigee crossing for 30 orbits with $e = 0.26$

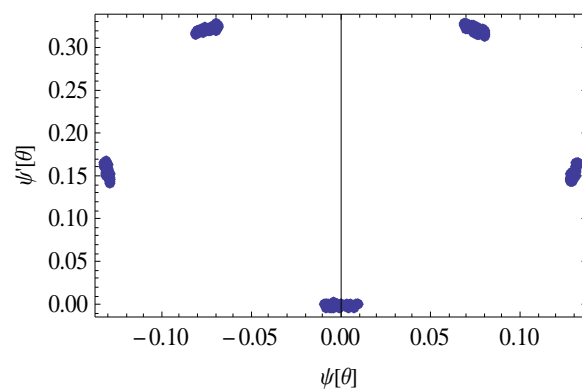


Figure 6.18 : Poincaré Map for the flexible tether, sampling at each perigee crossing for 150 orbits with $e = 0.26$

Integrating the equations of motion for rigid body tether with similar eccentricity and initial condition, the rigid body tether shows the different dynamic conditions when integrated over 150 orbits. Quasi-periodic motion has appeared, depicted by the closed curve seen in the Poincaré map in Figure 6.19, and it is shown here that the flexibility of the tether is strongly influencing the tether's global motion.

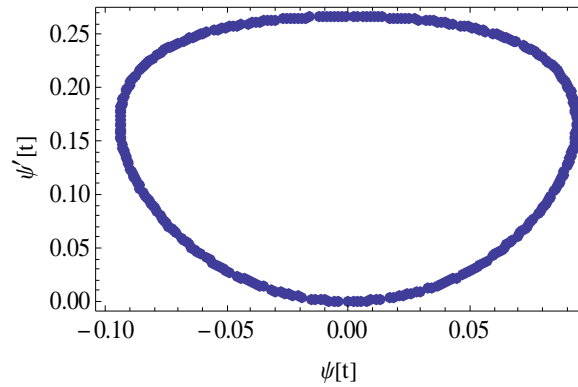


Figure 6.19 : Poincaré map for the rigid body tether, sampling at each perigee crossing for 150 orbits with $e = 0.26$

In the case of initial conditions of $\psi(0) = 0.5$ rad and $\dot{\psi}(0) = 0$ rad/s, the bifurcation diagrams for the flexible and rigid body tethers can be seen in Figures 6.20 and 6.21.

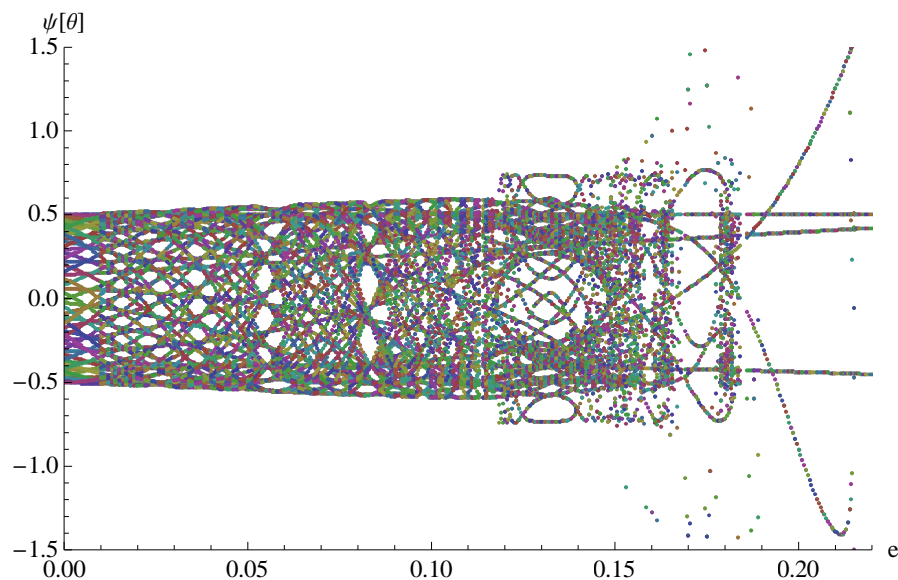


Figure 6.20 : Bifurcation Diagram of the angular displacement of the flexible model with respect to the orbit eccentricity with initial conditions $\psi(0) = 0.5$ rad, and $\dot{\psi}(0) = 0$ rad/s and a step size of $e = 0.0005$.

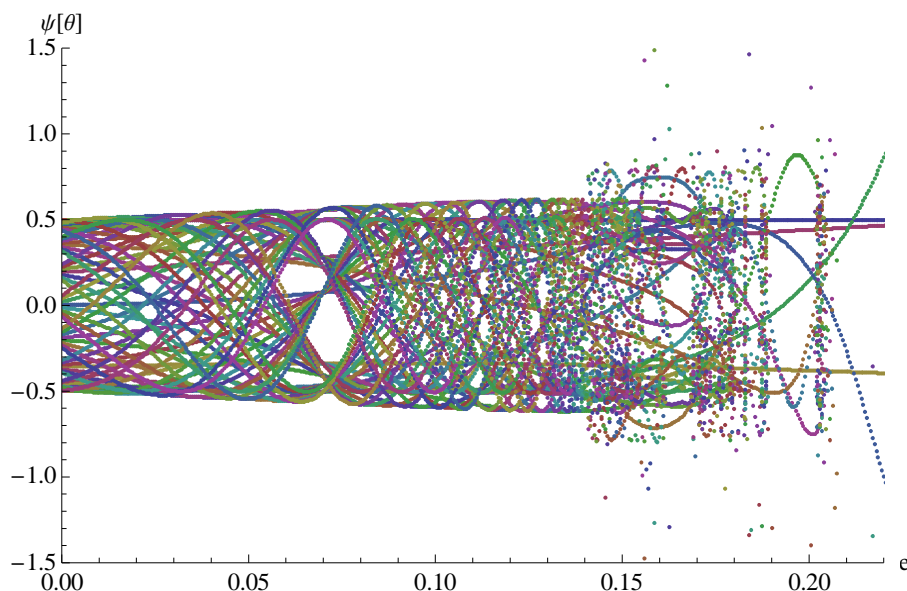


Figure 6.21 : Bifurcation Diagram of the angular displacement of the rigid body model with respect to the orbit eccentricity with initial conditions $\psi(0) = 0.5$ rad, and $\dot{\psi}(0) = 0$ rad/s and a step size of $e = 0.0005$.

The points at which the tether commences to visit all regions reduce from $e = 0.28$ to $e = 0.11$ and it is seen that the initial angular velocity has a significant influence on the start of the chaotic motion. In comparison between the flexible and rigid body models, the region of chaos starts at $e = 0.14$ for the rigid body tether. Consequently, the flexibility of the tether is seen, in addition to the eccentricity and initial conditions, to have an influence on the onset of chaos.

The initial conditions are then changed to $\psi(0) = -0.5$ rad, $\dot{\psi}(0) = -0$ rad/s to observe the motion of the tether with negative initial conditions, and the bifurcation diagram is shown in Figure 6.22. In general, the bifurcation diagram in Figure 6.22 is seen to have a nearly similar shape to Figure 6.20. However, the difference can be seen from the region where the chaos just starts to begin at approximately $e \approx 0.12$. The diagram shows the points in Figure 6.20 and 6.22 dispersed in different trajectories when entering the chaotic region.

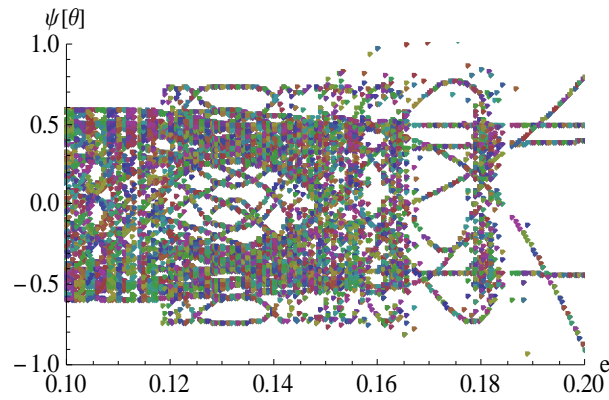


Figure 6.22 : Bifurcation Diagram of the angular displacement of the flexible model with respect to the orbit eccentricity between $0.1 \leq e \leq 0.2$ with initial conditions $\psi(0) = -0.5$ rad, and $\dot{\psi}(0) = -0$ rad/s for a step size of $e = 0.0005$.

Figure 6.23 sampling the points with the same eccentricity to show the difference motion between the different initial conditions.

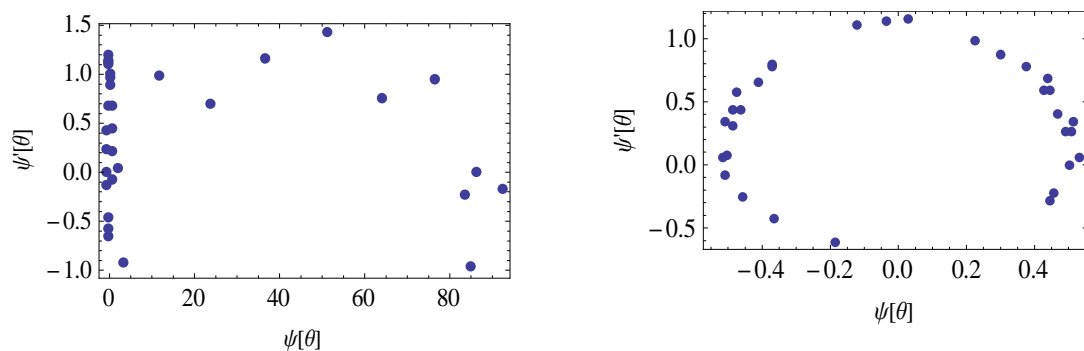


Figure 6.23 : Poincaré map for the flexible tether with initial condition a) $\psi(0) = -0.5$ rad and b) $\psi(0) = 0.5$ rad at $e = 0.15$ for 30 orbits.

6.6 Comparison between the Onset of Spin and Chaos

The route to chaos for planar motion is investigated by observing the dynamic transitions of the flexible tether between $e = 0.28$ to $e = 0.28195$. Figures 6.23 to 6.28 show the tether motion in six different orbits for $e = 0.28, 0.281, 0.28189, 0.281895, 0.28191$ and 0.28195 , from zero initial conditions for 30 orbits. That range of eccentricities consists of motion from steady state libration through to chaos. Figures 6.24 and 6.25 show that the tether motion is in steady-state libration where the quasiperiodic motion has taken place, shown by the Poincaré map and the phase plane. When tether moves with an orbital eccentricity of $e = 0.28189$ as shown in Figure 6.26, some of the points visit the region far from the initial conditions as seen clearly in the Poincaré map, and the frequency spectrum shows an unusual curve when compared with the one in the stable region. However by increasing the eccentricity of the tether, the motion returns to the quasiperiodic motion of Figure 6.27.

The tether moves from librating to tumbling at $e = 0.28191$ where from the time history and the phase plane it is shown that the tether starts to tumble when it reaches the 22nd orbit, and returns to libration before starting to tumble, and these two motions interchange between the 22nd orbit to the 30th orbit. The Poincaré map and the frequency spectrum in Figure 6.28 both suggest that the chaotic region is starting to arise.

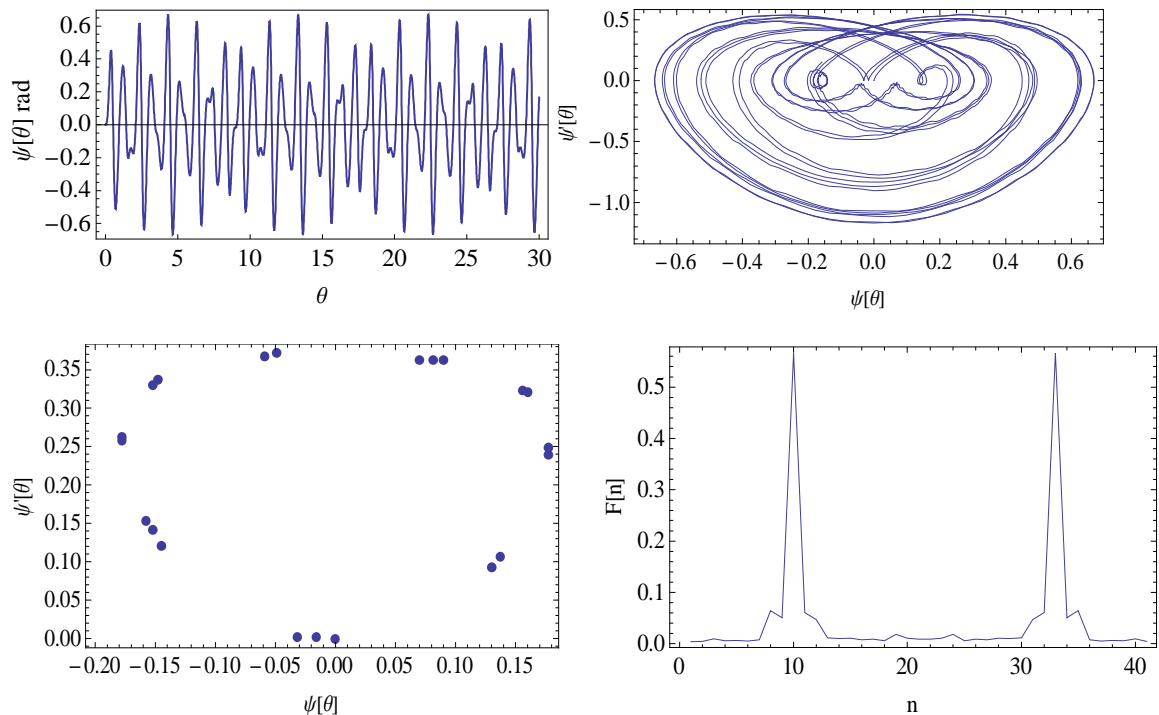


Figure 6.24 : Time history, phase plane, Poincaré map and power spectrum for the flexible tether with $e = 0.28$ and $\psi(0) = 0$ rad, $\psi'(0) = 0$ rad/s

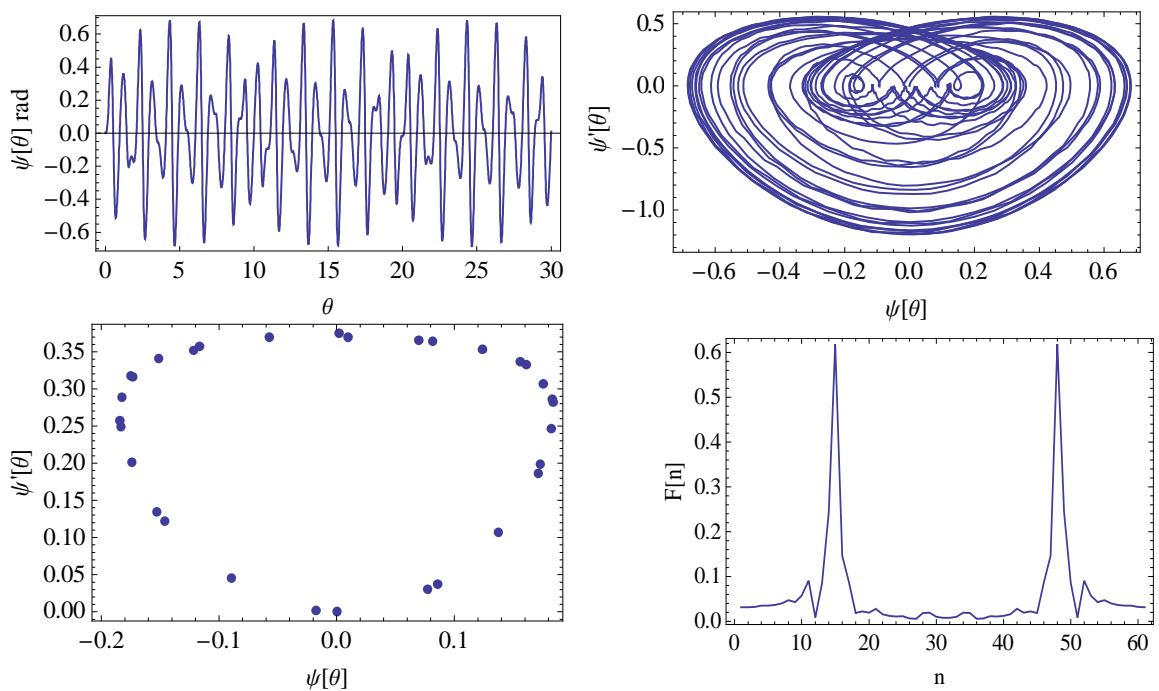


Figure 6.25 : Time history, phase Plane, Poincaré map and power spectrum for the flexible tether with $e = 0.281$ and $\psi(0) = 0$ rad, $\psi'(0) = 0$ rad/s

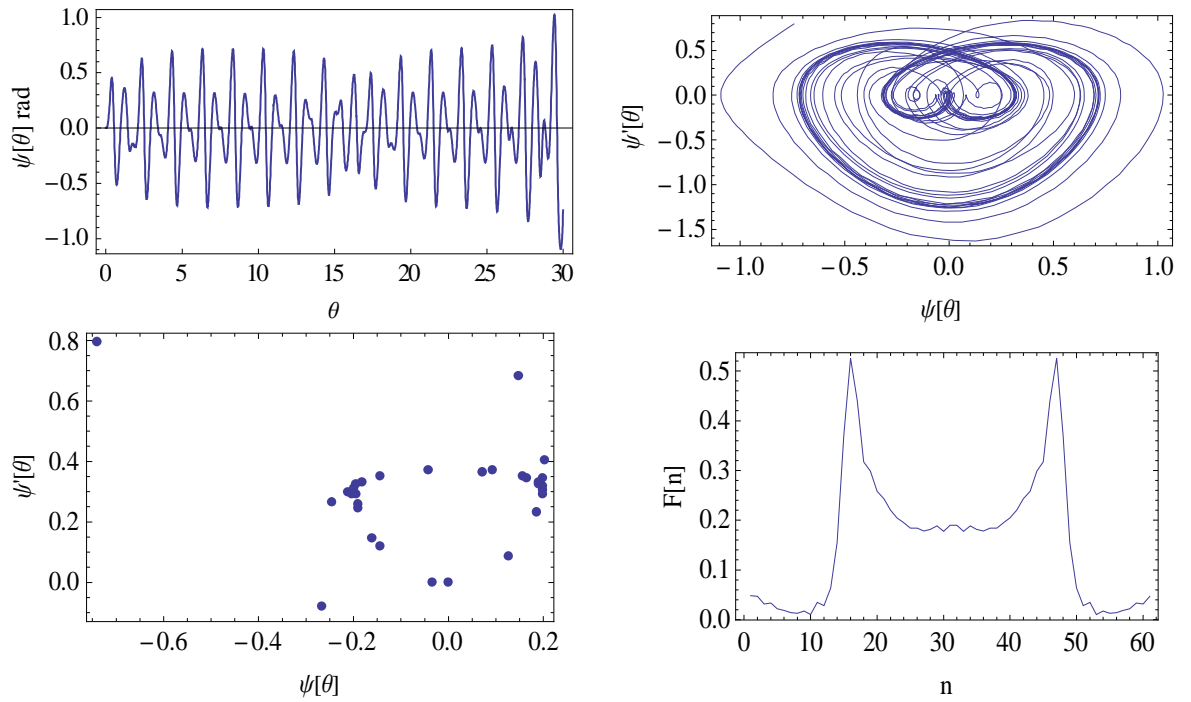


Figure 6.26 : Time history, phase plane, Poincaré map and power spectrum for the flexible tether with $e = 0.28189$ and $\psi(0) = 0$ rad, $\psi'(0) = 0$ rad/s

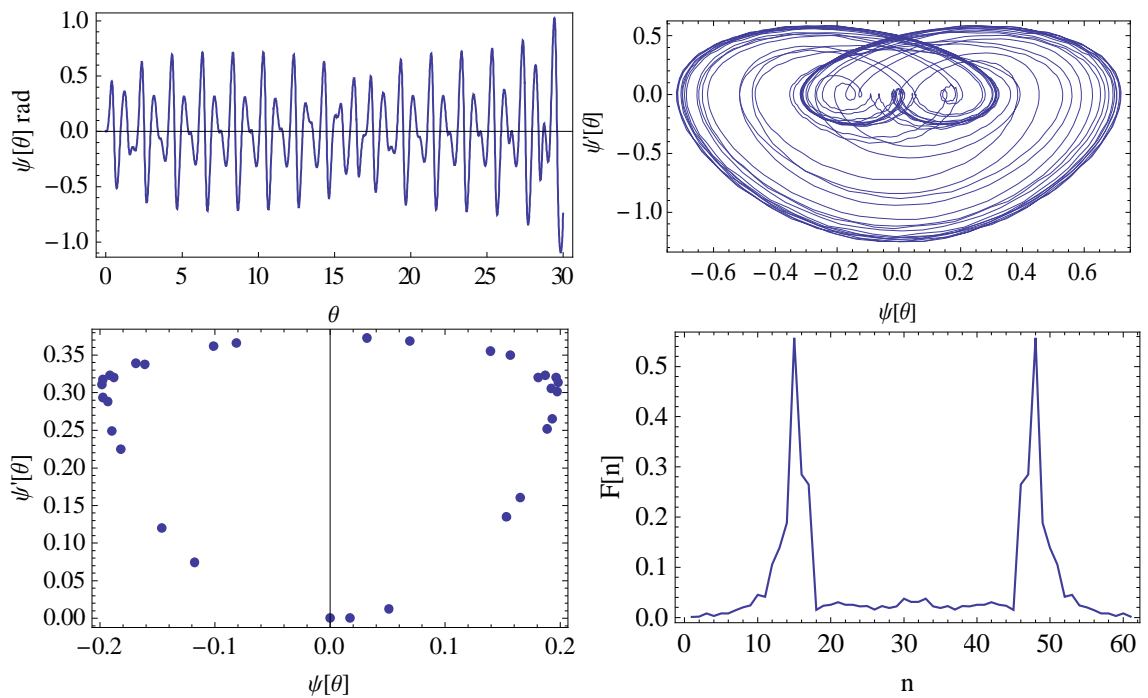


Figure 6.27 : Time history, phase plane, Poincaré map and power spectrum for the flexible tether with $e = 0.281895$ and $\psi(0) = 0$ rad, $\psi'(0) = 0$ rad/s

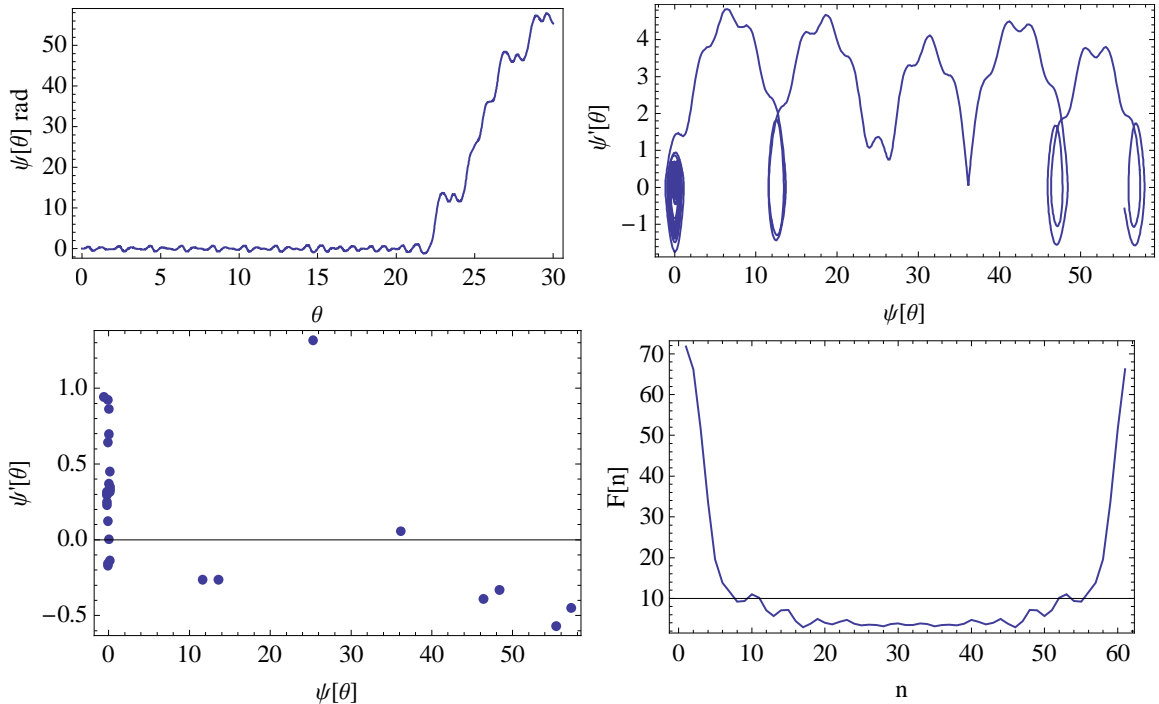


Figure 6.28 : Time history, phase plane, Poincaré map and power spectrum for the flexible tether with $e = 0.28191$ and $\psi(0) = 0$ rad, $\psi'(0) = 0$ rad/s

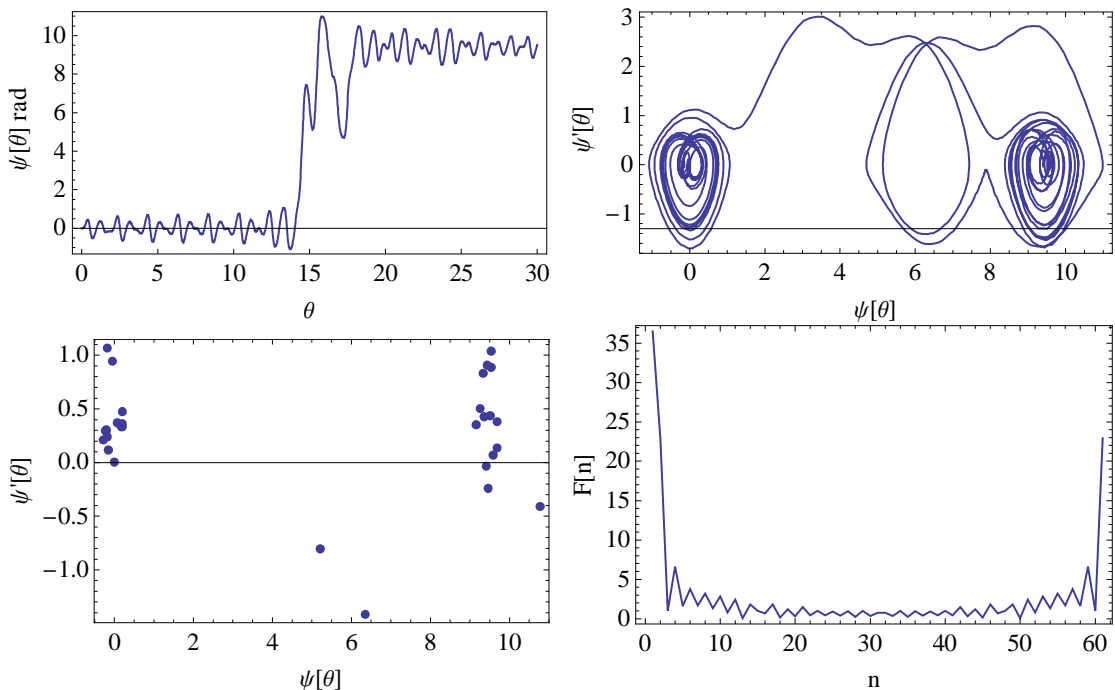


Figure 6.29 : Time history, phase plane, Poincaré map and power spectrum for the flexible tether with $e = 0.28195$ and $\psi(0) = 0$ rad, $\psi'(0) = 0$ rad/s

The non-zero initial conditions applied in Figure 6.30 and 6.31 depicted that the motion of flexible tether moves from tumbling to chaotic from $e = 0.1495$ and change to $e = 0.1496$. The additional observation made on the tethers that initially have local displacement in

longitudinal and transverse direction. The motions of those tethers appear to have no significant change as without initial displacement.

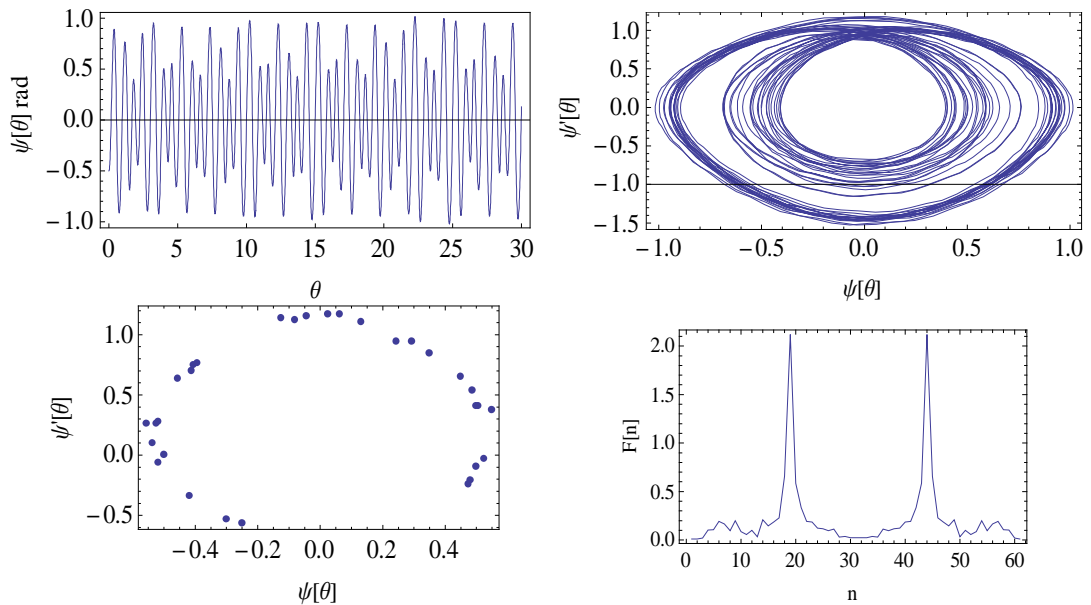


Figure 6.30 : Time history, phase plane, Poincaré map and power spectrum for the flexible tether with $e = 0.1495$ and $\psi(0) = 0.5$ rad, $\psi'(0) = 0$ rad/s

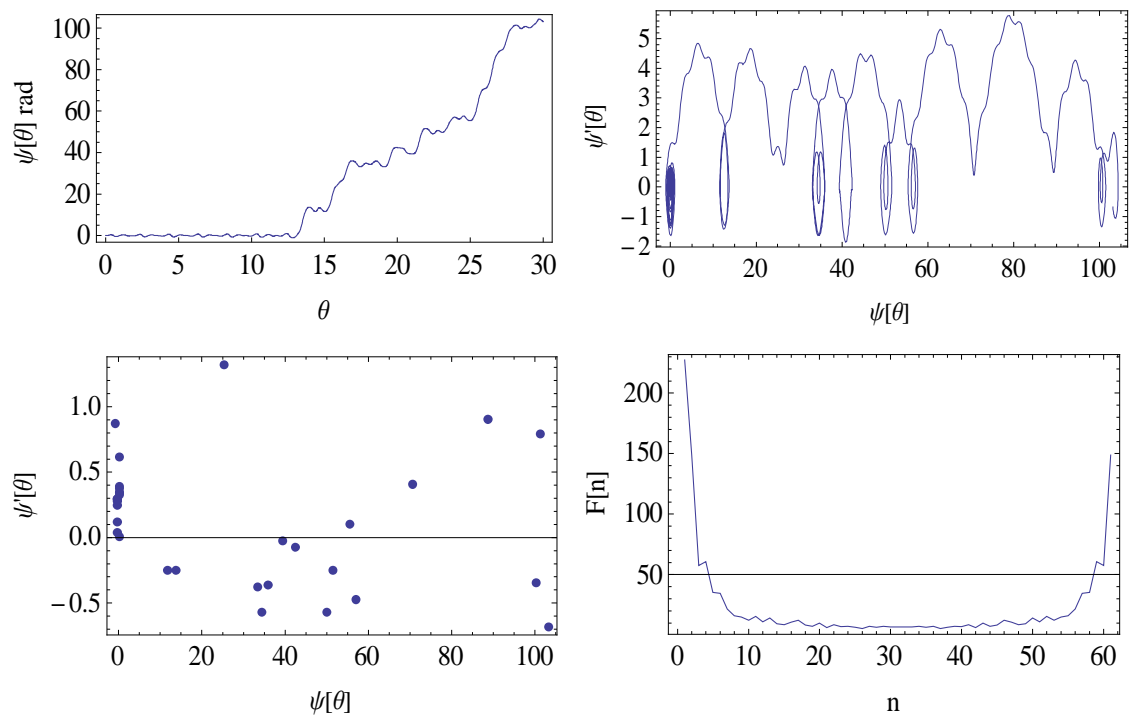


Figure 6.31 : Time history, phase plane, Poincaré map and power spectrum for the flexible tether with $e = 0.1496$ and $\psi(0) = 0.5$ rad, $\psi'(0) = 0$ rad/s

6.7 Route to Chaos for a Three Dimensional Flexible Tether

In the previous analysis of planar motion of a flexible tether, the computing time required for a single bifurcation diagram was nearly one day to complete. This was by discretisation of the simulation period into a shorter length using 30 unit of computers with 4GB RAM for each unit. The non-planar motion is more computationally complex still and longer computing times are required. Therefore, the dynamical analysis for the three dimensional model of the flexible tether is limited to the route to chaos and the analysis of the transition between libration and tumbling has to be abandoned for the time being.

Figure 6.32 shows the bifurcation diagram in the form of a conical shape for the nonplanar motion of the flexible tether with initial condition $\psi(0) = 0$ rad, $\psi'(0) = 0$ rad/s and $\alpha(0) = 0.1$ rad for $0.1 \leq e \leq 0.3$. From Figure 6.32, chaos is found, starting approximately at $e \approx 0.28$, in which it is similar inform to the planar motion of Figure 6.11. This agrees with Figure 4.19 in Chapter 4 where it is stated that the initial displacement of α does not significantly influence the planar motion of flexible tether with the initial condition of $\psi(0) = 0$.

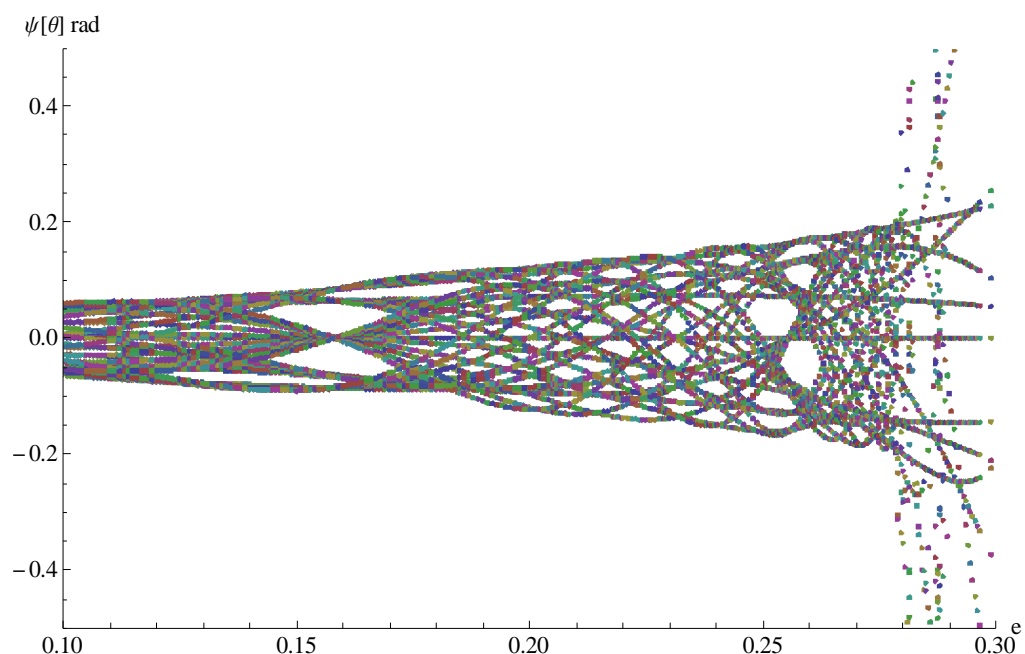


Figure 6.32 : Bifurcation Diagram of the angular displacement of the rigid body model with respect to the orbit eccentricity with initial conditions $\psi(0) = 0$ rad, $\psi'(0) = 0$ rad/s, $\alpha(0) = 0.1$ rad and a step size of $e = 0.00075$.

In comparison with the three dimensional motion of rigid tether, Figure 6.33 samples the point at $e = 0.15$, $\psi(0) = 0$ rad and $\psi'(0) = 0$ rad/s for both models and the results evidently show the Poincaré Map of the flexible model does not display the same motion as the rigid body. This again shows that the flexibility of the tether has a significant impact on the global motion.

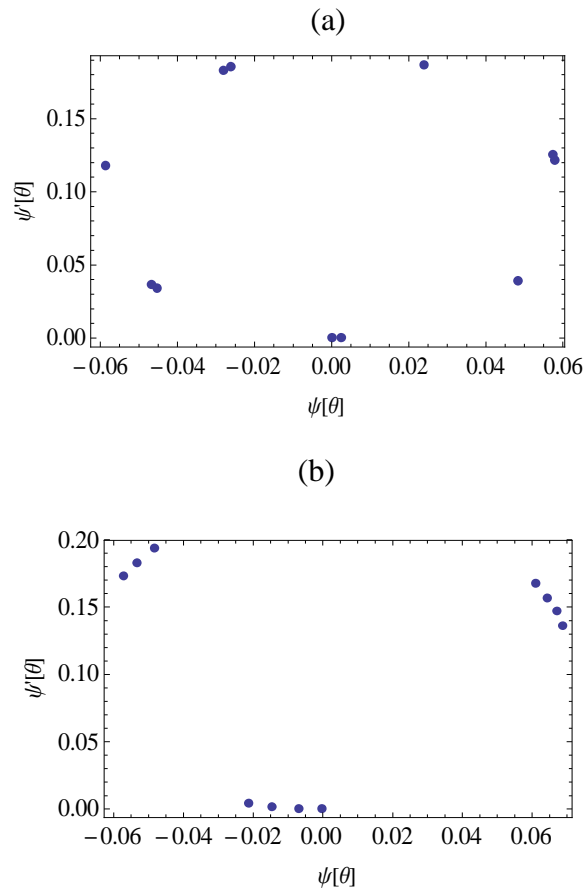


Figure 6.33 : Poincaré map of the tether with initial conditions $\psi(0) = 0$ rad $\psi'(0) = 0$ rad/s, $\alpha(0) = 0.1$ rad at $e = 0.15$ for 230 orbits . (a) Rigid body tether and (b) flexible tether.

The influence of non-planar motion, and the coupling between planar and nonplanar variables to the route to chaos are explored through Figure 6.34 to Figure 6.41. The observation starts with a circular orbit and zero initial conditions for the planar angle, and is followed by an investigation into the elliptical orbit with the paired initial conditions between the planar and non-planar displacement angles. The analysis includes the response of the local displacement in the transverse and longitudinal directions in order to observe the influence of the initial conditions on the tether flexibility. The influences of non-zero initial longitudinal and transverse displacements are also observed.

For the given initial conditions in Figures 6.34 to 6.36 the flexible tether experiences librational motion. The motion moves from periodic to quasi-periodic and in Figure 6.34 a drifted period eight motion is shown on the non planar displacement, and a quasi-periodic motion on the planar displacement. Figures 6.35 and 6.36 suggest that both the planar and nonplanar displacements are quasi-periodic. The frequency spectrum for those three Figures shows that the motion is in the stable condition. The displacements of the tether in the longitudinal and two transverse conditions are almost similar in those three Figures. Figures 6.37 and 6.38 agree with Figure 6.22, in which the same values of negative and non-negative initial conditions do not portray a mirror image motion. Figure 6.37 shows that the tether previously in libration tumbles on the 68th orbit and then returns to libration an orbit after that. The attitude trajectory of the tether shows it moves from one stable point to the next stable point after tumbling occurs. The Poincaré map for non-planar displacement shows a cloud of dots which represent chaotic motion, and this is supported by the frequency spectrum. In comparison, the motion of negative initial conditions is more chaotic where the tether tumbles in three region of time, and shows in the time history and the 2D attitude trajectory of the tether. The frequency spectrum of the planar displacement suggests that the motion is chaotic and this is supported by the Poincaré map. In both the motions of the negative and non-negative initial conditions, the three dimensional displacement of the tether is unchanged, suggesting that the influence on the local displacement is insignificant.

By increasing the initial nonplanar displacement Figure 6.39 shows that chaotic motion has taken place in planar motion. The flexible tether experience quasi-periodic motions when increasing the eccentricity to 0.1 with the given initial conditions of Figure 6.40. The frequency spectrum shows that the motion is stable and the phase plane of the local displacement also shows the stable condition. The eccentricity is then increased to 0.3 in Figure 6.41. With the given initial conditions, the tether starts to spin up, and the 2D attitude trajectory shows that the planar displacement is higher than for the nonplanar case. The points in the Poincaré map are scattered over the phase plane of the planar displacement and for the nonplanar motion. A few points move away from the group of points, showing that the chaotic motions are taking place in both planes. The longitudinal and transverse displacements of the stable tether are shown by the bounded phase plane.

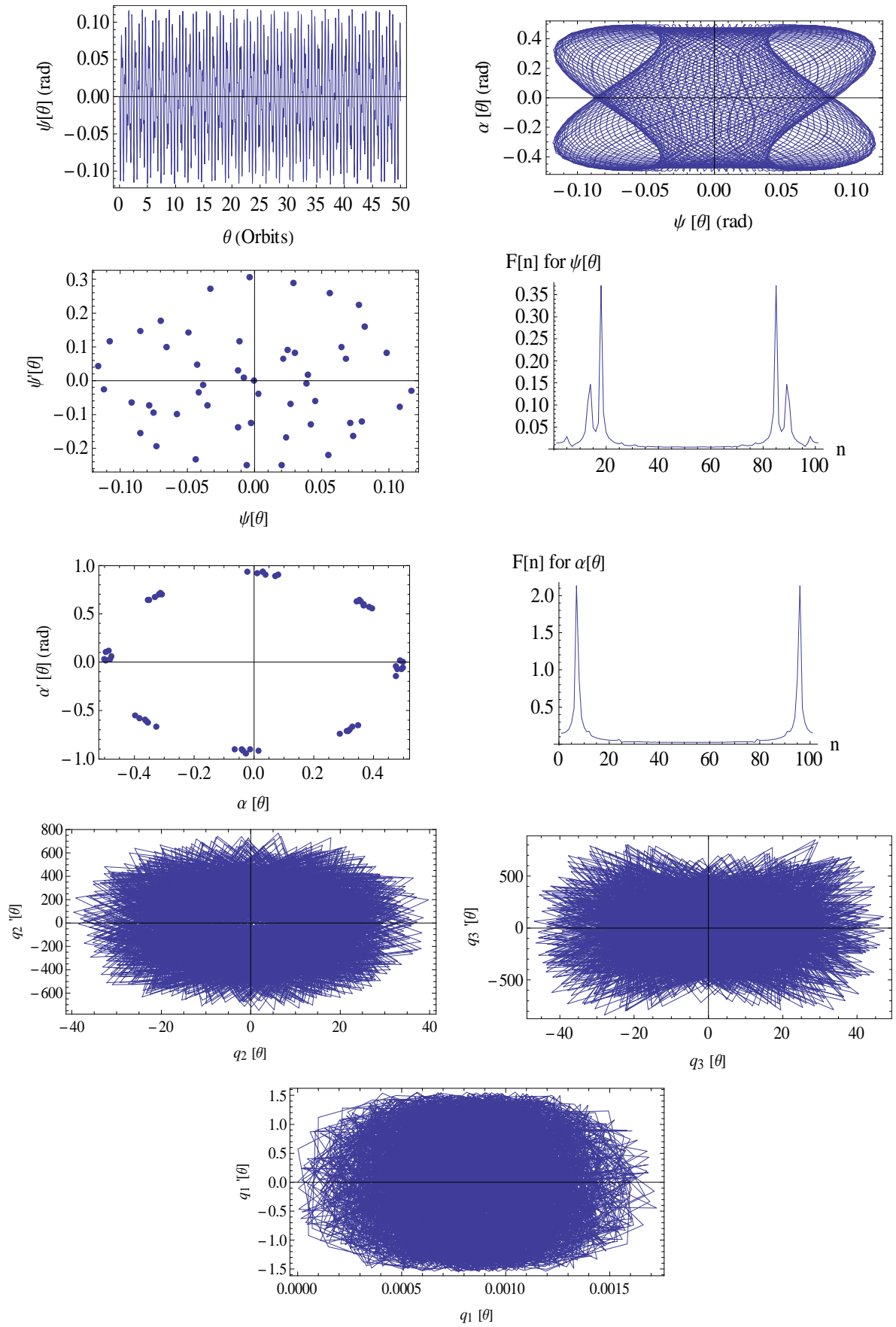


Figure 6.34 : Time history of the tether’s pitch motion, tether attitude trajectory plotted in 2D, Poincaré map, frequency spectrum, phase plane of longitudinal, transverse and lateral displacement of the flexible tether with $\mathbf{e} = 0$, $\psi'(0) = \alpha'(0) = 0$ rad/s, $\psi(0) = 0$ rad, $\alpha(0) = 0.5$ rad

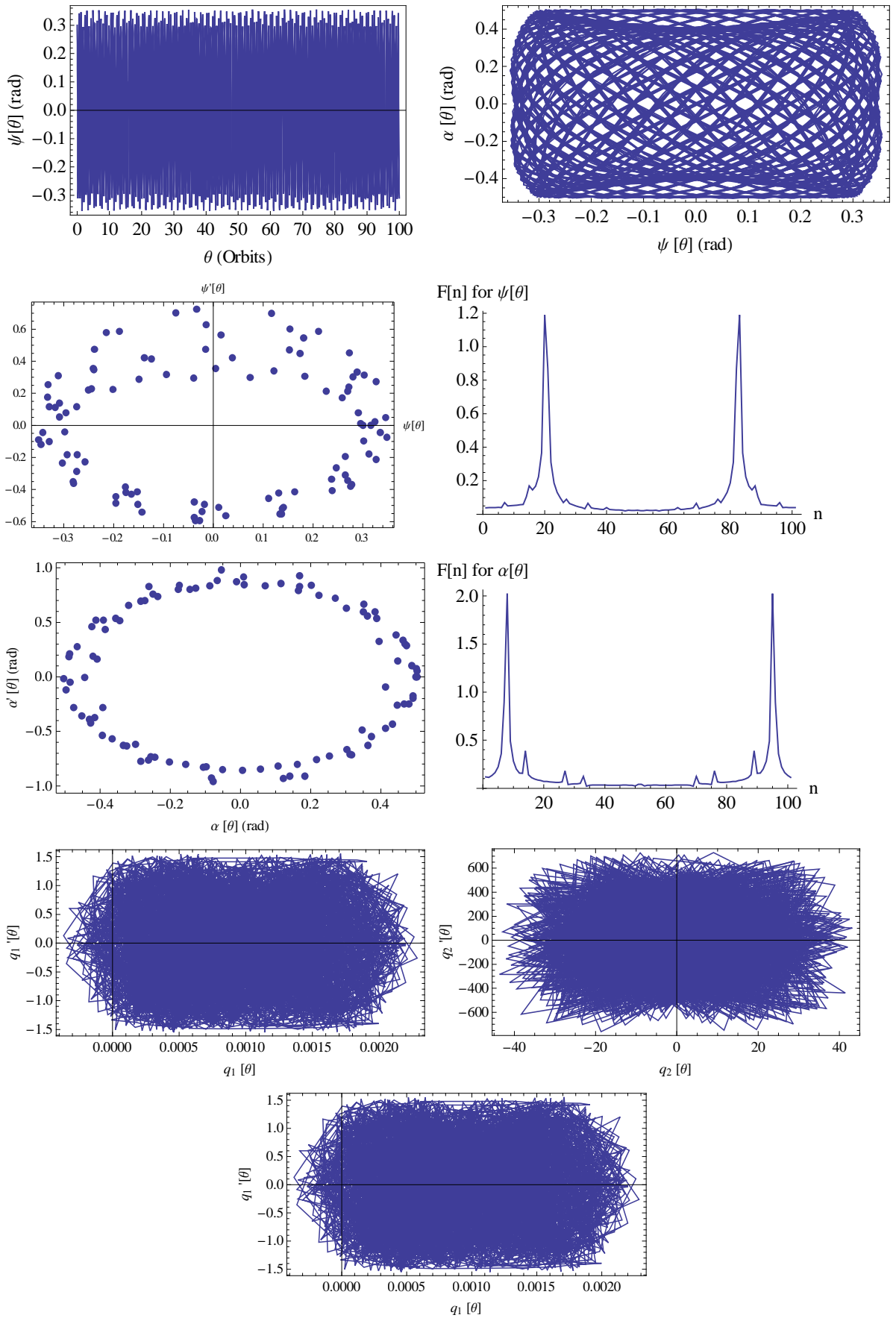


Figure 6.35 : Time history of the tether's pitch motion, tether attitude trajectory plotted in 2D, Poincaré map, frequency spectrum, phase plane of longitudinal, transverse and lateral displacement of the flexible tether with $e = 0$, $\psi'(0) = \alpha'(0) = 0$ rad/s, $\psi(0) = 0.5$ rad, $\alpha(0) = 0.3$ rad

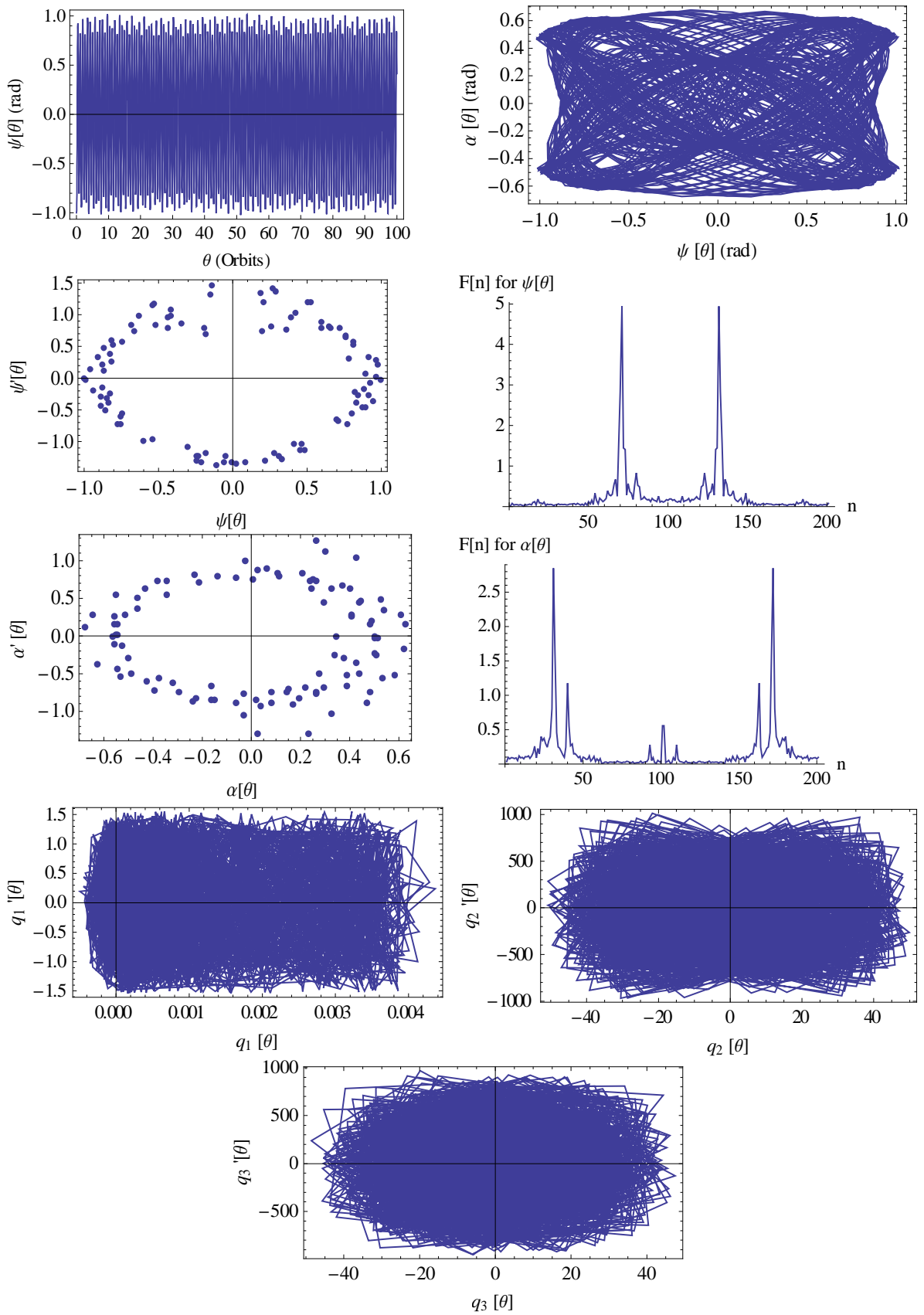


Figure 6.36 : Time history of the tether’s pitch motion, tether attitude trajectory plotted in 2D, Poincaré map, frequency spectrum, phase plane of longitudinal, transverse and lateral displacement of the flexible tether with $e = 0$, $\psi'(0) = \alpha'(0) = 0$ rad/s, $\psi(0) = -1.0$ rad, $\alpha(0) = 0.5$ rad

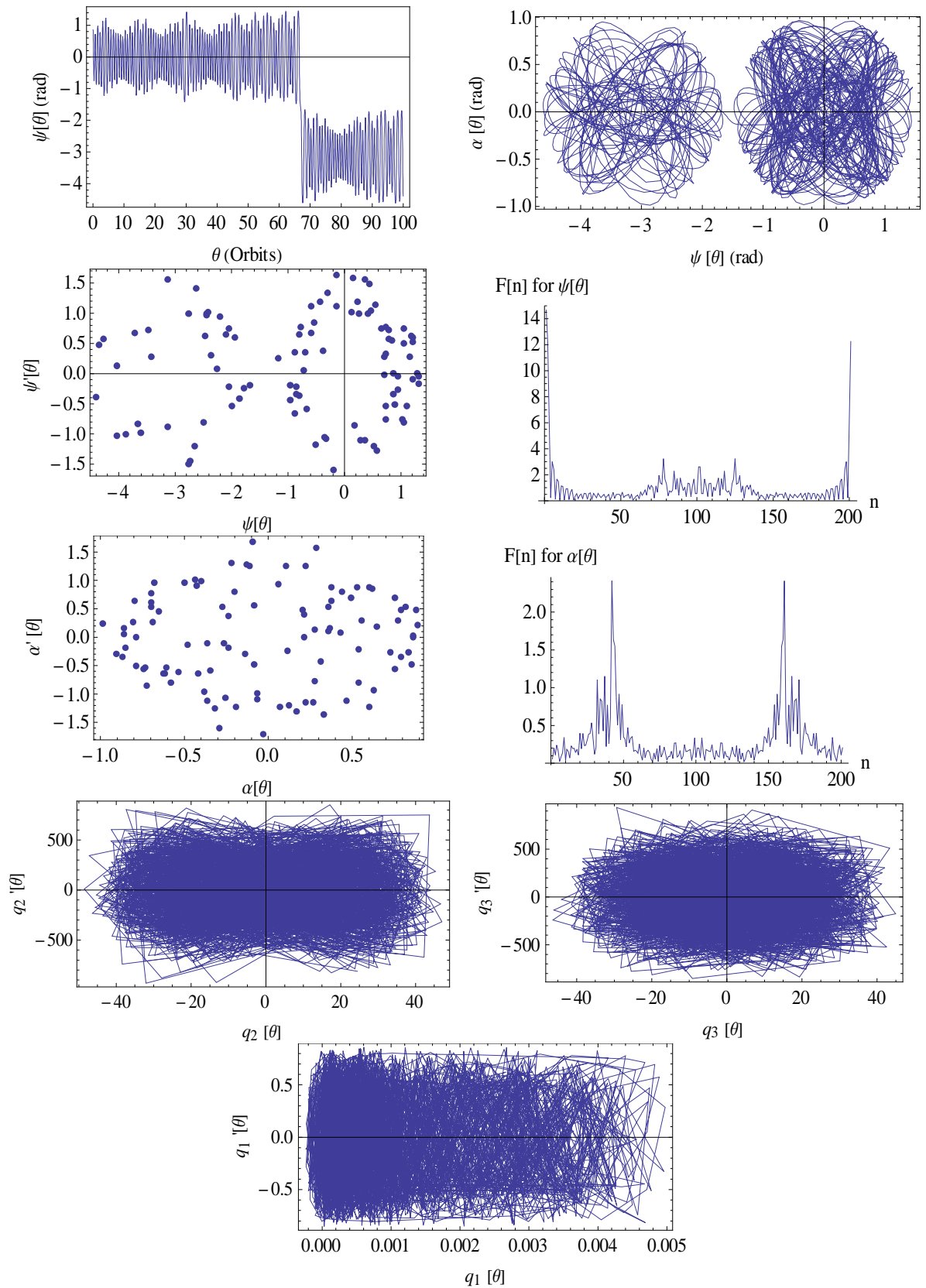


Figure 6.37 : Time history of the tether’s pitch motion, tether attitude trajectory plotted in 2D, Poincaré map, frequency spectrum, phase plane of longitudinal, transverse and lateral displacement of the flexible tether with $e = 0$, $\psi'(0) = \alpha'(0) = 0$ rad/s, $\psi(0) = 0.86$ rad, $\alpha(0) = 0.86$ rad

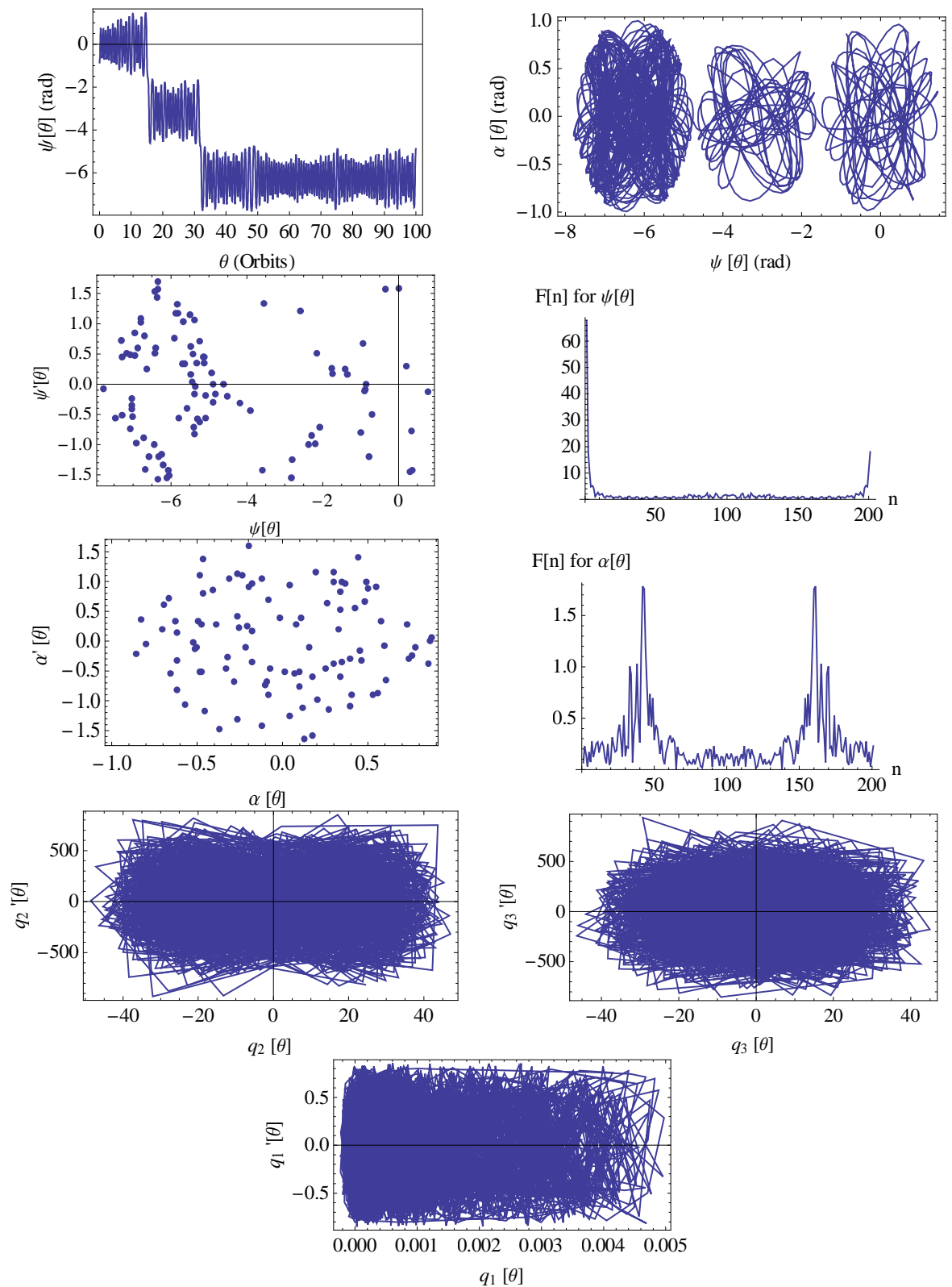


Figure 6.38 : Time history of the tether's pitch motion, tether attitude trajectory plotted in 2D, Poincaré map, frequency spectrum, phase plane of longitudinal, transverse and lateral displacement of the flexible tether with $e = 0$, $\psi'(0) = \alpha'(0) = 0$ rad/s, $\psi(0) = -0.86$ rad, $\alpha(0) = 0.86$ rad

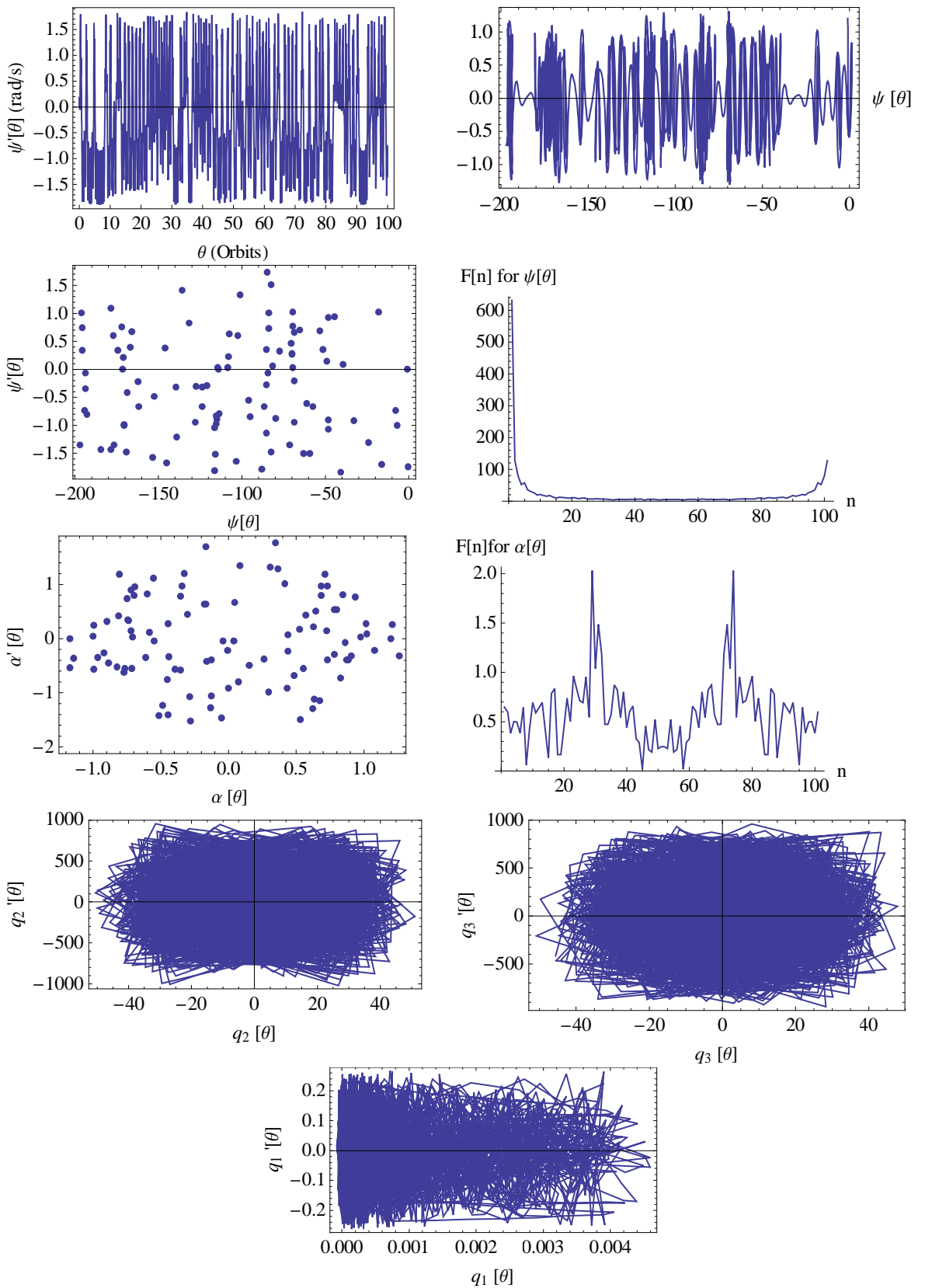


Figure 6.39 : Time history of the tether's pitch motion, tether attitude trajectory plotted in 2D, Poincaré map, frequency spectrum, phase plane of longitudinal, transverse and lateral displacement of the flexible tether with $e = 0$, $\psi'(0) = \alpha'(0) = 0$ rad/s, $\psi(0) = -0.1$ rad, $\alpha(0) = 1.2$ rad

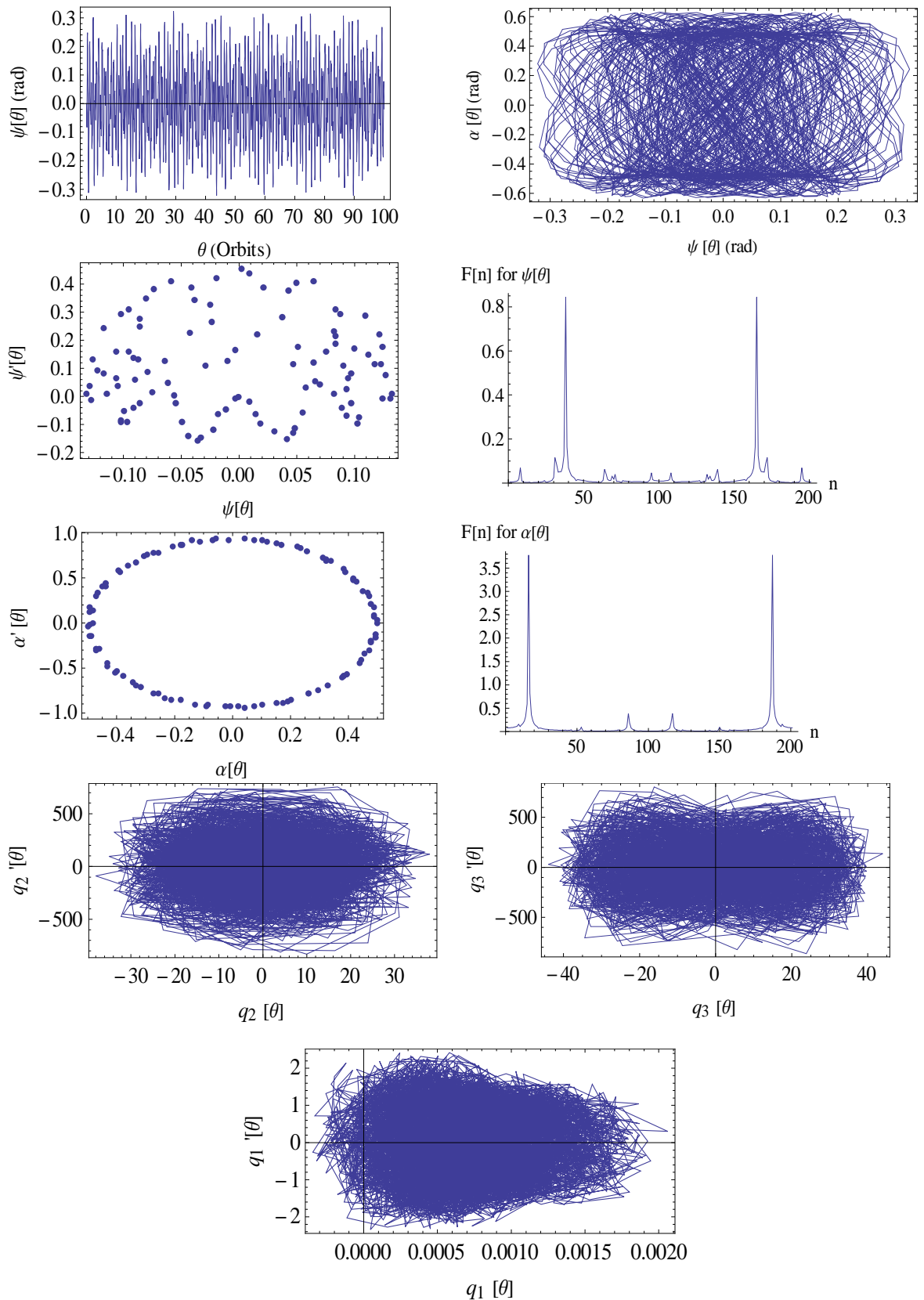


Figure 6.40 : Time history of the tether’s pitch motion, tether attitude trajectory plotted in 2D, Poincaré map, frequency spectrum, phase plane of longitudinal, transverse and lateral displacement of the flexible tether with $e = 0.1$, $\psi'(0) = \alpha'(0) = 0$ rad/s, $\psi(0) = 0$ rad, $\alpha(0) = 0.5$ rad

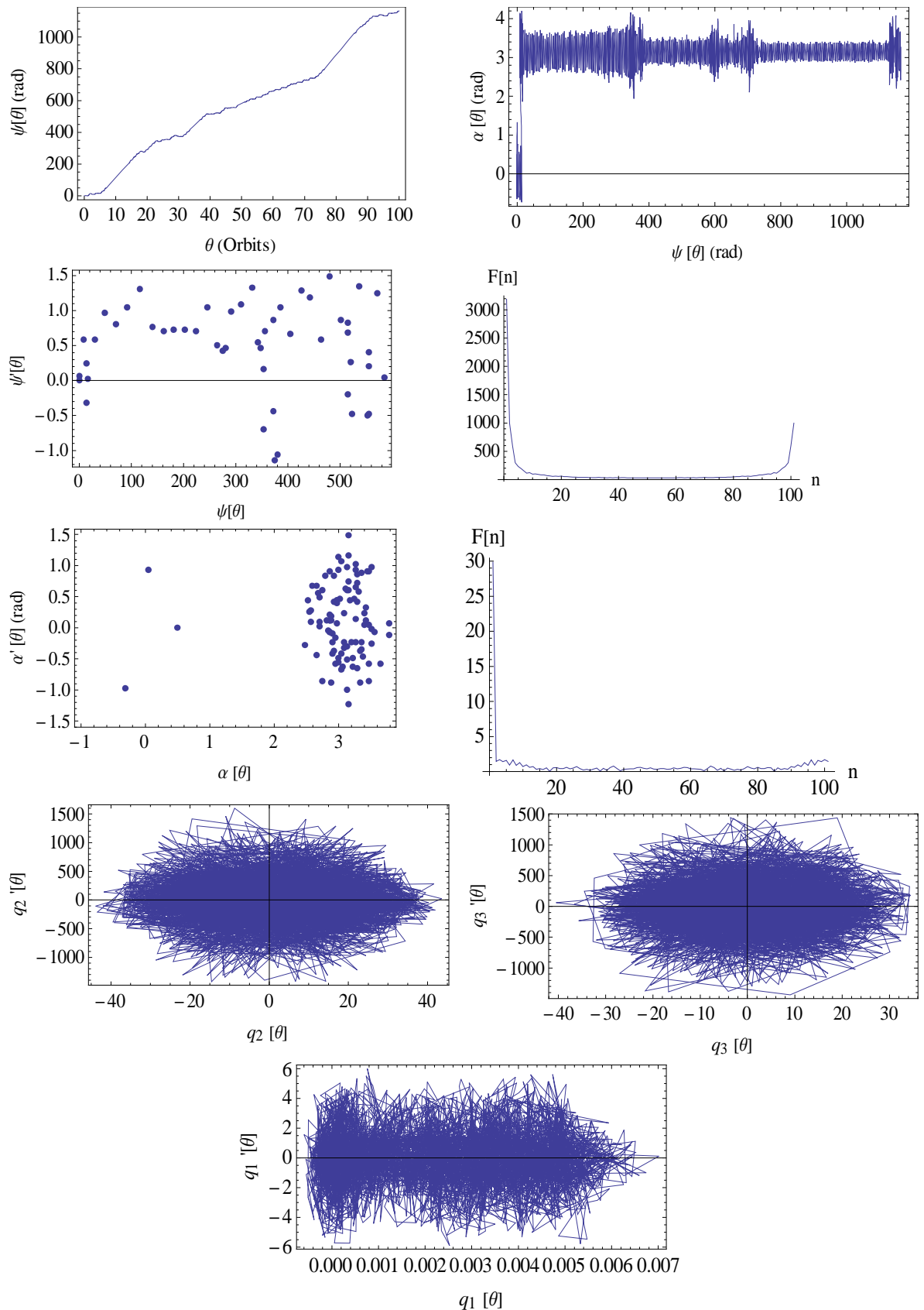


Figure 6.41 : Time history of the tether's pitch motion, tether attitude trajectory plotted in 2D, Poincaré map, frequency spectrum, phase plane of longitudinal, transverse and lateral displacement of the flexible tether with $e = 0.3$, $\psi'(0) = \alpha'(0) = 0$ rad/s, $\psi(0) = 0$ rad, $\alpha(0) = 0.5$ rad

6.8 Velocity Increment Generation for the Flexible Tether.

The main benefit of the MMET design is the generation of velocity increments by powering the tether to spin up using an electrical motor. However, the tether can self-achieve spin-up by exploiting the tether and orbital parameters. Therefore, this section studies the generation of velocity via spinning motion of the tether that is generated due to the exploitation of the nonlinear dynamics of a planar tether on an elliptical orbit.

The tether's tip velocity is given by,

$$\Delta V = L \frac{d\psi}{dt} \quad (6.21)$$

Converting from time to the true anomaly, as discussed by Ziegler (2003), gives a formula for tether tip velocity as,

$$\Delta V = L \sqrt{\frac{\mu(1+e)}{r^3}} \frac{d\psi}{d\theta} \quad (6.22)$$

Figures 6.42 to 6.45 were obtained by numerically integrated equation (6.18) and applying equation (6.22). A similar approach was taken by Ziegler (2003) but this recent study has also investigated the influence of the flexibility of the tether in generating the velocity increment by comparing the results for this with those of the rigid body tether. The numerical integrations were started at perigee, with initial conditions of $\psi'(0) = 0$ rad/s and an initial angular displacement between $-\pi/2 \leq \psi(0) \leq \pi/2$. The angular displacement and ΔV were recorded at each perigee point after the tether had completed a full orbit. The tether was assumed to be in libration for the angular displacement between $-\pi/2 \leq \psi(\theta) \leq \pi/2$. The obtained results may not be as precise as those given by Ziegler (2003) due to larger step sizes for eccentricities in order to save computing time.

Figure 6.42 and 6.43 shows the ψ_p in which refers to the angular displacement at perigee and the ΔV of the flexible tether in comparison with those for the rigid body tether, obtained at perigee, with respect to the orbit eccentricity. The results suggest that the flexible tether reaches onset of spinning at $e = 0.462$ as showed by the transition from a 'near to straight' line to the curve that is increasing for the increasing values of the eccentricities. The body rigid tether shows the onset of spin at $e = 0.478$. Both results agree with the findings in Figures 6.7 and 6.8. The maximum ΔV reaches by the flexible tether

during the libration period is at 8.61 m/s with $\psi_p = -0.31$ rad and the maximum ΔV during the spin condition is 9.046 m/s at $\psi_p = 2.141$ rad. Figures 6.29 and 6.30 suggest that the flexible model has reached the onset of the tumbling/spin condition earlier than the rigid body model. This shows that the flexural effect of the tether may lead to earlier chaotic motion.

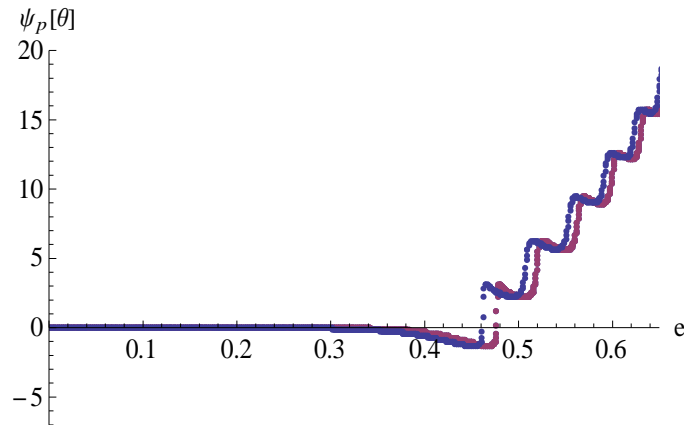


Figure 6.42 : Comparison of ψ_p obtained at perigee after a full orbit with respect to e for $\psi(0) = 0$ rad with a step size in e of 0.0005. Blue = flexible tether, red = rigid body tether.

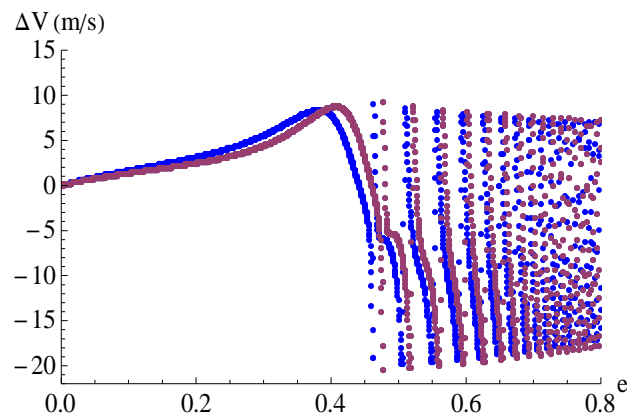


Figure 6.43 : Comparison of ΔV obtained at perigee after a full orbit with respect to e for $\psi(0) = 0$ rad with a step size in e of 0.0005. Blue = flexible tether, red = rigid body tether.

Figures 6.44 and 6.45 show the effect of changing the initial conditions on the generation of velocity. The negative initial condition in Figure 6.44 suggest that higher ΔV is generated during libration as compared to Figure 6.45. Figure 6.45 also shows the

retrograde spinning of the flexible tether with a higher ΔV between $e = 0.6$ to 0.8 for positive values of initial conditions.

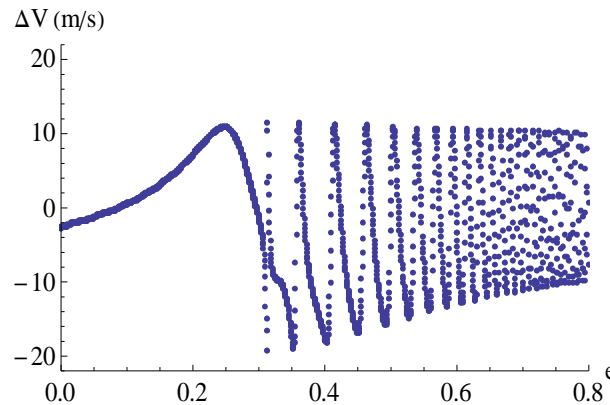


Figure 6.44 : ΔV obtained at perigee after a full orbit with respect to e for $\psi(0) = -0.3$ rad with a step size in e of 0.0005.

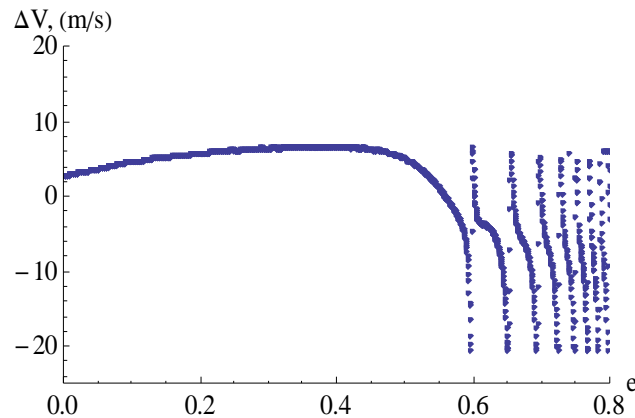


Figure 6.45 : ΔV obtained at perigee after a full orbit with respect to e for $\psi(0) = 0.3$ rad with a step size in e of 0.0005.

Interesting results have been shown by Ziegler (2003) and are reproduced here for the flexible model shown in Figure 6.42. That Figure suggests that with the negative initial conditions of angular displacement at $e = 0.1$, the tether can generate a higher ΔV and this applies for both models. However, the rigid body model is shown to develop a little bit higher ΔV as is given by 18.63 m/s as compared with 18.14 m/s for the ΔV of the flexible model. Even though the difference is seen to be small, it will still influence the incoming trajectory of the payload that will be transferred using the MMET, or may lead to unsuccessful payload capture. Therefore, the flexibility is again shown to a significant influence on generating the ΔV of the tether. This will be explored more in the next chapter.

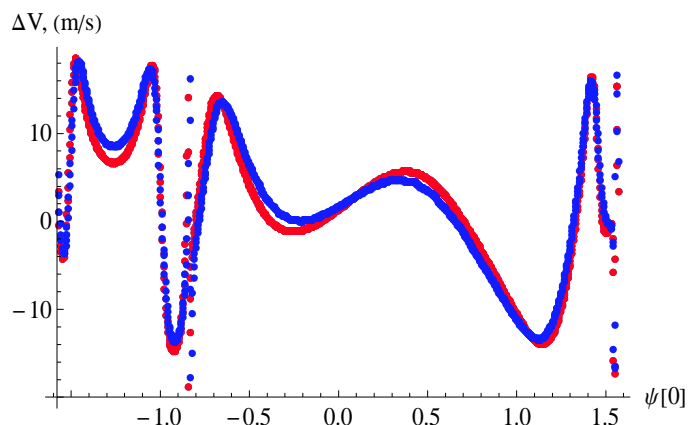


Figure 6.46 : Comparison of ΔV obtained at perigee after a full orbit with respect to $\psi(0)$ for $e = 0.1$ with a step size in $\psi(0)$ of $\pi/1000$ rad . Blue = Flexible tether, Red = Rigid body tether

6.9 Conclusions

The planar and nonplanar attitude dynamics of a flexible tether on circular and elliptical orbits have been investigated in this chapter. The orbit eccentricity and the initial conditions are found to have a strong influence on the tether libration, and also on the occurrence of tumbling motion. The tether's flexibility also has a significant effect on the tether's motion. The long term boundary between libration and spin is found to be qualitatively similar to the rigid body tether in which the symmetrical and asymmetrical libration/spin boundaries for the long-term orbit and the first completed orbit have been uncovered. The eccentricity and initial conditions are also found to influence the onset of chaos. However, non-zero initial conditions for the longitudinal and transverse displacements were not shown to have significant influence on the route to chaotic motion. Finally, the generation of velocity increment upon completion of a single orbit is found to be a function of the initial conditions and eccentricity. The flexibility of the tether was again found to affect the generation of velocity based on a comparative study between the flexible and the rigid body tether.

Chapter 7

In-service Power Requirements for the Motorised Momentum Exchange Tether

7.1 Introduction

The MMET is a symmetrical momentum exchange system using motorized spin up against a substantial counter-inertia termed here the outrigger tether system, and is likely to be driven by a large electric gear-motor consuming between 100 and 500 kW of power, possibly a bit more, dependent on key parameters which drive the performance of the MMET. The performance of the tether is influenced by the altitude, payload mass, length of tether span, area tensile strength and also the density of material of the tether. The definition of the power requirement of the MMET is derived from the torque required to spin up the tether to the required tangential velocity, and the terminal velocity achieved for the orbital conditions under consideration. This chapter explores the minimum torque and power requirement for the MMET in various operation conditions for the rigid body and flexible body model.

The MMET has the potential for reducing the operational cost of space transportation. Therefore, there is the need to study the power profile required for the tether in order to optimize the cost. The use of the tether for interplanetary missions can be one of the options in reducing the propellant cost to the mission. Arnold and Thomson (1992) studied the use of a spinning tether in transporting oxygen from the Moon to LEO, in which application of the 100km tether was used to collect the payload from the orbital transfer vehicle (OTV). In 1999, Cartmell and Ziegler proposed a preliminary design for a mission architecture for an Earth-Moon payload exchange system using the MMET concept. The system was then developed further by Cartmell *et al.* (2004) and this work underlines the practical requirements for this system.

7.2 Escape velocity

The inclusion of an electric motor in the tether system can result in additional total velocity. The potential maximum escape velocity is given by the sum of the orbital and tangential velocities which are subsequently available at the tether tip, and defined by the following,

$$V_{Total} = V_{orbit} + \Delta V \quad (7.1)$$

provided that the tether is aligned normal to the tangent to the orbit, otherwise a component of the tangential velocity vector is required. The orbital velocity, V_{orbit} considered for this study could emanate from orbits which are either circular or elliptical, and is given for a circular orbit by

$$V_{circularorbit} = \sqrt{\frac{\mu}{r_{circular}}} \quad (7.2)$$

and for an elliptic orbit by,

$$V_{ellipticalorbit} = \sqrt{\frac{2\mu}{r_{elliptical}} - \frac{\mu}{a}} \quad (7.3)$$

where r is the radius of the orbit and a is the semi major axis and μ is the gravitational constant. The velocity of the tether relative to its centre of rotation is given by equation (6.21).

7.3 Minimum Torque Analysis

Generally, a useful tether response can be classified either as an oscillation or a pure spin condition, dependent on the amount of the applied torque, location, initial conditions, and prevailing orbital elements. For interplanetary payload injection the response should ideally be in the form of a monotonic spin, for some minimised value of torque so that the angular velocity eventually increases to the required level, in order to achieve escape for the payload when released.

In this study, the initial work of Ismail (2007) on the power requirements for the MMET operating in practice is further developed, and a single tether system model as rigid body tether as shown Figure 7.1 is considered for transferring payloads to the required orbit. The payload is assumed to be transported from the Earth to the designated orbit using a conventional rocket and will be collected by the tether.

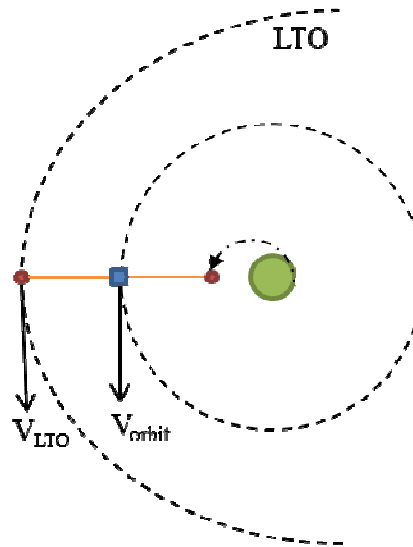


Figure 7.1 : Single staging tether for payload transfer

Certain default material parameters and the density for Spectra 2000 and tether geometry are used for the analysis given by:

$$L = 50 \text{ km}, M_p = 1000 \text{ kg}, M_m = 5000 \text{ kg}, A = 62.83 \times 10^{-6} \text{ m}^2, r_m = r_p = 0.5 \text{ m}, \rho = 970 \text{ kg m}^{-3}, \mu = 3.9877848 \times 10^{14} \text{ m}^3/\text{s}^2, E = 113 \text{ GPa}$$

7.3.1 Circular orbit

Using the chosen default values mentioned above, the tether is first driven with a low torque which is then gradually increased until the tether achieves monotonic spin. On increasing the torque the tether is found to reach the monotonic spin condition for default values for the geometrical and mass properties of the system when the torque is 2.94 MNm. Both responses are depicted in Figure 7.2 and Figure 7.3 as follows,

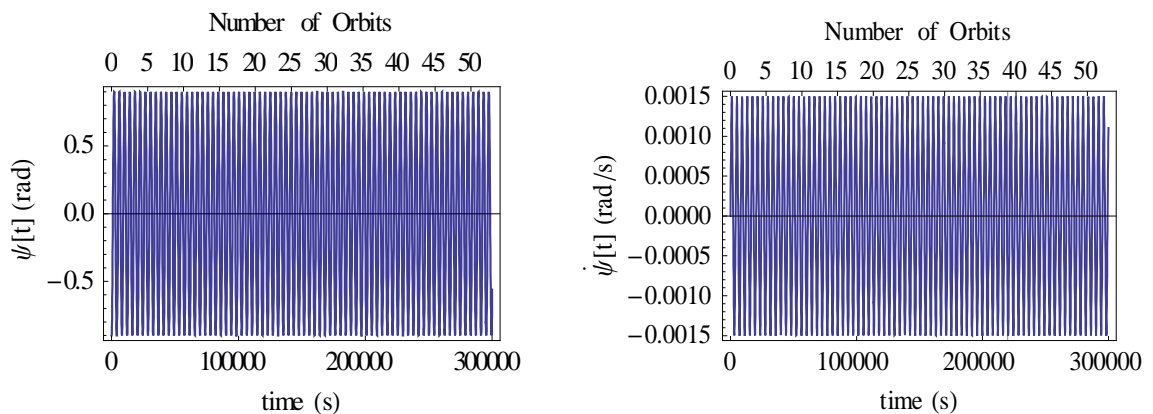


Figure 7.2 : Oscillation conditions on a circular orbit for untorqued tether.

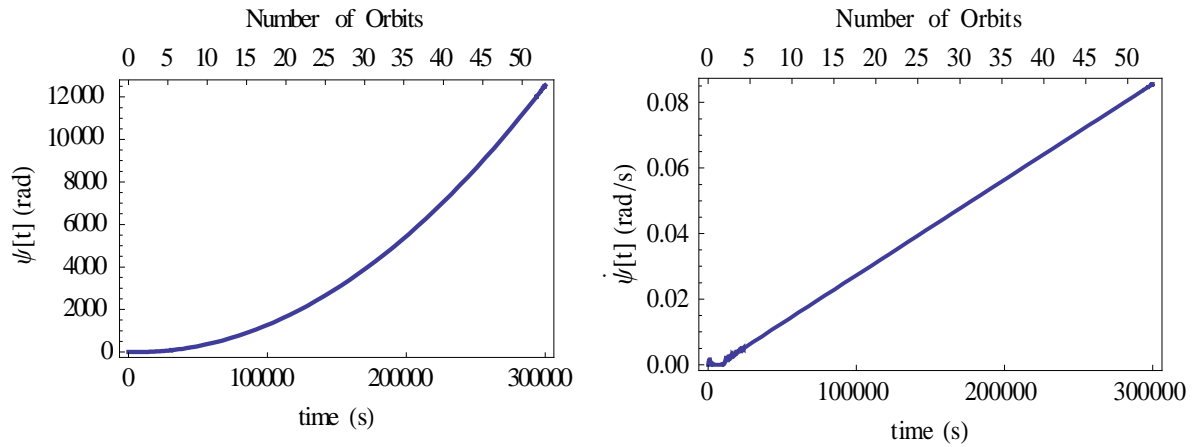


Figure 7.3 : Pure spin conditions on a circular orbit with application of 2.94 MNm torque

This minimum torque analysis is also influenced by the geometrical and physical properties of the tether, namely the sub-span length and material density of the tether. By focusing on the influence of the tether length, analysis shows that the higher the tether length the greater the required torque. Figure 7.4 shows the minimum torque for three different sub-span lengths: 50 km, 75km and 100 km and the time to release the payload. This is based on the value of escape velocity to Lunar Transfer Orbit, V_{LTO} in the Earth-Moon mission studied by Cartmell and Ziegler (1999), for which the calculated V_{LTO} is 10.78 km/s. It shows that the longer the sub-span the shorter the time required to release the payload, but the torque has to be increased sufficiently to achieve the monotonic spin condition.

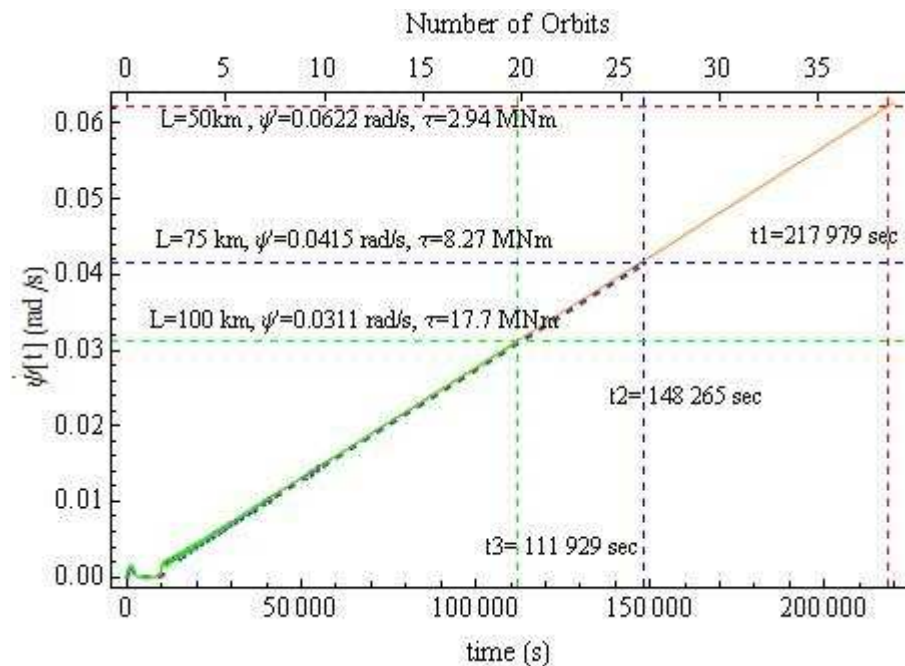


Figure 7.4 : Angular velocity for tether sub-span lengths of 50km, 75km and 100km

7.3.2 Elliptical orbit

The analysis continues for the tether on an elliptical orbit using the following orbital parameters,

$$r_{perigee} = 7000 \text{ km}, e = 0.1$$

The tether position on this orbit is initially assumed to be at perigee, for which the initial true anomaly and radius are,

$$\theta(0) = 0, \text{ rad}, \dot{\theta}(0) = 0.001131, \text{ rad/s}, R(0) = 7000 \text{ km}, \dot{R}(0) = 0 \text{ km/s}$$

and the initial conditions for the angular displacement and angular velocity are as established in Ziegler (2003) and given by,

$$\psi(0) = -0.575, \text{ rad}, \dot{\psi}(0) = 0 \text{ rad/s}$$

Figure 7.5 shows the oscillation condition for the tether on the elliptical orbit. The simulation shows that a minimum torque value of 2.35 MNm is required for the tether to reach the spin up condition with the above orbital parameters and initial conditions, and this is shown in Figure 7.6.

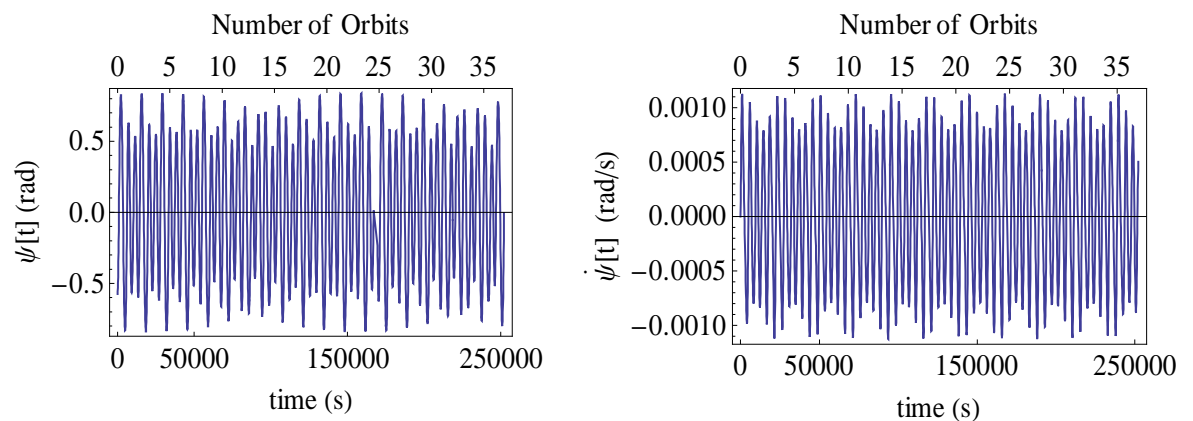


Figure 7.5 : Tether in an oscillation condition on an elliptical orbit

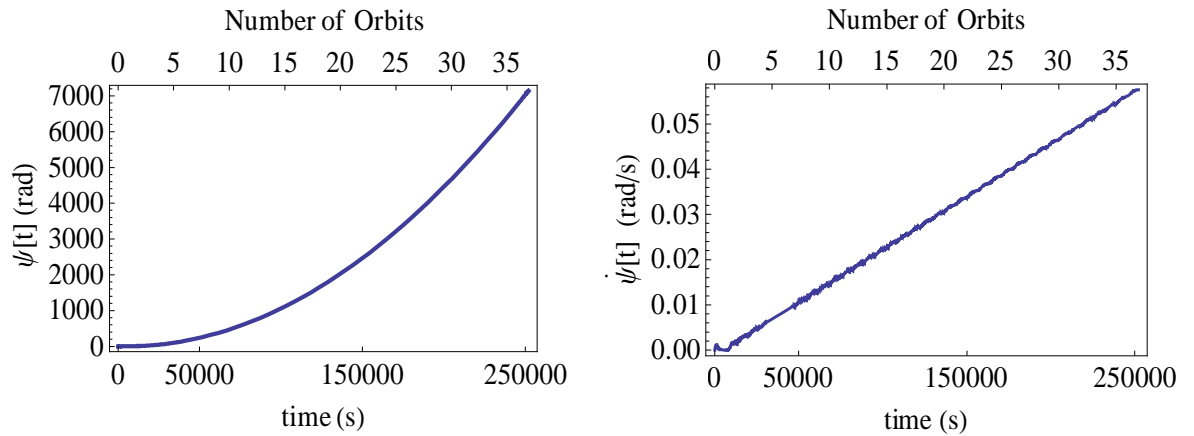


Figure 7.6 : Tether in the pure spin condition with an applied torque of 2.35 MNm on an elliptical orbit

The orbital parameters for the tether are varied throughout the integration time and are shown in Figure 7.7 below,

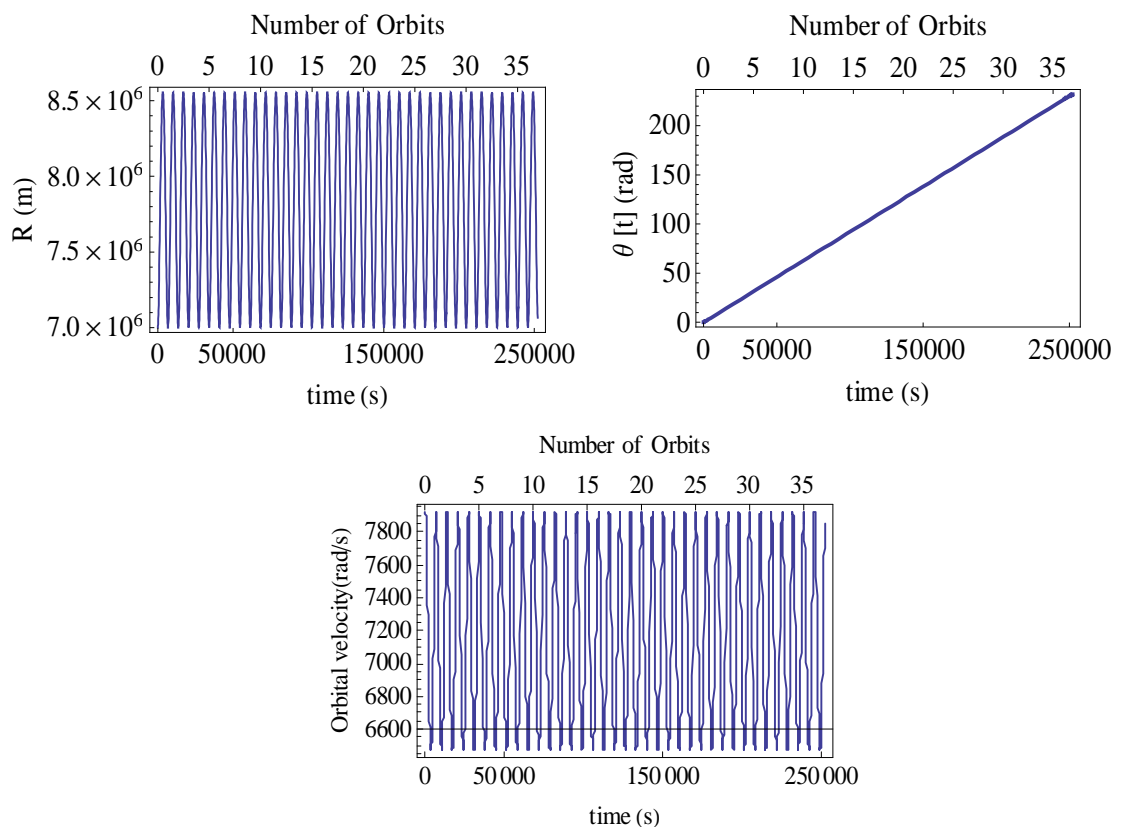


Figure 7.7 : Orbital parameters for an elliptical orbit with a minimum torque of 2.35 MNm

The coupling of the orbital and tether tip velocities on the elliptical orbit advantageously provides a number of possible payload release times, thereby providing possible windows for release to LTO as in Figure 7.8 and defined by t_{r1} , t_{r2} , t_{r3} , and t_{r4} .

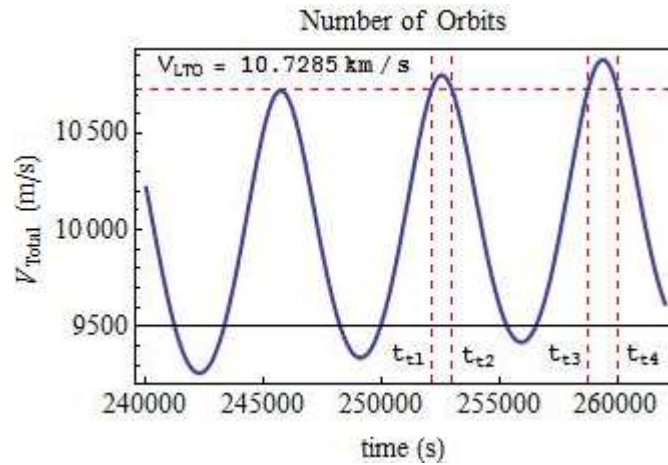


Figure 7.8 : The release payload windows on an elliptical orbit

A different tether length is used for the elliptical orbit analysis and shows the same result as for the circular orbit for which a longer sub-span length and torque value are both necessary to achieve the monotonic spin condition but in a shorter time to payload release, as shown in Figure 7.9 and Figure 7.10.

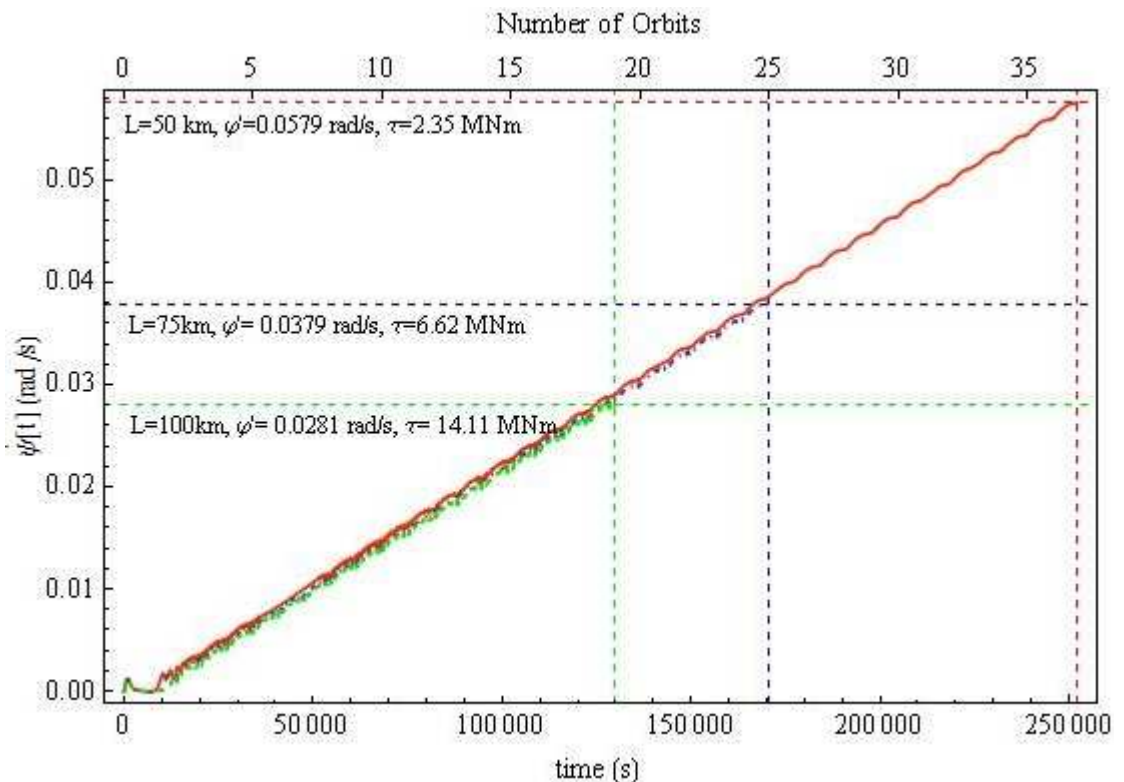


Figure 7.9 : Angular velocity for the spin up condition for a tether on an elliptical orbit.

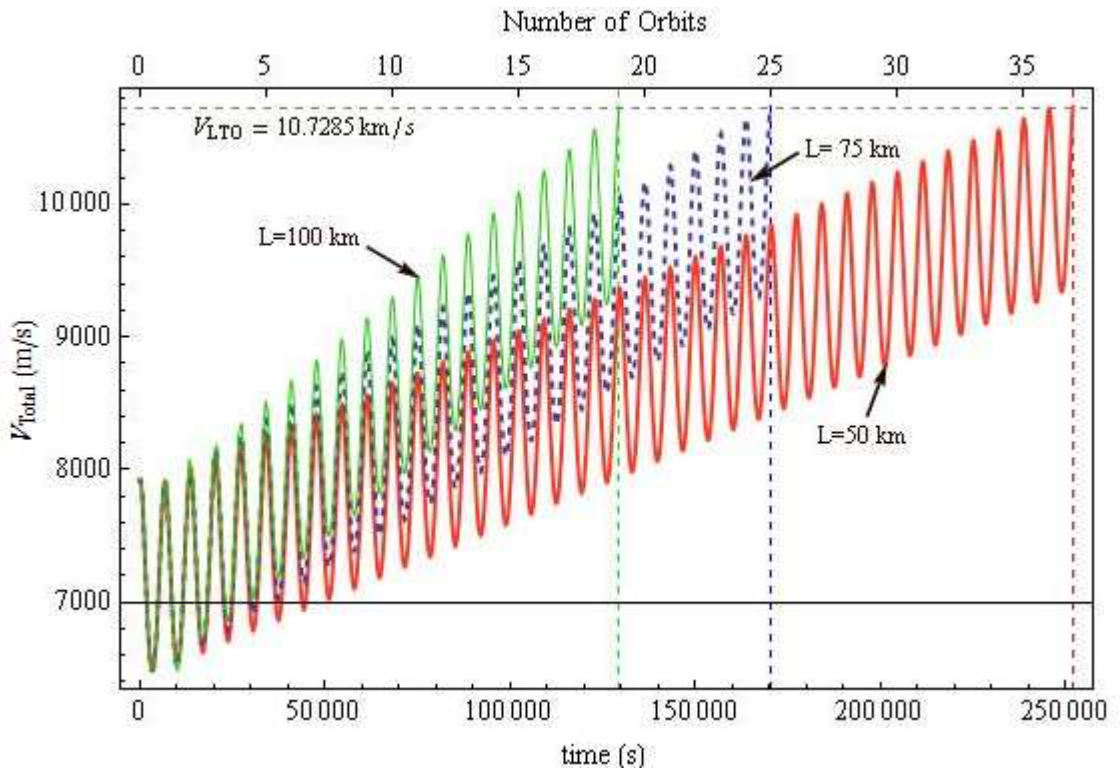


Figure 7.10 : Time to release the payload for L=50km (red), 75km (blue), and 100km (green)

7.4 Comparison of Orbital Performance.

Figure 7.11 shows the differences in angular velocity and time required to release the payload for the tether located on circular and elliptical orbits.

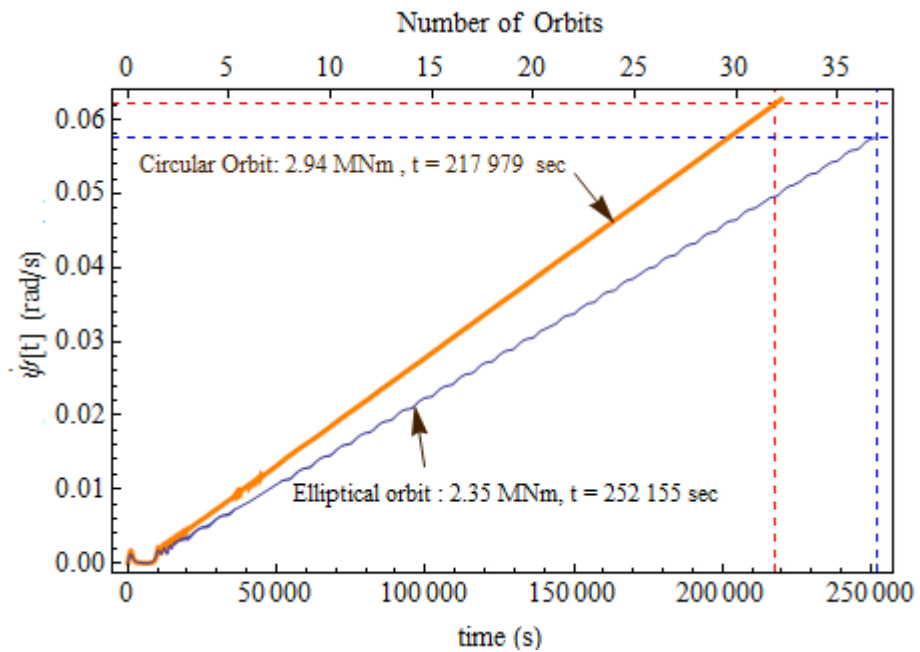


Figure 7.11 : Angular velocity for the tether on circular and elliptical orbits with the application of minimum torque.

With the same length of tether sub-span, the tether on the circular orbit requires more torque to achieve the spin up condition but requires less time to get to the point where the payload can be released, as compared with the tether on the elliptical orbit.

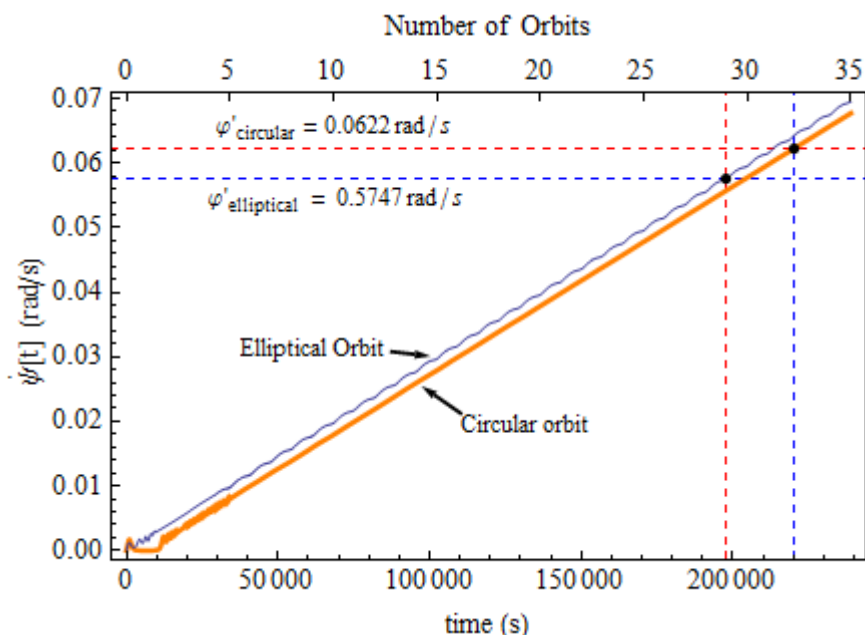


Figure 7.12 : Angular velocity of the tether on circular and elliptical orbits with 2.94 MNm torque

However, with the same amount of torque it is seen that the elliptical orbit provides a higher angular velocity over time than that attainable on the circular orbit, as shown in Figure 7.12. The circular orbit condition reaches the right velocity for payload release later than the elliptical orbit configuration, which suggests that placing the tether on the elliptical orbit can reduce the power requirement for the system on the simple basis of power equating to the product of applied torque and angular velocity.

7.5 Operational conditions

The operational conditions for an MMET over one duty cycle proposed in Ismail (2007), and in the further study by Gandara and Cartmell (2009) consist of spin-up, torque off and de-spin conditions.

7.5.1 Spin-up

This is the conditions in which the angular velocity monotonically increases and in which there is coupling with the orbital velocity to achieve escape velocity for payload release. The examples of tether response in this condition are shown in Figure 7.3 and Figure 7.6.

7.5.2 Torque off

The condition approaches when the tether reaches its required tangential velocity and the payload is released. The torque is switched off for a few second before being reversed to slow the tether down to zero angular velocity. In this study the torque is reduced to zero for 60 seconds. Figure 7.13 and 7.14 show the tether responses in the torque off condition over 60 seconds for both orbits.

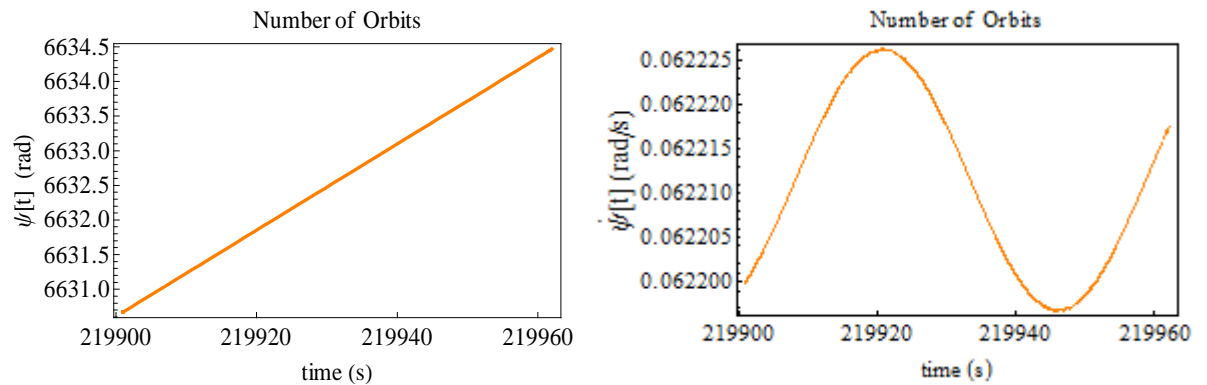


Figure 7.13 : Tether responses in the torque off condition for the circular orbit

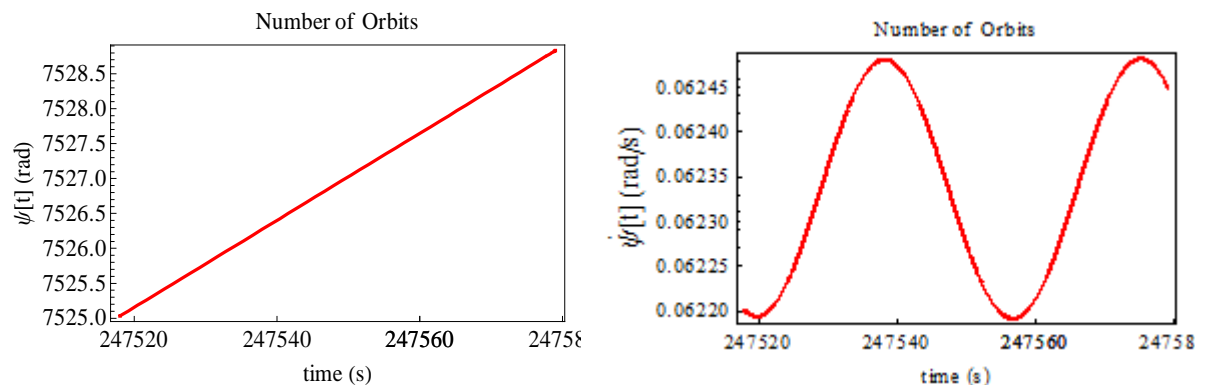


Figure 7.14 : Tether responses in the torque off condition for the elliptical orbit

7.5.3 De-Spin

A reverse torque is applied so that the tether decelerates to an angular velocity of zero before starting to spin up in the opposite direction. This analysis provides a better understanding of the dynamics, and the controllability of the MMET system, and is particular important if there is a tendency for instabilities to occur after payload release.

Figure 7.15 below shows that the tether reaches zero angular velocity for circular and elliptical orbits and the angular displacement is reducing which suggests that the tether is spinning in the opposite direction.

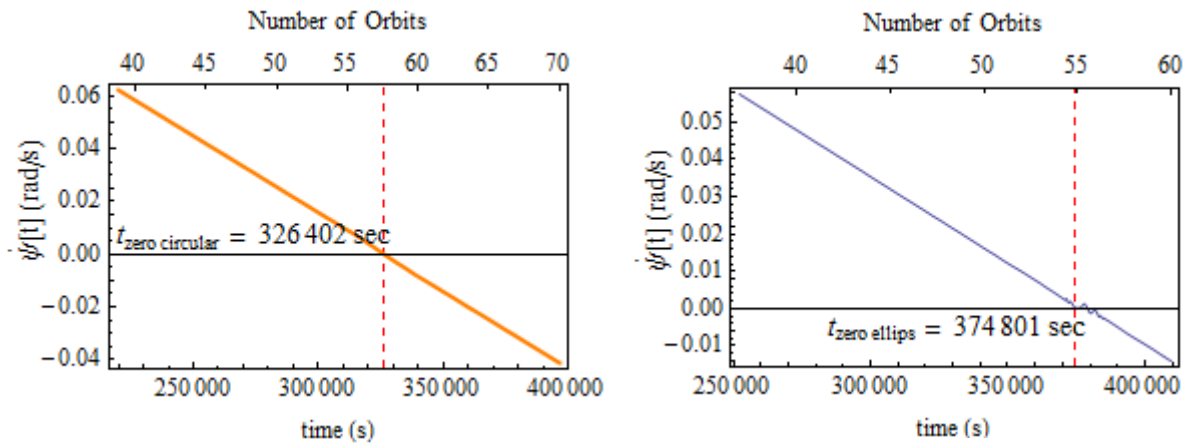


Figure 7.15 : The angular velocity of the tether on circular and elliptical orbits in the de-spin condition.

7.5.4 Complete Profile

The full profiles for one operational cycle for both the circular and elliptical orbits are presented in Figure 7.16 and 7.17, noting the different minimum applied torques. The time for payload release for the circular orbit is at $t = 219\,901$ s, and $t = 252\,115$ s for the tether on the elliptical orbit.

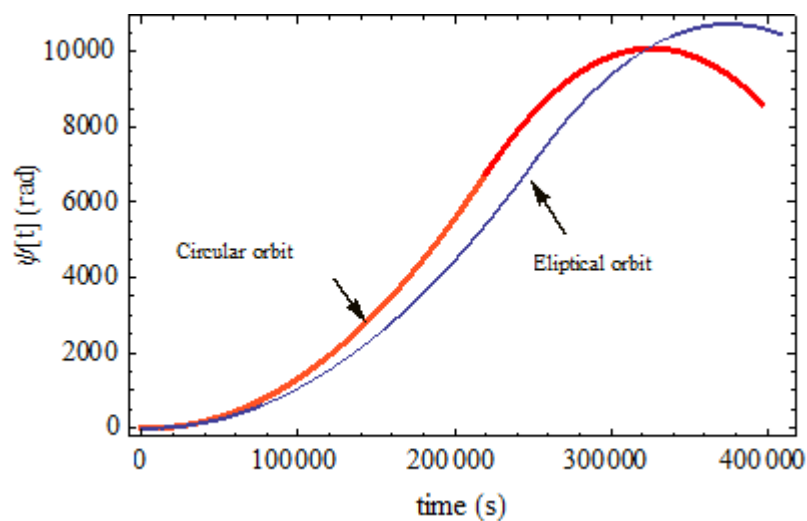


Figure 7.16 : Profile of the angular displacement for one cycle of the operational conditions

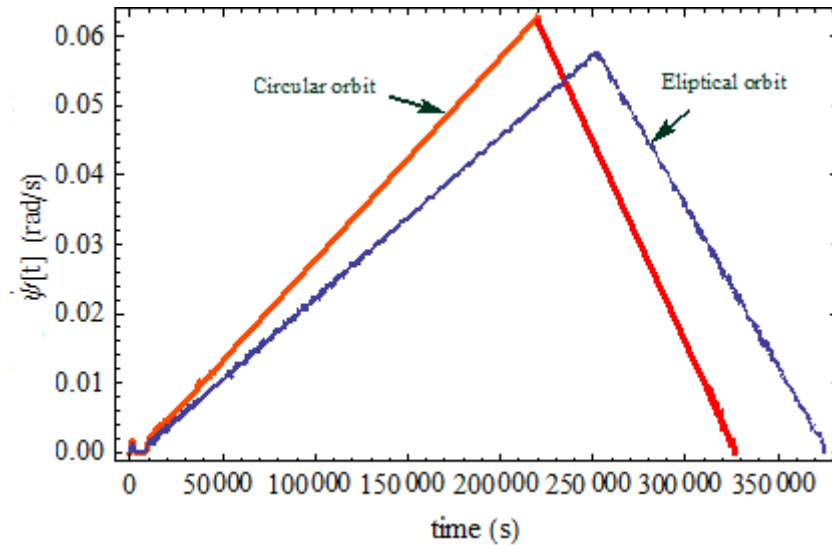


Figure 7.17 : Profile of the angular velocity for one cycle of the operational conditions

7.6 Power Consumption and Energy

The power consumed by the tether is simply calculated from,

$$P_t = \tau \dot{\psi} \quad (7.4)$$

where τ is the applied torque and $\dot{\psi}$ is the angular velocity of the tether. The total cyclical energy demand for the tether is calculated from,

$$E_t = P_t t_{total} \quad (7.5)$$

where t_{total} is the period of operation.

The power profiles for the tether operating on both orbits are presented in Figure 7.18. The tether on the circular orbit consumed a maximum of 185.6 kW to spin up to the required angular velocity. Also, the energy of the tether is depicted by the area under the power/time plots for which 29.67 GJ. The tether on the elliptical orbit used a maximum power of 135.6 kW to spin up the tether and the total energy used by the tether was 25.29 GJ. In comparison, the tether on the elliptical orbit generally used less than the circular configuration, with a nominal difference of around 4.38 GJ.

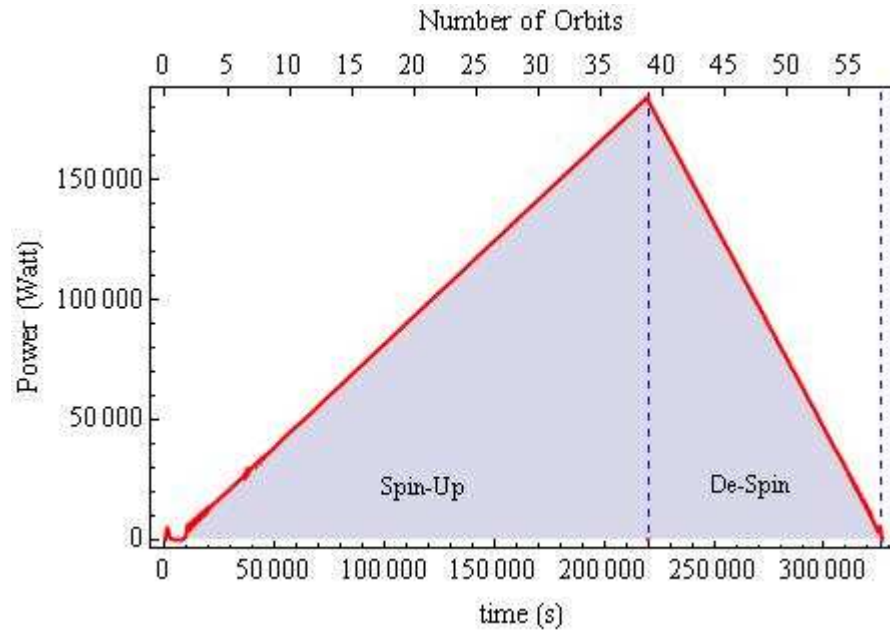


Figure 7.18 : Power profile for the tether on a circular orbit

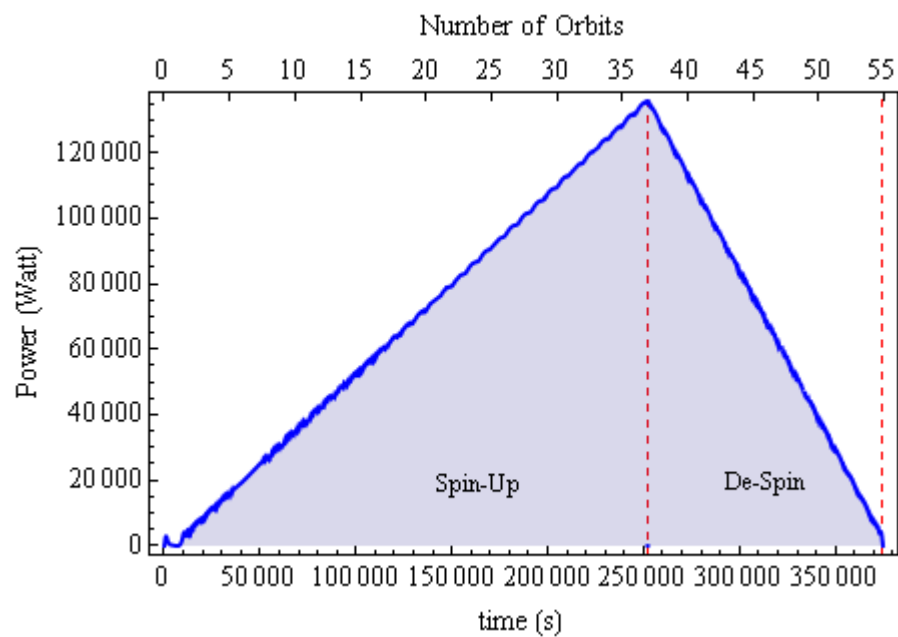


Figure 7.19 : Power profile for the tether on an elliptical orbit

7.7 Power Profile of Rigid and Flexible Tether Models

The simple rigid body model discounts all potentially important flexural characteristics of the tether sub-spans, and significant phenomena may not be captured as a result of such simplification. However, power consumption calculations can be more tractable when based on rigid body models and so in this section some useful comparisons are made between the two modelling paradigms by Ziegler (2001) and the model proposed by Ismail

and Cartmell (2009), for a nominal sub-span length of 50 km. The difference of the power consumed between both models is due to the difference of $\dot{\psi}$ value.

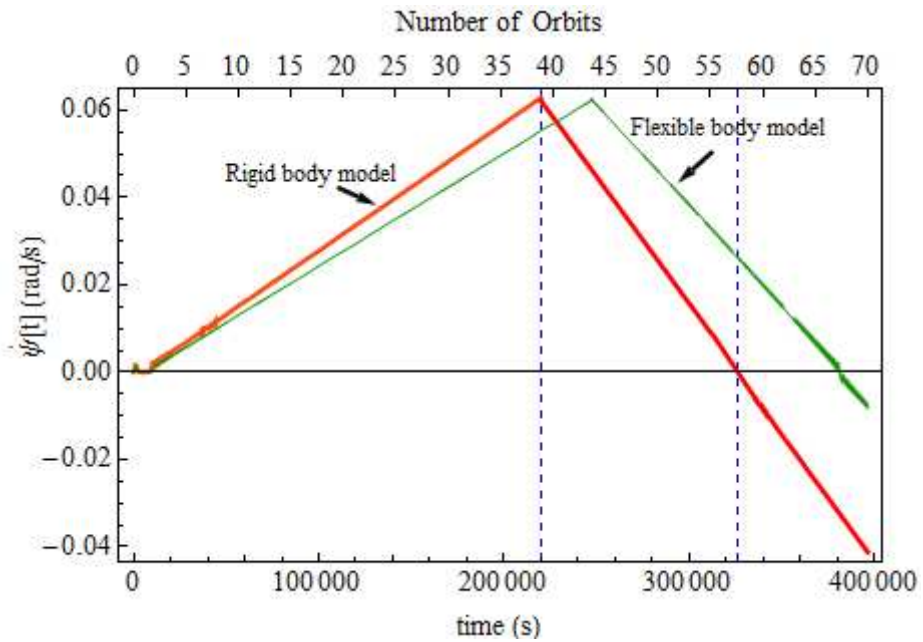


Figure 7.20 : The difference in angular velocities between the rigid body model and flexible model of the tether on a circular orbit

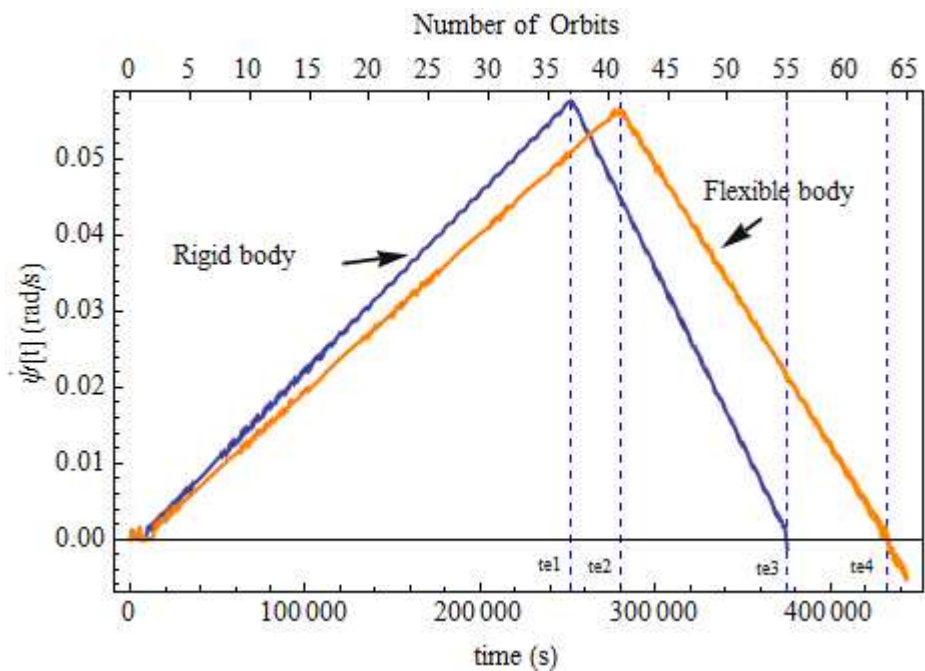


Figure 7.21 : The difference in angular velocities between the rigid body model and the flexible model on an elliptical orbit

Figures 7.20 and 7.21 show the differences in angular velocities predicted by both models when on circular and elliptical orbits. It shows that the more flexible the tether the slower the response. Furthermore, the power consumption for both models on the circular orbit is shown in Figure 7.22 where the total energy used by the rigid body model is 29.67 GJ and

34.66 GJ for the flexible model, the rigid body tether on the elliptical orbit is shown in Figure 7.23 and uses 25.41 GJ of energy, and 28.79 GJ for the flexible tether model. This indicates that the less tractable flexible model dynamics are actually far more useful in practice.

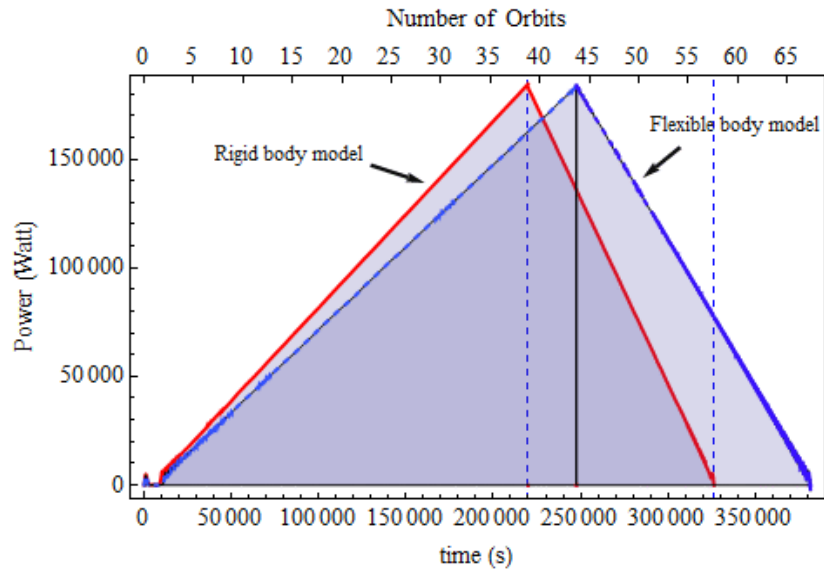


Figure 7.22 : Power profile for the rigid body and flexible models of the tether on a circular orbit

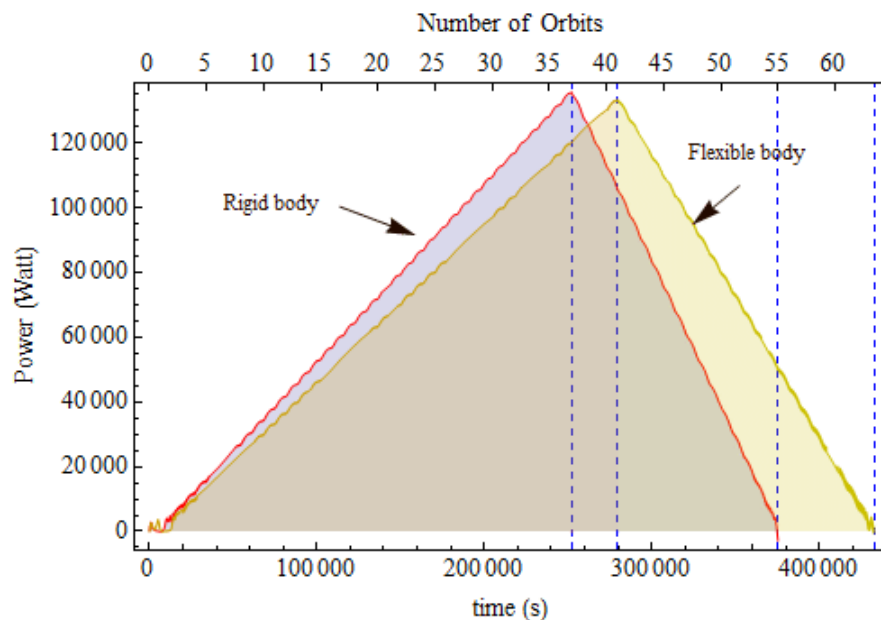


Figure 7.23 : Power profile for the rigid body and flexible models of the tether on an elliptical orbit

7.8 Outrigger system

The outrigger system comprises a pair of tethers attached to the gear-motor stator and necessarily spins up in the opposite direction to the propulsion tether hitherto discussed. In this study, the outrigger tether sub-span is assumed to be 25 km in length, with symmetrically positioned end masses, each of 500 km. Clearly each tether experiences an equal and opposite torque. Figure 7.24 and Figure 7.25 show a full cycle profile of the outrigger system on the circular orbit.

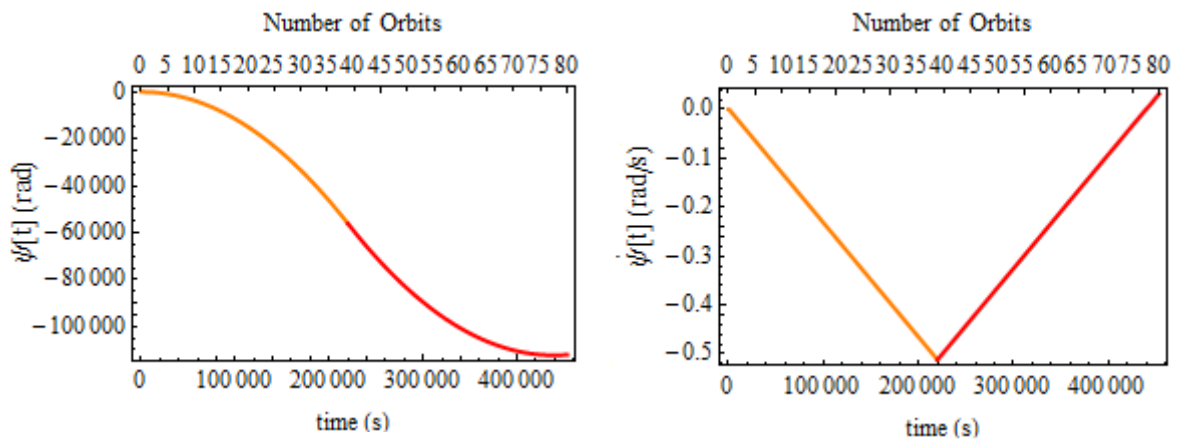


Figure 7.24 : Responses of the outrigger system on a circular orbit

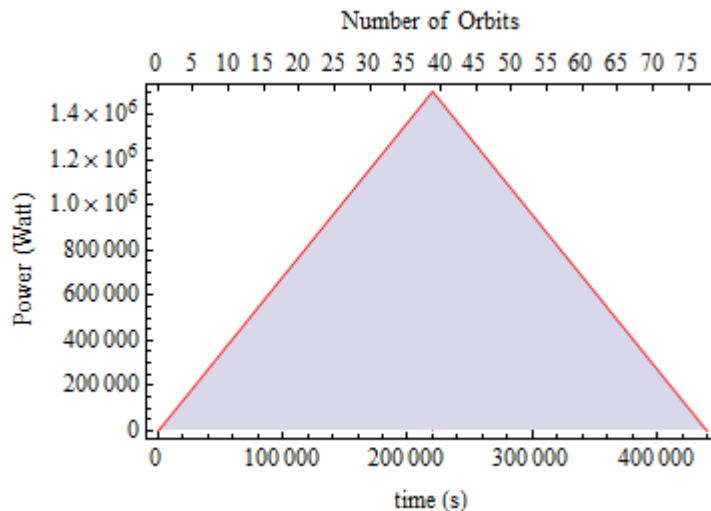


Figure 7.25 : Power consumption of the outrigger system on the circular orbit

Figure 7.26 and Figure 7.27 compare the angular velocities of the outrigger and propulsion tethers on the circular orbits and shows a residual spin of the outrigger system when the propulsion system has come to absolute rest. This indicates that additional energy is needed to de-spin the whole system to absolute zero.

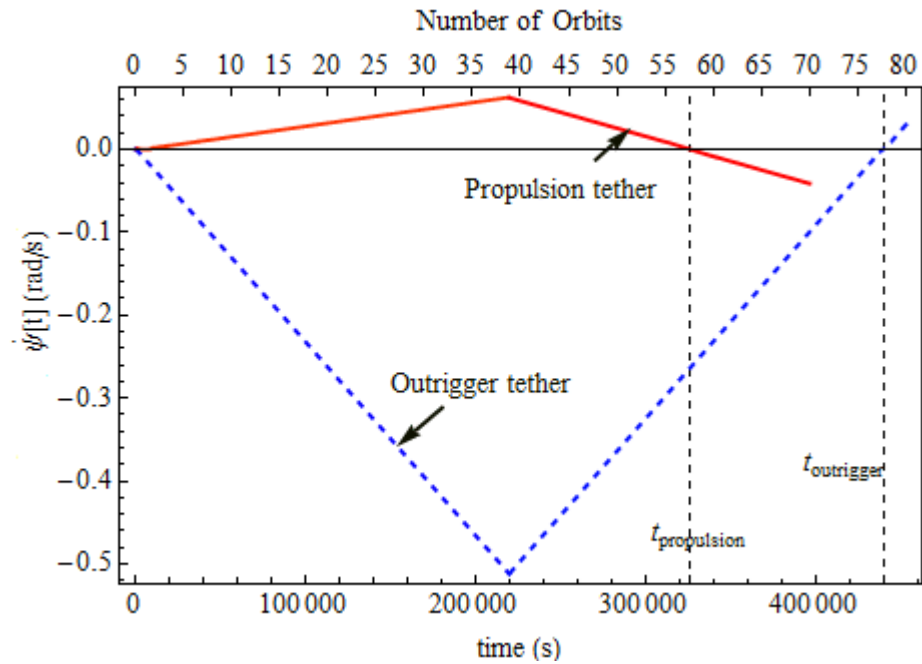


Figure 7.26 : Angular velocity profile for the propulsion and outrigger tethers on a circular orbit

At payload release a very large proportion of the mass on the propulsion tether side of the system is removed, and so the associated angular momentum goes with that payload. This affects the next stage of calculation when the torque is to be switched off and then de-spin initiated. Clearly angular momentum is conserved across the whole system, as required and so additional energy is required to de-spin the remaining propulsion side as well as the outrigger side. It is also evident from Figure 7.26 that the outrigger tether is fully de-spun at the 79th orbit, and substantial energy is required to achieve this, nominally 330 GJ.

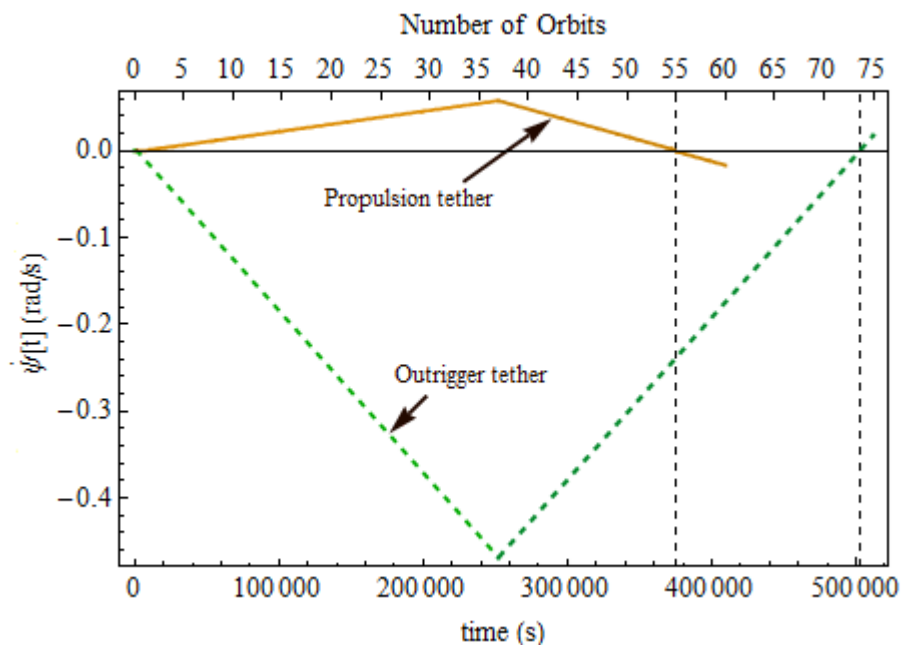


Figure 7.27 : Angular velocity profile for the propulsion and outrigger tethers on an elliptical orbit.

Ziegler (2003) discussed the design of the outrigger system to meet the requirements, as the shorter outrigger requires larger end masses than the longer propulsion tether, with obvious reduction in outrigger end-mass requirements as outrigger sub-spans are increased. Recalculating the energy consumed by the outrigger system for an MMET on a circular orbit until the time reached for full de-spin suggests a figure of 286.3 GJ, with a total cyclical energy requirement of 316 GJ. This is substantially more than 265.5 GJ calculated for the same system operating on an elliptical orbit, which is shown on Figure 7.27 where the outrigger system is fully de-spun by the 75th orbit.

7.9 Energy Comparison

The benefit of having a space tether to transport payload is to save on total operational cost. Therefore, a comparative study in term of energy consumed to transport a payload to desired orbit between the tethers with a conventional system has been carried out. The conventional system, used for in this study, refers to a rocket system.

7.9.1 Rocket System

The rocket performance in term of energy is given by the following equation,

$$KE = \frac{1}{2}mv^2 = \frac{1}{2}m(Isp \cdot g_o)^2 \quad (7.6)$$

Where Isp is the specific impulse of the rocket, g_o is gravity constant which is 9.81 m/s^2 , and m is the fuel mass of the rocket and v is refers to velocity of exhaust gases.

The energy comparison between the tether system and a conventional system is based on earlier work of Cartmell *et al.* (2006). The study shows that the total ΔV for a translunar rocket approach is 4.5766 km/s, and that for rocket fuel alone, 8.76 GJ is required to get the reducing mass of fuel into translunar injection. The energy consumed is higher still when it includes the payload mass and the mass of rocket structure.

The conventional rocket system is also non-reusable and it should also be noted that the electricity required for the gear-motor could provide by high capacity batteries, backed up by suitable solar photovoltaics. The energy demand could also be substantially reduced by employing a multi-staging tether as described by Cartmell and Ziegler (1999) where less power is required to operate the system.

Parameters	Tether at LEO	Tether at EEO
Angular Velocity (rad/s)	$\omega_{LEO} = 0.00437$	$\omega_{EEO} = 0.01065$
Sub-span length (km)	$L_{LEO} = 200$	$L_{EEO} = 75$
Semi major axis (km)	$a_{LEO} = 7922.57$	$a_{EEO} = 26159.8$
Perigee (km)	$rp_{LEO} = 6728$	$rp_{EEO} = 7003$
Period (sec)	$P_{LEO} = 7017.95$	$P_{EEO} = 42107.7$
Velocity tether tip (km/s)	$V_{LEOTip} = 0.874$	$V_{EEOtip} = 0.798$

Table 7.1 : Orbital and tether parameters for the Earth-Moon Payload Exchange, after Cartmell & Ziegler, 1999.

Therefore, the total power to transfer the payload from Sub-Earth Orbit to Lunar Transfer orbit is 43.2 kW which equates to a total energy demand of 3.63 GJ, not including the energy associated with the outrigger system. Applying the default values for the system the calculation of power consumption and outrigger energy demand can be estimated from numerical integration of the system equation of motion, leading to prediction of 11.0 GJ for the LEO system outrigger and 4.89 GJ for the EEO tether outrigger using the outrigger data as in Table 7.2. On this basis the total energy demand is 19.52 GJ.

Outrigger Tether Parameters	Tether at LEO	Tether at EEO
Length (km)	$L_{O,LEO} = 50$	$L_{O,EEO} = 35$
Velocity tether tip (km/s)	$M_{LEOoutrigger} = 0.874$	$M_{EEOoutrigger} = 0.798$

Table 7.2 : Parameters for the outrigger system

7.9.3 Systems Comparison

The energy usage by single and multi-staging tether systems for payload transfer to Lunar Transfer Orbit are compared in Table 7.3 below,

Single Tether system	Staged system
188.00 GJ	19.52 GJ

Table 7.3 : Energy usage comparison for payload transfer to the moon

Apparently, the staged system provides a substantial ten-times reduction in the predicted energy requirement for the lunar transfer mission. Also, MMET energy usage may be reduced even more if the outrigger system properties are manipulated further.

7.10 Conclusions

The power requirements for the MMET have been investigated and a comparison has been made with a conventional chemical rocket propulsion system to observe the significance of the use of the MMET for space transportation. The analysis shows that the power requirement for single tether is very high when compared with a conventional system but it should be emphasized that the energy of conventional rocket system is for one-off use, and cannot be reused. The energy usage could also be reduced by implementing multi-staging tethers to transfer the payload. The energy resource for the tether could be generated by a solar power system and could be virtually continuously available dependent on the system's location with respect to the sun, which makes the MMET is potentially rather superior to chemical propulsion.

Chapter 8

Conclusions

8.1 Summary and Conclusions

The equations of motion for two dimensional modelled as an assumed string have been derived by applying Lagrange's equation for the tether on circular and elliptical orbits. The tether equations of motion are nonlinear differential equations up to cubic orders of nonlinearity, and also show coupling terms between the longitudinal and transverse coordinates. This 2D study gives a good basis in understanding how the flexibility changes the tether's motion in space. The comparative studies presented in this chapter have shown that the flexibility changes the global motion of the tether in both the torque and untorqued conditions. The changes, however, are small but can be significant in cases where the precise prediction of motion required. For the case of the MMET, this will impact on the vital application of payload catching and release when used as a payload exchange system.

The relationships between planar and nonplanar motions have been explored in Chapter 4 and the 3D local displacements have been included in the tether's equation of motion. In the beginning of Chapter 4, different models for tethers have been considered and the different responses between them have been investigated. The results have clearly shown that for the tether with the inclusion of rotational kinetic energy the frequency of non-planar motion increase. By introducing flexibility into the tether, the planar motion shows insignificant differences from that of the rigid body tether, for both the untorqued and torqued conditions in circular and elliptical orbits. But, the difference is evident in the nonplanar motion in both conditions. In comparison with the 2D model, the existence of the non-planar variable (α) in the EOM of the 3D model does not provide significant influence on the planar motion of the tether. In this chapter, the transverse vibration was again to be found to behave in terms of decaying motion with the application of torque. With an applied torque the displacement in the longitudinal direction increases, but both the transverse and lateral displacements reduce. This phenomenon is connected to the stiffening effect due to the centripetal load experienced by the spinning tether. The centripetal load in the longitudinal direction increases the axial displacement, whilst the lateral stiffening effect reduces the vibration in the transverse and lateral directions. The exponential growth of the longitudinal displacement in torqued condition suggests the relationship between the displacement and the force applied to the tether and in the case of

spinning tether, the force refers to the centripetal force. Therefore, the increase of the applied torque has increased the centripetal force and consequently increases the axial displacement.

In Chapter 5, new boundary conditions have been introduced for developing the equations of motion for the flexible tether. This study has shown that the selection of mode shapes and boundary conditions have significant influences on the global motion of the tether. The natural frequencies for the static boundary conditions and dynamic boundary conditions have shown measureable differences. The frequency is also found to be affected by the physical configuration of the tether where the longer tether has a lower frequency as compared to that of the shorter tether. The complexity of the mode shape function, derived by applying dynamic boundary conditions has contributed to the presence of a third order time derivative in the equation of motion. This chapter also suggests that the longitudinal mode shape function is more complex than that for the transverse direction.

The dynamics of the flexible tether are investigated using the dynamical tools in Chapter 6 to study the links between regular and chaotic motion. The eccentricity and the initial conditions have been found to have a strong influence on the libration/spin motion, and also the variation of those parameters we seen to contribute to the route to chaotic motion. The flexural effect in the tether has been proven to be significant in a faster route to motion in tumbling and chaos. In the flexible model, the variation of initial conditions in the local displacement does not alter the total global motion of the tether. The velocity increment has also found to be affected by the variation of orbit eccentricity and the initial conditions. The flexibility alters the differences in the total response, but at lower value. In the payload transfer application, the ΔV requirement needs to be precisely met to ensure that the tether is able to catch the payload and also to deliver it to the designated orbit. So, even small differences in ΔV may affect this transfer process. This small difference effect was uncovered in this chapter, when the response between the rigid body tether and the flexible tether are mutually compared.

Finally, the effect of the flexibility of the tether was explored further for the payload transfer application by comparing the power requirement for the MMET using a flexible and rigid body model. This study shows that the less tractable flexible model dynamics are actually far more useful in practice. The analysis has shown that the power requirement for a single tether is very high when compared with a conventional system, but it should be

emphasized that the energy needed for a conventional rocket system is for one-off use, and it cannot be reused.

8.2 Future work

The dynamics of the flexible tether can be explored further by investigating the effect of flexibility on the tether deployment and retrieval. These two phases are critical to the tether's dynamics. Therefore, there should be more interesting work to be done to uncover the connection between tether's flexibility and the variation of tether length.

- The simple assumption may provide a good basis for study, but it is suggested to include all perturbation factors in developing the flexible model of the tether.
- The study of longitudinal vibration with dynamic boundary conditions can also be further investigated in the future with the availability of more advanced computing software and hardware.
- The route to chaotic motion can be further explored by using other dynamical tools such as Lyapunov exponents and basin of attraction to provide more evidence that the flexibility may affect the tether's motion to chaos.
- Finally, further work is suggested on the analysis of tether strength and material, with a suggestion for the tether's structure for engineering design so that more in-depth analysis can be carried to understand the dynamics of the flexible tether.

References

- ARNOLD, J. R. and THOMPSON, W. B. (1992). "Advanced Propulsion for LEO-Moon Transport. 2: Tether Configurations in the LEO-Moon System", *The Second Conference on Lunar Bases and Space Activities of the 21st Century*, NASA, Johnson Space Center, Vol. 1, pp. 55-59.
- ASHIDA, H., FUJIHASHI, K., INAGAWA, S., MIURA, Y., OMAGARI, K., MIYASHITA, N., MATUNAGA, S., TOIZUMI, T., KATAOKA, J., and KAWAI, N. (2010). "Design of Tokyo Tech nano-satellite Cute-1.7+APD II and its Operation", *Acta Astronautica*, Vol. 66, No.9, pp. 1412-1424.
- BAINUM, P.M., AND KUMAR, V.K. (1980). "Optimal Control of the Shuttle-tethered System", *Acta Astronautica*, Vol. 7, pp. 1333–1348.
- BANERJEE, A.K. (1990). "Dynamics of Tethered Payloads with deployment Rate Control", *Journal of Guidance Control and Dynamics*, Vol. 13, pp. 759-762.
- BEKEY, I. (1983). "Tethers open new space options", *Astronautics and Aeronautics*, Vol. 21, No. 4, pp. 32–40.
- BEKEY, I., and PENZO, P.A. (1986). "Tether propulsion", *Aerospace America*, Vol. 24, No.7, pp. 40–43.
- BELETSKY, V.V, and LEVIN, E.M. (1985). "Dynamics of the Orbital Cable System", *Acta Astronautica*, Vol. 12, Issue 5, pp. 285-291.
- BELETSKY, V.V., and LEVIN, E.M. (1983). "Dynamics of the Orbital Cable System", *Proceeding of 34th International Astronautical Congress*, International Astronautical Federation 10-15 October, Budapest, Hungary.
- BELETSKY, V.V, and LEVIN, E.M. (1993). "Dynamics of Space Tether Systems", Vol.83, *Advance in the Astronautical Sciences*, American Astronautical Society, San Diego, USA.
- BISWELL, B.L., PUIG-SUARI, J., LONGUSKI, J.M, and TRAGESSE, S.G. (1998). "Three-Dimensional Hinged-rod Model for Elastic Aerobraking Tethers," *Journal of Guidance Control and Dynamics*, Vol. 21, pp. 286-295.
- BISWELL, B.L, and PUIG-SUARI, J. (1998). "Lifting Body Effects on the Equilibrium Orientation of Tethers in the Atmosphere", *Acta Astronautica*, Vol. 43, No. 9-10, pp. 521-529.

- CARROLL, J.A. (1986). "Tether Applications in Space Transportation," *Acta Astronautica* Vol. 13, No.4, pp. 165–174.
- CARROLL, J.A., and OLDSON, J. (1995). "SEDS Characteristics and Capabilities", Proceeding of 4th International Conference on Tethers in Space, pp. 1079-1090.
- CARTMELL, M. P. (1998) "Generating Velocity Increments by Means of a Spinning Motorized Tether", 34th AIAA/ASME/SAE/ASEE Joint Propulsion Conference and Exhibit, Cleveland, AIAA Paper 98-3739, 20-24 June, Ohio, USA.
- CARTMELL, M. P., and MCKENZIE D.J. (2008), "A review of Space Tether Research" *Progress in Aerospace Sciences*, Vol. 44, No.1, pp. 1-21.
- CARTMELL, M. P., and ZIEGLER, S.W. (1999). "Symmetrically Laden Motorised Tethers for Continuous Two-way Interplanetary Payload Exchange" 35th AIAA/ASME/SAE/ASEE Joint Propulsion Conference & Exhibit, AIAA Paper 99-2840, 20-24 June, Los Angeles, California, USA.
- CARTMELL, M.P. (1999). Personal Communication, String Modelling Notes, University of Glasgow.
- CARTMELL, M.P., and MCKENZIE, D..J (2006). "Large Tether and Web Structures in Space", Proceeding of Symposium on the Mechanics of Slender Structures, University of Northampton & Institute of Physics, 28-29 September, Northampton, UK.
- CARTMELL, M.P., MURRAY, C., RADICE, G., VASILE, M., and VILLANTI, M. (2006). "Lunar Exploration Architecture, Continuous Earth Moon Cargo Exchange Using Tethers and Hybrids Propulsion", Department of Aerospace Engineering and Department of Mechanical Engineering, University of Glasgow, UK.
- CHAPEL J.D., and FLANDERS, H. (1993) "Tether Dynamics and Control Result for Tethered Satellite System Initial Flight", in *Journal Guidance, Dynamic and Control*, Vol. 81, pp. 327-346.
- CHEN, Y. (2009). "Dynamical Modelling of a Flexible Motorised Momentum Exchange Tether and Hybrid Fuzzy Sliding Mode Control for Spin-up", PhD. Thesis, Department of Mechanical Engineering, University of Glasgow, Glasgow, UK.
- CHEN, Y., and CARTMELL, M.P. (2007). "Multi-objective optimization of the Motorised Momentum Exchange Tether for Payload Orbital Transfer", *IEEE Congress on Evolutionary Computation*, 25-28 September, Singapore.

- CLARKE, A.C. (1981). "The Space Elevator: Thought Experiment or Key to the Universe" *Advanced in Earth Oriented Applications of Space Technology*, Vol. 1, pp. 39-48.
- COLOMBO, G., GOPOSCHKIN, E. M., GROSSI, M. D., and WEIFFENBACH, G.C. (1974). "Shuttle Borne Skyhook : A New Tool for Low-Orbital-Altitude Research" Smithsonian Inst. Astrophysical Observatory Rept. Contract NAS8-02138, Cambridge, MA.
- COLOMBO, G., MARTINEZ-SANCHEZ, M., and ARNOLD, D. (1982). *The Use of Tethers for Payload Orbital Transfer*, Smithsonian Astrophysical Observatory NASA-CR-170714, NAS8-33691, Cambridge, MA.
- COSMO, M. L., and LORENZINI, E. C. (1997). *Tethers in Space Handbook*, 3rd Edition, Smithsonian Astrophysical Observatory, Grant NAG8-1160.
- DANILIN, A.N., GRISHANINA T.V., SHKLYARCHUK F.N., and BUZLAEV D.V. (1999) "Dynamics of a Space Vehicle with Elastic Deploying Tether", *Computers and Structures*, Vol. 72, No.1, pp. 141-147.
- DECOU, A.B. (1989). "Tether Static Shape for Rotating MultiMasses, Multitether, Spacecraft for Triangle Michelson Interferometer", *Journal of Guidance, Control and Dynamics*, Vol. 12, No.2, pp. 273-275.
- ESTES, R.D., LORENZINI, E.C., SANMARTIN, J., PELAEZ, J., MARTINEZ-SANCHEZ, M., JOHNSON, C.L., and VAS, I. E. (2000). "Bare Tether for Electrodynamic Spacecraft Propulsion", *Journal of Spacecraft and Rocket*, Vol. 37, No.2, pp. 205-211.
- FUJII, H. A., and ICHIKI, W. (1997). "Nonlinear Dynamics of the Tethered Subsatellite System in the Station Keeping Phase", *Journal of Guidance, Control and Dynamics*, Vol. 20, No.2, pp. 403-406.
- FUJII, H. and ISHIJIMA, S. (1989). "Mission Function Control for Deployment and Retrieval of a Subsatellite" *Journal of Guidance, Control, and Dynamics*, Vol. 12, No. 2, pp.243-247.
- FUNG, Y.C. (1994). *A First Course in Continuum Mechanics*, 3rd Edition, Prentice-Hall, Englewood Cliffs.
- GANDARA, C.C., and CARTMELL, M.P. (2009). "De-Spin of a Motorised Momentum Exchange Tether" *Proceeding of XXXVII International Summer School on Advanced Problem in Mechanics*, St Petersburg, Russia.
- HAMMOND, W.E., (1999). *Space transportation: A Systems Approach to Analysis and Design*, Volume 1, American Institute of Aeronautics and Astronautics, Reston, VA.

- HE, X., and POWELL, J.D. (1990), "Tether Damping in Space", *Journal of Guidance, Control, and Dynamics*, Vol. 13, pp. 104-112.
- HOYT, R.P., and UPHOFF, C. (2000). "Cislunar Tether Transport System", *Journal of Spacecraft and Rocket*, Vol. 37, No. 2, 177-186.
- ISAACS, J., ET AL (1966) Satellite Elongation into a True "Sky-Hook", *Science*, Vol.151, pp. 682-683.
- ISHIGE, Y., KAWAMOTO, S., and KIBE, S. (2004). "Study on Electrodynamic Tether System for Space Debris Removal", *Acta Astronautica*, Vol. 55, No.11, pp. 917-929.
- ISMAIL, N.A., and CARTMELL, M.P. (2009). "Modelling of a Flexible Elastic Tether for the Motorised Momentum Exchange Tether Concept", *Proceeding of. RANM2009*, 24 – 27 August, Kuala Lumpur Malaysia .
- ISMAIL, N.A., and CARTMELL, M.P. (2010a). "The Dynamics of a Flexible Motorised Momentum Exchange Tether with Dynamics Boundary Conditions", *Proceeding of RASD2010*, 12-14 July, Southampton UK .
- ISMAIL, N.A.,and CARTMELL, M.P. (2010b). "In Service Power requirement for a Motorised Momentum Exchange Tether". *Proceeding of 61st International Astronautical Congress*, 27 September to 1 October, Prague, Czech Republic.
- ISMAIL,N.A. (2007). *In Service Power Requirements for a Motorised Momentum Exchange Tether*, MSc Thesis, Department of Aerospace Engineering, University of Glasgow.
- JOKIC, M. D., and LONGUSKI, J. M. (2002). "Design of a Tether Sling for Human Transportation Systems between Earth and Mars", *AIAA/AAS Astrodynamics Specialist Conference and Exhibit*, 5-8 August, Monterey, USA.
- KARASOPOULOS, H., and RICHARDSON, D. L. (1992). "Chaos in the Pitch Equation of Motion for the Gravity Gradient Satellite", *Proceedings of the AIAA/AAS Astrodynamics Conference*, AIAA Paper 92-4369-CP, pp. 53-65m, Hilton Head, South Carolina, USA.
- KAWASHIMA, N., SASAKI, S., OYAMA, K. I., HIRAO, K., ODAYASHI, T., RAITT, W. J., WHITE, A. B., WILLIAMSON, P. R., BANKS, P. M., and SHARP, W. F. (1988). "Results from a Tethered Rocket Experiment (Charge-2)" *Advances in Space Research*, Vol.8, No.1, pp. 197-201.

- KESHMIRI, M., MISRA, A.K., and MODI, V.J. (1996). "General Formulation for N-body Tethered Satellite System Dynamics," *Journal of Guidance Control and Dynamics*, Vol. 19, pp. 75-83.
- KIM, E. and VADALI, S.R. (1995). "Modelling Issues Related to Retrieval of Flexible Tethered Satellite Systems" *Journal Guidance, Control and Dynamic*, Vol. 18, No.5, pp.1169-1176.
- KOKUBUN, K., and FUJII, H.A. (1996) "Deployment/Retrieval Control of a Tethered Subsatellite Under Effect of Tether Elasticity", *Journal of Guidance, Control, and Dynamics*, Vol. 19, No.1, pp. 84-90.
- KROLL, K.R. (1985). "Tethered Propellant Resupply Technique for Space Station", *Acta Astronautica*, Vol. 12, No.12, pp. 987-993.
- KRUIJFF, M., and VAN DER HEIDE, E. J. (2009). "Qualification and in-flight demonstration of a European tether deployment system on YES2", *Acta Astronautica*, Vol. 64, No. 9-10, pp. 882-905.
- KUMAR, K.D. (2006). "Review of Dynamics and Control of Nanoelectrodynamic Tethered Satellite Systems", *Journal of Spacecraft and Rockets*, Vol. 43, pp.705-720.
- LIAW, D.C. and ABED, E. H.(1990). "Stabilization of Tethered Satellites during Station Keeping", *IEEE Transactions on Automatic Control*, Vol. 35, pp. 1186-1196.
- LONGUSKI, J.M., PUIG-SUARI, J., and MECHALAS, J. (1995). "Aerobraking Tethers for the Exploration of the Solar system", *Acta Astronautica*, Vol.35 , pp. 205–214.
- LORENZI, E.C., COSMO, M.L., KAISER, M., BANGHAM, M.E., VONDERWELL, D.J, and JOHNSON, L. (2000). "Mission Analysis of Spinning System for Transfers from Low Orbits to Geostationary", *Journal of Spacecraft and Rocket*, Vol. 37, No.2, pp. 165-172.
- LORENZINI, E. C., GROSSI, M. D., and COSMO, M. (1990). "Low Altitude Tethered Mars Probe", *Acta Astronautica*, Vol. 21, No.1, pp. 1-12.
- LORENZINI, E.C. (2004). "Error-Tolerant Technique for Catching a Spacecraft with a Spinning Tether", *Journal of Vibration and Control*. Vol.10, No.10, pp. 1473-1491.
- LUO, C.J., HAN, R.P.S, TYC, G., MODI, V. J., and MISRA, A.K. (1996). "Analytical Vibration and Resonant Motion of a Stretched Spinning Nonlinear Tether", *Journal Guidance, Control and Dynamics*, Vol. 19, No.5, pp. 1162-1171.
- LUONGO, A., and VESTRONI, F. (1994). "Nonlinear Free Vibrations of a Tethered Satellite System", *Journal of Sound and Vibrations*, Vol.175, pp. 299–315.

- MCINNES, C.R, and CARTMELL M.P. (2006). “Orbital Mechanics of Propellantless Propulsion System”, In: P.Gurfil *Modern Astrodynamics*. Oxford, UK: Academic Press. pp. 218-221.
- MCKENZIE, D.J., “*The Dynamics of Tethers and Space-webs*”, PhD. Thesis, Department of Mechanical Engineering, University of Glasgow, Glasgow, UK, 2010.
- MCKENZIE, D.J., and CARTMELL, M.P. (2004). “On the Performance of a Motorised Tether using a Ballistic Launch Method, 55th *International Astronautical Congress*, Vancouver, Canada.
- MEIROVITCH, L. (2001). *Fundamental of Vibration*, McGraw-Hill, New York.
- MIN, B. Y., MISRA, A. K, and MODI, V. J. (1999). “Nonlinear Free Vibration of a Spinning Tether”, *Journal of the Astronautical Sciences*, Vol. 47, No.1-2, pp. 1-23.
- MISRA, A. K. (2008). “Dynamics and control of tethered satellite systems”, *Acta Astronautica*, Vol. 63, No. 11-12, pp. 1169-1177.
- MISRA, A. K., and MODI, V. J. (1982) “Deployment and Retrieval of Shuttle Supported Tethered Satellites”, *Journal Guidance, Control and Dynamics*, Vol.5, No.3, pp. 278-285.
- MISRA, A. K., and MODI, V. J. (1986). “A Survey on the Dynamics and Control of Tethered Satellite System”, *Advance In the Astronautical Science*, Vol. 62, pp. 667-719.
- MISRA, A.K., and COHEN, S.S. (2007). “Elastic Oscillations Of Space Tethers And The Space Elevator”, In: İnan, E.,Sengupta, D.,Banerjee, M., Mukhopadhyay, B., and Demiray, H. *Vibration Problems ICOVP-2007*, Springer, pp. 281-290, Netherlands.
- MODI, V.J., and BRERETON, R.C (1966). “Libration Analysis of a Dumbbell Satellite Using the WKBJ Method”, *Journal of Applied Mechanics*, Vol. 33, No.3, pp. 676-678.
- MODI, V.J. and MISRA, A.K. (1986). “ A Survey on the Dynamics and Control of Tethered Satellite System”, *Advance In the Astronautical Science*, Vol. 62, pp. 667-719.
- MODI, V.J. and MISRA, A.K.(1979). “On the Deployment Dynamics of Tether Connected Two-body System”, *Acta Astronautica*, Vol.6, pp. 1183–1197.
- MODI, V.J., MISRA, A.K., and GENG, C.G. (1981). “Effect of Damping on the Control Dynamics of the Space Shuttle based tethered system, *Proceedings of the Astrodynamics Conference*, August 3-5, North Lake Tahoe, NV.
- MORAVEC, H. (1977). “A Non-synchronous Orbital Skyhook,” *Journal of the Astronautical Sciences*, Vol. 25, No.4, pp. 307–322.

- NAKASUKA, S., AOKI, T., IKEDA, I., TSUDA, Y., and KAWAKATSU, Y. (2001). “ ‘Furoshiki Satellite’ a Large Membrane Structure as a Novel Space System”, *Acta Astronautica*, Vol. 48, No.5-12, pp.461–468.
- NAKASUKA, S., FUNANE, T., NAKAMURA, Y., NOJIRI, Y., SAHARA, H., SASAKI, F., and KAYA, N. (2006). “Sounding Rocket Flight Experiment for demonstrating “Furoshiki Satellite” for Large Phased Array Antenna”, *Acta Astronautica*, Vol.59, No.1-5, pp. 200-205.
- NAYFEH, A.H, and MOOK, D.T. (1979). *Nonlinear Oscillations*, J. Wiley, New York.
- NETZER, E., and KANE, T.R. (1993). "Deployment and Retrieval Optimization of a Tethered Satellite System", *Journal of Guidance Control and Dynamics*, Vol. 6, pp. 1085-1091.
- NETZER, E., and KANE, T.R. (1995). "Estimation and Control of Tethered Satellite Systems”, *Journal of Guidance Control and Dynamics*, Vol.18, pp. 851-858.
- NO, T. S., and COCHRAN JR. J. E. (1995). “Dynamics and Control of a Tethered Flight Vehicle”, *Journal of Guidance, Control, and Dynamics*, Vol. 18, No.1, pp. 66-72 .
- PEARSON, J. (1975). “The Orbital Tower: A Spacecraft Launcher using the Earth’s Rotational Energy”, *Acta Astronautica*, Vol. 2, No. 9-10, pp.785–799.
- PEARSON, J. (1979). “Anchored Lunar Satellites for Cislunar Transportation and Communication”, *Journal of Astronautical Sciences*, Vol. 27, No.1, pp. 36-62.
- PUIG-SUARI, J., LONGUSKI, J. M., and TRAGESSE, S. G. (1995). “A Tether Sling for Lunar and Interplanetary Exploration”, *Acta Astronautica*, Vol.36, No.6, pp. 291–295.
- PUIG-SUARI, J., LONGUSKI, J. M., TRAGESSE, S. (1993). “A three-dimensional Hinged-rod Model for Flexible-elastic Aerobraking Tethers” *Proceeding of American Astronautical Society/AIAA Astrodynamic Conference*, AAS Paper 93-7300, Victoria, BC, Canada .
- PUIG-SUARI, J., LONGUSKI, J. M., and MECHALAS, J. (1992). “Aerobraking Tethers for the Exploration of the Solar System”, *International Astronautical Congress*, 43rd, IAF Aug. 28-Sept. 5, Washington.
- PUIG-SUARI, J. and LONGUSKI, J.M. (1991). “Modelling and analysis of tethers in an atmosphere”, *Acta Astronautica*, Vol. 25, pp. 679–686.
- RAO, S.S, (2007). *Vibration of Continuous System*, John Wiley & Sons, New Jersey.

- SAMANTHA ROY, R. I., HASTING, D. E., and AHEDO, E. (1992). "System Analysis of Electrodynamic Tether", *Journal of Spacecraft and Rockets*, Vol. 29, No.3, pp. 415-424.
- SASAKI, S., TANAKA, K., HIGUCHI, K., OKUIZUMI, N., SHINOHARA, N., SENDA, K., and ISHIMURA, K. (2007). "A new concept of solar power satellite: Tethered-SPS", *Acta Astronautica*, Vol. 60, No.3, pp. 153-165.
- SHUM, W. S. and ENTWISTLE, R.D. (2006). "Longitudinal vibration frequencies of steadily whirling rods", *The Journal of the Acoustical Society of America*. Vol. 119, No.2, p.p 909-916.
- STEINER, W., STEINDL, A. and TROGER H. (1995). "Dynamics of a Space Tethered Satellite System with Two Rigid Endbodies", *Proceedings of the Fourth International Conference on Tethers in Space*, Washington DC.
- STONE, N. H., RAITT, W. J., and WRIGHT JR, K. H. (1999). "The TSS-1R Electrodynamic Tether Experiment: Scientific and Technological Results", *Advances in Space Research*, Vol. 24, No.8, pp. 1037-1045.
- TAKEICHI, N., NATORI, M. C, and OKUIZUMI, N.. (2001). "In-Plane/Out-of-Plane Librations of a Tethered System in Elliptical Orbits", *Trans. Japan Soc. Aero. S Sci.*, Vol. 43, No. 142, pp. 196-202.
- THOMSEN, J.J. (2003). *Vibrations and Stability: Advanced theory, Analysis, and Tools*. 2nd edition, Springer, Berlin, Germany.
- THORNTON, R. D. (1973). "Design Principles for Magnetic Levitation", *Proceedings of the IEEE*, Vol. 61, No.5, pp. 586-598.
- TYC, G., and HAN ,R. P. S. (2001). "On the Dynamics of Spinning Tethered Space Vehicles", *The Philosophical Transactions of the Royal Society*, Vol. 359, No.1788, pp. 2161.
- Vallado, D.A, (2004). *Fundamentals of astrodynamics and applications* (Space Technology Library v. 12) , 2nd Edition, Kluwer Academic Publishers, Netherlands.
- VAN PELT, M. (2009). *Space Tether and Space Elevator*, Copernicus Books, New York, United States of America.
- VAS, I.E., KELLY, T. J, and SCARL, A. (2000). "Space Station Reboost with Electrodynamic Tethers", *Journal of Spacecraft and Rocket*, Vol. 37, No.2, pp.154-164.

WANG,L.S, CHERN, S.H., and SHIN, C.W. (1994).“On the Dynamics of a Tethered Satellite System” *Archive for Rational Mechanics and Analysis*, Vol. 127, No.4, pp. 297-318.

ZIEGLER, S. W., and CARTMELL, M. P. (2001) “Using Motorized Tethers for Payload Orbital Transfer,” *Journal of Spacecraft and Rockets*, Vol. 38, No.6, pp. 904–913.

ZIEGLER, S.W. (2003). “The Rigid Body Dynamic of Tethers in Space”, PhD. Thesis, Department of Mechanical Engineering, University of Glasgow, Glasgow, UK.

Publications

The work presented in this thesis has so far either contributed or led to the following publications:

ISMAIL, N.A., and CARTMELL, M.P. (2009). “Modelling of a Flexible Elastic Tether for the Motorised Momentum Exchange Tether Concept”, *Proceeding of. RANM2009*, 24 – 27 August, Kuala Lumpur Malaysia .

ISMAIL, N.A., and CARTMELL, M.P. (2010a). “The Dynamics of a Flexible Motorised Momentum Exchange Tether with Dynamics Boundary Conditions”, *Proceeding of RASD2010*, 12-14 July, Southampton UK .

ISMAIL, N.A.,and CARTMELL, M.P. (2010b). “In Service Power requirement for a Motorised Momentum Exchange Tether”. *Proceeding of 61st International Astronautical Congress*, 27 September to 1 October, Prague, Czech Republic.

Appendix A

i. Kinetic Energy

Tk =

$$\begin{aligned} & \frac{1}{8} \left((12 h^2 + 18 L^2 + A L^3 \rho + 10 L^2 \cos[2 \alpha 1[t]] - A L^3 \rho \cos[2 \alpha 1[t]] + M_m r_m^2 + 2 M_p \right. \\ & \quad \left. (4 L^2 \sin[\alpha 1[t]]^2 + r_p^2) + 2 L \pi \rho r_{T1}^4 - 2 L \pi \rho r_{T2}^4) \alpha 1'[t]^2 + \right. \\ & \quad \left. (2 M_m (r_m^2 + 2 r_c[t]^2) + L (8 L + A L^2 \rho + A L^2 \rho \cos[2 \alpha 1[t]] + 2 \pi \rho r_{T1}^4 - \right. \\ & \quad \left. 2 \pi \rho r_{T2}^4 + 8 A \rho r_c[t]^2) + 4 M_p (r_p^2 + 2 (L^2 \cos[\alpha 1[t]]^2 + r_c[t]^2))) \right. \\ & \quad \left. \theta'[t]^2 + 2 (2 M_m r_m^2 + 4 M_p (2 L^2 \cos[\alpha 1[t]]^2 + r_p^2) + \right. \\ & \quad \left. L (L (8 + A L \rho + A L \rho \cos[2 \alpha 1[t]]) + 2 \pi \rho r_{T1}^4 - 2 \pi \rho r_{T2}^4)) \theta'[t] \psi'[t] + \right. \\ & \quad \left. 8 L^2 \psi'[t]^2 + A L^3 \rho \psi'[t]^2 + A L^3 \rho \cos[2 \alpha 1[t]] \psi'[t]^2 + \right. \\ & \quad \left. 4 L^2 M_p \psi'[t]^2 + 4 L^2 \cos[2 \alpha 1[t]] M_p \psi'[t]^2 + 2 M_m r_m^2 \psi'[t]^2 + \right. \\ & \quad \left. 4 M_p r_p^2 \psi'[t]^2 + 2 L \pi \rho r_{T1}^4 \psi'[t]^2 - 2 L \pi \rho r_{T2}^4 \psi'[t]^2 + \right. \\ & \quad \left. 8 A L \rho r_c'[t]^2 + 4 M_m r_c'[t]^2 + 8 M_p r_c'[t]^2) \right) \end{aligned}$$

ii. Potential Energy

$$\begin{aligned} U_p = & - \sum_{i=1}^n \frac{A L \mu \rho}{n \sqrt{\frac{(-1+2i)^2 L^2}{4n^2} - \frac{(-1+2i) L \cos[\alpha 1[t]] \cos[\psi[t]] r_c[t]}{n} + r_c[t]^2}} - \\ & \sum_{i=1}^n \frac{A L \mu \rho}{n \sqrt{\frac{(-1+2i)^2 L^2}{4n^2} + \frac{(-1+2i) L \cos[\alpha 1[t]] \cos[\psi[t]] r_c[t]}{n} + r_c[t]^2}} - \\ & \frac{\mu M_m}{r_c[t]} - \frac{\mu M_p}{\sqrt{L^2 - 2 L \cos[\alpha 1[t]] \cos[\psi[t]] r_c[t] + r_c[t]^2}} - \\ & \frac{\mu M_p}{\sqrt{L^2 + 2 L \cos[\alpha 1[t]] \cos[\psi[t]] r_c[t] + r_c[t]^2}} \end{aligned}$$

iii. EOM

For $\psi[t]$:

$$\begin{aligned}
& \frac{1}{4} \left(-4 \tau \text{Cos}[\alpha[t]] \text{Cos}[\gamma[t]] - \right. \\
& 4 \sum_{i=1}^n - \left(A (-1 + 2i) L^2 \mu \rho \text{Cos}[\alpha[t]] \text{Sin}[\psi[t]] r_c[t] \right) / \\
& \left(2 n^2 \left(\frac{(-1 + 2i)^2 L^2}{4 n^2} - \right. \right. \\
& \left. \left. \frac{(-1 + 2i) L \text{Cos}[\alpha[t]] \text{Cos}[\psi[t]] r_c[t]}{n} + r_c[t]^2 \right)^{3/2} \right) - \\
& 4 \sum_{i=1}^n \left(A (-1 + 2i) L^2 \mu \rho \text{Cos}[\alpha[t]] \text{Sin}[\psi[t]] r_c[t] \right) / \\
& \left(2 n^2 \left(\frac{(-1 + 2i)^2 L^2}{4 n^2} + \right. \right. \\
& \left. \left. \frac{(-1 + 2i) L \text{Cos}[\alpha[t]] \text{Cos}[\psi[t]] r_c[t]}{n} + r_c[t]^2 \right)^{3/2} \right) + \\
& \frac{4 L \mu \text{Cos}[\alpha[t]] \text{Sin}[\psi[t]] M_p r_c[t]}{(L^2 - 2 L \text{Cos}[\alpha[t]] \text{Cos}[\psi[t]] r_c[t] + r_c[t]^2)^{3/2}} - \\
& \frac{4 L \mu \text{Cos}[\alpha[t]] \text{Sin}[\psi[t]] M_p r_c[t]}{(L^2 + 2 L \text{Cos}[\alpha[t]] \text{Cos}[\psi[t]] r_c[t] + r_c[t]^2)^{3/2}} - \\
& 2 A L^3 \rho \text{Sin}[2 \alpha[t]] \alpha'[t] \theta'[t] - \\
& 8 L^2 \text{Sin}[2 \alpha[t]] M_p \alpha'[t] \theta'[t] - \\
& 2 A L^3 \rho \text{Sin}[2 \alpha[t]] \alpha'[t] \psi'[t] - \\
& 8 L^2 \text{Sin}[2 \alpha[t]] M_p \alpha'[t] \psi'[t] + 8 L^2 \theta''[t] + \\
& A L^3 \rho \theta''[t] + A L^3 \rho \text{Cos}[\alpha[t]]^2 \theta''[t] - \\
& A L^3 \rho \text{Sin}[\alpha[t]]^2 \theta''[t] + 4 L^2 M_p \theta''[t] + \\
& 4 L^2 \text{Cos}[\alpha[t]]^2 M_p \theta''[t] - 4 L^2 \text{Sin}[\alpha[t]]^2 M_p \theta''[t] + \\
& 2 M_m r_m^2 \theta''[t] + 4 M_p r_p^2 \theta''[t] + 2 L \pi \rho r_{T1}^4 \theta''[t] - \\
& 2 L \pi \rho r_{T2}^4 \theta''[t] + 8 L^2 \psi''[t] + A L^3 \rho \psi''[t] + \\
& A L^3 \rho \text{Cos}[\alpha[t]]^2 \psi''[t] - A L^3 \rho \text{Sin}[\alpha[t]]^2 \psi''[t] + \\
& 4 L^2 M_p \psi''[t] + 4 L^2 \text{Cos}[\alpha[t]]^2 M_p \psi''[t] - \\
& 4 L^2 \text{Sin}[\alpha[t]]^2 M_p \psi''[t] + 2 M_m r_m^2 \psi''[t] + \\
& \left. 4 M_p r_p^2 \psi''[t] + 2 L \pi \rho r_{T1}^4 \psi''[t] - 2 L \pi \rho r_{T2}^4 \psi''[t] \right) = 0
\end{aligned}$$

For $\theta[t]$:

$$\begin{aligned}
& \frac{1}{4} \\
& (-2 L^2 \text{Sin}[2 \alpha[t]] (A L \rho + 4 M_p) \alpha'[t] (\theta'[t] + \psi'[t]) + 8 (M_m + 2 (A L \rho + M_p)) \\
& r_c[t] \theta'[t] r_c'[t] + 4 (M_m + 2 (A L \rho + M_p)) r_c[t]^2 \theta''[t] +
\end{aligned}$$

$$(2 M_m r_m^2 + 4 M_p (2 L^2 \cos[\alpha[t]]^2 + r_p^2) + L (L (8 + A L \rho + A L \rho \cos[2 \alpha[t]]) + 2 \pi \rho r_{T1}^4 - 2 \pi \rho r_{T2}^4)) (\theta''[t] + \psi''[t]) = 0$$

For $R[t]$:

$$\begin{aligned} & -\frac{1}{2} \sqrt{L^2 - 2 L \cos[\alpha[t]] \cos[\psi[t]] r_c[t] + r_c[t]^2} \\ & \sqrt{L^2 + 2 L \cos[\alpha[t]] \cos[\psi[t]] r_c[t] + r_c[t]^2} \\ & (2 L^4 - L^2 (-2 + 2 \cos[2 \alpha[t]] + \cos[2 (\alpha[t] - \psi[t])]) + \\ & \quad 2 \cos[2 \psi[t]] + \cos[2 (\alpha[t] + \psi[t])]) r_c[t]^2 + 2 r_c[t]^4) \\ & \left(r_c[t]^2 \left(\sum_{i=1}^n - \left(A L \mu \rho \left(-\frac{(-1 + 2 i) L \cos[\alpha[t]] \cos[\psi[t]]}{n} + 2 r_c[t] \right) \right) \right) / \right. \\ & \quad \left(2 n \left(\frac{(-1 + 2 i)^2 L^2}{4 n^2} - \right. \right. \\ & \quad \quad \left. \left. \frac{(-1 + 2 i) L \cos[\alpha[t]] \cos[\psi[t]] r_c[t]}{n} + r_c[t]^2 \right)^{3/2} \right) + \\ & \quad \left. \sum_{i=1}^n - \left(A L \mu \rho \left(\frac{(-1 + 2 i) L \cos[\alpha[t]] \cos[\psi[t]]}{n} + 2 r_c[t] \right) \right) / \right. \\ & \quad \left(2 n \left(\frac{(-1 + 2 i)^2 L^2}{4 n^2} + \frac{(-1 + 2 i) L \cos[\alpha[t]] \cos[\psi[t]] r_c[t]}{n} + \right. \right. \\ & \quad \quad \left. \left. r_c[t]^2 \right)^{3/2} \right) + 2 A L \rho (r_c[t] \theta'[t]^2 - r_c''[t]) \left. \right) - \\ & \quad \left. M_m (\mu - r_c[t])^3 \theta'[t]^2 + r_c[t]^2 r_c''[t] \right) + M_p r_c[t]^2 \\ & (-2 r_c[t]^5 \sqrt{L^2 - 2 L \cos[\alpha[t]] \cos[\psi[t]] r_c[t] + r_c[t]^2} \\ & \quad \sqrt{L^2 + 2 L \cos[\alpha[t]] \cos[\psi[t]] r_c[t] + r_c[t]^2} \theta'[t]^2 + \\ & \quad L^2 r_c[t] \left(-\frac{1}{4} \mu (-2 + 2 \cos[2 \alpha[t]] + \cos[2 (\alpha[t] - \psi[t])]) + \right. \\ & \quad \quad \left. 2 \cos[2 \psi[t]] + \cos[2 (\alpha[t] + \psi[t])]) \right) \\ & \quad \left(\sqrt{L^2 - 2 L \cos[\alpha[t]] \cos[\psi[t]] r_c[t] + r_c[t]^2} + \right. \\ & \quad \quad \left. \sqrt{L^2 + 2 L \cos[\alpha[t]] \cos[\psi[t]] r_c[t] + r_c[t]^2} \right) - \\ & \quad 2 L^2 \sqrt{L^2 - 2 L \cos[\alpha[t]] \cos[\psi[t]] r_c[t] + r_c[t]^2} \\ & \quad \sqrt{L^2 + 2 L \cos[\alpha[t]] \cos[\psi[t]] r_c[t] + r_c[t]^2} \theta'[t]^2 + \\ & \quad r_c[t]^3 \left(\mu \left(\sqrt{L^2 - 2 L \cos[\alpha[t]] \cos[\psi[t]] r_c[t] + r_c[t]^2} + \right. \right. \\ & \quad \quad \left. \left. \sqrt{L^2 + 2 L \cos[\alpha[t]] \cos[\psi[t]] r_c[t] + r_c[t]^2} \right) + \right. \\ & \quad \quad \left. L^2 (-2 + 2 \cos[2 \alpha[t]] + \cos[2 (\alpha[t] - \psi[t])]) + \right. \\ & \quad \quad \left. 2 \cos[2 \psi[t]] + \cos[2 (\alpha[t] + \psi[t])]) \right) \end{aligned}$$

$$\begin{aligned}
& \sqrt{L^2 - 2 L \cos[\alpha[t]] \cos[\psi[t]] r_c[t] + r_c[t]^2} \\
& \sqrt{L^2 + 2 L \cos[\alpha[t]] \cos[\psi[t]] r_c[t] + r_c[t]^2} \theta'[t]^2) + \\
& 2 r_c[t]^4 \sqrt{L^2 - 2 L \cos[\alpha[t]] \cos[\psi[t]] r_c[t] + r_c[t]^2} \\
& \sqrt{L^2 + 2 L \cos[\alpha[t]] \cos[\psi[t]] r_c[t] + r_c[t]^2} \\
& r_c''[t] + L^3 \left(\mu \cos[\alpha[t]] \cos[\psi[t]] \right. \\
& \quad \left(\sqrt{L^2 - 2 L \cos[\alpha[t]] \cos[\psi[t]] r_c[t] + r_c[t]^2} - \right. \\
& \quad \left. \sqrt{L^2 + 2 L \cos[\alpha[t]] \cos[\psi[t]] r_c[t] + r_c[t]^2} \right) + \\
& \quad 2 L \sqrt{L^2 - 2 L \cos[\alpha[t]] \cos[\psi[t]] r_c[t] + r_c[t]^2} \\
& \quad \left. \sqrt{L^2 + 2 L \cos[\alpha[t]] \cos[\psi[t]] r_c[t] + r_c[t]^2} r_c''[t] \right) + \\
& L r_c[t]^2 \left(\mu \cos[\alpha[t]] \cos[\psi[t]] \right. \\
& \quad \left(-\sqrt{L^2 - 2 L \cos[\alpha[t]] \cos[\psi[t]] r_c[t] + r_c[t]^2} + \right. \\
& \quad \left. \sqrt{L^2 + 2 L \cos[\alpha[t]] \cos[\psi[t]] r_c[t] + r_c[t]^2} \right) - \\
& \quad L (-2 + 2 \cos[2 \alpha[t]] + \cos[2 (\alpha[t] - \psi[t])] + \\
& \quad 2 \cos[2 \psi[t]] + \cos[2 (\alpha[t] + \psi[t])]) \\
& \quad \left. \sqrt{L^2 - 2 L \cos[\alpha[t]] \cos[\psi[t]] r_c[t] + r_c[t]^2} \right. \\
& \quad \left. \sqrt{L^2 + 2 L \cos[\alpha[t]] \cos[\psi[t]] r_c[t] + r_c[t]^2} r_c''[t] \right) \Big) / \\
& \left(r_c[t]^2 (L^2 - 2 L \cos[\alpha[t]] \cos[\psi[t]] r_c[t] + r_c[t]^2)^{3/2} \right. \\
& \quad \left. (L^2 + 2 L \cos[\alpha[t]] \cos[\psi[t]] r_c[t] + r_c[t]^2)^{3/2} \right) = 0
\end{aligned}$$

For $\alpha[t]$:

$$\begin{aligned}
& \frac{1}{4} \left(-4 \tau \sin[\gamma[t]] - 4 \sum_{i=1}^n - (A (-1 + 2 i) L^2 \mu \rho \cos[\psi[t]] \sin[\alpha[t]] r_c[t]) \Big) / \\
& \quad \left(2 n^2 \left(\frac{(-1 + 2 i)^2 L^2}{4 n^2} - \right. \right. \\
& \quad \quad \left. \left. \frac{(-1 + 2 i) L \cos[\alpha[t]] \cos[\psi[t]] r_c[t]}{n} + r_c[t]^2 \right)^{3/2} \right) - \\
& 4 \sum_{i=1}^n (A (-1 + 2 i) L^2 \mu \rho \cos[\psi[t]] \sin[\alpha[t]] r_c[t]) \Big) / \\
& \quad \left(2 n^2 \left(\frac{(-1 + 2 i)^2 L^2}{4 n^2} + \right. \right. \\
& \quad \quad \left. \left. \frac{(-1 + 2 i) L \cos[\alpha[t]] \cos[\psi[t]] r_c[t]}{n} + r_c[t]^2 \right)^{3/2} \right) +
\end{aligned}$$

$$\begin{aligned}
& \frac{4 L \mu \operatorname{Cos}[\psi[t]] \operatorname{Sin}[\alpha[t]] M_p r_c[t]}{(L^2 - 2 L \operatorname{Cos}[\alpha[t]] \operatorname{Cos}[\psi[t]] r_c[t] + r_c[t]^2)^{3/2}} - \\
& \frac{4 L \mu \operatorname{Cos}[\psi[t]] \operatorname{Sin}[\alpha[t]] M_p r_c[t]}{(L^2 + 2 L \operatorname{Cos}[\alpha[t]] \operatorname{Cos}[\psi[t]] r_c[t] + r_c[t]^2)^{3/2}} - \\
& 10 L^2 \operatorname{Sin}[2 \alpha[t]] \alpha'[t]^2 + \\
& A L^3 \rho \operatorname{Sin}[2 \alpha[t]] \alpha'[t]^2 + \\
& 4 L^2 \operatorname{Sin}[2 \alpha[t]] M_p \alpha'[t]^2 + \\
& A L^3 \rho \operatorname{Sin}[2 \alpha[t]] \theta'[t]^2 + \\
& 4 L^2 \operatorname{Sin}[2 \alpha[t]] M_p \theta'[t]^2 + \\
& 2 A L^3 \rho \operatorname{Sin}[2 \alpha[t]] \theta'[t] \psi'[t] + \\
& 8 L^2 \operatorname{Sin}[2 \alpha[t]] M_p \theta'[t] \psi'[t] + \\
& A L^3 \rho \operatorname{Sin}[2 \alpha[t]] \psi'[t]^2 + 4 L^2 \operatorname{Sin}[2 \alpha[t]] M_p \psi'[t]^2 + \\
& 12 h^2 \alpha''[t] + 18 L^2 \alpha''[t] + A L^3 \rho \alpha''[t] + \\
& 10 L^2 \operatorname{Cos}[\alpha[t]]^2 \alpha''[t] - A L^3 \rho \operatorname{Cos}[\alpha[t]]^2 \alpha''[t] - \\
& 10 L^2 \operatorname{Sin}[\alpha[t]]^2 \alpha''[t] + A L^3 \rho \operatorname{Sin}[\alpha[t]]^2 \alpha''[t] + \\
& 4 L^2 M_p \alpha''[t] - 4 L^2 \operatorname{Cos}[\alpha[t]]^2 M_p \alpha''[t] + \\
& 4 L^2 \operatorname{Sin}[\alpha[t]]^2 M_p \alpha''[t] + M_m r_m^2 \alpha''[t] + \\
& \left. 2 M_p r_p^2 \alpha''[t] + 2 L \pi \rho r_{T1}^4 \alpha''[t] - 2 L \pi \rho r_{T2}^4 \alpha''[t] \right) = 0
\end{aligned}$$

Appendix B

Flexible Tether (3 D)

i. Kinetic Energy

$$\begin{aligned}
 T_k = & \frac{1}{4} A L \rho q_1' [t]^2 + \frac{1}{4} A L \rho \cos [2 \alpha [t]] q_1' [t]^2 + \frac{1}{2} A L \rho \sin [\alpha [t]]^2 q_1' [t]^2 + \\
 & \frac{1}{2} A L \rho q_2' [t]^2 + A L \rho \cos [\alpha [t]] \sin [\alpha [t]] q_1' [t] q_3' [t] - \\
 & \frac{1}{2} A L \rho \sin [2 \alpha [t]] q_1' [t] q_3' [t] + \frac{1}{4} A L \rho q_3' [t]^2 + \\
 & \frac{1}{2} A L \rho \cos [\alpha [t]]^2 q_3' [t]^2 - \frac{1}{4} A L \rho \cos [2 \alpha [t]] q_3' [t]^2 + \\
 & A L \rho R' [t]^2 + \frac{1}{2} \cos [\theta [t]]^2 M_m R' [t]^2 + \frac{1}{2} \sin [\theta [t]]^2 M_m R' [t]^2 + \\
 & \cos [\theta [t]]^2 M_p R' [t]^2 + \sin [\theta [t]]^2 M_p R' [t]^2 - \\
 & \frac{1}{2} A L \rho q_3 [t] q_1' [t] \alpha' [t] - \frac{1}{2} A L \rho \cos [2 \alpha [t]] q_3 [t] q_1' [t] \alpha' [t] + \\
 & \frac{2 A L^2 \rho \cos [\alpha [t]] \sin [\alpha [t]] q_1' [t] \alpha' [t]}{\pi} + \\
 & A L \rho \cos [\alpha [t]] q_1 [t] \sin [\alpha [t]] q_1' [t] \alpha' [t] - \\
 & A L \rho q_3 [t] \sin [\alpha [t]]^2 q_1' [t] \alpha' [t] - \frac{A L^2 \rho \sin [2 \alpha [t]] q_1' [t] \alpha' [t]}{\pi} - \\
 & \frac{1}{2} A L \rho q_1 [t] \sin [2 \alpha [t]] q_1' [t] \alpha' [t] + \frac{A L^2 \rho q_3' [t] \alpha' [t]}{\pi} + \\
 & \frac{2 A L^2 \rho \cos [\alpha [t]]^2 q_3' [t] \alpha' [t]}{\pi} - \frac{A L^2 \rho \cos [2 \alpha [t]] q_3' [t] \alpha' [t]}{\pi} + \\
 & \frac{1}{2} A L \rho q_1 [t] q_3' [t] \alpha' [t] + A L \rho \cos [\alpha [t]]^2 q_1 [t] q_3' [t] \alpha' [t] - \\
 & \frac{1}{2} A L \rho \cos [2 \alpha [t]] q_1 [t] q_3' [t] \alpha' [t] - \\
 & A L \rho \cos [\alpha [t]] q_3 [t] \sin [\alpha [t]] q_3' [t] \alpha' [t] + \\
 & \frac{1}{2} A L \rho q_3 [t] \sin [2 \alpha [t]] q_3' [t] \alpha' [t] + \frac{3}{2} h^2 \alpha' [t]^2 + \\
 & L^2 \alpha' [t]^2 + \frac{1}{6} A L^3 \rho \alpha' [t]^2 + \frac{1}{3} A L^3 \rho \cos [\alpha [t]]^2 \alpha' [t]^2 - \\
 & \frac{1}{6} A L^3 \rho \cos [2 \alpha [t]] \alpha' [t]^2 + \frac{A L^2 \rho q_1 [t] \alpha' [t]^2}{\pi} + \\
 & \frac{2 A L^2 \rho \cos [\alpha [t]]^2 q_1 [t] \alpha' [t]^2}{\pi} - \frac{A L^2 \rho \cos [2 \alpha [t]] q_1 [t] \alpha' [t]^2}{\pi} + \\
 & \frac{1}{4} A L \rho q_1 [t]^2 \alpha' [t]^2 + \frac{1}{2} A L \rho \cos [\alpha [t]]^2 q_1 [t]^2 \alpha' [t]^2 - \\
 & \frac{1}{4} A L \rho \cos [2 \alpha [t]] q_1 [t]^2 \alpha' [t]^2 + \frac{1}{4} A L \rho q_3 [t]^2 \alpha' [t]^2 +
 \end{aligned}$$

$$\begin{aligned}
& \frac{1}{4} A L \rho \cos[2 \alpha[t]] q_3[t]^2 \alpha'[t]^2 - \frac{A L^2 \rho \cos[\alpha[t]] q_3[t] \sin[\alpha[t]] \alpha'[t]^2}{\pi} - \\
& A L \rho \cos[\alpha[t]] q_1[t] q_3[t] \sin[\alpha[t]] \alpha'[t]^2 + \\
& \frac{1}{2} A L \rho q_3[t]^2 \sin[\alpha[t]]^2 \alpha'[t]^2 + \frac{A L^2 \rho q_3[t] \sin[2 \alpha[t]] \alpha'[t]^2}{2 \pi} + \\
& \frac{1}{2} A L \rho q_1[t] q_3[t] \sin[2 \alpha[t]] \alpha'[t]^2 + L^2 \cos[\alpha[t]]^2 M_p \alpha'[t]^2 + \\
& L^2 \cos[\theta[t] + \varphi[t]]^2 \sin[\alpha[t]]^2 M_p \alpha'[t]^2 + \\
& L^2 \sin[\alpha[t]]^2 \sin[\theta[t] + \varphi[t]]^2 M_p \alpha'[t]^2 + \frac{1}{8} M_m r_m^2 \alpha'[t]^2 + \frac{1}{4} M_p r_p^2 \alpha'[t]^2 + \\
& \frac{1}{4} M_p r_T^2 \alpha'[t]^2 + \frac{3}{2} h^2 \gamma'[t]^2 + \frac{1}{8} M_m r_m^2 \gamma'[t]^2 + \frac{1}{4} M_p r_p^2 \gamma'[t]^2 + \frac{1}{2} A L \rho r_T^2 \gamma'[t]^2 - \\
& A L \rho \cos[\alpha[t]] q_2[t] q_1'[t] \theta'[t] + \frac{2 A L^2 \rho \cos[\alpha[t]] q_2'[t] \theta'[t]}{\pi} + \\
& A L \rho \cos[\alpha[t]] q_1[t] q_2'[t] \theta'[t] - A L \rho q_3[t] \sin[\alpha[t]] q_2'[t] \theta'[t] + \\
& A L \rho q_2[t] \sin[\alpha[t]] q_3'[t] \theta'[t] + A L \rho \cos[\alpha[t]] q_2[t] q_3[t] \alpha'[t] \theta'[t] + \\
& \frac{2 A L^2 \rho q_2[t] \sin[\alpha[t]] \alpha'[t] \theta'[t]}{\pi} + \\
& A L \rho q_1[t] q_2[t] \sin[\alpha[t]] \alpha'[t] \theta'[t] + L^2 \theta'[t]^2 + \\
& \frac{1}{6} A L^3 \rho \theta'[t]^2 + \frac{1}{6} A L^3 \rho \cos[2 \alpha[t]] \theta'[t]^2 + \frac{A L^2 \rho q_1[t] \theta'[t]^2}{\pi} + \\
& \frac{A L^2 \rho \cos[2 \alpha[t]] q_1[t] \theta'[t]^2}{\pi} + \frac{1}{4} A L \rho q_1[t]^2 \theta'[t]^2 + \\
& \frac{1}{4} A L \rho \cos[2 \alpha[t]] q_1[t]^2 \theta'[t]^2 + \frac{1}{2} A L \rho q_2[t]^2 \theta'[t]^2 + \\
& \frac{1}{4} A L \rho q_3[t]^2 \theta'[t]^2 - \frac{1}{4} A L \rho \cos[2 \alpha[t]] q_3[t]^2 \theta'[t]^2 + A L \rho R[t]^2 \theta'[t]^2 - \\
& \frac{A L^2 \rho q_3[t] \sin[2 \alpha[t]] \theta'[t]^2}{\pi} - \frac{1}{2} A L \rho q_1[t] q_3[t] \sin[2 \alpha[t]] \theta'[t]^2 + \\
& \frac{1}{2} \cos[\theta[t]]^2 R[t]^2 M_m \theta'[t]^2 + \frac{1}{2} R[t]^2 \sin[\theta[t]]^2 M_m \theta'[t]^2 + \\
& L^2 \cos[\alpha[t]]^2 \cos[\theta[t] + \varphi[t]]^2 M_p \theta'[t]^2 + \cos[\theta[t]]^2 R[t]^2 M_p \theta'[t]^2 + \\
& R[t]^2 \sin[\theta[t]]^2 M_p \theta'[t]^2 + L^2 \cos[\alpha[t]]^2 \sin[\theta[t] + \varphi[t]]^2 M_p \theta'[t]^2 + \\
& \frac{1}{4} M_m r_m^2 \theta'[t]^2 + \frac{1}{2} M_p r_p^2 \theta'[t]^2 + \frac{1}{4} M_p r_T^2 \theta'[t]^2 - \\
& A L \rho \cos[\alpha[t]] q_2[t] q_1'[t] \varphi'[t] + \frac{2 A L^2 \rho \cos[\alpha[t]] q_2'[t] \varphi'[t]}{\pi} + \\
& A L \rho \cos[\alpha[t]] q_1[t] q_2'[t] \varphi'[t] - A L \rho q_3[t] \sin[\alpha[t]] q_2'[t] \varphi'[t] + \\
& A L \rho q_2[t] \sin[\alpha[t]] q_3'[t] \varphi'[t] + A L \rho \cos[\alpha[t]] q_2[t] q_3[t] \alpha'[t] \varphi'[t] + \\
& \frac{2 A L^2 \rho q_2[t] \sin[\alpha[t]] \alpha'[t] \varphi'[t]}{\pi} + A L \rho q_1[t] q_2[t] \\
& \sin[\alpha[t]] \alpha'[t] \varphi'[t] + 2 L^2 \theta'[t] \varphi'[t] + \frac{1}{3} A L^3 \rho \theta'[t] \varphi'[t] + \\
& \frac{1}{3} A L^3 \rho \cos[2 \alpha[t]] \theta'[t] \varphi'[t] + \frac{2 A L^2 \rho q_1[t] \theta'[t] \varphi'[t]}{\pi} + \\
& \frac{2 A L^2 \rho \cos[2 \alpha[t]] q_1[t] \theta'[t] \varphi'[t]}{\pi} + \frac{1}{2} A L \rho q_1[t]^2 \theta'[t] \varphi'[t] + \\
& \frac{1}{2} A L \rho \cos[2 \alpha[t]] q_1[t]^2 \theta'[t] \varphi'[t] + A L \rho q_2[t]^2 \theta'[t] \varphi'[t] +
\end{aligned}$$

$$\begin{aligned}
& \frac{1}{2} A L \rho q_3[t]^2 \theta'[t] \varphi'[t] - \frac{1}{2} A L \rho \cos[2\alpha[t]] q_3[t]^2 \theta'[t] \varphi'[t] - \\
& \frac{2 A L^2 \rho q_3[t] \sin[2\alpha[t]] \theta'[t] \varphi'[t]}{\pi} - A L \rho q_1[t] q_3[t] \sin[2\alpha[t]] \\
& \theta'[t] \varphi'[t] + 2 L^2 \cos[\alpha[t]]^2 \cos[\theta[t] + \varphi[t]]^2 M_p \theta'[t] \varphi'[t] + \\
& 2 L^2 \cos[\alpha[t]]^2 \sin[\theta[t] + \varphi[t]]^2 M_p \theta'[t] \varphi'[t] + \frac{1}{2} M_m r_m^2 \theta'[t] \varphi'[t] + \\
& M_p r_p^2 \theta'[t] \varphi'[t] + \frac{1}{2} M_p r_I^2 \theta'[t] \varphi'[t] + L^2 \varphi'[t]^2 + \frac{1}{6} A L^3 \rho \varphi'[t]^2 + \\
& \frac{1}{6} A L^3 \rho \cos[2\alpha[t]] \varphi'[t]^2 + \frac{A L^2 \rho q_1[t] \varphi'[t]^2}{\pi} + \\
& \frac{A L^2 \rho \cos[2\alpha[t]] q_1[t] \varphi'[t]^2}{\pi} + \frac{1}{4} A L \rho q_1[t]^2 \varphi'[t]^2 + \\
& \frac{1}{4} A L \rho \cos[2\alpha[t]] q_1[t]^2 \varphi'[t]^2 + \frac{1}{2} A L \rho q_2[t]^2 \varphi'[t]^2 + \\
& \frac{1}{4} A L \rho q_3[t]^2 \varphi'[t]^2 - \frac{1}{4} A L \rho \cos[2\alpha[t]] q_3[t]^2 \varphi'[t]^2 - \\
& \frac{A L^2 \rho q_3[t] \sin[2\alpha[t]] \varphi'[t]^2}{\pi} - \frac{1}{2} A L \rho q_1[t] q_3[t] \sin[2\alpha[t]] \varphi'[t]^2 + \\
& L^2 \cos[\alpha[t]]^2 \cos[\theta[t] + \varphi[t]]^2 M_p \varphi'[t]^2 + \\
& L^2 \cos[\alpha[t]]^2 \sin[\theta[t] + \varphi[t]]^2 M_p \varphi'[t]^2 + \\
& \frac{1}{4} M_m r_m^2 \varphi'[t]^2 + \frac{1}{2} M_p r_p^2 \varphi'[t]^2 + \frac{1}{4} M_p r_I^2 \varphi'[t]^2
\end{aligned}$$

ii. Potential Energy

$$\begin{aligned}
 U_P = & \frac{A E_0 \pi^2 q_1[t]^2}{2 L} - \frac{3 A E_0 \pi^4 q_1[t]^2 q_2[t]^2}{8 L^3} + \frac{3 A E_0 \pi^4 q_2[t]^4}{32 L^3} - \\
 & \frac{3 A E_0 \pi^4 q_1[t]^2 q_3[t]^2}{8 L^3} + \frac{3 A E_0 \pi^4 q_2[t]^2 q_3[t]^2}{16 L^3} + \frac{3 A E_0 \pi^4 q_3[t]^4}{32 L^3} - \\
 & \frac{\mu M_m}{R[t]} - \frac{\mu M_p}{\sqrt{L^2 - 2 L \cos[\alpha[t]] \cos[\varphi[t]] R[t] + R[t]^2}} - \\
 & \frac{\mu M_p}{\sqrt{L^2 + 2 L \cos[\alpha[t]] \cos[\varphi[t]] R[t] + R[t]^2}} + \frac{L T_0}{A E_0} + \frac{15 \pi^4 q_1[t]^4 T_0}{32 L^3} + \\
 & \frac{\pi^2 q_2[t]^2 T_0}{2 L} + \frac{3 \pi^4 q_1[t]^2 q_2[t]^2 T_0}{8 L^3} - \frac{3 \pi^4 q_2[t]^4 T_0}{32 L^3} + \frac{\pi^2 q_3[t]^2 T_0}{2 L} + \\
 & \frac{3 \pi^4 q_1[t]^2 q_3[t]^2 T_0}{8 L^3} - \frac{3 \pi^4 q_2[t]^2 q_3[t]^2 T_0}{16 L^3} - \frac{3 \pi^4 q_3[t]^4 T_0}{32 L^3} - \\
 & \sum_{i=1}^n \frac{A L \mu \rho}{n \sqrt{\frac{(-1+2 i)^2 L^2}{4 n^2} - \frac{(-1+2 i) L \cos[\alpha[t]] \cos[\varphi[t]] R[t]}{n} + R[t]^2}} - \\
 & \sum_{i=1}^n \frac{A L \mu \rho}{n \sqrt{\frac{(-1+2 i)^2 L^2}{4 n^2} + \frac{(-1+2 i) L \cos[\alpha[t]] \cos[\varphi[t]] R[t]}{n} + R[t]^2}}
 \end{aligned}$$

Appendix C

EOM Flexible Tether

i. For $\varphi[t]$

$$- \tau \text{Cos}[\alpha[t]] \text{Cos}[\gamma[t]] +$$

$$L \mu \text{Cos}[\alpha[t]] R[t] \left(\frac{1}{(L^2 - 2 L \text{Cos}[\alpha[t]] \text{Cos}[\varphi[t]] R[t] + R[t]^2)^{3/2}} - \frac{1}{(L^2 + 2 L \text{Cos}[\alpha[t]] \text{Cos}[\varphi[t]] R[t] + R[t]^2)^{3/2}} \right) \text{Sin}[\varphi[t]] M_p -$$

$$\sum_{i=1}^n \frac{A (-1 + 2 i) L^2 \mu \rho \text{Cos}[\alpha[t]] R[t] \text{Sin}[\varphi[t]]}{2 n^2 \left(\frac{(-1+2i)^2 L^2}{4 n^2} - \frac{(-1+2i) L \text{Cos}[\alpha[t]] \text{Cos}[\varphi[t]] R[t]}{n} + R[t]^2 \right)^{3/2}} -$$

$$\sum_{i=1}^n \frac{A (-1 + 2 i) L^2 \mu \rho \text{Cos}[\alpha[t]] R[t] \text{Sin}[\varphi[t]]}{2 n^2 \left(\frac{(-1+2i)^2 L^2}{4 n^2} + \frac{(-1+2i) L \text{Cos}[\alpha[t]] \text{Cos}[\varphi[t]] R[t]}{n} + R[t]^2 \right)^{3/2}} +$$

$$\frac{1}{6 \pi} (12 A L \pi \rho q_2[t] q_2'[t] (\theta'[t] + \varphi'[t]) -$$

$$2 L (-6 A \rho \text{Cos}[\alpha[t]] (2 L \text{Cos}[\alpha[t]] + \pi \text{Cos}[\alpha[t]] q_1[t] - \pi q_3[t] \text{Sin}[\alpha[t])) q_1'[t] - 3 A \pi \rho q_3[t]^2 \text{Sin}[2 \alpha[t]] \alpha'[t] + 6 A \rho q_3[t] (-\pi \text{Sin}[\alpha[t]]^2 q_3'[t] + \text{Cos}[2 \alpha[t]] (2 L + \pi q_1[t]) \alpha'[t]) + \text{Sin}[2 \alpha[t]] (3 A \rho (2 L + \pi q_1[t]) q_3'[t] + (12 A L \rho q_1[t] + 3 A \pi \rho q_1[t]^2 + 2 L \pi (A L \rho + 3 M_p)) \alpha'[t])) (\theta'[t] + \varphi'[t]) + 6 A L \rho (2 L \text{Cos}[\alpha[t]] + \pi \text{Cos}[\alpha[t]] q_1[t] - \pi q_3[t] \text{Sin}[\alpha[t])) q_2''[t] + 6 A L \rho q_2[t] (2 \pi \text{Sin}[\alpha[t]] q_1'[t] \alpha'[t] + 2 \pi \text{Cos}[\alpha[t]] q_3'[t] \alpha'[t] + 2 L \text{Cos}[\alpha[t]] \alpha'[t]^2 + \pi \text{Cos}[\alpha[t]] q_1[t] \alpha'[t]^2 - \pi q_3[t] \text{Sin}[\alpha[t]] \alpha'[t]^2 - \pi \text{Cos}[\alpha[t]] q_1''[t] + \pi \text{Sin}[\alpha[t]] q_3''[t] + \pi \text{Cos}[\alpha[t]] q_3[t] \alpha''[t] + 2 L \text{Sin}[\alpha[t]] \alpha''[t] + \pi q_1[t] \text{Sin}[\alpha[t]] \alpha''[t]) + 6 A L \pi \rho q_2[t]^2 (\theta''[t] + \varphi''[t]) + (6 A L \pi \rho \text{Cos}[\alpha[t]]^2 q_1[t]^2 + 6 A L \pi \rho q_3[t]^2 \text{Sin}[\alpha[t]]^2 + 12 A L \rho \text{Cos}[\alpha[t]] q_1[t] (2 L \text{Cos}[\alpha[t]] - \pi q_3[t] \text{Sin}[\alpha[t])) - 12 A L^2 \rho q_3[t] \text{Sin}[2 \alpha[t]] + \pi (2 L^2 (6 + A L \rho + A L \rho \text{Cos}[2 \alpha[t])) + 3 M_m r_m^2 + 3 M_p (4 L^2 \text{Cos}[\alpha[t]]^2 + 2 r_p^2 + r_T^2))) (\theta''[t] + \varphi''[t])) = 0$$

ii. For $\theta[t]$

$$\begin{aligned}
& \frac{1}{6\pi} \left(6AL\pi\rho q_3[t] q_3'[t] \theta'[t] - 6AL\pi\rho \cos[2\alpha[t]] q_3[t] q_3'[t] \theta'[t] - \right. \\
& 12AL^2\rho \sin[2\alpha[t]] q_3'[t] \theta'[t] - 6AL\pi\rho q_1[t] \sin[2\alpha[t]] \\
& q_3'[t] \theta'[t] + 24AL\pi\rho R[t] R'[t] \theta'[t] + 12\pi R[t] M_m R'[t] \theta'[t] + \\
& 24\pi R[t] M_p R'[t] \theta'[t] - 24AL^2\rho \cos[2\alpha[t]] q_3[t] \alpha'[t] \theta'[t] - \\
& 12AL\pi\rho \cos[2\alpha[t]] q_1[t] q_3[t] \alpha'[t] \theta'[t] - \\
& 4AL^3\pi\rho \sin[2\alpha[t]] \alpha'[t] \theta'[t] - 24AL^2\rho q_1[t] \sin[2\alpha[t]] \alpha'[t] \theta'[t] - \\
& 6AL\pi\rho q_1[t]^2 \sin[2\alpha[t]] \alpha'[t] \theta'[t] + 6AL\pi\rho q_3[t]^2 \\
& \sin[2\alpha[t]] \alpha'[t] \theta'[t] - 12L^2\pi \sin[2\alpha[t]] M_p \alpha'[t] \theta'[t] + \\
& 6AL\pi\rho q_3[t] q_3'[t] \varphi'[t] - 6AL\pi\rho \cos[2\alpha[t]] q_3[t] q_3'[t] \varphi'[t] - \\
& 12AL^2\rho \sin[2\alpha[t]] q_3'[t] \varphi'[t] - 6AL\pi\rho q_1[t] \sin[2\alpha[t]] \\
& q_3'[t] \varphi'[t] - 24AL^2\rho \cos[2\alpha[t]] q_3[t] \alpha'[t] \varphi'[t] - \\
& 12AL\pi\rho \cos[2\alpha[t]] q_1[t] q_3[t] \alpha'[t] \varphi'[t] - \\
& 4AL^3\pi\rho \sin[2\alpha[t]] \alpha'[t] \varphi'[t] - 24AL^2\rho q_1[t] \sin[2\alpha[t]] \alpha'[t] \varphi'[t] - \\
& 6AL\pi\rho q_1[t]^2 \sin[2\alpha[t]] \alpha'[t] \varphi'[t] + \\
& 6AL\pi\rho q_3[t]^2 \sin[2\alpha[t]] \alpha'[t] \varphi'[t] - \\
& 12L^2\pi \sin[2\alpha[t]] M_p \alpha'[t] \varphi'[t] + 12AL\rho \cos[\alpha[t]] \\
& (2L \cos[\alpha[t]] + \pi \cos[\alpha[t]] q_1[t] - \pi q_3[t] \sin[\alpha[t]]) \\
& q_1'[t] (\theta'[t] + \varphi'[t]) + 12AL^2\rho \cos[\alpha[t]] q_2''[t] + \\
& 6AL\pi\rho \cos[\alpha[t]] q_1[t] q_2''[t] - 6AL\pi\rho q_3[t] \sin[\alpha[t]] q_2''[t] + \\
& 6AL\rho q_2[t] (2\pi \sin[\alpha[t]] q_1'[t] \alpha'[t] + 2\pi \cos[\alpha[t]] q_3'[t] \alpha'[t] + \\
& 2L \cos[\alpha[t]] \alpha'[t]^2 + \pi \cos[\alpha[t]] q_1[t] \alpha'[t]^2 - \\
& \pi q_3[t] \sin[\alpha[t]] \alpha'[t]^2 + 2\pi q_2'[t] \theta'[t] + 2\pi q_2'[t] \varphi'[t] - \\
& \pi \cos[\alpha[t]] q_1''[t] + \pi \sin[\alpha[t]] q_3''[t] + \pi \cos[\alpha[t]] q_3[t] \alpha''[t] + \\
& 2L \sin[\alpha[t]] \alpha''[t] + \pi q_1[t] \sin[\alpha[t]] \alpha''[t]) + \\
& 12L^2\pi \theta''[t] + 2AL^3\pi\rho \theta''[t] + 2AL^3\pi\rho \cos[2\alpha[t]] \theta''[t] + \\
& 12AL^2\rho q_1[t] \theta''[t] + 12AL^2\rho \cos[2\alpha[t]] q_1[t] \theta''[t] + \\
& 3AL\pi\rho q_1[t]^2 \theta''[t] + 3AL\pi\rho \cos[2\alpha[t]] q_1[t]^2 \theta''[t] + \\
& 3AL\pi\rho q_3[t]^2 \theta''[t] - 3AL\pi\rho \cos[2\alpha[t]] q_3[t]^2 \theta''[t] + \\
& 12AL\pi\rho R[t]^2 \theta''[t] - 12AL^2\rho q_3[t] \sin[2\alpha[t]] \theta''[t] - \\
& 6AL\pi\rho q_1[t] q_3[t] \sin[2\alpha[t]] \theta''[t] + 6\pi R[t]^2 M_m \theta''[t] + \\
& 6L^2\pi M_p \theta''[t] + 6L^2\pi \cos[2\alpha[t]] M_p \theta''[t] + 12\pi R[t]^2 M_p \theta''[t] + \\
& 3\pi M_m r_m^2 \theta''[t] + 6\pi M_p r_p^2 \theta''[t] + 3\pi M_p r_T^2 \theta''[t] + 12L^2\pi \varphi''[t] + \\
& 2AL^3\pi\rho \varphi''[t] + 2AL^3\pi\rho \cos[2\alpha[t]] \varphi''[t] + 12AL^2\rho q_1[t] \varphi''[t] + \\
& 12AL^2\rho \cos[2\alpha[t]] q_1[t] \varphi''[t] + 3AL\pi\rho q_1[t]^2 \varphi''[t] + \\
& 3AL\pi\rho \cos[2\alpha[t]] q_1[t]^2 \varphi''[t] + 3AL\pi\rho q_3[t]^2 \varphi''[t] - \\
& 3AL\pi\rho \cos[2\alpha[t]] q_3[t]^2 \varphi''[t] - 12AL^2\rho q_3[t] \sin[2\alpha[t]] \varphi''[t] - \\
& 6AL\pi\rho q_1[t] q_3[t] \sin[2\alpha[t]] \varphi''[t] + 6L^2\pi M_p \varphi''[t] + \\
& 6L^2\pi \cos[2\alpha[t]] M_p \varphi''[t] + 3\pi M_m r_m^2 \varphi''[t] + 6\pi M_p r_p^2 \varphi''[t] + \\
& 3\pi M_p r_T^2 \varphi''[t] + 6AL\pi\rho q_2[t]^2 (\theta''[t] + \varphi''[t]) = 0
\end{aligned}$$

iii. For $q_1[t]$

$$\frac{1}{8 L^3 \pi} \left(15 \pi^5 q_1[t]^3 T_0 - 2 \pi q_1[t] \left(3 \pi^4 q_2[t]^2 (A E_0 - T_0) + 3 \pi^4 q_3[t]^2 (A E_0 - T_0) + 2 A L^2 (-2 E_0 \pi^2 + 2 L^2 \rho \alpha'[t]^2 + 2 L^2 \rho \cos[\alpha[t]]^2 \theta'[t]^2 + 4 L^2 \rho \cos[\alpha[t]]^2 \theta'[t] \varphi'[t] + L^2 \rho \varphi'[t]^2 + L^2 \rho \cos[2 \alpha[t]] \varphi'[t]^2 \right) \right) - 4 A L^4 \rho \left(4 \pi q_3'[t] \alpha'[t] + 4 L \alpha'[t]^2 + 4 \pi \cos[\alpha[t]] q_2'[t] \theta'[t] + 2 L \theta'[t]^2 + 2 L \cos[2 \alpha[t]] \theta'[t]^2 - \pi q_3[t] \sin[2 \alpha[t]] \theta'[t]^2 + 4 \pi \cos[\alpha[t]] q_2'[t] \varphi'[t] + 4 L \theta'[t] \varphi'[t] + 4 L \cos[2 \alpha[t]] \theta'[t] \varphi'[t] - 2 \pi q_3[t] \sin[2 \alpha[t]] \theta'[t] \varphi'[t] + 2 L \varphi'[t]^2 + 2 L \cos[2 \alpha[t]] \varphi'[t]^2 - \pi q_3[t] \sin[2 \alpha[t]] \varphi'[t]^2 - 2 \pi q_1''[t] + 2 \pi q_3[t] \alpha''[t] + 2 \pi \cos[\alpha[t]] q_2[t] \theta''[t] + 2 \pi \cos[\alpha[t]] q_2[t] \varphi''[t] \right)$$

iv. For $q_2[t]$

$$\frac{1}{8 L^3 \pi} \left(3 \pi^5 q_2[t]^3 (A E_0 - T_0) + 6 \pi^5 q_1[t]^2 q_2[t] (-A E_0 + T_0) + \pi q_2[t] \left(3 \pi^4 q_3[t]^2 (A E_0 - T_0) - 8 (-L^2 \pi^2 T_0 + A L^4 \rho (\theta'[t] + \varphi'[t])^2) \right) - 8 A L^4 \rho \left(2 \pi \cos[\alpha[t]] q_3[t] \alpha'[t] \theta'[t] + 4 L \sin[\alpha[t]] \alpha'[t] \theta'[t] + 2 \pi \cos[\alpha[t]] q_3[t] \alpha'[t] \varphi'[t] + 4 L \sin[\alpha[t]] \alpha'[t] \varphi'[t] - 2 \pi \cos[\alpha[t]] q_1'[t] (\theta'[t] + \varphi'[t]) + 2 \pi \sin[\alpha[t]] q_3'[t] (\theta'[t] + \varphi'[t]) - \pi q_2''[t] - 2 L \cos[\alpha[t]] \theta''[t] + \pi q_3[t] \sin[\alpha[t]] \theta''[t] - 2 L \cos[\alpha[t]] \varphi''[t] + \pi q_3[t] \sin[\alpha[t]] \varphi''[t] - 8 A L^4 \pi \rho q_1[t] (2 \sin[\alpha[t]] \alpha'[t] (\theta'[t] + \varphi'[t]) - \cos[\alpha[t]] (\theta''[t] + \varphi''[t])) \right)$$

v. For $q_3[t]$

$$\frac{1}{8 L^3 \pi} \left(3 A E_0 \pi^5 q_3[t]^3 + 3 \pi^5 q_2[t]^2 q_3[t] (A E_0 - T_0) + 8 L^2 \pi^3 q_3[t] T_0 - 3 \pi^5 q_3[t]^3 T_0 + 6 \pi^5 q_1[t]^2 q_3[t] (-A E_0 + T_0) + 16 A L^4 \pi \rho q_1'[t] \alpha'[t] - 8 A L^4 \pi \rho q_3[t] \alpha'[t]^2 + 16 A L^4 \pi \rho \sin[\alpha[t]] q_2'[t] \theta'[t] - 4 A L^4 \pi \rho q_3[t] \theta'[t]^2 + 4 A L^4 \pi \rho \cos[2 \alpha[t]] q_3[t] \theta'[t]^2 + 8 A L^5 \rho \sin[2 \alpha[t]] \theta'[t]^2 + 16 A L^4 \pi \rho \sin[\alpha[t]] q_2'[t] \varphi'[t] - 8 A L^4 \pi \rho q_3[t] \theta'[t] \varphi'[t] + 8 A L^4 \pi \rho \cos[2 \alpha[t]] q_3[t] \theta'[t] \varphi'[t] + 16 A L^5 \rho \sin[2 \alpha[t]] \theta'[t] \varphi'[t] - 4 A L^4 \pi \rho q_3[t] \varphi'[t]^2 + 4 A L^4 \pi \rho \cos[2 \alpha[t]] q_3[t] \varphi'[t]^2 + 8 A L^5 \rho \sin[2 \alpha[t]] \varphi'[t]^2 + 8 A L^4 \pi \rho q_3''[t] + 16 A L^5 \rho \alpha''[t] + 4 A L^4 \pi \rho q_1[t] (\sin[2 \alpha[t]] \theta'[t]^2 + 2 \sin[2 \alpha[t]] \theta'[t] \varphi'[t] + \sin[2 \alpha[t]] \varphi'[t]^2 + 2 \alpha''[t]) + 8 A L^4 \pi \rho q_2[t] \sin[\alpha[t]] (\theta''[t] + \varphi''[t]) \right) = 0$$

vi. For $\alpha[t]$

$$- \tau \sin[\gamma[t]] +$$

$$L \mu \cos[\varphi[t]] R[t] \left(\frac{1}{(L^2 - 2 L \cos[\alpha[t]] \cos[\varphi[t]] R[t] + R[t]^2)^{3/2}} - \right.$$

$$\begin{aligned}
& \left. \frac{1}{(L^2 + 2 L \cos[\alpha[t]] \cos[\varphi[t]] R[t] + R[t]^2)^{3/2}} \right\} \sin[\alpha[t]] M_p - \\
& \sum_{i=1}^n - (A (-1 + 2 i) L^2 \mu \rho \cos[\varphi[t]] R[t] \sin[\alpha[t]]) / \left(2 n^2 \right. \\
& \quad \left. \left(\frac{(-1 + 2 i)^2 L^2}{4 n^2} - \frac{(-1 + 2 i) L \cos[\alpha[t]] \cos[\varphi[t]] R[t]}{n} + R[t]^2 \right)^{3/2} \right) - \\
& \sum_{i=1}^n (A (-1 + 2 i) L^2 \mu \rho \cos[\varphi[t]] R[t] \sin[\alpha[t]]) / \\
& \quad \left(2 n^2 \left(\frac{(-1 + 2 i)^2 L^2}{4 n^2} + \frac{(-1 + 2 i) L \cos[\alpha[t]] \cos[\varphi[t]] R[t]}{n} + R[t]^2 \right)^{3/2} \right) + \\
& \frac{4 A L^2 \rho q_1'[t] \alpha'[t]}{\pi} + 2 A L \rho q_1[t] q_1'[t] \alpha'[t] + \\
& 2 A L \rho q_3[t] q_3'[t] \alpha'[t] + 2 A L \rho \cos[\alpha[t]] q_3[t] q_2'[t] \theta'[t] + \\
& \frac{4 A L^2 \rho \sin[\alpha[t]] q_2'[t] \theta'[t]}{\pi} + \\
& 2 A L \rho q_1[t] \sin[\alpha[t]] q_2'[t] \theta'[t] + \\
& \frac{2 A L^2 \rho \cos[2 \alpha[t]] q_3[t] \theta'[t]^2}{\pi} + A L \rho \cos[2 \alpha[t]] q_1[t] q_3[t] \theta'[t]^2 + \\
& A L \rho \cos[\alpha[t]] q_1[t]^2 \sin[\alpha[t]] \theta'[t]^2 - \\
& A L \rho \cos[\alpha[t]] q_3[t]^2 \sin[\alpha[t]] \theta'[t]^2 + \frac{1}{3} A L^3 \rho \sin[2 \alpha[t]] \theta'[t]^2 + \\
& \frac{2 A L^2 \rho q_1[t] \sin[2 \alpha[t]] \theta'[t]^2}{\pi} + L^2 \sin[2 \alpha[t]] M_p \theta'[t]^2 + \\
& 2 A L \rho \cos[\alpha[t]] q_3[t] q_2'[t] \varphi'[t] + \frac{4 A L^2 \rho \sin[\alpha[t]] q_2'[t] \varphi'[t]}{\pi} + \\
& 2 A L \rho q_1[t] \sin[\alpha[t]] q_2'[t] \varphi'[t] + \frac{4 A L^2 \rho \cos[2 \alpha[t]] q_3[t] \theta'[t] \varphi'[t]}{\pi} + \\
& 2 A L \rho \cos[2 \alpha[t]] q_1[t] q_3[t] \theta'[t] \varphi'[t] + \frac{2}{3} A L^3 \rho \sin[2 \alpha[t]] \theta'[t] \varphi'[t] + \\
& \frac{4 A L^2 \rho q_1[t] \sin[2 \alpha[t]] \theta'[t] \varphi'[t]}{\pi} + A L \rho q_1[t]^2 \sin[2 \alpha[t]] \theta'[t] \varphi'[t] - \\
& A L \rho q_3[t]^2 \sin[2 \alpha[t]] \theta'[t] \varphi'[t] + 2 L^2 \sin[2 \alpha[t]] M_p \theta'[t] \varphi'[t] + \\
& \frac{2 A L^2 \rho \cos[2 \alpha[t]] q_3[t] \varphi'[t]^2}{\pi} + A L \rho \cos[2 \alpha[t]] q_1[t] q_3[t] \varphi'[t]^2 + \\
& A L \rho \cos[\alpha[t]] q_1[t]^2 \sin[\alpha[t]] \varphi'[t]^2 - \\
& A L \rho \cos[\alpha[t]] q_3[t]^2 \sin[\alpha[t]] \varphi'[t]^2 + \\
& \frac{1}{3} A L^3 \rho \sin[2 \alpha[t]] \varphi'[t]^2 + \frac{2 A L^2 \rho q_1[t] \sin[2 \alpha[t]] \varphi'[t]^2}{\pi} + \\
& L^2 \sin[2 \alpha[t]] M_p \varphi'[t]^2 - A L \rho q_3[t] q_1''[t] + \frac{2 A L^2 \rho q_3''[t]}{\pi} + \\
& A L \rho q_1[t] q_3''[t] + 3 h^2 \alpha''[t] + 2 L^2 \alpha''[t] + \frac{2}{3} A L^3 \rho \alpha''[t] + \\
& \frac{4 A L^2 \rho q_1[t] \alpha''[t]}{\pi} + A L \rho q_1[t]^2 \alpha''[t] + A L \rho q_3[t]^2 \alpha''[t] +
\end{aligned}$$

$$\begin{aligned}
& 2 L^2 M_p \alpha'' [t] + \frac{1}{4} M_m r_m^2 \alpha'' [t] + \frac{1}{2} M_p r_p^2 \alpha'' [t] + \frac{1}{2} M_p r_T^2 \alpha'' [t] + \\
& A L \rho \cos [\alpha [t]] q_2 [t] q_3 [t] \theta'' [t] + \frac{2 A L^2 \rho q_2 [t] \sin [\alpha [t]] \theta'' [t]}{\pi} + \\
& A L \rho q_1 [t] q_2 [t] \sin [\alpha [t]] \theta'' [t] + A L \rho \cos [\alpha [t]] q_2 [t] q_3 [t] \theta'' [t] + \\
& \frac{2 A L^2 \rho q_2 [t] \sin [\alpha [t]] \theta'' [t]}{\pi} + A L \rho q_1 [t] q_2 [t] \sin [\alpha [t]] \theta'' [t] = 0
\end{aligned}$$

vii. For R [t]

$$\begin{aligned}
& \frac{1}{2} \left(\frac{2 \mu M_m}{R [t]^2} + \frac{\mu (-2 L \cos [\alpha [t]] \cos [\varphi [t]] + 2 R [t]) M_p}{(L^2 - 2 L \cos [\alpha [t]] \cos [\varphi [t]] R [t] + R [t]^2)^{3/2}} + \right. \\
& \left. \frac{2 \mu (L \cos [\alpha [t]] \cos [\varphi [t]] + R [t]) M_p}{(L^2 + 2 L \cos [\alpha [t]] \cos [\varphi [t]] R [t] + R [t]^2)^{3/2}} - \right. \\
& \left. 2 \sum_{i=1}^n - \left(A L \mu \rho \left(- \frac{(-1 + 2 i) L \cos [\alpha [t]] \cos [\varphi [t]]}{n} + 2 R [t] \right) \right) / \right. \\
& \left. \left(2 n \left(\frac{(-1 + 2 i)^2 L^2}{4 n^2} - \frac{(-1 + 2 i) L \cos [\alpha [t]] \cos [\varphi [t]] R [t]}{n} + R [t]^2 \right)^{3/2} \right) - \right. \\
& \left. 2 \sum_{i=1}^n - \left(A L \mu \rho \left(\frac{(-1 + 2 i) L \cos [\alpha [t]] \cos [\varphi [t]]}{n} + 2 R [t] \right) \right) / \right. \\
& \left. \left(2 n \left(\frac{(-1 + 2 i)^2 L^2}{4 n^2} + \frac{(-1 + 2 i) L \cos [\alpha [t]] \cos [\varphi [t]] R [t]}{n} + R [t]^2 \right)^{3/2} \right) \right) - \\
& R [t] (M_m + 2 (A L \rho + M_p)) \theta' [t]^2 + (M_m + 2 (A L \rho + M_p)) \\
& R'' [\\
& t] = 0
\end{aligned}$$

Appendix D

Derivation of mode shape function

$$u[t] = \left(A1 * \sin\left[\frac{\omega * x}{c}\right] + B1 * \cos\left[\frac{\omega * x}{c}\right] \right) * \sin[\omega * t];$$

$$u' = D[u[t], t]$$

$$u'' = D[u', t]$$

$$ux' = D[u[t], x]$$

$$\omega \cos[t \omega] \left(B1 \cos\left[\frac{x \omega}{c}\right] + A1 \sin\left[\frac{x \omega}{c}\right] \right)$$

$$-\omega^2 \sin[t \omega] \left(B1 \cos\left[\frac{x \omega}{c}\right] + A1 \sin\left[\frac{x \omega}{c}\right] \right)$$

$$\sin[t \omega] \left(\frac{A1 \omega \cos\left[\frac{x \omega}{c}\right]}{c} - \frac{B1 \omega \sin\left[\frac{x \omega}{c}\right]}{c} \right)$$

(*at x=r_m, the ux' and u'' become=...*)

$$u_{r_m} = -\omega^2 \sin[t \omega] \left(B1 \cos\left[\frac{r_m \omega}{c}\right] + A1 \sin\left[\frac{r_m \omega}{c}\right] \right);$$

$$ux_{r_m} = \sin[t \omega] \left(\frac{A1 \omega \cos\left[\frac{r_m \omega}{c}\right]}{c} - \frac{B1 \omega \sin\left[\frac{r_m \omega}{c}\right]}{c} \right);$$

$$t1 = (L - r_m) * ((\varphi'[t])^2) \left(\frac{\rho * A * (L - r_m)}{2} + M_p \right) + Eo * A * ux_{r_m} + M_m * u_{r_m}$$

$$A Eo \sin[t \omega] \left(\frac{A1 \omega \cos\left[\frac{\omega r_m}{c}\right]}{c} - \frac{B1 \omega \sin\left[\frac{\omega r_m}{c}\right]}{c} \right) -$$

$$\omega^2 \sin[t \omega] \left(B1 \cos\left[\frac{\omega r_m}{c}\right] + A1 \sin\left[\frac{\omega r_m}{c}\right] \right) M_m +$$

$$\left(M_p + \frac{1}{2} A \rho (L - r_m) \right) (L - r_m) \varphi'[t]^2$$

(*at $x=r_m$, the u_x' and u'' become=...*)

$$u_{(L-r_p)} = -\omega^2 \sin[t \omega] \left(B1 \cos\left[\frac{(L-r_p) \omega}{c}\right] + A1 \sin\left[\frac{(L-r_p) \omega}{c}\right] \right);$$

$$u_x_{(L-r_p)} = \sin[t \omega] \left(\frac{A1 \omega \cos\left[\frac{(L-r_p) \omega}{c}\right]}{c} - \frac{B1 \omega \sin\left[\frac{(L-r_p) \omega}{c}\right]}{c} \right);$$

$$t2 = r_p * ((\phi' [t])^2) \left(\frac{\rho * A * r_p}{2} + M_p \right) + Eo * A * u_x_{(L-r_p)} + M_p * u_{(L-r_p)}$$

$$A Eo \sin[t \omega] \left(\frac{A1 \omega \cos\left[\frac{\omega (L-r_p)}{c}\right]}{c} - \frac{B1 \omega \sin\left[\frac{\omega (L-r_p)}{c}\right]}{c} \right) -$$

$$\omega^2 \sin[t \omega] \left(B1 \cos\left[\frac{\omega (L-r_p)}{c}\right] + A1 \sin\left[\frac{\omega (L-r_p)}{c}\right] \right) M_p +$$

$$r_p \left(M_p + \frac{1}{2} A \rho r_p \right) \phi' [t]^2$$

eqn = {t1 == 0, t2 == 0}

$$\left\{ A Eo \sin[t \omega] \left(\frac{A1 \omega \cos\left[\frac{\omega r_m}{c}\right]}{c} - \frac{B1 \omega \sin\left[\frac{\omega r_m}{c}\right]}{c} \right) - \right.$$

$$\omega^2 \sin[t \omega] \left(B1 \cos\left[\frac{\omega r_m}{c}\right] + A1 \sin\left[\frac{\omega r_m}{c}\right] \right) M_m +$$

$$\left(M_p + \frac{1}{2} A \rho (L - r_m) \right) (L - r_m) \phi' [t]^2 = 0,$$

$$A Eo \sin[t \omega] \left(\frac{A1 \omega \cos\left[\frac{\omega (L-r_p)}{c}\right]}{c} - \frac{B1 \omega \sin\left[\frac{\omega (L-r_p)}{c}\right]}{c} \right) - \omega^2 \sin[t \omega]$$

$$\left(B1 \cos\left[\frac{\omega (L-r_p)}{c}\right] + A1 \sin\left[\frac{\omega (L-r_p)}{c}\right] \right) M_p + r_p \left(M_p + \frac{1}{2} A \rho r_p \right) \phi' [t]^2 = 0 \}$$

Solve[eqn, {A1, B1}]

$$\left\{ \left\{ A1 \rightarrow - \frac{r_p \left(M_p + \frac{1}{2} A \rho r_p \right) \phi' [t]^2}{\frac{A Eo \omega \cos\left[\frac{\omega (L-r_p)}{c}\right] \sin[t \omega]}{c} - \omega^2 \sin[t \omega] \sin\left[\frac{\omega (L-r_p)}{c}\right] M_p} + \right.$$

$$\left(\left(- \frac{A Eo \omega \sin[t \omega] \sin\left[\frac{\omega (L-r_p)}{c}\right]}{c} - \omega^2 \cos\left[\frac{\omega (L-r_p)}{c}\right] \sin[t \omega] M_p \right) \right)$$

$$\left(\left(\frac{A Eo \omega \cos\left[\frac{\omega (L-r_p)}{c}\right] \sin[t \omega]}{c} - \omega^2 \sin[t \omega] \sin\left[\frac{\omega (L-r_p)}{c}\right] M_p \right) \right)$$

$$\left(M_p + \frac{1}{2} A \rho (L - r_m) \right) (L - r_m) \phi' [t]^2 - \left(\frac{A Eo \omega \cos\left[\frac{\omega r_m}{c}\right] \sin[t \omega]}{c} - \right.$$

$$\left. \left. \omega^2 \sin[t \omega] \sin\left[\frac{\omega r_m}{c}\right] M_m \right) r_p \left(M_p + \frac{1}{2} A \rho r_p \right) \phi' [t]^2 \right) \Big/$$

$$\begin{aligned}
& \left(\left(\frac{A E \omega \cos \left[\frac{\omega (L-r_p)}{c} \right] \sin [t \omega]}{c} - \omega^2 \sin [t \omega] \sin \left[\frac{\omega (L-r_p)}{c} \right] M_p \right) \right. \\
& \left. - \left(\frac{A E \omega \cos \left[\frac{\omega r_m}{c} \right] \sin [t \omega]}{c} - \omega^2 \sin [t \omega] \sin \left[\frac{\omega r_m}{c} \right] M_m \right) \right. \\
& \left. \left(- \frac{A E \omega \sin [t \omega] \sin \left[\frac{\omega (L-r_p)}{c} \right]}{c} - \omega^2 \cos \left[\frac{\omega (L-r_p)}{c} \right] \sin [t \omega] M_p \right) + \right. \\
& \left. \left(- \frac{A E \omega \sin [t \omega] \sin \left[\frac{\omega r_m}{c} \right]}{c} - \omega^2 \cos \left[\frac{\omega r_m}{c} \right] \sin [t \omega] M_m \right) \right. \\
& \left. \left(\frac{A E \omega \cos \left[\frac{\omega (L-r_p)}{c} \right] \sin [t \omega]}{c} - \omega^2 \sin [t \omega] \sin \left[\frac{\omega (L-r_p)}{c} \right] M_p \right) \right) \Bigg) , \\
B1 \rightarrow & - \left(\frac{A E \omega \cos \left[\frac{\omega (L-r_p)}{c} \right] \sin [t \omega]}{c} - \omega^2 \sin [t \omega] \sin \left[\frac{\omega (L-r_p)}{c} \right] M_p \right) \\
& \left(M_p + \frac{1}{2} A \rho (L-r_m) \right) (L-r_m) \varphi' [t]^2 - \\
& \left(\frac{A E \omega \cos \left[\frac{\omega r_m}{c} \right] \sin [t \omega]}{c} - \omega^2 \sin [t \omega] \sin \left[\frac{\omega r_m}{c} \right] M_m \right) \\
& r_p \left(M_p + \frac{1}{2} A \rho r_p \right) \varphi' [t]^2 \Bigg) / \\
& \left(- \left(\frac{A E \omega \cos \left[\frac{\omega r_m}{c} \right] \sin [t \omega]}{c} - \omega^2 \sin [t \omega] \sin \left[\frac{\omega r_m}{c} \right] M_m \right) \right. \\
& \left. \left(- \frac{A E \omega \sin [t \omega] \sin \left[\frac{\omega (L-r_p)}{c} \right]}{c} - \omega^2 \cos \left[\frac{\omega (L-r_p)}{c} \right] \sin [t \omega] M_p \right) + \right. \\
& \left. \left(- \frac{A E \omega \sin [t \omega] \sin \left[\frac{\omega r_m}{c} \right]}{c} - \omega^2 \cos \left[\frac{\omega r_m}{c} \right] \sin [t \omega] M_m \right) \right. \\
& \left. \left(\frac{A E \omega \cos \left[\frac{\omega (L-r_p)}{c} \right] \sin [t \omega]}{c} - \omega^2 \sin [t \omega] \sin \left[\frac{\omega (L-r_p)}{c} \right] M_p \right) \right) \Bigg) \Bigg\} \\
A1 = & - \frac{r_p \left(M_p + \frac{1}{2} A \rho r_p \right) \varphi' [t]^2}{\frac{A E \omega \cos \left[\frac{\omega (L-r_p)}{c} \right] \sin [t \omega]}{c} - \omega^2 \sin [t \omega] \sin \left[\frac{\omega (L-r_p)}{c} \right] M_p} + \\
& \left(\left(- \frac{A E \omega \sin [t \omega] \sin \left[\frac{\omega (L-r_p)}{c} \right]}{c} - \omega^2 \cos \left[\frac{\omega (L-r_p)}{c} \right] \sin [t \omega] M_p \right) \right. \\
& \left. \left(\frac{A E \omega \cos \left[\frac{\omega (L-r_p)}{c} \right] \sin [t \omega]}{c} - \omega^2 \sin [t \omega] \sin \left[\frac{\omega (L-r_p)}{c} \right] M_p \right) \right)
\end{aligned}$$

$$\begin{aligned}
& \left(M_P + \frac{1}{2} A \rho (L - r_m) \right) (L - r_m) \varphi' [t]^2 - \left(\frac{A E \omega \cos \left[\frac{\omega r_m}{c} \right] \sin [t \omega]}{c} - \right. \\
& \left. \omega^2 \sin [t \omega] \sin \left[\frac{\omega r_m}{c} \right] M_m \right) r_P \left(M_P + \frac{1}{2} A \rho r_P \right) \varphi' [t]^2 \Bigg) / \\
& \left(\left(\frac{A E \omega \cos \left[\frac{\omega (L - r_P)}{c} \right] \sin [t \omega]}{c} - \omega^2 \sin [t \omega] \sin \left[\frac{\omega (L - r_P)}{c} \right] M_P \right) \right. \\
& \left(- \left(\frac{A E \omega \cos \left[\frac{\omega r_m}{c} \right] \sin [t \omega]}{c} - \omega^2 \sin [t \omega] \sin \left[\frac{\omega r_m}{c} \right] M_m \right) \right. \\
& \left(- \frac{A E \omega \sin [t \omega] \sin \left[\frac{\omega (L - r_P)}{c} \right]}{c} - \omega^2 \cos \left[\frac{\omega (L - r_P)}{c} \right] \sin [t \omega] M_P \right) + \\
& \left(- \frac{A E \omega \sin [t \omega] \sin \left[\frac{\omega r_m}{c} \right]}{c} - \omega^2 \cos \left[\frac{\omega r_m}{c} \right] \sin [t \omega] M_m \right) \\
& \left. \left. \left. \left(\frac{A E \omega \cos \left[\frac{\omega (L - r_P)}{c} \right] \sin [t \omega]}{c} - \omega^2 \sin [t \omega] \sin \left[\frac{\omega (L - r_P)}{c} \right] M_P \right) \right) \right) \right); \\
B1 = & - \left(\left(\frac{A E \omega \cos \left[\frac{\omega (L - r_P)}{c} \right] \sin [t \omega]}{c} - \omega^2 \sin [t \omega] \sin \left[\frac{\omega (L - r_P)}{c} \right] M_P \right) \right. \\
& \left(M_P + \frac{1}{2} A \rho (L - r_m) \right) (L - r_m) \varphi' [t]^2 - \\
& \left(\frac{A E \omega \cos \left[\frac{\omega r_m}{c} \right] \sin [t \omega]}{c} - \omega^2 \sin [t \omega] \sin \left[\frac{\omega r_m}{c} \right] M_m \right) \\
& \left. r_P \left(M_P + \frac{1}{2} A \rho r_P \right) \varphi' [t]^2 \right) / \\
& \left(- \left(\frac{A E \omega \cos \left[\frac{\omega r_m}{c} \right] \sin [t \omega]}{c} - \omega^2 \sin [t \omega] \sin \left[\frac{\omega r_m}{c} \right] M_m \right) \right. \\
& \left(- \frac{A E \omega \sin [t \omega] \sin \left[\frac{\omega (L - r_P)}{c} \right]}{c} - \omega^2 \cos \left[\frac{\omega (L - r_P)}{c} \right] \sin [t \omega] M_P \right) + \\
& \left(- \frac{A E \omega \sin [t \omega] \sin \left[\frac{\omega r_m}{c} \right]}{c} - \omega^2 \cos \left[\frac{\omega r_m}{c} \right] \sin [t \omega] M_m \right) \\
& \left. \left. \left. \left(\frac{A E \omega \cos \left[\frac{\omega (L - r_P)}{c} \right] \sin [t \omega]}{c} - \omega^2 \sin [t \omega] \sin \left[\frac{\omega (L - r_P)}{c} \right] M_P \right) \right) \right) \right); \\
\text{phi} = & A1 * \sin \left[\frac{x \omega}{c} \right] + B1 * \cos \left[\frac{x \omega}{c} \right] \\
& - \left(\cos \left[\frac{x \omega}{c} \right] \left(\left(\frac{A E \omega \cos \left[\frac{\omega (L - r_P)}{c} \right] \sin [t \omega]}{c} - \omega^2 \sin [t \omega] \sin \left[\frac{\omega (L - r_P)}{c} \right] M_P \right) \right. \right.
\end{aligned}$$

$$\begin{aligned}
& \left(M_P + \frac{1}{2} A \rho (L - r_m) \right) (L - r_m) \varphi' [t]^2 - \\
& \left(\frac{A E o \omega \cos \left[\frac{\omega r_m}{c} \right] \sin [t \omega]}{c} - \omega^2 \sin [t \omega] \sin \left[\frac{\omega r_m}{c} \right] M_m \right) \\
& r_P \left(M_P + \frac{1}{2} A \rho r_P \right) \varphi' [t]^2 \Bigg) / \\
& \left(\left(- \frac{A E o \omega \cos \left[\frac{\omega r_m}{c} \right] \sin [t \omega]}{c} + \omega^2 \sin [t \omega] \sin \left[\frac{\omega r_m}{c} \right] M_m \right) \right. \\
& \left(- \frac{A E o \omega \sin [t \omega] \sin \left[\frac{\omega (L - r_P)}{c} \right]}{c} - \omega^2 \cos \left[\frac{\omega (L - r_P)}{c} \right] \sin [t \omega] M_P \right) + \\
& \left(- \frac{A E o \omega \sin [t \omega] \sin \left[\frac{\omega r_m}{c} \right]}{c} - \omega^2 \cos \left[\frac{\omega r_m}{c} \right] \sin [t \omega] M_m \right) \\
& \left. \left(\frac{A E o \omega \cos \left[\frac{\omega (L - r_P)}{c} \right] \sin [t \omega]}{c} - \omega^2 \sin [t \omega] \sin \left[\frac{\omega (L - r_P)}{c} \right] M_P \right) \right) + \\
& \sin \left[\frac{x \omega}{c} \right] \left(- \frac{r_P \left(M_P + \frac{1}{2} A \rho r_P \right) \varphi' [t]^2}{\frac{A E o \omega \cos \left[\frac{\omega (L - r_P)}{c} \right] \sin [t \omega]}{c} - \omega^2 \sin [t \omega] \sin \left[\frac{\omega (L - r_P)}{c} \right] M_P} + \right. \\
& \left(- \frac{A E o \omega \sin [t \omega] \sin \left[\frac{\omega (L - r_P)}{c} \right]}{c} - \omega^2 \cos \left[\frac{\omega (L - r_P)}{c} \right] \sin [t \omega] M_P \right) \\
& \left(\left(\frac{A E o \omega \cos \left[\frac{\omega (L - r_P)}{c} \right] \sin [t \omega]}{c} - \omega^2 \sin [t \omega] \sin \left[\frac{\omega (L - r_P)}{c} \right] M_P \right) \right. \\
& \left. \left(M_P + \frac{1}{2} A \rho (L - r_m) \right) (L - r_m) \varphi' [t]^2 - \left(\frac{A E o \omega \cos \left[\frac{\omega r_m}{c} \right] \sin [t \omega]}{c} - \right. \right. \\
& \left. \left. \omega^2 \sin [t \omega] \sin \left[\frac{\omega r_m}{c} \right] M_m \right) r_P \left(M_P + \frac{1}{2} A \rho r_P \right) \varphi' [t]^2 \right) / \\
& \left(\left(\frac{A E o \omega \cos \left[\frac{\omega (L - r_P)}{c} \right] \sin [t \omega]}{c} - \omega^2 \sin [t \omega] \sin \left[\frac{\omega (L - r_P)}{c} \right] M_P \right) \right. \\
& \left(- \frac{A E o \omega \cos \left[\frac{\omega r_m}{c} \right] \sin [t \omega]}{c} + \omega^2 \sin [t \omega] \sin \left[\frac{\omega r_m}{c} \right] M_m \right) \\
& \left(- \frac{A E o \omega \sin [t \omega] \sin \left[\frac{\omega (L - r_P)}{c} \right]}{c} - \omega^2 \cos \left[\frac{\omega (L - r_P)}{c} \right] \sin [t \omega] M_P \right) + \\
& \left. \left(- \frac{A E o \omega \sin [t \omega] \sin \left[\frac{\omega r_m}{c} \right]}{c} - \omega^2 \cos \left[\frac{\omega r_m}{c} \right] \sin [t \omega] M_m \right) \right)
\end{aligned}$$

$$\begin{aligned}
& \left(\frac{A E_0 \omega \cos \left[\frac{\omega (L - r_p)}{c} \right] \sin [t \omega]}{c} - \omega^2 \sin [t \omega] \sin \left[\frac{\omega (L - r_p)}{c} \right] M_p \right) \Bigg) \Bigg) \Bigg) \\
& \left(c \csc [t \omega] \left(2 c \omega \sin \left[\frac{\omega (-L + x + r_p)}{c} \right] M_p^2 (L - r_m) + \right. \right. \\
& M_p \left(A L \left(2 E_0 \cos \left[\frac{\omega (-L + x + r_p)}{c} \right] + c L \rho \omega \sin \left[\frac{\omega (-L + x + r_p)}{c} \right] \right) - \right. \\
& 2 A \left(E_0 \cos \left[\frac{\omega (-L + x + r_p)}{c} \right] + c L \rho \omega \sin \left[\frac{\omega (-L + x + r_p)}{c} \right] \right) r_m + \\
& A c \rho \omega \sin \left[\frac{\omega (-L + x + r_p)}{c} \right] r_m^2 - \\
& 2 \left(A E_0 \cos \left[\frac{\omega (x - r_m)}{c} \right] + c \omega \sin \left[\frac{\omega (x - r_m)}{c} \right] M_m \right) r_p \Bigg) + \\
& A \rho \left(A E_0 L^2 \cos \left[\frac{\omega (-L + x + r_p)}{c} \right] - 2 A E_0 L \cos \left[\frac{\omega (-L + x + r_p)}{c} \right] r_m + \right. \\
& A E_0 \cos \left[\frac{\omega (-L + x + r_p)}{c} \right] r_m^2 - \\
& \left. \left(A E_0 \cos \left[\frac{\omega (x - r_m)}{c} \right] + c \omega \sin \left[\frac{\omega (x - r_m)}{c} \right] M_m \right) r_p^2 \right) \Bigg) \varphi' [t]^2 \Bigg) / \\
& \left(2 \omega \left(A E_0 \left(A E_0 \sin \left[\frac{\omega (-L + r_m + r_p)}{c} \right] - c \omega \cos \left[\frac{\omega (-L + r_m + r_p)}{c} \right] M_p \right) + \right. \right. \\
& \left. \left. c \omega M_m \left(A E_0 \cos \left[\frac{\omega (-L + r_m + r_p)}{c} \right] + c \omega \sin \left[\frac{\omega (-L + r_m + r_p)}{c} \right] M_p \right) \right) \right) \Bigg)
\end{aligned}$$

Mode Shape Function :

$$\begin{aligned}
\phi [x] = & \left(c \csc [t \omega] \left(2 c \omega \sin [\alpha] M_p^2 (L - r_m) + M_p \left(A L \left(2 E_0 \cos [\alpha] + c L \rho \omega \sin [\alpha] \right) - \right. \right. \right. \\
& 2 A \left(E_0 \cos [\alpha] + c L \rho \omega \sin [\alpha] \right) r_m + A c \rho \omega \sin [\alpha] r_m^2 - \\
& 2 \left(A E_0 \cos [\beta] + c \omega \sin [\beta] M_m \right) r_p \Bigg) + \\
& A \rho \left(A E_0 L^2 \cos [\alpha] - 2 A E_0 L \cos [\alpha] r_m + A E_0 \cos [\alpha] r_m^2 - \right. \\
& \left. \left(A E_0 \cos [\beta] + c \omega \sin [\beta] M_m \right) r_p^2 \right) \Bigg) \varphi' [t]^2 \Bigg) / \\
& \left(2 \omega \left(A E_0 \left(A E_0 \sin [\alpha] - c \omega \cos [\alpha] M_p \right) + c \omega M_m \left(A E_0 \cos [\alpha] + c \omega \sin [\alpha] M_p \right) \right) \right)
\end{aligned}$$

where,

$$\begin{aligned}
\alpha &= \frac{\omega (-L + x + r_p)}{c} \\
\beta &= \frac{\omega (x - r_m)}{c}
\end{aligned}$$

Appendix E

EOM : fixed – mass boundary condition (axial vibration)

$$U1 = \frac{r_p * ((\varphi' [t])^2) \left(\frac{\rho A x r_p}{2} + M_p \right)}{M_p * (\omega^2) * \sin\left[\frac{\omega L}{c1}\right]}$$

(*Introduce Ax, Bx,

and Cx in mode shape function for position of Mp and Mm*)

i. For $\varphi [t]$

$$\begin{aligned} \text{eqns1} = & \left(\left(\csc [t \omega]^3 \left(-24 L^3 \mu \omega^2 R [t] \left(\sqrt{L^2 - 2 L \cos [\varphi [t]] R [t] + R [t]^2} - \right. \right. \right. \right. \\ & \left. \left. \left. \sqrt{L^2 + 2 L \cos [\varphi [t]] R [t] + R [t]^2} \right) \sin [t \omega]^3 \sin [\varphi [t]] M_p - \right. \right. \\ & \left. \left. 24 L \mu \omega^2 R [t]^3 \left(\sqrt{L^2 - 2 L \cos [\varphi [t]] R [t] + R [t]^2} - \right. \right. \right. \\ & \left. \left. \left. \sqrt{L^2 + 2 L \cos [\varphi [t]] R [t] + R [t]^2} \right) \sin [t \omega]^3 \sin [\varphi [t]] M_p + \right. \right. \\ & \left. L^4 \sqrt{L^2 - 2 L \cos [\varphi [t]] R [t] + R [t]^2} \sqrt{L^2 + 2 L \cos [\varphi [t]] R [t] + R [t]^2} \right. \\ & \left. \left(-24 \omega^2 \sin [t \omega]^3 \sum_{i=1}^n - (A (-1 + 2 i) L^2 \mu \rho R [t] \sin [\varphi [t]]) \right) / \left(2 n^2 \right. \right. \\ & \left. \left. \left(\frac{(-1 + 2 i)^2 L^2}{4 n^2} - \frac{(-1 + 2 i) L \cos [\varphi [t]] R [t]}{n} + R [t]^2 \right)^{3/2} \right) \right) - \\ & 24 \omega^2 \sin [t \omega]^3 \sum_{i=1}^n (A (-1 + 2 i) L^2 \mu \rho R [t] \sin [\varphi [t]]) / \left(2 n^2 \right. \\ & \left. \left(\frac{(-1 + 2 i)^2 L^2}{4 n^2} + \frac{(-1 + 2 i) L \cos [\varphi [t]] R [t]}{n} + R [t]^2 \right)^{3/2} \right) - \\ & 48 A L U1^2 \rho \omega^3 \cos [t \omega] q1 [t]^2 \theta' [t] + 24 A c1 U1^2 \rho \omega^2 \\ & \cos [t \omega] q1 [t]^2 \sin \left[\frac{2 L \omega}{c1} \right] \theta' [t] + \\ & 48 A c1 L U1 \rho \omega^2 \cos \left[\frac{L \omega}{c1} \right] q1 [t] \sin [2 t \omega] \theta' [t] - \\ & 48 A c1^2 U1 \rho \omega q1 [t] \sin \left[\frac{L \omega}{c1} \right] \sin [2 t \omega] \theta' [t] - \\ & 48 U1^2 \omega^3 \cos [t \omega] q1 [t]^2 M_p \theta' [t] + 48 U1^2 \omega^3 \cos \left[\frac{L \omega}{c1} \right]^2 \cos [t \omega] \\ & q1 [t]^2 M_p \theta' [t] - 48 U1^2 \omega^3 \cos [t \omega] q1 [t]^2 \sin \left[\frac{L \omega}{c1} \right]^2 M_p \theta' [t] - \\ & 48 L U1 \omega^3 q1 [t] \sin \left[\frac{L \omega}{c1} \right] \sin [2 t \omega] M_p \theta' [t] - \\ & 48 A c1 L U1 \rho \omega \cos \left[\frac{L \omega}{c1} \right] q1' [t] \theta' [t] + 48 A c1 L U1 \rho \omega \cos \left[\frac{L \omega}{c1} \right] \end{aligned}$$

$$\begin{aligned}
& \text{Cos}[t \omega]^2 q1'[t] \theta'[t] + 48 A c1^2 U1 \rho \text{Sin}\left[\frac{L \omega}{c1}\right] q1'[t] \theta'[t] - \\
& 48 A c1^2 U1 \rho \text{Cos}[t \omega]^2 \text{Sin}\left[\frac{L \omega}{c1}\right] q1'[t] \theta'[t] + \\
& 48 A L U1^2 \rho \omega^2 q1[t] \text{Sin}[t \omega] q1'[t] \theta'[t] - \\
& 24 A c1 U1^2 \rho \omega q1[t] \text{Sin}\left[\frac{2 L \omega}{c1}\right] \text{Sin}[t \omega] q1'[t] \theta'[t] - \\
& 48 A c1 L U1 \rho \omega \text{Cos}\left[\frac{L \omega}{c1}\right] \text{Sin}[t \omega]^2 q1'[t] \theta'[t] + \\
& 48 A c1^2 U1 \rho \text{Sin}\left[\frac{L \omega}{c1}\right] \text{Sin}[t \omega]^2 q1'[t] \theta'[t] + \\
& 48 L U1 \omega^2 \text{Sin}\left[\frac{L \omega}{c1}\right] M_p q1'[t] \theta'[t] - 48 L U1 \omega^2 \text{Cos}[t \omega]^2 \text{Sin}\left[\frac{L \omega}{c1}\right] \\
& M_p q1'[t] \theta'[t] + 48 U1^2 \omega^2 q1[t] \text{Sin}[t \omega] M_p q1'[t] \theta'[t] - \\
& 48 U1^2 \omega^2 \text{Cos}\left[\frac{L \omega}{c1}\right]^2 q1[t] \text{Sin}[t \omega] M_p q1'[t] \theta'[t] + \\
& 48 U1^2 \omega^2 q1[t] \text{Sin}\left[\frac{L \omega}{c1}\right]^2 \text{Sin}[t \omega] M_p q1'[t] \theta'[t] + \\
& 48 L U1 \omega^2 \text{Sin}\left[\frac{L \omega}{c1}\right] \text{Sin}[t \omega]^2 M_p q1'[t] \theta'[t] - \\
& 48 A L U1^2 \rho \omega^3 \text{Cos}[t \omega] q1[t]^2 \phi'[t] + \\
& 24 A c1 U1^2 \rho \omega^2 \text{Cos}[t \omega] q1[t]^2 \text{Sin}\left[\frac{2 L \omega}{c1}\right] \phi'[t] + \\
& 48 A c1 L U1 \rho \omega^2 \text{Cos}\left[\frac{L \omega}{c1}\right] q1[t] \text{Sin}[2 t \omega] \phi'[t] - \\
& 48 A c1^2 U1 \rho \omega q1[t] \text{Sin}\left[\frac{L \omega}{c1}\right] \text{Sin}[2 t \omega] \phi'[t] - \\
& 48 U1^2 \omega^3 \text{Cos}[t \omega] q1[t]^2 M_p \phi'[t] + 48 U1^2 \omega^3 \text{Cos}\left[\frac{L \omega}{c1}\right]^2 \text{Cos}[t \omega] \\
& q1[t]^2 M_p \phi'[t] - 48 U1^2 \omega^3 \text{Cos}[t \omega] q1[t]^2 \text{Sin}\left[\frac{L \omega}{c1}\right]^2 M_p \phi'[t] - \\
& 48 L U1 \omega^3 q1[t] \text{Sin}\left[\frac{L \omega}{c1}\right] \text{Sin}[2 t \omega] M_p \phi'[t] - \\
& 48 A c1 L U1 \rho \omega \text{Cos}\left[\frac{L \omega}{c1}\right] q1'[t] \phi'[t] + 48 A c1 L U1 \rho \omega \text{Cos}\left[\frac{L \omega}{c1}\right] \\
& \text{Cos}[t \omega]^2 q1'[t] \phi'[t] + 48 A c1^2 U1 \rho \text{Sin}\left[\frac{L \omega}{c1}\right] q1'[t] \phi'[t] - \\
& 48 A c1^2 U1 \rho \text{Cos}[t \omega]^2 \text{Sin}\left[\frac{L \omega}{c1}\right] q1'[t] \phi'[t] + \\
& 48 A L U1^2 \rho \omega^2 q1[t] \text{Sin}[t \omega] q1'[t] \phi'[t] - \\
& 24 A c1 U1^2 \rho \omega q1[t] \text{Sin}\left[\frac{2 L \omega}{c1}\right] \text{Sin}[t \omega] q1'[t] \phi'[t] - \\
& 48 A c1 L U1 \rho \omega \text{Cos}\left[\frac{L \omega}{c1}\right] \text{Sin}[t \omega]^2 q1'[t] \phi'[t] + \\
& 48 A c1^2 U1 \rho \text{Sin}\left[\frac{L \omega}{c1}\right] \text{Sin}[t \omega]^2 q1'[t] \phi'[t] + \\
& 48 L U1 \omega^2 \text{Sin}\left[\frac{L \omega}{c1}\right] M_p q1'[t] \phi'[t] - 48 L U1 \omega^2 \text{Cos}[t \omega]^2 \text{Sin}\left[\frac{L \omega}{c1}\right] \\
& M_p q1'[t] \phi'[t] + 48 U1^2 \omega^2 q1[t] \text{Sin}[t \omega] M_p q1'[t] \phi'[t] - \\
& 48 U1^2 \omega^2 \text{Cos}\left[\frac{L \omega}{c1}\right]^2 q1[t] \text{Sin}[t \omega] M_p q1'[t] \phi'[t] +
\end{aligned}$$

$$\begin{aligned}
& 48 U_1^2 \omega^2 q_1[t] \sin\left[\frac{L\omega}{c_1}\right]^2 \sin[t\omega] M_p q_1'[t] \varphi'[t] + \\
& 48 L U_1 \omega^2 \sin\left[\frac{L\omega}{c_1}\right] \sin[t\omega]^2 M_p q_1'[t] \varphi'[t] - \\
& 48 A c_1 L U_1 \rho \omega \cos\left[\frac{L\omega}{c_1}\right] q_1[t] \theta''[t] + 48 A c_1 L U_1 \rho \omega \cos\left[\frac{L\omega}{c_1}\right] \\
& \quad \cos[t\omega]^2 q_1[t] \theta''[t] + 48 A c_1^2 U_1 \rho q_1[t] \sin\left[\frac{L\omega}{c_1}\right] \theta''[t] - \\
& 48 A c_1^2 U_1 \rho \cos[t\omega]^2 q_1[t] \sin\left[\frac{L\omega}{c_1}\right] \theta''[t] + \\
& 15 A L^3 \rho \omega^2 \sin[t\omega] \theta''[t] - 15 A L^3 \rho \omega^2 \cos[t\omega]^2 \sin[t\omega] \theta''[t] + \\
& 24 A L U_1^2 \rho \omega^2 q_1[t]^2 \sin[t\omega] \theta''[t] - \\
& 12 A c_1 U_1^2 \rho \omega q_1[t]^2 \sin\left[\frac{2L\omega}{c_1}\right] \sin[t\omega] \theta''[t] - \\
& 48 A c_1 L U_1 \rho \omega \cos\left[\frac{L\omega}{c_1}\right] q_1[t] \sin[t\omega]^2 \theta''[t] + \\
& 48 A c_1^2 U_1 \rho q_1[t] \sin\left[\frac{L\omega}{c_1}\right] \sin[t\omega]^2 \theta''[t] + \\
& 5 A L^3 \rho \omega^2 \sin[t\omega]^3 \theta''[t] + 48 L U_1 \omega^2 q_1[t] \sin\left[\frac{L\omega}{c_1}\right] M_p \theta''[t] - \\
& 48 L U_1 \omega^2 \cos[t\omega]^2 q_1[t] \sin\left[\frac{L\omega}{c_1}\right] M_p \theta''[t] + \\
& 36 L^2 \omega^2 \sin[t\omega] M_p \theta''[t] - 36 L^2 \omega^2 \cos[t\omega]^2 \sin[t\omega] M_p \theta''[t] + \\
& 24 U_1^2 \omega^2 q_1[t]^2 \sin[t\omega] M_p \theta''[t] - 24 U_1^2 \omega^2 \cos\left[\frac{L\omega}{c_1}\right]^2 q_1[t]^2 \\
& \quad \sin[t\omega] M_p \theta''[t] + 24 U_1^2 \omega^2 q_1[t]^2 \sin\left[\frac{L\omega}{c_1}\right]^2 \sin[t\omega] M_p \theta''[t] + \\
& 48 L U_1 \omega^2 q_1[t] \sin\left[\frac{L\omega}{c_1}\right] \sin[t\omega]^2 M_p \theta''[t] + \\
& 12 L^2 \omega^2 \sin[t\omega]^3 M_p \theta''[t] + 9 \omega^2 \sin[t\omega] M_{mm} r_m^2 \theta''[t] - \\
& 9 \omega^2 \cos[t\omega]^2 \sin[t\omega] M_{mm} r_m^2 \theta''[t] + 3 \omega^2 \sin[t\omega]^3 M_{mm} r_m^2 \theta''[t] + \\
& 18 \omega^2 \sin[t\omega] M_p r_p^2 \theta''[t] - 18 \omega^2 \cos[t\omega]^2 \sin[t\omega] M_p r_p^2 \theta''[t] + \\
& 6 \omega^2 \sin[t\omega]^3 M_p r_p^2 \theta''[t] + 9 A L \rho \omega^2 \sin[t\omega] r_T^2 \theta''[t] - \\
& 9 A L \rho \omega^2 \cos[t\omega]^2 \sin[t\omega] r_T^2 \theta''[t] + 3 A L \rho \omega^2 \sin[t\omega]^3 \\
& \quad r_T^2 \theta''[t] - 48 A c_1 L U_1 \rho \omega \cos\left[\frac{L\omega}{c_1}\right] q_1[t] \varphi''[t] + \\
& 48 A c_1 L U_1 \rho \omega \cos\left[\frac{L\omega}{c_1}\right] \cos[t\omega]^2 q_1[t] \varphi''[t] + \\
& 48 A c_1^2 U_1 \rho q_1[t] \sin\left[\frac{L\omega}{c_1}\right] \varphi''[t] - \\
& 48 A c_1^2 U_1 \rho \cos[t\omega]^2 q_1[t] \sin\left[\frac{L\omega}{c_1}\right] \varphi''[t] + \\
& 15 A L^3 \rho \omega^2 \sin[t\omega] \varphi''[t] - 15 A L^3 \rho \omega^2 \cos[t\omega]^2 \sin[t\omega] \varphi''[t] + \\
& 24 A L U_1^2 \rho \omega^2 q_1[t]^2 \sin[t\omega] \varphi''[t] - \\
& 12 A c_1 U_1^2 \rho \omega q_1[t]^2 \sin\left[\frac{2L\omega}{c_1}\right] \sin[t\omega] \varphi''[t] - \\
& 48 A c_1 L U_1 \rho \omega \cos\left[\frac{L\omega}{c_1}\right] q_1[t] \sin[t\omega]^2 \varphi''[t] + \\
& 48 A c_1^2 U_1 \rho q_1[t] \sin\left[\frac{L\omega}{c_1}\right] \sin[t\omega]^2 \varphi''[t] +
\end{aligned}$$

$$\begin{aligned}
& 5 A L^3 \rho \omega^2 \sin[t \omega]^3 \varphi''[t] + 48 L U_1 \omega^2 q_1[t] \sin\left[\frac{L \omega}{c_1}\right] M_p \varphi''[t] - \\
& 48 L U_1 \omega^2 \cos[t \omega]^2 q_1[t] \sin\left[\frac{L \omega}{c_1}\right] M_p \varphi''[t] + \\
& 36 L^2 \omega^2 \sin[t \omega] M_p \varphi''[t] - 36 L^2 \omega^2 \cos[t \omega]^2 \sin[t \omega] M_p \varphi''[t] + \\
& 24 U_1^2 \omega^2 q_1[t]^2 \sin[t \omega] M_p \varphi''[t] - 24 U_1^2 \omega^2 \cos\left[\frac{L \omega}{c_1}\right]^2 q_1[t]^2 \\
& \sin[t \omega] M_p \varphi''[t] + 24 U_1^2 \omega^2 q_1[t]^2 \sin\left[\frac{L \omega}{c_1}\right]^2 \sin[t \omega] M_p \varphi''[t] + \\
& 48 L U_1 \omega^2 q_1[t] \sin\left[\frac{L \omega}{c_1}\right] \sin[t \omega]^2 M_p \varphi''[t] + \\
& 12 L^2 \omega^2 \sin[t \omega]^3 M_p \varphi''[t] + 9 \omega^2 \sin[t \omega] M_{mm} r_m^2 \varphi''[t] - \\
& 9 \omega^2 \cos[t \omega]^2 \sin[t \omega] M_{mm} r_m^2 \varphi''[t] + 3 \omega^2 \sin[t \omega]^3 M_{mm} r_m^2 \varphi''[t] + \\
& 18 \omega^2 \sin[t \omega] M_p r_p^2 \varphi''[t] - 18 \omega^2 \cos[t \omega]^2 \sin[t \omega] M_p r_p^2 \varphi''[t] + \\
& 6 \omega^2 \sin[t \omega]^3 M_p r_p^2 \varphi''[t] + 9 A L \rho \omega^2 \sin[t \omega] r_T^2 \varphi''[t] - 9 A L \rho \\
& \omega^2 \cos[t \omega]^2 \sin[t \omega] r_T^2 \varphi''[t] + 3 A L \rho \omega^2 \sin[t \omega]^3 r_T^2 \varphi''[t] \Big) + \\
& R[t]^4 \sqrt{L^2 - 2 L \cos[\varphi[t]]} R[t] + R[t]^2 \\
& \sqrt{L^2 + 2 L \cos[\varphi[t]]} R[t] + R[t]^2 \\
& \left(-24 \omega^2 \sin[t \omega]^3 \sum_{i=1}^n - (A (-1 + 2 i) L^2 \mu \rho R[t] \sin[\varphi[t]]) \right) / \left(2 n^2 \right. \\
& \left. \left(\frac{(-1 + 2 i)^2 L^2}{4 n^2} - \frac{(-1 + 2 i) L \cos[\varphi[t]] R[t]}{n} + R[t]^2 \right)^{3/2} \right) - \\
& 24 \omega^2 \sin[t \omega]^3 \sum_{i=1}^n (A (-1 + 2 i) L^2 \mu \rho R[t] \sin[\varphi[t]]) / \left(2 n^2 \right. \\
& \left. \left(\frac{(-1 + 2 i)^2 L^2}{4 n^2} + \frac{(-1 + 2 i) L \cos[\varphi[t]] R[t]}{n} + R[t]^2 \right)^{3/2} \right) - \\
& 48 A L U_1^2 \rho \omega^3 \cos[t \omega] q_1[t]^2 \theta'[t] + 24 A c_1 U_1^2 \rho \omega^2 \\
& \cos[t \omega] q_1[t]^2 \sin\left[\frac{2 L \omega}{c_1}\right] \theta'[t] + \\
& 48 A c_1 L U_1 \rho \omega^2 \cos\left[\frac{L \omega}{c_1}\right] q_1[t] \sin[2 t \omega] \theta'[t] - \\
& 48 A c_1^2 U_1 \rho \omega q_1[t] \sin\left[\frac{L \omega}{c_1}\right] \sin[2 t \omega] \theta'[t] - \\
& 48 U_1^2 \omega^3 \cos[t \omega] q_1[t]^2 M_p \theta'[t] + 48 U_1^2 \omega^3 \cos\left[\frac{L \omega}{c_1}\right]^2 \cos[t \omega] \\
& q_1[t]^2 M_p \theta'[t] - 48 U_1^2 \omega^3 \cos[t \omega] q_1[t]^2 \sin\left[\frac{L \omega}{c_1}\right]^2 M_p \theta'[t] - \\
& 48 L U_1 \omega^3 q_1[t] \sin\left[\frac{L \omega}{c_1}\right] \sin[2 t \omega] M_p \theta'[t] - \\
& 48 A c_1 L U_1 \rho \omega \cos\left[\frac{L \omega}{c_1}\right] q_1'[t] \theta'[t] + 48 A c_1 L U_1 \rho \omega \cos\left[\frac{L \omega}{c_1}\right] \\
& \cos[t \omega]^2 q_1'[t] \theta'[t] + 48 A c_1^2 U_1 \rho \sin\left[\frac{L \omega}{c_1}\right] q_1'[t] \theta'[t] - \\
& 48 A c_1^2 U_1 \rho \cos[t \omega]^2 \sin\left[\frac{L \omega}{c_1}\right] q_1'[t] \theta'[t] +
\end{aligned}$$

$$\begin{aligned}
& 48 A L U 1^2 \rho \omega^2 q_1[t] \sin[t \omega] q_1'[t] \theta'[t] - \\
& 24 A c_1 U 1^2 \rho \omega q_1[t] \sin\left[\frac{2 L \omega}{c_1}\right] \sin[t \omega] q_1'[t] \theta'[t] - \\
& 48 A c_1 L U 1 \rho \omega \cos\left[\frac{L \omega}{c_1}\right] \sin[t \omega]^2 q_1'[t] \theta'[t] + \\
& 48 A c_1^2 U 1 \rho \sin\left[\frac{L \omega}{c_1}\right] \sin[t \omega]^2 q_1'[t] \theta'[t] + \\
& 48 L U 1 \omega^2 \sin\left[\frac{L \omega}{c_1}\right] M_p q_1'[t] \theta'[t] - 48 L U 1 \omega^2 \cos[t \omega]^2 \sin\left[\frac{L \omega}{c_1}\right] \\
& M_p q_1'[t] \theta'[t] + 48 U 1^2 \omega^2 q_1[t] \sin[t \omega] M_p q_1'[t] \theta'[t] - \\
& 48 U 1^2 \omega^2 \cos\left[\frac{L \omega}{c_1}\right]^2 q_1[t] \sin[t \omega] M_p q_1'[t] \theta'[t] + \\
& 48 U 1^2 \omega^2 q_1[t] \sin\left[\frac{L \omega}{c_1}\right]^2 \sin[t \omega] M_p q_1'[t] \theta'[t] + \\
& 48 L U 1 \omega^2 \sin\left[\frac{L \omega}{c_1}\right] \sin[t \omega]^2 M_p q_1'[t] \theta'[t] - \\
& 48 A L U 1^2 \rho \omega^3 \cos[t \omega] q_1[t]^2 \phi'[t] + \\
& 24 A c_1 U 1^2 \rho \omega^2 \cos[t \omega] q_1[t]^2 \sin\left[\frac{2 L \omega}{c_1}\right] \phi'[t] + \\
& 48 A c_1 L U 1 \rho \omega^2 \cos\left[\frac{L \omega}{c_1}\right] q_1[t] \sin[2 t \omega] \phi'[t] - \\
& 48 A c_1^2 U 1 \rho \omega q_1[t] \sin\left[\frac{L \omega}{c_1}\right] \sin[2 t \omega] \phi'[t] - \\
& 48 U 1^2 \omega^3 \cos[t \omega] q_1[t]^2 M_p \phi'[t] + 48 U 1^2 \omega^3 \cos\left[\frac{L \omega}{c_1}\right]^2 \cos[t \omega] \\
& q_1[t]^2 M_p \phi'[t] - 48 U 1^2 \omega^3 \cos[t \omega] q_1[t]^2 \sin\left[\frac{L \omega}{c_1}\right]^2 M_p \phi'[t] - \\
& 48 L U 1 \omega^3 q_1[t] \sin\left[\frac{L \omega}{c_1}\right] \sin[2 t \omega] M_p \phi'[t] - \\
& 48 A c_1 L U 1 \rho \omega \cos\left[\frac{L \omega}{c_1}\right] q_1'[t] \phi'[t] + 48 A c_1 L U 1 \rho \omega \cos\left[\frac{L \omega}{c_1}\right] \\
& \cos[t \omega]^2 q_1'[t] \phi'[t] + 48 A c_1^2 U 1 \rho \sin\left[\frac{L \omega}{c_1}\right] q_1'[t] \phi'[t] - \\
& 48 A c_1^2 U 1 \rho \cos[t \omega]^2 \sin\left[\frac{L \omega}{c_1}\right] q_1'[t] \phi'[t] + \\
& 48 A L U 1^2 \rho \omega^2 q_1[t] \sin[t \omega] q_1'[t] \phi'[t] - \\
& 24 A c_1 U 1^2 \rho \omega q_1[t] \sin\left[\frac{2 L \omega}{c_1}\right] \sin[t \omega] q_1'[t] \phi'[t] - \\
& 48 A c_1 L U 1 \rho \omega \cos\left[\frac{L \omega}{c_1}\right] \sin[t \omega]^2 q_1'[t] \phi'[t] + \\
& 48 A c_1^2 U 1 \rho \sin\left[\frac{L \omega}{c_1}\right] \sin[t \omega]^2 q_1'[t] \phi'[t] + \\
& 48 L U 1 \omega^2 \sin\left[\frac{L \omega}{c_1}\right] M_p q_1'[t] \phi'[t] - 48 L U 1 \omega^2 \cos[t \omega]^2 \sin\left[\frac{L \omega}{c_1}\right] \\
& M_p q_1'[t] \phi'[t] + 48 U 1^2 \omega^2 q_1[t] \sin[t \omega] M_p q_1'[t] \phi'[t] - \\
& 48 U 1^2 \omega^2 \cos\left[\frac{L \omega}{c_1}\right]^2 q_1[t] \sin[t \omega] M_p q_1'[t] \phi'[t] + \\
& 48 U 1^2 \omega^2 q_1[t] \sin\left[\frac{L \omega}{c_1}\right]^2 \sin[t \omega] M_p q_1'[t] \phi'[t] + \\
& 48 L U 1 \omega^2 \sin\left[\frac{L \omega}{c_1}\right] \sin[t \omega]^2 M_p q_1'[t] \phi'[t] -
\end{aligned}$$

$$\begin{aligned}
& 48 A c_1 L U_1 \rho \omega \cos\left[\frac{L \omega}{c_1}\right] q_1[t] \theta''[t] + 48 A c_1 L U_1 \rho \omega \cos\left[\frac{L \omega}{c_1}\right] \\
& \cos[t \omega]^2 q_1[t] \theta''[t] + 48 A c_1^2 U_1 \rho q_1[t] \sin\left[\frac{L \omega}{c_1}\right] \theta''[t] - \\
& 48 A c_1^2 U_1 \rho \cos[t \omega]^2 q_1[t] \sin\left[\frac{L \omega}{c_1}\right] \theta''[t] + \\
& 15 A L^3 \rho \omega^2 \sin[t \omega] \theta''[t] - 15 A L^3 \rho \omega^2 \cos[t \omega]^2 \sin[t \omega] \theta''[t] + \\
& 24 A L U_1^2 \rho \omega^2 q_1[t]^2 \sin[t \omega] \theta''[t] - \\
& 12 A c_1 U_1^2 \rho \omega q_1[t]^2 \sin\left[\frac{2 L \omega}{c_1}\right] \sin[t \omega] \theta''[t] - \\
& 48 A c_1 L U_1 \rho \omega \cos\left[\frac{L \omega}{c_1}\right] q_1[t] \sin[t \omega]^2 \theta''[t] + \\
& 48 A c_1^2 U_1 \rho q_1[t] \sin\left[\frac{L \omega}{c_1}\right] \sin[t \omega]^2 \theta''[t] + \\
& 5 A L^3 \rho \omega^2 \sin[t \omega]^3 \theta''[t] + 48 L U_1 \omega^2 q_1[t] \sin\left[\frac{L \omega}{c_1}\right] M_p \theta''[t] - \\
& 48 L U_1 \omega^2 \cos[t \omega]^2 q_1[t] \sin\left[\frac{L \omega}{c_1}\right] M_p \theta''[t] + \\
& 36 L^2 \omega^2 \sin[t \omega] M_p \theta''[t] - 36 L^2 \omega^2 \cos[t \omega]^2 \sin[t \omega] M_p \theta''[t] + \\
& 24 U_1^2 \omega^2 q_1[t]^2 \sin[t \omega] M_p \theta''[t] - \\
& 24 U_1^2 \omega^2 \cos\left[\frac{L \omega}{c_1}\right]^2 q_1[t]^2 \sin[t \omega] M_p \theta''[t] + \\
& 24 U_1^2 \omega^2 q_1[t]^2 \sin\left[\frac{L \omega}{c_1}\right]^2 \sin[t \omega] M_p \theta''[t] + \\
& 48 L U_1 \omega^2 q_1[t] \sin\left[\frac{L \omega}{c_1}\right] \sin[t \omega]^2 M_p \theta''[t] + \\
& 12 L^2 \omega^2 \sin[t \omega]^3 M_p \theta''[t] + 9 \omega^2 \sin[t \omega] M_{mm} r_m^2 \theta''[t] - \\
& 9 \omega^2 \cos[t \omega]^2 \sin[t \omega] M_{mm} r_m^2 \theta''[t] + 3 \omega^2 \sin[t \omega]^3 M_{mm} r_m^2 \theta''[t] + \\
& 18 \omega^2 \sin[t \omega] M_p r_p^2 \theta''[t] - 18 \omega^2 \cos[t \omega]^2 \sin[t \omega] M_p r_p^2 \theta''[t] + \\
& 6 \omega^2 \sin[t \omega]^3 M_p r_p^2 \theta''[t] + 9 A L \rho \omega^2 \sin[t \omega] r_T^2 \theta''[t] - \\
& 9 A L \rho \omega^2 \cos[t \omega]^2 \sin[t \omega] r_T^2 \theta''[t] + 3 A L \rho \omega^2 \sin[t \omega]^3 \\
& r_T^2 \theta''[t] - 48 A c_1 L U_1 \rho \omega \cos\left[\frac{L \omega}{c_1}\right] q_1[t] \varphi''[t] + \\
& 48 A c_1 L U_1 \rho \omega \cos\left[\frac{L \omega}{c_1}\right] \cos[t \omega]^2 q_1[t] \varphi''[t] + \\
& 48 A c_1^2 U_1 \rho q_1[t] \sin\left[\frac{L \omega}{c_1}\right] \varphi''[t] - \\
& 48 A c_1^2 U_1 \rho \cos[t \omega]^2 q_1[t] \sin\left[\frac{L \omega}{c_1}\right] \varphi''[t] + \\
& 15 A L^3 \rho \omega^2 \sin[t \omega] \varphi''[t] - 15 A L^3 \rho \omega^2 \cos[t \omega]^2 \sin[t \omega] \varphi''[t] + \\
& 24 A L U_1^2 \rho \omega^2 q_1[t]^2 \sin[t \omega] \varphi''[t] - \\
& 12 A c_1 U_1^2 \rho \omega q_1[t]^2 \sin\left[\frac{2 L \omega}{c_1}\right] \sin[t \omega] \varphi''[t] - \\
& 48 A c_1 L U_1 \rho \omega \cos\left[\frac{L \omega}{c_1}\right] q_1[t] \sin[t \omega]^2 \varphi''[t] + \\
& 48 A c_1^2 U_1 \rho q_1[t] \sin\left[\frac{L \omega}{c_1}\right] \sin[t \omega]^2 \varphi''[t] + \\
& 5 A L^3 \rho \omega^2 \sin[t \omega]^3 \varphi''[t] + 48 L U_1 \omega^2 q_1[t] \sin\left[\frac{L \omega}{c_1}\right] M_p \varphi''[t] - \\
& 48 L U_1 \omega^2 \cos[t \omega]^2 q_1[t] \sin\left[\frac{L \omega}{c_1}\right] M_p \varphi''[t] +
\end{aligned}$$

$$\begin{aligned}
& 36 L^2 \omega^2 \sin[t \omega] M_p \varphi''[t] - 36 L^2 \omega^2 \cos[t \omega]^2 \sin[t \omega] M_p \varphi''[t] + \\
& 24 U_1^2 \omega^2 q_1[t]^2 \sin[t \omega] M_p \varphi''[t] - \\
& 24 U_1^2 \omega^2 \cos\left[\frac{L \omega}{c_1}\right]^2 q_1[t]^2 \sin[t \omega] M_p \varphi''[t] + \\
& 24 U_1^2 \omega^2 q_1[t]^2 \sin\left[\frac{L \omega}{c_1}\right]^2 \sin[t \omega] M_p \varphi''[t] + \\
& 48 L U_1 \omega^2 q_1[t] \sin\left[\frac{L \omega}{c_1}\right] \sin[t \omega]^2 M_p \varphi''[t] + \\
& 12 L^2 \omega^2 \sin[t \omega]^3 M_p \varphi''[t] + 9 \omega^2 \sin[t \omega] M_{mm} r_m^2 \varphi''[t] - \\
& 9 \omega^2 \cos[t \omega]^2 \sin[t \omega] M_{mm} r_m^2 \varphi''[t] + 3 \omega^2 \sin[t \omega]^3 M_{mm} r_m^2 \varphi''[t] + \\
& 18 \omega^2 \sin[t \omega] M_p r_p^2 \varphi''[t] - 18 \omega^2 \cos[t \omega]^2 \sin[t \omega] M_p r_p^2 \varphi''[t] + \\
& 6 \omega^2 \sin[t \omega]^3 M_p r_p^2 \varphi''[t] + 9 A L \rho \omega^2 \sin[t \omega] r_T^2 \varphi''[t] - 9 A L \rho \\
& \left. \omega^2 \cos[t \omega]^2 \sin[t \omega] r_T^2 \varphi''[t] + 3 A L \rho \omega^2 \sin[t \omega]^3 r_T^2 \varphi''[t] \right) - \\
& L^2 R[t]^2 \left(2 \cos[2 \varphi[t]] \sqrt{L^2 - 2 L \cos[\varphi[t]] R[t] + R[t]^2} \right. \\
& \left. \sqrt{L^2 + 2 L \cos[\varphi[t]] R[t] + R[t]^2} \left(-24 \omega^2 \sin[t \omega]^3 \sum_{i=1}^n - (A (-1 + \right. \right. \\
& \left. \left. 2 i) L^2 \mu \rho R[t] \sin[\varphi[t]]) \right) / \left(2 n^2 \left(\frac{(-1 + 2 i)^2 L^2}{4 n^2} - \right. \right. \right. \\
& \left. \left. \left. \frac{(-1 + 2 i) L \cos[\varphi[t]] R[t]}{n} + R[t]^2 \right)^{3/2} \right) - \right. \\
& \left. 24 \omega^2 \sin[t \omega]^3 \sum_{i=1}^n (A (-1 + 2 i) L^2 \mu \rho R[t] \sin[\varphi[t]]) / \right. \\
& \left. \left(2 n^2 \left(\frac{(-1 + 2 i)^2 L^2}{4 n^2} + \frac{(-1 + 2 i) L \cos[\varphi[t]] R[t]}{n} + \right. \right. \right. \\
& \left. \left. \left. R[t]^2 \right)^{3/2} \right) - 48 A L U_1^2 \rho \omega^3 \cos[t \omega] q_1[t]^2 \theta'[t] + \right. \\
& 24 A c_1 U_1^2 \rho \omega^2 \cos[t \omega] q_1[t]^2 \sin\left[\frac{2 L \omega}{c_1}\right] \theta'[t] + \\
& 48 A c_1 L U_1 \rho \omega^2 \cos\left[\frac{L \omega}{c_1}\right] q_1[t] \sin[2 t \omega] \theta'[t] - \\
& 48 A c_1^2 U_1 \rho \omega q_1[t] \sin\left[\frac{L \omega}{c_1}\right] \sin[2 t \omega] \theta'[t] - \\
& 48 A c_1 L U_1 \rho \omega \cos\left[\frac{L \omega}{c_1}\right] q_1'[t] \theta'[t] + 48 A c_1 L U_1 \rho \omega \cos\left[\right. \\
& \left. \frac{L \omega}{c_1} \right] \cos[t \omega]^2 q_1'[t] \theta'[t] + 48 A c_1^2 U_1 \rho \sin\left[\frac{L \omega}{c_1}\right] q_1'[t] \\
& \left. \theta'[t] - 48 A c_1^2 U_1 \rho \cos[t \omega]^2 \sin\left[\frac{L \omega}{c_1}\right] q_1'[t] \theta'[t] + \right. \\
& 48 A L U_1^2 \rho \omega^2 q_1[t] \sin[t \omega] q_1'[t] \theta'[t] - 24 A c_1 U_1^2 \\
& \rho \omega q_1[t] \sin\left[\frac{2 L \omega}{c_1}\right] \sin[t \omega] q_1'[t] \theta'[t] - 48 A c_1 L U_1 \rho \\
& \left. \omega \cos\left[\frac{L \omega}{c_1}\right] \sin[t \omega]^2 q_1'[t] \theta'[t] + 48 A c_1^2 U_1 \rho \sin\left[\frac{L \omega}{c_1}\right] \right)
\end{aligned}$$

$$\begin{aligned}
& \sin[t\omega]^2 q_1'[t] \theta'[t] - 48 A L U_1^2 \rho \omega^3 \cos[t\omega] q_1[t]^2 \varphi'[t] + \\
& 24 A c_1 U_1^2 \rho \omega^2 \cos[t\omega] q_1[t]^2 \sin\left[\frac{2L\omega}{c_1}\right] \varphi'[t] + \\
& 48 A c_1 L U_1 \rho \omega^2 \cos\left[\frac{L\omega}{c_1}\right] q_1[t] \sin[2t\omega] \varphi'[t] - \\
& 48 A c_1^2 U_1 \rho \omega q_1[t] \sin\left[\frac{L\omega}{c_1}\right] \sin[2t\omega] \varphi'[t] - \\
& 48 A c_1 L U_1 \rho \omega \cos\left[\frac{L\omega}{c_1}\right] q_1'[t] \varphi'[t] + 48 A c_1 L U_1 \rho \omega \cos\left[\frac{L\omega}{c_1}\right] \\
& \cos[t\omega]^2 q_1'[t] \varphi'[t] + 48 A c_1^2 U_1 \rho \sin\left[\frac{L\omega}{c_1}\right] q_1'[t] \\
& t] \varphi'[t] - 48 A c_1^2 U_1 \rho \cos[t\omega]^2 \sin\left[\frac{L\omega}{c_1}\right] q_1'[t] \varphi'[t] + \\
& 48 A L U_1^2 \rho \omega^2 q_1[t] \sin[t\omega] q_1'[t] \varphi'[t] - \\
& 24 A c_1 U_1^2 \rho \omega q_1[t] \sin\left[\frac{2L\omega}{c_1}\right] \sin[t\omega] q_1'[t] \varphi'[t] - \\
& 48 A c_1 L U_1 \rho \omega \cos\left[\frac{L\omega}{c_1}\right] \sin[t\omega]^2 q_1'[t] \varphi'[t] + \\
& 48 A c_1^2 U_1 \rho \sin\left[\frac{L\omega}{c_1}\right] \sin[t\omega]^2 q_1'[t] \varphi'[t] - \\
& 48 A c_1 L U_1 \rho \omega \cos\left[\frac{L\omega}{c_1}\right] q_1[t] \theta''[t] + 48 A c_1 L U_1 \rho \omega \cos\left[\frac{L\omega}{c_1}\right] \\
& \cos[t\omega]^2 q_1[t] \theta''[t] + 48 A c_1^2 U_1 \rho q_1[t] \sin\left[\frac{L\omega}{c_1}\right] \\
& \theta''[t] - 48 A c_1^2 U_1 \rho \cos[t\omega]^2 q_1[t] \sin\left[\frac{L\omega}{c_1}\right] \theta''[t] + \\
& 15 A L^3 \rho \omega^2 \sin[t\omega] \theta''[t] - 15 A L^3 \rho \omega^2 \cos[t\omega]^2 \sin[t\omega] \\
& \theta''[t] + 24 A L U_1^2 \rho \omega^2 q_1[t]^2 \sin[t\omega] \theta''[t] - \\
& 12 A c_1 U_1^2 \rho \omega q_1[t]^2 \sin\left[\frac{2L\omega}{c_1}\right] \sin[t\omega] \theta''[t] - \\
& 48 A c_1 L U_1 \rho \omega \cos\left[\frac{L\omega}{c_1}\right] q_1[t] \sin[t\omega]^2 \theta''[t] + 48 A c_1^2 U_1 \rho \\
& q_1[t] \sin\left[\frac{L\omega}{c_1}\right] \sin[t\omega]^2 \theta''[t] + 5 A L^3 \rho \omega^2 \sin[t\omega]^3 \theta''[t] + \\
& 9 \omega^2 \sin[t\omega] M_{mm} r_m^2 \theta''[t] - 9 \omega^2 \cos[t\omega]^2 \sin[t\omega] M_{mm} r_m^2 \theta''[t] \\
& + 3 \omega^2 \sin[t\omega]^3 M_{mm} r_m^2 \theta''[t] + 9 A L \rho \omega^2 \sin[t\omega] r_T^2 \theta''[t] - \\
& 9 A L \rho \omega^2 \cos[t\omega]^2 \sin[t\omega] r_T^2 \theta''[t] + 3 A L \rho \omega^2 \sin[t\omega]^3 \\
& r_T^2 \theta''[t] - 48 A c_1 L U_1 \rho \omega \cos\left[\frac{L\omega}{c_1}\right] q_1[t] \varphi''[t] + 48 A c_1 L U_1 \\
& \rho \omega \cos\left[\frac{L\omega}{c_1}\right] \cos[t\omega]^2 q_1[t] \varphi''[t] + 48 A c_1^2 U_1 \rho q_1[t] \sin\left[\frac{L\omega}{c_1}\right] \\
& \varphi''[t] - 48 A c_1^2 U_1 \rho \cos[t\omega]^2 q_1[t] \sin\left[\frac{L\omega}{c_1}\right] \varphi''[t] + \\
& 15 A L^3 \rho \omega^2 \sin[t\omega] \varphi''[t] - 15 A L^3 \rho \omega^2 \cos[t\omega]^2 \sin[t\omega] \\
& \varphi''[t] + 24 A L U_1^2 \rho \omega^2 q_1[t]^2 \sin[t\omega] \varphi''[t] - \\
& 12 A c_1 U_1^2 \rho \omega q_1[t]^2 \sin\left[\frac{2L\omega}{c_1}\right] \sin[t\omega] \varphi''[t] - \\
& 48 A c_1 L U_1 \rho \omega \cos\left[\frac{L\omega}{c_1}\right] q_1[t] \sin[t\omega]^2 \varphi''[t] + \\
& 48 A c_1^2 U_1 \rho q_1[t] \sin\left[\frac{L\omega}{c_1}\right] \sin[t\omega]^2 \varphi''[t] +
\end{aligned}$$

ii. For $q_1[t]$

$$\begin{aligned}
 \text{eqn1} &= \frac{1}{2 c_1^2 \omega^2} U_1 \text{Csc}[t \omega] \\
 &\left(U_1 \omega \text{Csc}[t \omega] q_1[t] \left(A \left(\omega^2 \left(2 L (E_0 - c_1^2 \rho) \omega + c_1 (E_0 + c_1^2 \rho) \sin\left[\frac{2 L \omega}{c_1}\right] - \right. \right. \right. \right. \\
 &\quad \left. \left. \left. 2 c_1^2 \rho \text{Csc}[t \omega]^2 \left(-2 L \omega + c_1 \sin\left[\frac{2 L \omega}{c_1}\right] \right) \right) \right) + c_1^2 \rho \right. \\
 &\quad \left. \left(-2 L \omega + c_1 \sin\left[\frac{2 L \omega}{c_1}\right] \right) \theta'[t]^2 + 2 c_1^2 \rho \left(-2 L \omega + c_1 \sin\left[\frac{2 L \omega}{c_1}\right] \right) \right. \\
 &\quad \left. \theta'[t] \varphi'[t] + c_1^2 \rho \left(-2 L \omega + c_1 \sin\left[\frac{2 L \omega}{c_1}\right] \right) \varphi'[t]^2 \right) + \\
 &\quad 2 c_1^2 \omega \text{Csc}[t \omega]^2 \sin\left[\frac{L \omega}{c_1}\right]^2 M_p \left(\omega^2 (3 + \text{Cos}[2 t \omega]) - \right. \\
 &\quad \left. \left. 2 \sin[t \omega]^2 \theta'[t]^2 - 4 \sin[t \omega]^2 \theta'[t] \varphi'[t] - 2 \sin[t \omega]^2 \varphi'[t]^2 \right) \right) - \\
 &c_1^2 \left(-4 \omega^2 \sin\left[\frac{L \omega}{c_1}\right] T_0 + 2 U_1 \omega^2 \text{Cot}[t \omega] \text{Csc}[t \omega] \right. \\
 &\quad \left. \left(A \rho \left(2 L \omega - c_1 \sin\left[\frac{2 L \omega}{c_1}\right] \right) + 4 \omega \sin\left[\frac{L \omega}{c_1}\right]^2 M_p \right) q_1'[t] - \right. \\
 &\quad 2 A c_1 \rho \omega^2 \text{Cot}[t \omega] R[t] \sin[\varphi[t]] \theta'[t] + \\
 &\quad 2 A c_1 \rho \omega^2 \text{Cos}\left[\frac{L \omega}{c_1}\right] \text{Cot}[t \omega] R[t] \sin[\varphi[t]] \theta'[t] + \\
 &\quad 4 A c_1 \rho \omega^2 \text{Cot}[t \omega] R[t] \sin\left[\frac{L \omega}{2 c_1}\right]^2 \sin[\varphi[t]] \theta'[t] - \\
 &\quad 4 A c_1 L \rho \omega \text{Cos}\left[\frac{L \omega}{c_1}\right] \theta'[t]^2 + 2 A c_1 \rho \omega \text{Cos}[\varphi[t]] R[t] \theta'[t]^2 - \\
 &\quad 2 A c_1 \rho \omega \text{Cos}\left[\frac{L \omega}{c_1}\right] \text{Cos}[\varphi[t]] R[t] \theta'[t]^2 - \\
 &\quad 4 A c_1 \rho \omega \text{Cos}[\varphi[t]] R[t] \sin\left[\frac{L \omega}{2 c_1}\right]^2 \theta'[t]^2 + 4 A c_1^2 \rho \sin\left[\frac{L \omega}{c_1}\right] \theta'[t]^2 + \\
 &\quad 4 L \omega^2 \sin\left[\frac{L \omega}{c_1}\right] M_p \theta'[t]^2 - 8 A c_1 L \rho \omega \text{Cos}\left[\frac{L \omega}{c_1}\right] \theta'[t] \varphi'[t] + \\
 &\quad 2 A c_1 \rho \omega \text{Cos}[\varphi[t]] R[t] \theta'[t] \varphi'[t] - \\
 &\quad 2 A c_1 \rho \omega \text{Cos}\left[\frac{L \omega}{c_1}\right] \text{Cos}[\varphi[t]] R[t] \theta'[t] \varphi'[t] - \\
 &\quad 4 A c_1 \rho \omega \text{Cos}[\varphi[t]] R[t] \sin\left[\frac{L \omega}{2 c_1}\right]^2 \theta'[t] \varphi'[t] + \\
 &\quad 8 A c_1^2 \rho \sin\left[\frac{L \omega}{c_1}\right] \theta'[t] \varphi'[t] + 8 L \omega^2 \sin\left[\frac{L \omega}{c_1}\right] M_p \theta'[t] \varphi'[t] - \\
 &\quad 4 A c_1 L \rho \omega \text{Cos}\left[\frac{L \omega}{c_1}\right] \varphi'[t]^2 + 4 A c_1^2 \rho \sin\left[\frac{L \omega}{c_1}\right] \varphi'[t]^2 + \\
 &\quad 4 L \omega^2 \sin\left[\frac{L \omega}{c_1}\right] M_p \varphi'[t]^2 - 2 A L U_1 \rho \omega^2 \text{Csc}[t \omega] q_1''[t] + \\
 &\quad A c_1 U_1 \rho \omega \text{Csc}[t \omega] \sin\left[\frac{2 L \omega}{c_1}\right] q_1''[t] - \\
 &\quad \left. \left. 4 U_1 \omega^2 \text{Csc}[t \omega] \sin\left[\frac{L \omega}{c_1}\right]^2 M_p q_1''[t] \right) \right)
 \end{aligned}$$

Appendix F

EOM 3 D Flexible Tether

i. For $\varphi[\theta]$

$$- \tau \text{Cos}[\alpha[\theta]] \text{Cos}[\gamma[\theta]] +$$

$$L \mu \text{Cos}[\alpha[\theta]] R[\theta] \left(\frac{1}{(L^2 - 2 L \text{Cos}[\alpha[\theta]] \text{Cos}[\varphi[\theta]] R[\theta] + R[\theta]^2)^{3/2}} - \frac{1}{(L^2 + 2 L \text{Cos}[\alpha[\theta]] \text{Cos}[\varphi[\theta]] R[\theta] + R[\theta]^2)^{3/2}} \right) \text{Sin}[\varphi[\theta]] M_p -$$

$$\sum_{i=1}^n \frac{A (-1 + 2 i) L^2 \mu \rho \text{Cos}[\alpha[\theta]] R[\theta] \text{Sin}[\varphi[\theta]]}{2 n^2 \left(\frac{(-1+2 i)^2 L^2}{4 n^2} - \frac{(-1+2 i) L \text{Cos}[\alpha[\theta]] \text{Cos}[\varphi[\theta]] R[\theta]}{n} + R[\theta]^2 \right)^{3/2}} -$$

$$\sum_{i=1}^n \frac{A (-1 + 2 i) L^2 \mu \rho \text{Cos}[\alpha[\theta]] R[\theta] \text{Sin}[\varphi[\theta]]}{2 n^2 \left(\frac{(-1+2 i)^2 L^2}{4 n^2} + \frac{(-1+2 i) L \text{Cos}[\alpha[\theta]] \text{Cos}[\varphi[\theta]] R[\theta]}{n} + R[\theta]^2 \right)^{3/2}} +$$

$$\frac{1}{6 \pi} \left(12 A L \pi \rho q_2[\theta] \theta' q_2'[\theta] (\theta' + \theta' \varphi'[\theta]) - 2 L (-6 A \rho \text{Cos}[\alpha[\theta]] (2 L \text{Cos}[\alpha[\theta]] + \pi \text{Cos}[\alpha[\theta]] q_1[\theta] - \pi q_3[\theta] \text{Sin}[\alpha[\theta]]) \theta' q_1'[\theta] - 3 A \pi \rho q_3[\theta]^2 \text{Sin}[2 \alpha[\theta]] \theta' \alpha'[\theta] + 6 A \rho q_3[\theta] (-\pi \text{Sin}[\alpha[\theta]]^2 \theta' q_3'[\theta] + \text{Cos}[2 \alpha[\theta]] (2 L + \pi q_1[\theta]) \theta' \alpha'[\theta]) + \text{Sin}[2 \alpha[\theta]] (3 A \rho (2 L + \pi q_1[\theta]) \theta' q_3'[\theta] + (12 A L \rho q_1[\theta] + 3 A \pi \rho q_1[\theta]^2 + 2 L \pi (A L \rho + 3 M_p)) \theta' \alpha'[\theta])) (\theta' + \theta' \varphi'[\theta]) + 6 A L \rho (2 L \text{Cos}[\alpha[\theta]] + \pi \text{Cos}[\alpha[\theta]] q_1[\theta] - \pi q_3[\theta] \text{Sin}[\alpha[\theta]]) (\theta' \dot{\theta}' q_2'[\theta] + (\theta')^2 q_2''[\theta]) + 6 A L \rho q_2[\theta] (2 \pi \text{Sin}[\alpha[\theta]] (\theta')^2 q_1'[\theta] \alpha'[\theta] + 2 \pi \text{Cos}[\alpha[\theta]] (\theta')^2 q_3'[\theta] \alpha'[\theta] + 2 L \text{Cos}[\alpha[\theta]] (\theta')^2 \alpha'[\theta]^2 + \pi \text{Cos}[\alpha[\theta]] q_1[\theta] (\theta')^2 \alpha'[\theta]^2 - \pi q_3[\theta] \text{Sin}[\alpha[\theta]] (\theta')^2 \alpha'[\theta]^2 - \pi \text{Cos}[\alpha[\theta]] (\theta' \dot{\theta}' q_1'[\theta] + (\theta')^2 q_1''[\theta]) + \pi \text{Sin}[\alpha[\theta]] (\theta' \dot{\theta}' q_3'[\theta] + (\theta')^2 q_3''[\theta]) + \pi \text{Cos}[\alpha[\theta]] q_3[\theta] (\theta' \dot{\theta}' \alpha'[\theta] + (\theta')^2 \alpha''[\theta]) + 2 L \text{Sin}[\alpha[\theta]] (\theta' \dot{\theta}' \alpha'[\theta] + (\theta')^2 \alpha''[\theta]) + \pi q_1[\theta] \text{Sin}[\alpha[\theta]] (\theta' \dot{\theta}' \alpha'[\theta] + (\theta')^2 \alpha''[\theta])) + 6 A L \pi \rho q_2[\theta]^2 (\theta' \dot{\theta}' + \theta' \dot{\theta}' \varphi'[\theta] + (\theta')^2 \varphi''[\theta]) + (6 A L \pi \rho \text{Cos}[\alpha[\theta]]^2 q_1[\theta]^2 + 6 A L \pi \rho q_3[\theta]^2 \text{Sin}[\alpha[\theta]]^2 + 12 A L \rho \text{Cos}[\alpha[\theta]] q_1[\theta] (2 L \text{Cos}[\alpha[\theta]] - \pi q_3[\theta] \text{Sin}[\alpha[\theta]]) - 12 A L^2 \rho q_3[\theta] \text{Sin}[2 \alpha[\theta]] + \pi (3 M_m r_m^2 + 6 M_p (2 L^2 \text{Cos}[\alpha[\theta]]^2 + r_p^2) + A L \rho (L^2 (3 + 2 \text{Cos}[2 \alpha[\theta]]) + 3 r_T^2))) (\theta' \dot{\theta}' + \theta' \dot{\theta}' \varphi'[\theta] + (\theta')^2 \varphi''[\theta]) \right) = 0$$

ii. For $q1[\theta]$

$$\begin{aligned} \text{eqn1} &= \frac{1}{8 L^3 \pi} \\ & \left(15 \pi^5 q1[\theta]^3 T_0 - 2 \pi q1[\theta] \left(3 \pi^4 q2[\theta]^2 (A E_0 - T_0) + 3 \pi^4 q3[\theta]^2 (A E_0 - T_0) + \right. \right. \\ & \quad 2 A L^2 \left(-2 E_0 \pi^2 + 2 L^2 \rho \text{Cos}[\alpha[\theta]]^2 (\theta')^2 + \right. \\ & \quad \quad 2 L^2 \rho (\theta')^2 \alpha'[\theta]^2 + 4 L^2 \rho \text{Cos}[\alpha[\theta]]^2 (\theta')^2 \varphi'[\theta] + \\ & \quad \quad \left. \left. L^2 \rho (\theta')^2 \varphi'[\theta]^2 + L^2 \rho \text{Cos}[2 \alpha[\theta]] (\theta')^2 \varphi'[\theta]^2 \right) \right) - \\ & 4 A L^4 \rho \left(2 L (\theta')^2 + 2 L \text{Cos}[2 \alpha[\theta]] (\theta')^2 - \pi q3[\theta] \text{Sin}[2 \alpha[\theta]] (\theta')^2 + \right. \\ & \quad 2 \pi \text{Cos}[\alpha[\theta]] q2[\theta] \theta' \dot{\theta} + 4 \pi \text{Cos}[\alpha[\theta]] (\theta')^2 q2'[\theta] + \\ & \quad 4 \pi (\theta')^2 q3'[\theta] \alpha'[\theta] + 4 L (\theta')^2 \alpha'[\theta]^2 + 4 L (\theta')^2 \varphi'[\theta] + \\ & \quad 4 L \text{Cos}[2 \alpha[\theta]] (\theta')^2 \varphi'[\theta] - 2 \pi q3[\theta] \text{Sin}[2 \alpha[\theta]] (\theta')^2 \varphi'[\theta] + \\ & \quad 4 \pi \text{Cos}[\alpha[\theta]] (\theta')^2 q2'[\theta] \varphi'[\theta] + 2 L (\theta')^2 \varphi'[\theta]^2 + \\ & \quad 2 L \text{Cos}[2 \alpha[\theta]] (\theta')^2 \varphi'[\theta]^2 - \pi q3[\theta] \text{Sin}[2 \alpha[\theta]] (\theta')^2 \varphi'[\theta]^2 - \\ & \quad 2 \pi (\theta' \dot{\theta} q1'[\theta] + (\theta')^2 q1''[\theta]) + 2 \pi q3[\theta] (\theta' \dot{\theta} \alpha'[\theta] + (\theta')^2 \alpha''[\theta]) + \\ & \quad \left. \left. 2 \pi \text{Cos}[\alpha[\theta]] q2[\theta] (\theta' \dot{\theta} \varphi'[\theta] + (\theta')^2 \varphi''[\theta]) \right) \right) \end{aligned}$$

iii. For $q2[\theta]$

$$\begin{aligned} & - \frac{1}{8 L^3 \pi} \left(3 \pi^5 q2[\theta]^3 (A E_0 - T_0) + 6 \pi^5 q1[\theta]^2 q2[\theta] (-A E_0 + T_0) + \right. \\ & \quad \pi q2[\theta] \left(3 \pi^4 q3[\theta]^2 (A E_0 - T_0) - 8 (-L^2 \pi^2 T_0 + A L^4 \rho (\theta' + \theta' \varphi'[\theta])^2) \right) - \\ & \quad 8 A L^4 \rho \left(-2 L \text{Cos}[\alpha[\theta]] \theta' \dot{\theta} + \pi q3[\theta] \text{Sin}[\alpha[\theta]] \theta' \dot{\theta} + \right. \\ & \quad \quad 2 \pi \text{Cos}[\alpha[\theta]] q3[\theta] (\theta')^2 \alpha'[\theta] + 4 L \text{Sin}[\alpha[\theta]] (\theta')^2 \alpha'[\theta] + \\ & \quad \quad 2 \pi \text{Cos}[\alpha[\theta]] q3[\theta] (\theta')^2 \alpha'[\theta] \varphi'[\theta] + \\ & \quad \quad 4 L \text{Sin}[\alpha[\theta]] (\theta')^2 \alpha'[\theta] \varphi'[\theta] - 2 \pi \text{Cos}[\alpha[\theta]] \theta' q1'[\theta] (\theta' + \theta' \varphi'[\theta]) + \\ & \quad \quad 2 \pi \text{Sin}[\alpha[\theta]] \theta' q3'[\theta] (\theta' + \theta' \varphi'[\theta]) - \pi (\theta' \dot{\theta} q2'[\theta] + (\theta')^2 q2''[\theta]) - \\ & \quad \quad 2 L \text{Cos}[\alpha[\theta]] (\theta' \dot{\theta} \varphi'[\theta] + (\theta')^2 \varphi''[\theta]) + \\ & \quad \quad \left. \left. \pi q3[\theta] \text{Sin}[\alpha[\theta]] (\theta' \dot{\theta} \varphi'[\theta] + (\theta')^2 \varphi''[\theta]) \right) \right) - \\ & 8 A L^4 \pi \rho q1[\theta] \left(2 \text{Sin}[\alpha[\theta]] \theta' \alpha'[\theta] (\theta' + \theta' \varphi'[\theta]) - \right. \\ & \quad \left. \text{Cos}[\alpha[\theta]] (\theta' \dot{\theta} + \theta' \dot{\theta} \varphi'[\theta] + (\theta')^2 \varphi''[\theta]) \right) = 0 \end{aligned}$$

iv. For $q3[\theta]$

$$\begin{aligned} & \frac{1}{8 L^3 \pi} \left(3 A E_0 \pi^5 q3[\theta]^3 + 3 \pi^5 q2[\theta]^2 q3[\theta] (A E_0 - T_0) + 8 L^2 \pi^3 q3[\theta] T_0 - \right. \\ & \quad 3 \pi^5 q3[\theta]^3 T_0 + 6 \pi^5 q1[\theta]^2 q3[\theta] (-A E_0 + T_0) - 4 A L^4 \pi \rho q3[\theta] (\theta')^2 + \\ & \quad 4 A L^4 \pi \rho \text{Cos}[2 \alpha[\theta]] q3[\theta] (\theta')^2 + 8 A L^5 \rho \text{Sin}[2 \alpha[\theta]] (\theta')^2 + \\ & \quad 16 A L^4 \pi \rho \text{Sin}[\alpha[\theta]] (\theta')^2 q2'[\theta] + 16 A L^4 \pi \rho (\theta')^2 q1'[\theta] \alpha'[\theta] - \\ & \quad 8 A L^4 \pi \rho q3[\theta] (\theta')^2 \alpha'[\theta]^2 - 8 A L^4 \pi \rho q3[\theta] (\theta')^2 \varphi'[\theta] + \\ & \quad 8 A L^4 \pi \rho \text{Cos}[2 \alpha[\theta]] q3[\theta] (\theta')^2 \varphi'[\theta] + 16 A L^5 \rho \text{Sin}[2 \alpha[\theta]] (\theta')^2 \varphi'[\theta] + \\ & \quad 16 A L^4 \pi \rho \text{Sin}[\alpha[\theta]] (\theta')^2 q2'[\theta] \varphi'[\theta] - 4 A L^4 \pi \rho q3[\theta] (\theta')^2 \varphi'[\theta]^2 + \\ & \quad 4 A L^4 \pi \rho \text{Cos}[2 \alpha[\theta]] q3[\theta] (\theta')^2 \varphi'[\theta]^2 + 8 A L^5 \rho \text{Sin}[2 \alpha[\theta]] (\theta')^2 \varphi'[\theta]^2 + \\ & \quad 8 A L^4 \pi \rho (\theta' \dot{\theta} q3'[\theta] + (\theta')^2 q3''[\theta]) + 16 A L^5 \rho (\theta' \dot{\theta} \alpha'[\theta] + (\theta')^2 \alpha''[\theta]) + \\ & \quad 4 A L^4 \pi \rho q1[\theta] \left(\text{Sin}[2 \alpha[\theta]] (\theta')^2 + 2 \text{Sin}[2 \alpha[\theta]] (\theta')^2 \varphi'[\theta] + \right. \\ & \quad \left. \left. \text{Sin}[2 \alpha[\theta]] (\theta')^2 \varphi'[\theta]^2 + 2 (\theta' \dot{\theta} \alpha'[\theta] + (\theta')^2 \alpha''[\theta]) \right) \right) + \end{aligned}$$

$$8 A L^4 \pi \rho q_2[\theta] \sin[\alpha[\theta]] \left(\theta' \dot{\theta}' + \theta' \dot{\theta}' \varphi'[\theta] + (\theta')^2 \varphi''[\theta] \right) = 0$$

v. For $\alpha[\theta]$

$$\text{eqn1} = -\tau \sin[\gamma[\theta]] +$$

$$\begin{aligned} & L \mu \cos[\varphi[\theta]] R[\theta] \left(\frac{1}{\left(L^2 - 2 L \cos[\alpha[\theta]] \cos[\varphi[\theta]] R[\theta] + R[\theta]^2 \right)^{3/2}} - \right. \\ & \quad \left. \frac{1}{\left(L^2 + 2 L \cos[\alpha[\theta]] \cos[\varphi[\theta]] R[\theta] + R[\theta]^2 \right)^{3/2}} \right) \sin[\alpha[\theta]] M_p - \\ & \sum_{i=1}^n \frac{A (-1 + 2i) L^2 \mu \rho \cos[\varphi[\theta]] R[\theta] \sin[\alpha[\theta]]}{2 n^2 \left(\frac{(-1+2i)^2 L^2}{4 n^2} - \frac{(-1+2i) L \cos[\alpha[\theta]] \cos[\varphi[\theta]] R[\theta]}{n} + R[\theta]^2 \right)^{3/2}} - \\ & \sum_{i=1}^n \frac{A (-1 + 2i) L^2 \mu \rho \cos[\varphi[\theta]] R[\theta] \sin[\alpha[\theta]]}{2 n^2 \left(\frac{(-1+2i)^2 L^2}{4 n^2} + \frac{(-1+2i) L \cos[\alpha[\theta]] \cos[\varphi[\theta]] R[\theta]}{n} + R[\theta]^2 \right)^{3/2}} + \\ & \frac{2 A L^2 \rho \cos[2 \alpha[\theta]] q_3[\theta] (\theta')^2}{\pi} + A L \rho \cos[2 \alpha[\theta]] q_1[\theta] q_3[\theta] (\theta')^2 + \\ & A L \rho \cos[\alpha[\theta]] q_1[\theta]^2 \sin[\alpha[\theta]] (\theta')^2 - \\ & A L \rho \cos[\alpha[\theta]] q_3[\theta]^2 \sin[\alpha[\theta]] (\theta')^2 + \frac{1}{3} A L^3 \rho \sin[2 \alpha[\theta]] (\theta')^2 + \\ & \frac{2 A L^2 \rho q_1[\theta] \sin[2 \alpha[\theta]] (\theta')^2}{\pi} + L^2 \sin[2 \alpha[\theta]] M_p (\theta')^2 + \\ & A L \rho \cos[\alpha[\theta]] q_2[\theta] q_3[\theta] \theta' \dot{\theta}' + \frac{2 A L^2 \rho q_2[\theta] \sin[\alpha[\theta]] \theta' \dot{\theta}'}{\pi} + \\ & A L \rho q_1[\theta] q_2[\theta] \sin[\alpha[\theta]] \theta' \dot{\theta}' + 2 A L \rho \cos[\alpha[\theta]] q_3[\theta] (\theta')^2 q_2'[\theta] + \\ & \frac{4 A L^2 \rho \sin[\alpha[\theta]] (\theta')^2 q_2'[\theta]}{\pi} + 2 A L \rho q_1[\theta] \sin[\alpha[\theta]] (\theta')^2 q_2'[\theta] + \\ & \frac{4 A L^2 \rho (\theta')^2 q_1'[\theta] \alpha'[\theta]}{\pi} + 2 A L \rho q_1[\theta] (\theta')^2 q_1'[\theta] \alpha'[\theta] + \\ & 2 A L \rho q_3[\theta] (\theta')^2 q_3'[\theta] \alpha'[\theta] + \frac{4 A L^2 \rho \cos[2 \alpha[\theta]] q_3[\theta] (\theta')^2 \varphi'[\theta]}{\pi} + \\ & 2 A L \rho \cos[2 \alpha[\theta]] q_1[\theta] q_3[\theta] (\theta')^2 \varphi'[\theta] + \\ & \frac{2}{3} A L^3 \rho \sin[2 \alpha[\theta]] (\theta')^2 \varphi'[\theta] + \frac{4 A L^2 \rho q_1[\theta] \sin[2 \alpha[\theta]] (\theta')^2 \varphi'[\theta]}{\pi} + \\ & A L \rho q_1[\theta]^2 \sin[2 \alpha[\theta]] (\theta')^2 \varphi'[\theta] - A L \rho q_3[\theta]^2 \sin[2 \alpha[\theta]] (\theta')^2 \varphi'[\theta] + \\ & 2 L^2 \sin[2 \alpha[\theta]] M_p (\theta')^2 \varphi'[\theta] + 2 A L \rho \cos[\alpha[\theta]] q_3[\theta] (\theta')^2 q_2'[\theta] \varphi'[\theta] + \\ & \frac{4 A L^2 \rho \sin[\alpha[\theta]] (\theta')^2 q_2'[\theta] \varphi'[\theta]}{\pi} + 2 A L \rho q_1[\theta] \sin[\alpha[\theta]] \\ & (\theta')^2 q_2'[\theta] \varphi'[\theta] + \frac{2 A L^2 \rho \cos[2 \alpha[\theta]] q_3[\theta] (\theta')^2 \varphi'[\theta]^2}{\pi} + \\ & A L \rho \cos[2 \alpha[\theta]] q_1[\theta] q_3[\theta] (\theta')^2 \varphi'[\theta]^2 + A L \rho \cos[\alpha[\theta]] q_1[\theta]^2 \\ & \sin[\alpha[\theta]] (\theta')^2 \varphi'[\theta]^2 - A L \rho \cos[\alpha[\theta]] q_3[\theta]^2 \sin[\alpha[\theta]] (\theta')^2 \varphi'[\theta]^2 + \\ & \frac{1}{3} A L^3 \rho \sin[2 \alpha[\theta]] (\theta')^2 \varphi'[\theta]^2 + \frac{2 A L^2 \rho q_1[\theta] \sin[2 \alpha[\theta]] (\theta')^2 \varphi'[\theta]^2}{\pi} + \\ & L^2 \sin[2 \alpha[\theta]] M_p (\theta')^2 \varphi'[\theta]^2 - A L \rho q_3[\theta] \left(\theta' \dot{\theta}' q_1'[\theta] + (\theta')^2 q_1''[\theta] \right) + \end{aligned}$$

$$\begin{aligned}
& \frac{2 \text{A L}^2 \rho (\theta' \dot{\theta}' \text{q3}' [\theta] + (\theta')^2 \text{q3}'' [\theta])}{\pi} + \\
& \text{A L} \rho \text{q1} [\theta] (\theta' \dot{\theta}' \text{q3}' [\theta] + (\theta')^2 \text{q3}'' [\theta]) + \frac{5}{6} \text{A L}^3 \rho (\theta' \dot{\theta}' \alpha' [\theta] + (\theta')^2 \alpha'' [\theta]) + \\
& \frac{4 \text{A L}^2 \rho \text{q1} [\theta] (\theta' \dot{\theta}' \alpha' [\theta] + (\theta')^2 \alpha'' [\theta])}{\pi} + \text{A L} \rho \text{q1} [\theta]^2 \\
& (\theta' \dot{\theta}' \alpha' [\theta] + (\theta')^2 \alpha'' [\theta]) + \text{A L} \rho \text{q3} [\theta]^2 (\theta' \dot{\theta}' \alpha' [\theta] + (\theta')^2 \alpha'' [\theta]) + \\
& \frac{1}{12} \text{h}^2 \text{M}_m (\theta' \dot{\theta}' \alpha' [\theta] + (\theta')^2 \alpha'' [\theta]) + \frac{1}{6} \text{h}^2 \text{M}_p (\theta' \dot{\theta}' \alpha' [\theta] + (\theta')^2 \alpha'' [\theta]) + \\
& 2 \text{L}^2 \text{M}_p (\theta' \dot{\theta}' \alpha' [\theta] + (\theta')^2 \alpha'' [\theta]) + \frac{1}{4} \text{M}_m \text{r}_m^2 (\theta' \dot{\theta}' \alpha' [\theta] + (\theta')^2 \alpha'' [\theta]) + \\
& \frac{1}{2} \text{M}_p \text{r}_p^2 (\theta' \dot{\theta}' \alpha' [\theta] + (\theta')^2 \alpha'' [\theta]) + \frac{1}{2} \text{A L} \rho \text{r}_T^2 (\theta' \dot{\theta}' \alpha' [\theta] + (\theta')^2 \alpha'' [\theta]) + \\
& \text{A L} \rho \text{Cos} [\alpha [\theta]] \text{q2} [\theta] \text{q3} [\theta] (\theta' \dot{\theta}' \varphi' [\theta] + (\theta')^2 \varphi'' [\theta]) + \\
& \frac{2 \text{A L}^2 \rho \text{q2} [\theta] \text{Sin} [\alpha [\theta]] (\theta' \dot{\theta}' \varphi' [\theta] + (\theta')^2 \varphi'' [\theta])}{\pi} + \\
& \text{A L} \rho \text{q1} [\theta] \text{q2} [\theta] \text{Sin} [\alpha [\theta]] (\theta' \dot{\theta}' \varphi' [\theta] + (\theta')^2 \varphi'' [\theta]) = 0
\end{aligned}$$

vi. For $\gamma [\theta]$

$$\frac{1}{12} (\text{M}_m (\text{h}^2 + 3 \text{r}_m^2) + 2 \text{M}_p (\text{h}^2 + 3 \text{r}_p^2 + 6 \text{r}_T^2)) (\theta' \dot{\theta}' \gamma' [\theta] + (\theta')^2 \gamma'' [\theta]) = 0$$